Title

Age-dependent increases in hepatic expression of OX40L and the abundance of ILC3s direct effective immunity to hepatitis B virus

Permalink

https://escholarship.org/uc/item/57j448zj

Author

Jespersen, Jillian Mary

Publication Date

2020

Peer reviewed|Thesis/dissertation

Age-dependent increases in hepatic expression of OX40L and the abundance of
ILC3s direct effective immunity to hepatitis B virus

by
Jillian Mary Jespersen

DISSERTATION
Submitted in partial satisfaction of the requirements for degree of
DOCTOR OF PHILOSOPHY

in

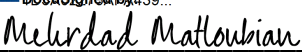Biomedical Sciences

in the

GRADUATE DIVISION
of the
UNIVERSITY OF CALIFORNIA, SAN FRANCISCO

Approved:

Lewis L. Lanier
_____
Chair

Jody Baron
_____

Mehrdad Matloubian
_____

_____

_____
Committee Members

Copyright 2020

by

Jillian M. Jespersen

Acknowledgments

I would like to thank my advisor, Dr. Jody Baron, for a tremendous amount of support and dedication over the last seven years. It's been a real pleasure to learn from you, both scientifically and otherwise. I can always count on you to bring perspective to our discussions, reminding us what we're here to accomplish and how it will help us reach our goals. Your scientific curiosity has driven me to think in new and creative ways. You never hesitated to start a new collaboration when there was a skill I wanted to learn or needed access to technologies and expertise that would propel my project forward. I am fortunate that you have always worked to foster my growth as a trainee and continue to express an openness and commitment to supporting whichever career path I choose. I have become a better scientist and a better person under your mentorship and will always be grateful for the opportunity to work in your lab.

I would also like to thank another close mentor and colleague, Dr. Jean Publicover. From my first days in the lab as a rotation student, to our time working together now, you have trained and mentored me is so many ways. Your patience and trust in teaching me has played an essential role in building my confidence as a scientist. I couldn't begin to count the number of proposals and grants you've edited, the presentations you've listened to and the amount of thoughtful feedback you've given, or the endless "quick questions" and longer discussions you've dedicated your time to – I couldn't have done this without you; thank you.

I'd also like to thank the other members of my lab and the lab of our close collaborator, Dr. Stewart Cooper, that have supported me throughout my graduate training. I've been fortunate to work in a collaborative group where everyone is always willing to lend a hand. Thank you to Dr. Lia Avanesyan, Anyuta Bogdanova, Amanda Goodsell, Rashaun Willett-Potts, Qian Du,

together; I am so grateful for the friendships we developed and can't wait for our next adventures together.

Contributions

The "OX40/OX40L directs HBV immunity" section within Chapter 1 contains text and figures modified from the following publication: Publicover J,* Gaggar A,* **Jespersen JM**,* Halac U, Johnson AJ, Goodsell A, Avanesyan L, Nishimura SL, Holdorf M, Mansfield KG, Judge JB, Koshti A, Croft M, Wakil AE, Rosenthal P, Pai E,Cooper S, Baron JL. 2018. An OX40/OX40L interaction directs successful immunity to hepatitis B virus. *Sci Transl Med.* doi: 10.1126/scitranslmed.aah5766. *These authors contributed equally to this work.* J.P., A. Gaggar, **J.M.J**., U.H., A.J.J., and L.A. performed the experiments, with assistance from A. Goodsell and E.P. S.L.N. processed and scored the H&E stain and interpreted the results. L.A., A.E.W., P.R., and S.C. helped in acquiring the human tissue samples, setting up the human T cell assays, and assisted with the analysis. M.H., K.G.M., J.B.J., and A.K. processed the tissues and ran the experiments for HBsAg Northern and immunohistochemical analysis. J.P., A. Gaggar, A.J.J., U.H., **J.M.J**., L.A., S.C., S.L.N., and J.L.B. analyzed the data. M.C. provided assistance with the experimental design, and antibodies to OX40 and OX40L. J.P., A. Gaggar, U.H., **J.M.J**., L.A., S.C., S.L.N., and J.L.B. designed the experiments and wrote the paper.

The remaining experiments were designed and executed by myself with input from Dr. Jody Baron. Additional technical support to facilitate processing of tissue from large sample sizes was provided by Jean Publicover and Qian Du. Adoptive transfer injections were completed together with Dr. Baron. IHC tissue staining in Chapters 2-4 was performed by UCSF's BTBTC imaging core, as specified. Image analysis (Chapter 2) with Ilastik software was performed in collaboration with Austin Edwards of UCSF's BIDC. Andrew Schroeder, of Dr.

Minnie Sarwal's laboratory, generated the heat map in Figure 1.17 (Chapter 1). Unless otherwise

specified, all data was analyzed by myself, with input from Dr. Baron. The text and figures in

this thesis were written and created by myself, with feedback from Dr. Baron.

Age-dependent increases in hepatic expression of OX40L and the abundance of ILC3s direct

effective immunity to hepatitis B virus

Jillian Mary Jespersen

Abstract

Hepatitis B virus (HBV) can cause either an acute infection with self-limiting disease or, instead, a persistent infection resulting in chronic, recurring disease. The major determinant of which disease outcome occurs is the age at which a person is infected with HBV. Greater than 95 percent of adults exposed to HBV will mount an effective immune response resulting in viral clearance, while greater than 90 percent of infants under one year of age and 30-50 percent of young children aged one to five years-old will generate an ineffective immune response that is unable to control the infection. Current therapies targeted at patients living with chronic HBV (CHB) mostly rely on suppression of viral replication, which is ineffective in inducing viral clearance and antibody seroconversion needed to achieve a functional cure. Thus, it is of great interest to characterize and understand the immunological mechanisms that dictate age-dependent disease outcomes of HBV in order to identify potential therapeutic pathways that can help shift the ineffective immune response in CHB patients to an effective response that results in viral control. Using a mouse model that mimics HBV infection in humans and the age-dependent disease outcomes, we were able to identify critical regulators of age-dependent immunity in the liver. Specifically, we identified an essential role for OX40/OX40L interactions in supporting the generation of effective CD4+ T cell responses including the differentiation of Tfh cells and their production of IL-21, as well as the priming of a robust and diverse antigen-specific IFNγ T cell response. We also found an age-dependent increase in the number of hepatic

ILC3s, which expressed MHC class II, CD69, and cytokines including GM-CSF, IL-22, and IL-17a. A loss of ILC3s either in genetically deficient *Rorc*(γt)-/- mice or in acutely depleted anti-Thy1.2 antibody-treated mice resulted in significantly impaired HBV antigen clearance and seroconversion. We identified a role for these ILC3s in supporting long-lived CD4+ T cell responses, the appropriate distribution and organization of hepatic immune cell clusters important in immune priming and sustained lymphocyte activation, as well as the early recruitment and effector functions of hepatic CD8+ T cells. Targeting the expansion and functional activities of mature hepatic ILC3s, thus, may represent a previously unidentified pathway that could improve HBV immune outcomes.

Table of Contents

List of Figures

Chapter 1. Age-dependent differences in hepatic immune populations correlate with effective HBV immunity

Introduction

Hepatitis B virus (HBV) is a hepatotropic pathogen that targets and infects human hepatocytes, the main parenchymal cell of the liver. The virus is non-cytopathic; thus, the damage that occurs to the liver during the course of an infection is immune-mediated (*1, 2*). The immune response initiated against HBV dictates whether a person will develop a persistent infection or clear the virus (*2*). The age at which a person is initially exposed to HBV is the major determinant of disease outcome: greater than 95 percent of infected adults will clear the infection – often with minimal signs of disease – while approximately 90 percent of infants less than one year old and 30 to 50 percent of children aged one to five years old will develop a persistent infection associated with chronic recurring disease (*3*). This latter group is also at high risk of developing HBV-associated hepatocellular carcinoma, cirrhosis, and liver failure later in life. Worldwide, there are approximately 240 million people living with chronic hepatitis B (CHB) and approximately one million of those individuals die each year due to liver-related disease (*4, 5*).

Due to the profound influence of age on the disease outcomes of hepatitis B infection, it is of great interest to understand how age influences immunity in the liver. Our lab developed an mouse model of hepatitis B disease that mimics the age-dependent disease outcome of humans and allows us to dissect the differences in hepatic immune responses between young and adult animals. Since mice cannot be naturally infected by HBV, the basis of our model relies on two strains of HBV transgenic mice (referred to as HBVtg), originally created by Dr. Frank Chisari

and colleagues (*6, 7*). The first, HBV Envelope (HBVEnv) mice, express the entire HBV envelope-coding region under the control of the mouse albumin promoter, leading to expression of the HBV envelope polypeptide and the secretion of hepatitis B surface antigen (HBsAg) subviral particles from hepatocytes in the liver (*6*). The second strain, HBV Replication (HBVRpl) mice, express a terminally redundant, replication-competent HBV transgene (HBV 1.3) that encodes the entire viral genome under the control of its own enhancers and promoters, which leads to high viral expression and secretion of viral particles primarily from hepatocytes (*7*). Secretion of viral particles and/or virus allows us to monitor HBV "infection" status serologically by measuring for the presence of important viral protein(s) (Hepatitis B Core Antigen, HBcAg; and Surface Antigen, HBsAg) and antibodies to these proteins (HBcAb and HBsAb for anti-Core and anti-Surface antibodies, respectively). Importantly, these are the same readouts that define viral clearance and persistence in human infection. In both mice and humans, chronic "infection" is defined as HBsAg+ HBsAb– HBcAb+, while a resolved infection is defined as HBsAg– HBsAb+ HBcAb+.

In order to study the immune response generated in the context of an HBV-naïve immune system, the HBV-tolerant immune system that develops in HBVtg mice is ablated by crossing these mice onto a *Recombinase activating gene 1* (*Rag1*)-deficient background, which lack mature T and B lymphocytes due an inability to rearrange their antigen-specific receptors. The resulting HBVtg*Rag1*-/- mice are then adoptively transferred with 10_8 HBV-naïve splenocytes from a wild-type (WT) mouse in order to reconstitute the recipient with immune cells that include T and B lymphocytes, and mimic primary HBV infection. After adoptive transfer, the immune response to HBV is initiated and primed within the liver in response to antigens that originate in the liver. In adult HBVtg*Rag1*-/- mice ($\geq$ 8 weeks), the immune response generated

results in peripheral viral antigen clearance and production of HBV-specific antibodies, defined as HBsAg– HBsAb+, while in young mice (≤ 3.5 weeks/at weaning), the immune response results in chronic "infection," serologically defined as HBsAg+ HBsAb–. In concordance with observations in human infants and children, HBcAb can also be detected in young mice when studying the HBVRpl strain. This indicates that while HBV is detected and an immune response is generated, that response is futile and does not affect viral clearance.

Over the years it has become well accepted that T cells play a critical role in HBV clearance. Studies in humans have shown that higher frequencies of antigen-specific T cells are associated with HBsAg clearance. Animal models have shown that even in the context of an HBV-tolerant immune system, transfer of HBV-specific cytotoxic CD8+ T lymphocytes (CTLs) can result in viral antigen clearance and viral suppression and CD4+ T cells play a critical role in supporting these activities (*2, 8*). Further investigation of CD4+ T cells has revealed a critical role for CD4+ T follicular helper (Tfh) cells and their production of interleukin (IL)-21 in age-dependent HBV clearance, both in humans and in animal models (*9, 10*). Work from our lab demonstrated that one of the major age-dependent differences detected in adult and young mice is the increased frequency of hepatic Tfh cells and IL-21 in adult mice (*9*). This work showed that adoptive transfer of *Il21r-/-* splenocytes into adult HBVtg*Rag1-/-* mice completely impaired their ability to clear HBsAg and produce HBsAb. Furthermore, the strength and diversity of the HBV-specific IFNγ CD8+ T cell response was impaired in the mice that received *Il21r-/-* splenocytes. Reciprocally, increased *IL21* expression is also associated with viral clearance in patients who experience acute HBV as compared to chronic hepatitis B patients (both during a hepatitic flare and in immune inactive "carriers") and healthy controls.

Beyond the T cell compartment, there is a mounting body of evidence indicating that B cells are critical for maintaining viral suppression. Interestingly, it is now understood that viral clearance in the case of hepatitis B is in fact immune-induced latency. HBV can form a covalently closed circular (ccc)DNA structure out of its genome that does not integrate into host DNA but is highly stable and capable of reactivating viral infection (*11*). Several case studies have shown that under the right conditions of immunological stress, the virus can reactivate in previously "cleared/cured" patients and cause fulminant hepatitis. One such circumstance is in patients who develop B cell cancers requiring treatment with B cell-depleting antibodies, such as Rituximab (*12, 13*). A consequence of this treatment is the depletion of HBV-specific B cells, as well as a decrease in anti-HBs antibody titers overtime, although Rituximab does not directly target antibody-secreting plasma cells. Through unknown mechanisms, the depletion of these cells allows the virus to resurface. These instances provide strong evidence that B cell responses are crucial for maintaining immune-induced latency of HBV and have since influenced treatment practices in patients with a history of HBV infection.

Beyond the adaptive immune compartment, there is also evidence that innate immune cells of the myeloid lineage play an important role in HBV immunity. A major benefit of studying an animal model of HBV is the insight we can gain into the hepatic immune response during the initial acute disease phase. It has been challenging to study this window in humans because it is neither practical nor ethical to collect tissue from young infants and children and because the acute phase of disease is often subclinical in adults, remaining undetected until well after the primary infection. Analysis of liver tissue isolated from adult and young mice during the peak of the acute disease phase (day 8 post-adoptive transfer) revealed that hepatic immune cell clusters form in adult mice, whereas cluster formation was dramatically reduced in the young

mice (*14*). Although these clusters are comprised of a variety of cell types including both lymphocytes and myeloid cells, they are primarily anchored by F4/80+ macrophages. Depletion of these macrophages in adult mice using clodronate liposomes results in both complete impairment in viral clearance and disruption of all cell clustering, including no macrophage-independent clustering of lymphocytes. Clodronate-treated mice also have severely blunted HBV-specific T cell responses similar to those observed in young mice, indicating a critical role for macrophages in hepatic immune priming and viral clearance of HBV.

Additionally, work from our lab and others have shown an association between increased expression of various proteins within the hepatic myeloid compartment of adult mice and humans and viral clearance. These proteins include the C-X-C Motif Chemokine Ligand 13 (CXCL13), the antigen presentation molecule major histocompatibility complex class II (MHCII), and the co-stimulatory molecules CD80 and CD86. Publicover, *et al.*, showed that CXCL13 is expressed in an age-dependent manner in macrophages and that *Cxcl13*-/- HBVtg*Rag1*-/- mice have a phenotype similar to young mice in their inability to clear HBsAg or make HBsAb after adoptive transfer (*14*). The chemokine receptor for CXCL13 is CXCR5 and expressed highly on Tfh and B cells, suggesting that macrophage-derived CXCL13 may play an important role in recruiting these cells to the liver. However, although both CXCL13 and CXCR5 were shown to be critical for viral clearance, deficiency of either molecule did not prevent the formation of hepatic leukocyte clusters, suggesting a yet unappreciated mechanism orchestrating immune cell organization in the liver.

The objective of the experiments described below were to further characterize the age-dependent immunological differences within the liver during the peak phase of early HBV immunity. We investigated the number and phenotype of hepatic innate and adaptive immune

cells by age, as well as the expression of molecules involved in antigen presentation, lymphoid organization, and immune priming. We further investigated the role of OX40/OX40L interactions in contributing to successful HBV immunity by blocking OX40 signaling in adult animals using an antagonistic antibody or *Ox40-/-* splenocytes and by augmenting OX40 signaling in young and "chronic" HBV mice with an agonistic antibody (*15*).

Results

1.1 OX40/OX40L directs HBV immunity

To elucidate what other effector molecules might be playing a crucial role in influencing age-dependent immunity, we isolated and compared antigen-presenting cells (APCs) from resting adult and young mice to reveal differences in expression of co-stimulatory molecules known to play a role in priming of CD4+ and CD8+ T cell responses. We identified age-dependent differences in the expression of *Tnfsf4* (tumor necrosis factor superfamily member 4; also known as *Ox40l*) mRNA and OX40L protein in hepatic macrophages, monocytes, and dendritic cells (**Fig. 1.1 A-B, D**). Additionally, we noted an increased frequency of OX40+ CD4+ T cells and OX40+ CXCR5+ICOS+CD4+ Tfh cells in adult mice compared to young mice indicating there was OX40L-dependent expansion of OX40+ T cells in an age-dependent manner (**Fig. 1.1 E-G**).
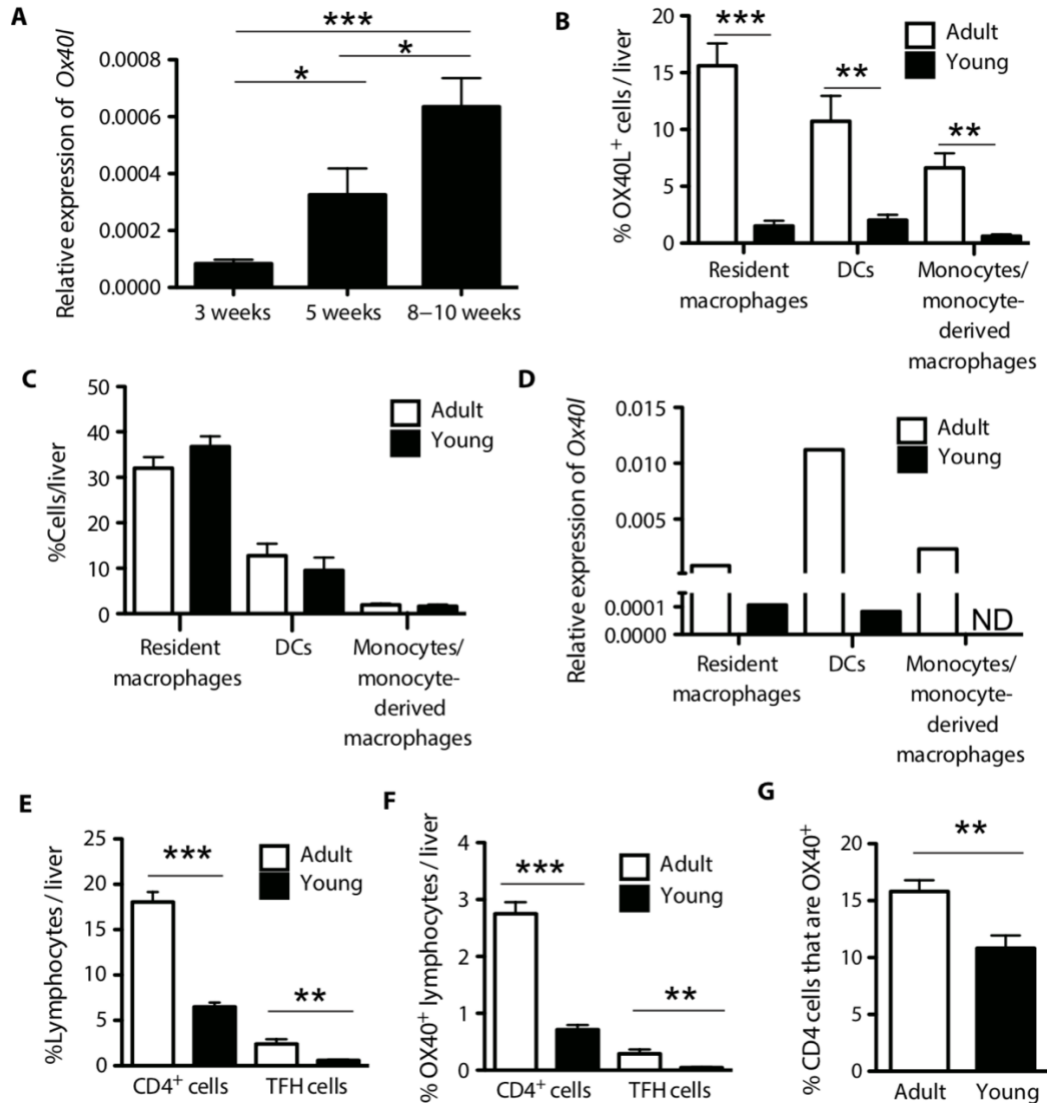
Figure 1.1. Age-dependent expression of OX40 ligand on hepatic APCs and age-dependent expression of OX40 on liver-derived CD4+ T cells during acute hepatitis. (A) *Ox40l* mRNA expression relative to *Gapdh* was determined by RT-PCR using mRNA derived from myeloid-enriched leukocyte preparations isolated from the liver of adult (8 to 11 weeks) and young (3 weeks) *Rag1−/−* mice (n = 10). (B and C) Percentages of OX40L+ (B) and percentages of all (C) resident macrophages [F4/80hi, CD11b+/intermediate(int), major histocompatibility complex (MHC) class II+/int, CD11c−, Ly6G−, Ly6C−, and NK1.1−], dendritic cells (DCs; CD11c+/hi, MHC class II+/hi, CD11b−, Ly6G−, Ly6C−, and NK1.1−), and monocytes/monocyte-derived macrophages (F4/80int, CD11b+/hi, MHC class II+/int, Ly6C+, Ly6G−, CD11c−, and NK1.1−) (n = 4). (D) Ox40l mRNA expression relative to Gapdh was determined by RT-PCR using mRNA derived from flow-sorted pooled cell populations from adult and young livers (n = 6 mice). ND, not detectable. (E to G) Lymphocytes were isolated from HBVEnvRag−/− mouse livers 8 days after adoptive transfer of splenocytes (n = 8). Flow cytometry was used to determine (E) percentages of CD4+ T cells [CD4+, T cell receptor b (TCRb)+, NK1.1−, CD8−, and CD19−] and T follicular helper (Tfh) cells (CD4+, TCRb+, CXCR5+, ICOS+, NK1.1−, CD8−, and CD19−), (F) percentages of OX40+ CD4+ T cells and OX40+ TFH cells, and (G) percentages of CD4+ T cells that are also OX40+ in the liver. Bars represent means ± SEM. Statistical significance was determined using the unpaired two-tailed t test. *P < 0.05, **P < 0.01, and ***P < 0.001.

7

In order to study the role that OX40/OX40L interactions have on HBV clearance, we adoptively transferred *Tnfsfr4* (*Ox40*)-/- splenocytes into adult HBVtg*Rag1*-/- mice and compared to mice adoptively transferred with WT *Ox40*+/+ splenocytes. To monitor liver inflammation, we collected longitudinal plasma samples from both mouse cohorts and measured changes in alanine aminotransferase (ALT), an enzyme released by necrotic hepatocytes. As HBV is a non-cytopathic virus, increased ALT correlates well with the degree of immune activation in the liver. To assess the productivity of the response, we measured clearance of HBsAg and production of HBsAb. Unlike the control group, mice that received *Ox40*-/- splenocytes had dramatically reduced liver inflammation (**Fig. 1.2A-C**), were unable to clear HBsAg (**Fig. 1.2 D**), and failed to produce HBsAb (**Fig. 1.2 E**). Decreased IFNγ production by hepatic lymphocytes in response to HBV peptide stimulation in the presence of APCs, as well as a reduction in the number of HBV epitopes (MHCI- and MHCII-restricted) recognized by lymphocytes from mice that received *Ox40*-/- splenocytes suggested impaired HBV-specific T cell responses (**Fig. 1.2 F-G**). Mice that received *Ox40*-/- splenocytes also had a specific reduction of CD4+ T cells, particularly Tfh cells, and impaired secretion of the critical effector molecule IL-21 compared to mice that received WT splenocytes (**Fig. 1.2 H-J**).
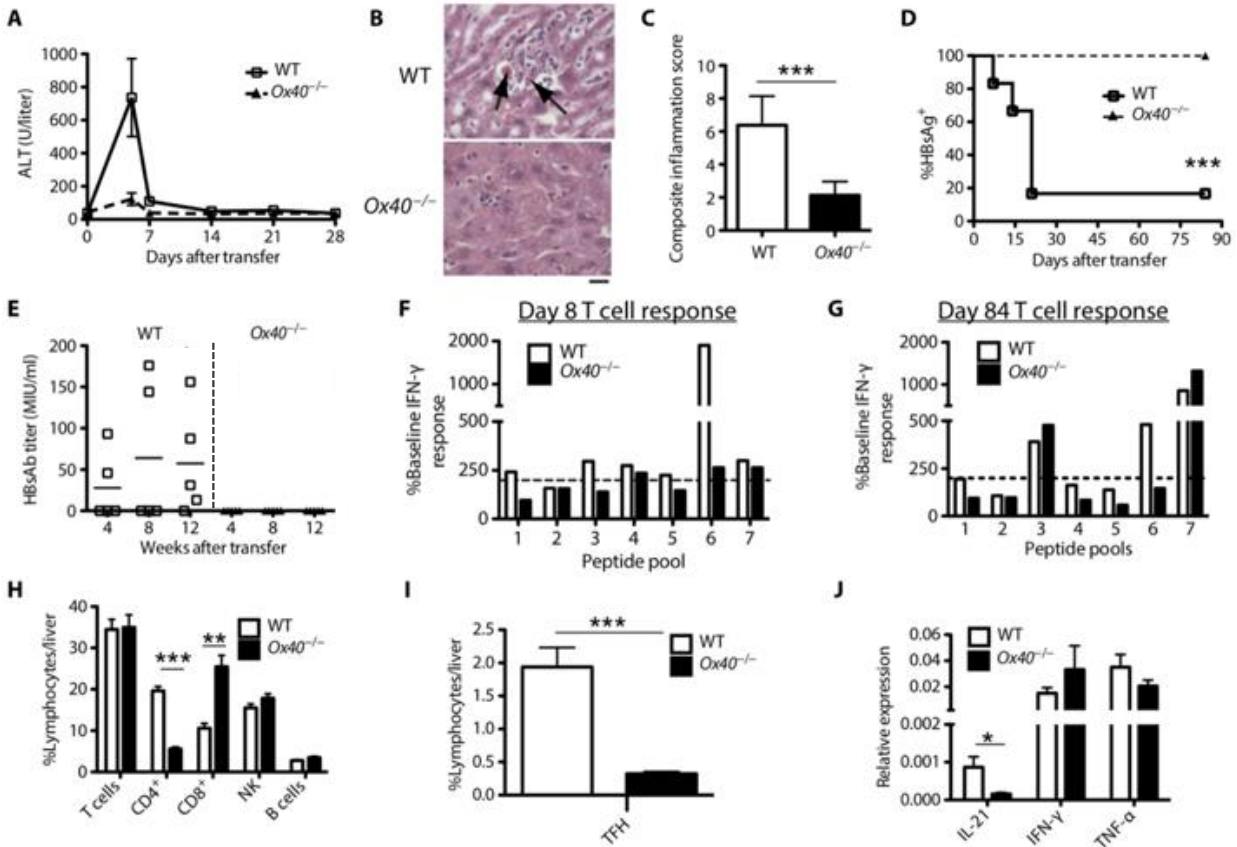
Figure 1.2. Adoptive transfer of adult *Ox40*–/– splenocytes into adult HBVEnv*Rag1*–/– mice alters hepatic inflammation, HBsAg clearance, HBsAb seroconversion, T cell responses, and cytokine production. (**A**) Plasma alanine aminotransferase (ALT) values, reflecting liver injury, were determined for HBVEnv*Rag1*–/– mice receiving wild-type (WT) (*Ox40*+/+) splenocytes (open squares, solid line) or *Ox40*–/– splenocytes (closed triangles, dotted line) at given time points after adoptive transfer ($n \geq 5$). (**B**) Hematoxylin and eosin staining of liver sections from adult HBVEnv*Rag1*–/– mice 8 days after adoptive transfer. Arrows indicate necrotic hepatocytes. Scale bar, 25 mm. (**C**) Composite score of hepatic necrosis, portal inflammation, and intraparenchymal inflammation in the liver sections determined by a pathologist blinded to sample identity. Statistical significance was determined using Mann-Whitney two-tailed (***$P = 0.0008$; $n = 8$ mice). (**D**) Plasma HBsAg loss and (**E**) HBsAb titer in HBVEnv*Rag1*–/– mice at given time points after adoptive transfer. Statistical significance was determined using the chi-square test (***$P < 0.001$; $n \geq 5$ mice). (**F** and **G**) Presence of hepatitis B virus (HBV)–specific T cells was determined using IFNγ enzyme-linked immunospot (ELISpot) 8 days (F) and 84 days (G) after adoptive transfer (data pooled from $n = 5$ mice). Threshold defining a positive response is $\geq 2 \times$ the baseline (dashed line). (**H** and **I**) Percentages of total lymphocyte subpopulations were determined by flow cytometry in the liver 8 days after adoptive transfer: T cells are CD19– and TCRβ+; CD4+ T cells are CD4+ CD8– TCRβ+ and CD19–; Tfh cells are CD4+ CD8– TCRβ+ CD19– CXCR5+, and ICOS+; CD8+ T cells are CD4– CD8+ TCRβ+ and CD19–; B cells are TCRβ– and CD19+; NK cells are TCRβ– CD19– and NK1.1+. Statistical significance was determined using the unpaired two-tailed *t* test (**$P < 0.01$ and ***$P < 0.001$; $n = 5$ mice). Bars represent means ± SEM. (**J**) Expression of various cytokine mRNAs relative to *Gapdh* was detected by RT-PCR on mRNA from liver lymphocytes 8 days after adoptive transfer ($n \geq 5$). Bars represent means ± SEM. Statistical significance was determined using the unpaired two-tailed *t* test (*$P < 0.05$).

9

Because IFNγ is known to play a direct role in suppressing HBV expression and OX40 contributes to the HBV-induced IFNγ response, we investigated whether the expression of viral RNA and proteins in the liver was influenced by transfer of *Ox40-/-* splenocytes. There was a general reduction in the large and middle/small surface antigen viral RNAs in both WT and in *Ox40-/-* splenocyte groups compared to the HBVtg mice that were not adoptively transferred (no anti-HBV immune response) (**Fig. 1.3 B-C, E**), indicating the immune response initiated by adoptive transfer does suppress viral replication intermediates. There was also evidence of a delay in early viral RNA suppression in mice that received *Ox40-/-* splenocytes compared to WT splenocytes (**Fig. 1.3 B-C**), suggesting that decreased *Ox40-/-* splenocytes are less effective at controlling early viral transcription. Expression of the full HBsAg protein was relatively high in the liver of mice at all time points and in all groups despite clearance of circulating antigen in the mice that received WT splenocytes, although there was a slight trend towards decreased antigen expression by this group relative to mice that received *Ox40-/-* or no splenocytes (**Fig. 1.3 D**).
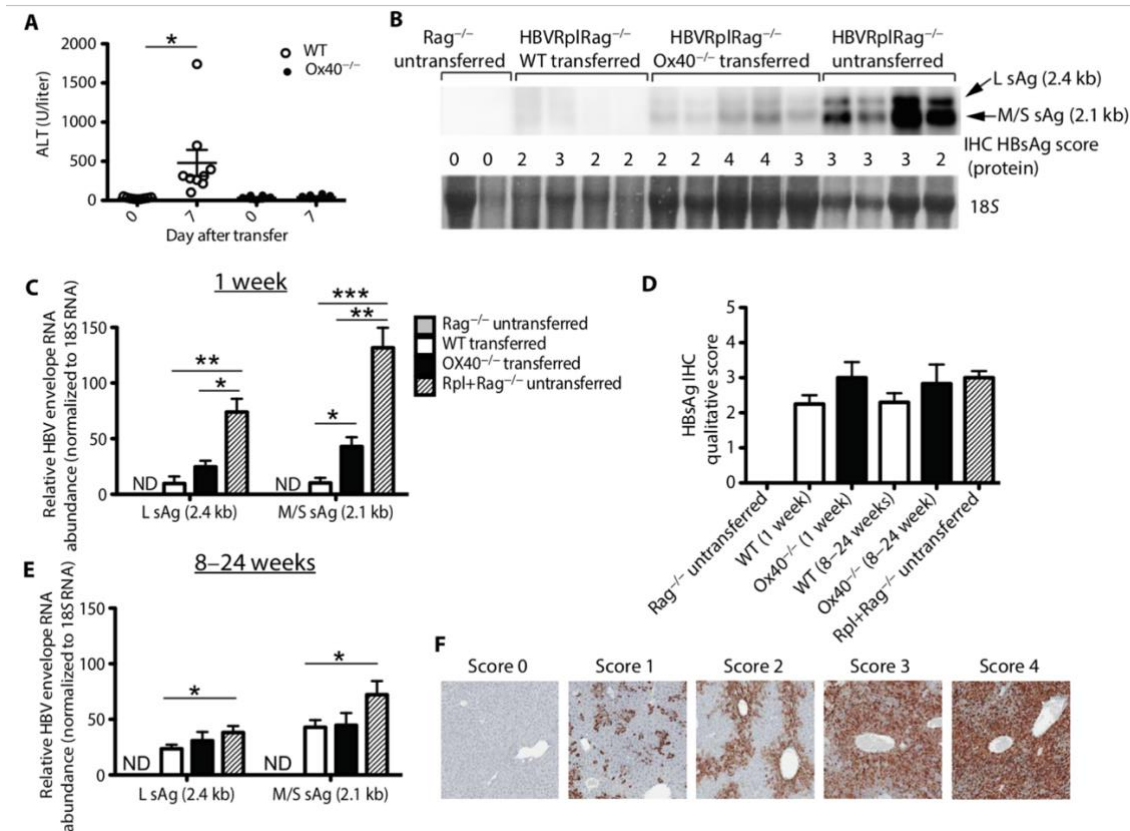
Figure 1.3. Hepatic HBV envelope RNA and protein expression levels in HBVRpl*Rag1*–/– mice 7 days (1 week) and 8 to 24 weeks after adoptive transfer with WT or *Ox40*–/– splenocytes show OX40-dependent suppression of viral replication intermediates. (**A**) Plasma ALT values, reflecting liver injury, were determined for HBVRpl*Rag1*–/– mice receiving WT splenocytes (open circles) or *Ox40*–/– splenocytes (closed circles) at day 7 after adoptive transfer (*n* ≥ 9). Statistical significance was determined using the paired two-tailed *t* test (*P < 0.05). Liver pieces were removed 7 days (**B-D**), 8 weeks, or 24 weeks (**D** and **E**) after adoptive transfer and either flash-frozen for RNA extraction or fixed in formalin for immunohistochemistry (IHC). (**B-C** and **E**) HBV envelope RNA was detected by Northern blot analysis using a DIG-labeled (−) strand HBV RNA probe. RNA transcript band intensities in WT or *Ox40*–/– transferred mice were compared to untransferred *Rag1*–/– negative controls or untransferred HBVRpl*Rag1*–/– positive controls and normalized to 18*S* RNA bands. Statistical significance was determined using the unpaired two-tailed *t* test (*P < 0.05; *n* ≥ 4 for all groups except *Rag1*–/– untransferred, where *n* = 2). Bars represent means ± SEM. (**D**) HBV envelope protein levels were measured by IHC staining of formalin-fixed liver tissue with an HBsAg-specific antibody and counterstained with hematoxylin. Stained sections were scored by a pathologist blinded to sample identities using the scoring system shown in (**F**); 0, no staining; 1, multifocal granular or diffuse staining in hepatocytes involving <25% of section; 2, granular or diffuse staining around centrilobular hepatocytes with no staining in portal regions; 3, diffuse positivity of hepatocytes restricted to centrilobular region; granular cytoplasmic positivity in remaining hepatocytes; and 4, diffuse positivity of hepatocytes restricted to centrilobular and mid zonal regions; granular cytoplasmic positivity in remaining hepatocytes. *n* ≥ 4 for all groups except *Rag1*–/– untransferred, where *n* = 2. Bars represent means ± SEM.

To further confirm the role of the receptor OX40 in regulation of HBV immunity, we used an OX40L-blocking antibody during the initial immune priming phase (days 0-6). These mice experienced blunted hepatitis (**Fig. 1.4 A**), a reduction in CD4+ T cell frequency with a trend towards decreased Tfh cells (**Fig. 1.4 B**), impaired HBV-specific IFNγ production (**Fig. 1.4 C**), and dramatically reduced *Il21* mRNA expression (**Fig. 1.4 D**) similar to the mice that received *Ox40-/-* splenocytes. However, this early blockade did not affect the long-term clearance of HBsAg or HBsAb, likely due to the short window of OX40L blockade efficacy.
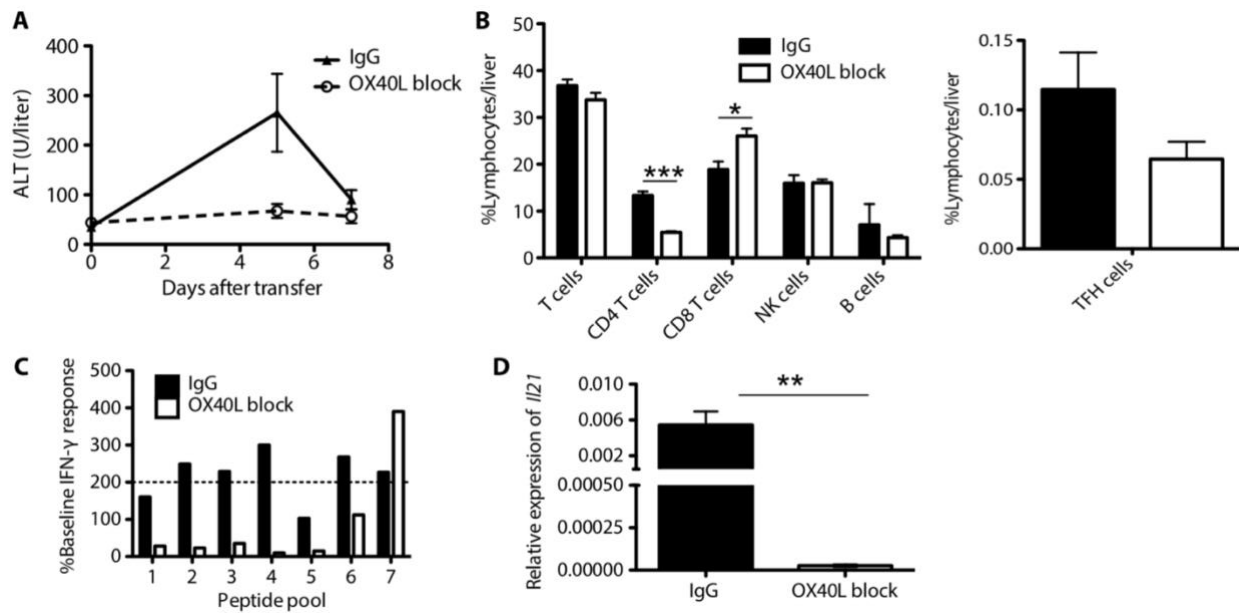
Figure 1.4. Adoptive transfer of adult WT splenocytes into HBVEnv*Rag1*–/– adult mice treated with an OX40L blocking antibody abrogates biochemical hepatitis and HBV-specific T cell responses and cytokine expression. (**A**) Plasma ALT values were determined in HBVEnv*Rag1*–/– adult mice receiving intraperitoneal injection of 100 μg of OX40 ligand (OX40L) block (RM134L) (open circles, dotted line) or control IgG (purified rat IgG2b isotype control; closed triangles, solid line) on days 0, 2, 4, and 6 after adoptive transfer of WT splenocytes (*n* = 7). (**B**) Eight days after transfer, percentages of lymphocyte populations were determined by flow cytometric analysis of liver lymphocytes derived from HBVEnv*Rag1*–/– mice treated with either control IgG (black bars) or OX40L block (white bars). Bars represent means ± SEM. Statistical significance was determined using the unpaired two-tailed *t* test (*$P < 0.05$ and ***$P < 0.001$; *n* = 6). (**C**) HBV-specific T cell responses were measured using IFN-g ELISpot assay 8 days after adoptive transfer. Threshold defining a positive response is ≥2× the baseline (dashed line; *n* = pooled from four mice). (**D**) Relative *Il21* expression compared to *Gapdh* was detected by RT-PCR on mRNA from liver lymphocytes isolated 8 days after adoptive transfer. Bars represent means ± SEM. Statistical significance was determined using the unpaired two-tailed *t* test (**$P < 0.01$; *n* = 6).

To determine whether age-dependent anti-viral immunity is a product of the reduced expression of OX40L in young mice, we sought to bypass this deficiency by agonizing the receptor OX40 with the agonistic antibody OX86. Young mice treated with OX86 on days 0, 3, and 6 after adoptive transfer with WT splenocytes showed improved anti-HBV immunity compared to isotype-matched control Ig-treated mice (**Fig. 1.5**). These mice experienced mild hepatitis (**Fig. 1.5 A**), indicating that inflammation was occurring, compared to isotype-matched control Ig-treated mice which did not have measurable hepatitis. Fifty percent of OX86-treated young mice were able to clear HBsAg compared to zero percent in the control group (**Fig. 1.5 C**). OX86 treatment drove increased expansion of CD4+ T cells, including Tfh cells (**Fig. 1.5 B**), and improved HBV-specific T cell responses as measured by IFNγ ELISpot assay with HBV-peptide/APC stimulation of hepatic lymphocytes (**Fig 1.5 C-E**). To test whether OX86 treatment could be effective in a chronic disease setting, we adoptively transferred young HBVtg*Rag1*-/- mice (three weeks old) and allowed them to age until 12 weeks old before confirming a serological profile of chronic HBV (HBsAg+ HBsAb–), after which we treated them with OX86. Although the OX86-treated mice did not clear HBsAg or produce HBsAb, these mice did generate detectable HBV-specific T cell responses while control mice did not (**Fig. 1.5 F-H**).
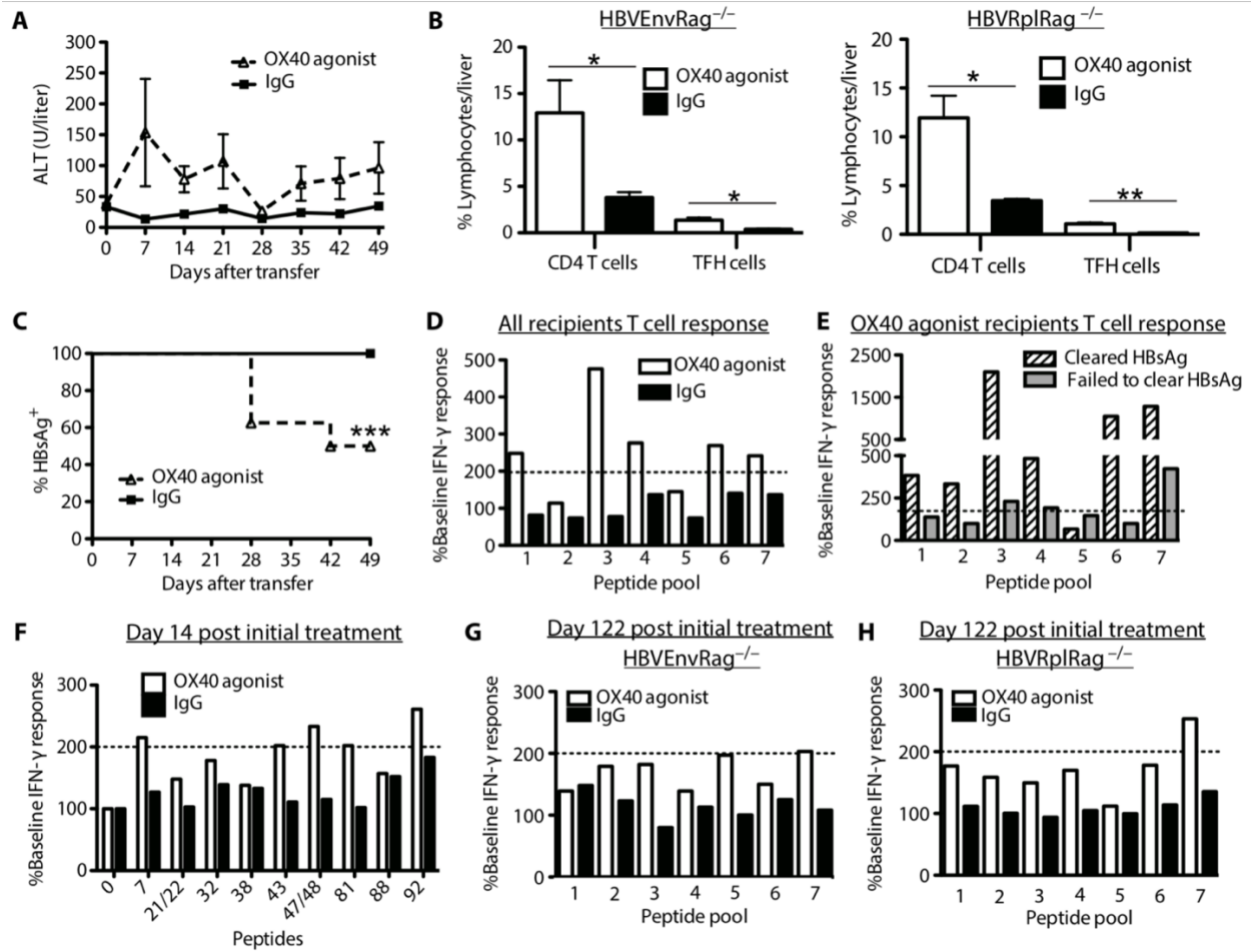
Figure 1.5. Treatment with an OX40 agonist antibody of 3-week-old HBVtg*Rag1*–/– mice or mice with chronic HBV disease results in an altered immune response to HBV. (**A**) Plasma ALT values from young HBVEnv*Rag1*–/– mice receiving intraperitoneal injection of 150 μg of OX40 agonist antibody (OX86; open triangles, dashed line) or control IgG (purified rat IgG1 isotype control; closed squares, solid line) on days 0, 3, and 5 after adoptive transfer of WT splenocytes (*n* = 4). (**B**) Percentages of CD4$^+$ T cells and T$_{FH}$ cells determined by flow cytometry in liver tissue 8 days after adoptive transfer into 3-week-old HBVEnv*Rag1*–/– (left panel) or HBVRpl*Rag1*–/– (right panel) treated with control IgG (black bars) or OX40 agonist (white bars). Bars represent means ± SEM. Statistical significance was determined using the unpaired two-tailed *t* test (**P* < 0.05 and ***P* < 0.01; *n* ≥ 3). (**C**) Presence of HBsAg in the plasma of young HBVEnv*Rag1*–/– mice treated with OX40 agonist (open triangles, dashed line) or control IgG (closed squares, solid line). Statistical significance was determined using the chi-square test (****P* < 0.001). Data were pooled from two experiments (*n* = 8 mice per group total). (**D**) Presence of HBV-specific T cells was determined using IFN-g ELISpot 56 days after adoptive transfer of young HBVEnv*Rag1*–/– mice injected with OX40 agonist (white bars) or control IgG (black bars). Data are representative of three individual experiments (*n* = pooled from four mice). (**E**) IFN-g ELISpot analysis of HBV-specific T cell responses on liver lymphocytes from mice treated with OX40 agonist that cleared HBsAg (striped bars) or treated with OX40 agonist and did not clear HBsAg (gray bars) (*n* = pooled from two mice). For (D) and (E), the threshold defining a positive response is ≥2× the baseline (dashed line). (**F** to **H**) HBVRpl*Rag1*–/– or HBVEnv*Rag1*–/– mice confirmed to have the serological profile of chronic HBV disease were treated with OX40 agonist (open bars) or control antibody (closed bars) (F) for eight

14

treatments 3×/week or (G and H) at days 84, 87, 89 and 168, 171, 173, 175 after adoptive transfer. Presence of HBV-specific T cells was determined using IFN-g ELISpot on liver lymphocytes after stimulation with (F) individually defined dominant and subdominant peptide epitopes or (G and H) pools of HBV peptides spanning the entire protein (F) 14 days or (G and H) 122 days after first treatment with OX40 agonist or control IgG (38 days after second treatment and 206 days after adoptive transfer) in (G) HBVEnv*Rag1*–/– mice and (H) HBVRpl*Rag1*–/– mice. Data are representative of two individual experiments (*n* = pooled from 2–4 mice). Threshold defining a positive response is ≥2× the baseline (dashed line).

In order to evaluate the relevance of our findings in the mouse model, we turned to

human patients for cells and tissue. We found that *OX40L* mRNA expression was increased in

the livers of adults compared to infants six-twelve weeks old (**Fig. 1.6 A**). Furthermore, we also

found that patients with acute HBV that go on to clear the infection have an increased frequency

of circulating CD4+ T cells, of which, a greater percentage of those cells are OX40+ compared

to patients with CHB or healthy controls (**Fig. 1.6 B-C**). These data demonstrate a crucial role

for an OX40/OX40L interaction in supporting effective immunity and viral clearance in the

context of HBV infection; moreover, they identify a targetable therapeutic avenue for the

millions of people living with chronic HBV.
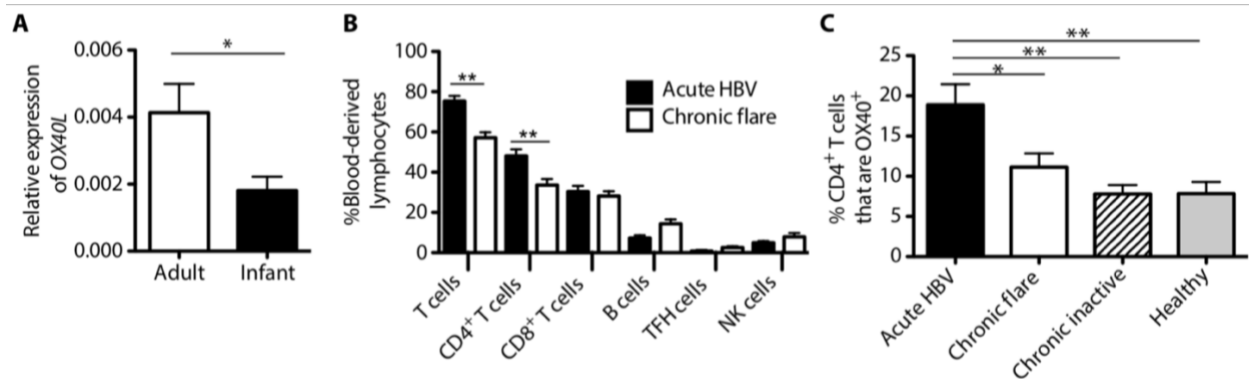
Figure 1.6. Adult human liver shows greater *OX40L* expression than infant liver, and patients with acute hepatitis B who clear the virus have significantly increased percentages of PBMC-derived CD4+ T cells, a greater percentage of which express OX40. (**A**) Expression of *OX40L* relative to *GAPDH* was determined by RT-PCR performed on RNA extracted from paraffin-embedded liver biopsy samples from infants 6 to 12 weeks of age (black bar, *n* = 24) and adults (white bar, *n* = 9). Bars represent means ± SEM. Statistical significance was determined using the unpaired two-tailed *t* test (*P < 0.05). (**B**) Flow cytometry analysis comparing lymphocyte populations in PBMC obtained from eight patients with confirmed acute HBV infection during active hepatitis and with confirmed subsequent viral clearance and HBsAb seroconversion, and eight patients with confirmed chronic HBV infection exhibiting a flare of

disease. T cells are TCRβ+ CD19- CD56-; CD4+ T cells are CD4+ CD8- TCRβ+ CD19-; Tfh cells are CD4+ CD8- TCRβ+ CD19- CXCR5+ ICOS+; CD8+ T cells are CD4- CD8+ TCRβ+ CD19-; B cells are TCRβ- CD19+; and NK cells are TCRβ- CD19- CD56+ CD16+. Bars represent means ± SEM. Statistical significance was determined using the unpaired two-tailed t test (**$P < 0.01$). (**C**) Percentage of CD4+ OX40+ T cells present in PBMC obtained from eight patients with acute HBV, eight patients with chronic HBV exhibiting a hepatitic flare of disease, as well as six untreated patients with confirmed chronic HBV with inactive disease (normal ALT), and six healthy individuals. Bars represent means ± SEM. Statistical significance was determined using Tukey's analysis of variance (ANOVA) multiple comparison test (*$P < 0.05$ and **$P < 0.01$).

1.2 - Adaptive Immunity in HBV Infection

In order to more fully characterize the immune landscape during the anti-HBV immune response and how it is influenced by age, I performed careful immune phenotyping of the adaptive immune compartment within the liver of adult and young HBVtg*Rag1*-/- mice by flow cytometry at the peak of the acute HBV immune response, which occurs eight days post-adoptive transfer. We focused on this phase of the response to understand the early events that lead to priming of the adaptive immune system and set the course of infection. A broad characterization revealed that adult mice have an increased number of total hepatic T cells, including increased numbers of CD8+ T cells, and NK1.1+ Natural Killer (NK)-like T cells (**Fig. 1.7 A**). Despite the overall increased numbers of B, T, and NK-like T cells in adult mice, the relative frequencies of each of these populations were similar by age (**Fig. 1.7 B**).
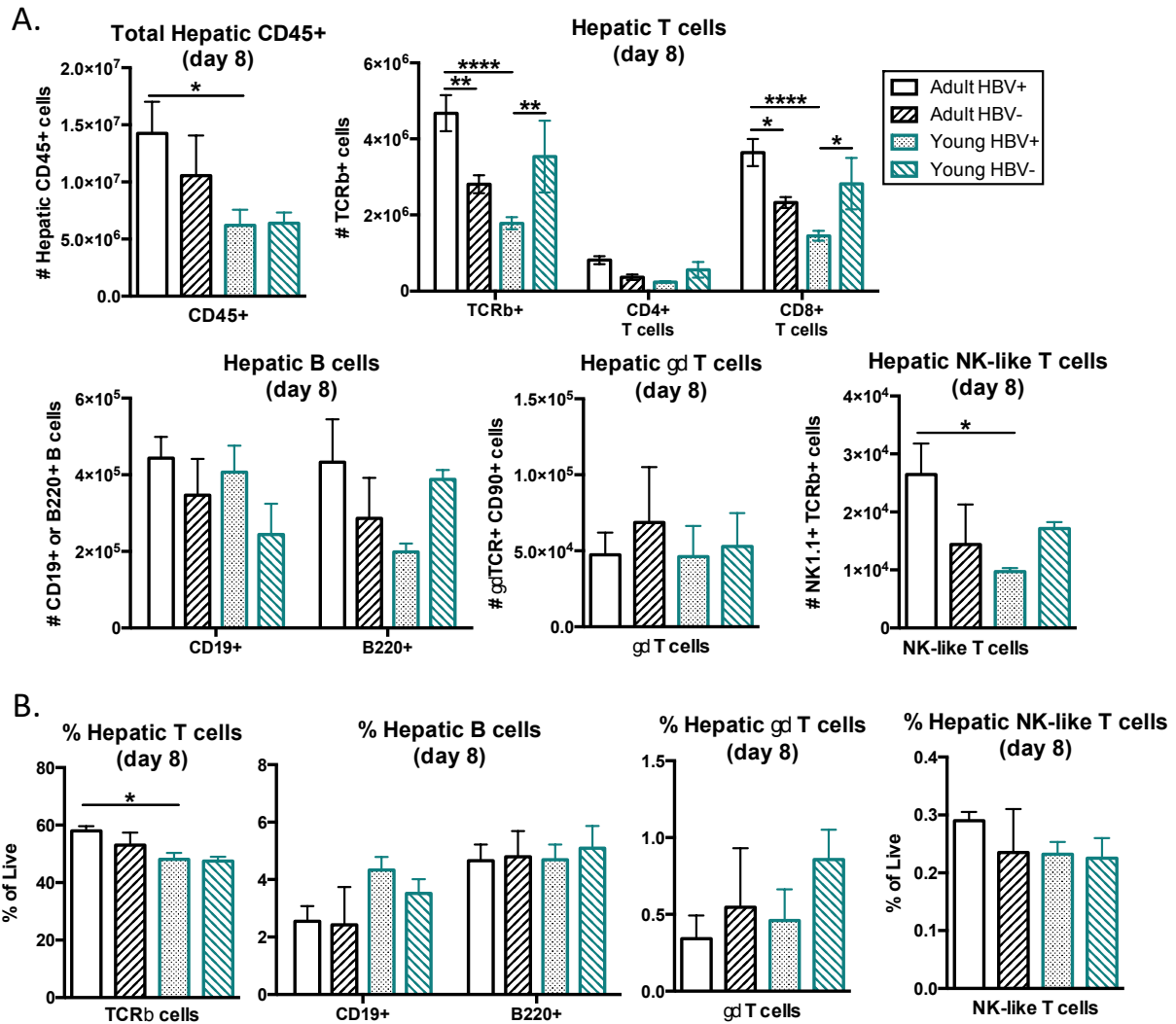
Figure 1.7. Differences in hepatic lymphocyte populations by age during acute HBV immunity.
Hepatic leukocyte fractions were enriched from HBVtgRag1-/- adult (>8 wks) and young (3 – 3.5 wks) animals eight days after adoptive transfer with HBV-naïve splenocytes. Total numbers (A) and percentage (B) of each lymphocytes population were measured, defined as follows: CD45+ (Live CD45+), T cells (Live TCRb+), CD4+ T cells (Live TCRb+ CD4+), CD8+ T cells (Live TCRb+ CD8+), B cells (CD19+ or B220+), γ**δ** T cells (Live TCRgd+ CD90+), NK-like T cells (Live TCRb+ NK1.1+). Data were analyzed using FlowJoᴛᴍ Software; statistics determined by Tukey's one-way ANOVA with GraphPad Prism Software; * p<0.05, ** p<0.01, *** p<0.001, **** p<0.0001; n ≥ 3 for HBV+ groups, n=2 for HBV- groups.

I examined the T cells within the HBV+ transgenic animals, as these are the antigen-

driven responses of interest. In these animals, the majority of hepatic T cells in both young and

adult mice are CD8+; however, adult mice have a slightly decreased frequency of CD8+ T cells

relative to young mice and, conversely, an increased frequency of CD4+ T cells compared to young mice (**Fig. 1.8 A**).

I then focused on functional subsets of CD4+ and CD8+ T lymphocytes, including T$_{naive}$ (CD62L+ CD44-), T$_{CM}$ (central memory; CD62L+ CD44+), T$_{Eff}$ (effector/effector memory; CD62L- CD44+), T$_{fh}$ (CD4+ CXCR5+ PD-1+), and CXCR5+ CD8+ T cells. Consistent with published literature (*9*), I observed that adult mice have increased hepatic T$_{fh}$ cells both in number and in proportion of CD4+ T cells, while the frequencies of CXCR5+ CD8+ T cells was similar by age (**Fig. 1.8 B**). Adult mice also have an increased frequency of T$_{Eff}$ in both CD4+ and CD8+ T cell compartments, with a reduced frequency of CD8+ T$_{CM}$ cells (**Fig. 1.8 C** and **E**). When evaluating CD4+ T cells using PSGL1 and Ly6c to identify memory precursor (PSGL1$_{hi}$ Ly6c$_{lo}$) versus more terminally differentiated effector (PSGL1$_{hi}$ Ly6c$_{hi}$) cells (*16*), there were no significant differences; but a similar trend towards more effector-like cells and fewer memory precursors in adults compared to young was observed, consistent with the T$_{CM}$ and T$_{Eff}$ phenotypes determined using CD44 and CD62L (**Fig. 1.8 D**). Taken together, these data indicate adult animals have an early effector T cell program with expanded CD4+ T cell differentiation relative to the increased CD8+ T cell differentiation with a more memory-like phenotype in young mice. Importantly, we also saw an overall expansion of both hepatic CD4+ and CD8+ T cell numbers in adult animals relative to young animals, suggesting the most impactful observations likely include the decreased abundance of CD4+ T cells, especially of the T$_{Eff}$ phenotype.
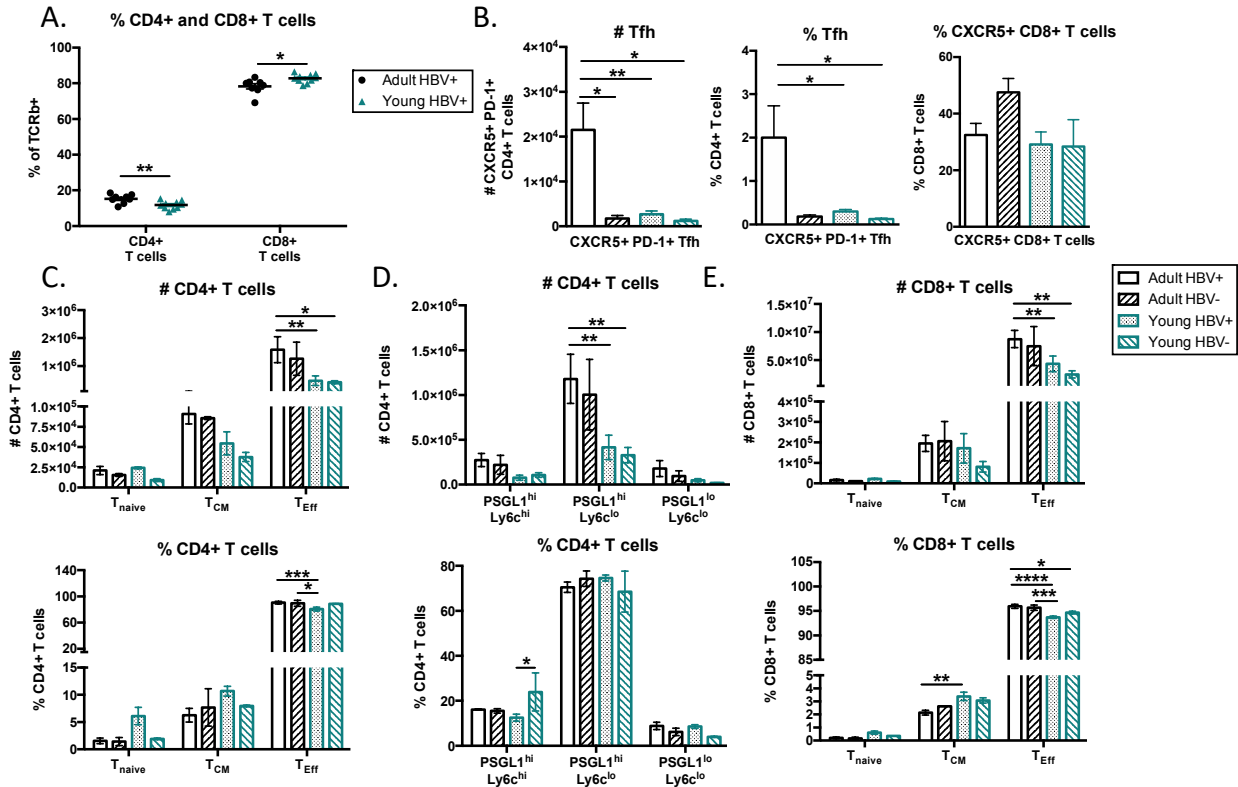
Figure 1.8. Hepatic CD4+ and CD8+ T cell functional subsets in adult and young mice during acute HBV immunity. CD4+ and CD8+ TCRb+ T cells were phenotypically characterized by flow cytometry from leukocyte-enriched liver cell suspensions eight days post-adoptive transfer in adult (>8 wks) and young (3 – 3.5 wks). A. CD4+ and CD8+ T cell subsets as a percentage of total TCRb+ cells in HBV+ animals (n=10). B. Total number and percentage of CXCR5+ PD-1+ CD4+ T follicular helper (Tfh) cells and percentage of CXCR5+ CD8+ T cells. C. Number and percentage of CD44- CD62L+ Tnaive, CD44+ CD62L+ TCM (central memory) and CD44+ CD62L- TEff (effector) CD4+ T cells. D. Number and percentage of PSGL1 and Ly6c subsets in CD4+ T cells. E. Number and percentage of CD44- CD62L+ Tnaive, CD44+ CD62L+ TCM and CD44+ CD62L- TEff CD8+ T cells. Data were analyzed using FlowJo™ Software; statistics determined by unpaired two-tailed t-test or Tukey's one-way ANOVA for two groups or more than two groups, respectively, with GraphPad Prism Software; * p<0.05, ** p<0.01, *** p<0.001, n=5 for HBV+ groups, n=2 for HBV- groups.

When looking at other phenotypic markers I observed increased expression of CXCR3, a chemokine receptor important for liver-residency, on CD8+ T cells in adult mice compared to young mice, though the trend was reversed for CXCR3+ CD4+ T cells (**Fig. 1.9 A**). These data suggest that the CD8+ T cell population in adults is a more liver-restricted response, whereas the CD4+ T cell population in adults may be more likely to circulate between liver and secondary lymphoid tissues, perhaps to aid in immune priming and differentiation in lymph nodes and

spleen. Using Ki67 as a marker for proliferation, I observed greater than 90 percent of T cells are actively proliferating in both adult and young hepatic populations; however, this is further increased for CD4+ and CD8+ T cells in adults compared to young (**Fig. 1.9 B**). There were no differences in the overall frequencies of PD-1+ (**Fig. 1.9 C**) or Tbet+ (**Fig. 1.9 D**) T cells in either the CD4+ or CD8+ compartments, which are associated with strength of activation and effector phenotypes, respectively.
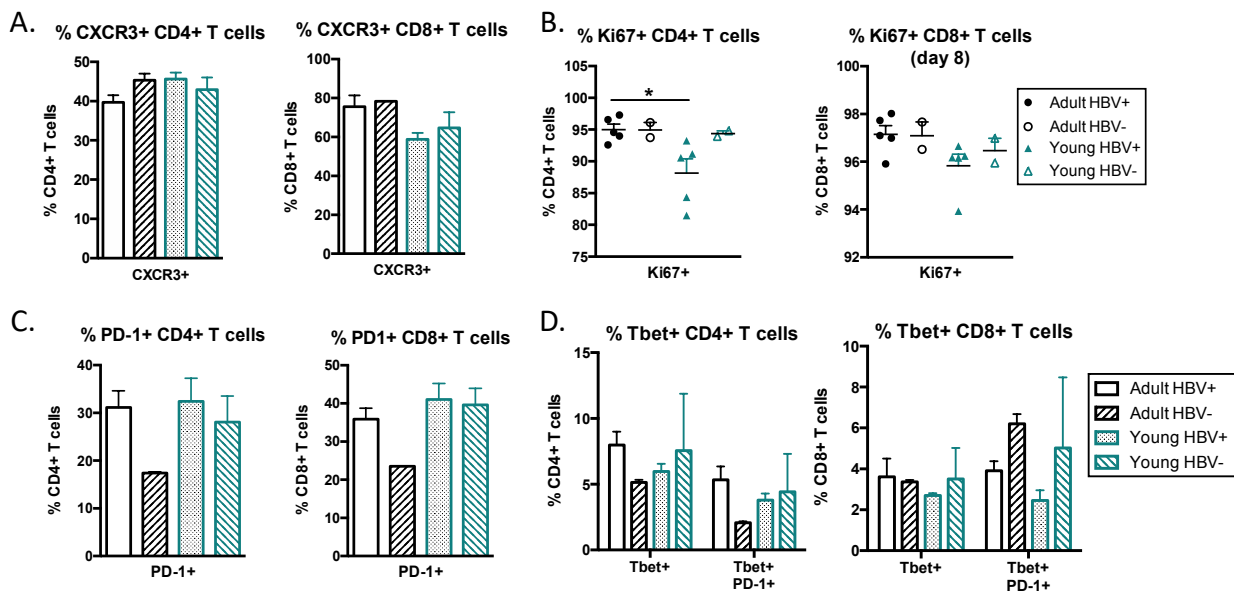
Figure 1.9. Expression of functional markers within adult and young CD4+ and CD8+ T cells during acute HBV immunity. Hepatic leukocyte fractions were enriched from HBVtg*Rag1*-/- adult (>8 wks) and young (3 – 3.5 wks) animals eight days after adoptive transfer with HBV-naïve splenocytes. Percentage of CXCR3+ (**A**) PD-1+ (**B**), Ki67+ (**C**) and Tbet+ (**D**) CD4+ and CD8+ T cells. Data were analyzed using FlowJo™ Software; statistics determined by Tukey's one-way ANOVA with GraphPad Prism Software; * $p < 0.05$; $n \geq 3$ for HBV+ groups, n=2 for HBV- groups.

Another important correlate of effective HBV immunity is a robust IFNγ response by T lymphocytes. In order to evaluate differences in IFNγ on an individual cell basis, I performed *ex vivo* cytokine secretion staining of hepatic lymphocytes using an IFNγ cytokine capture assay, which captures and sequesters IFNγ as it is secreted by cells onto their cell surface for subsequent detection with a secondary antibody. I used this assay together with additional

surface and intracellular antibody staining to characterize the quantitative and phenotypic differences in adult and young IFNγ+ T lymphocytes.

Within CD4+ T cells, there was an increased frequency of total IFNγ+ cells in adult mice (**Fig. 1.10 A**). This was mostly due to an increase in IFNγ+ cells within the T_Eff subset, though there was a similar trend towards increased IFNγ+ T_CM as well (**Fig. 1.10 B**). There were no age-dependent differences in the expression of Ki67, PD-1, or Tbet within IFNγ+ T cells, nor was there a difference in the proportion of IFNγ+ cells that had a Tfh phenotype (**Fig. 1.10 C-F**).
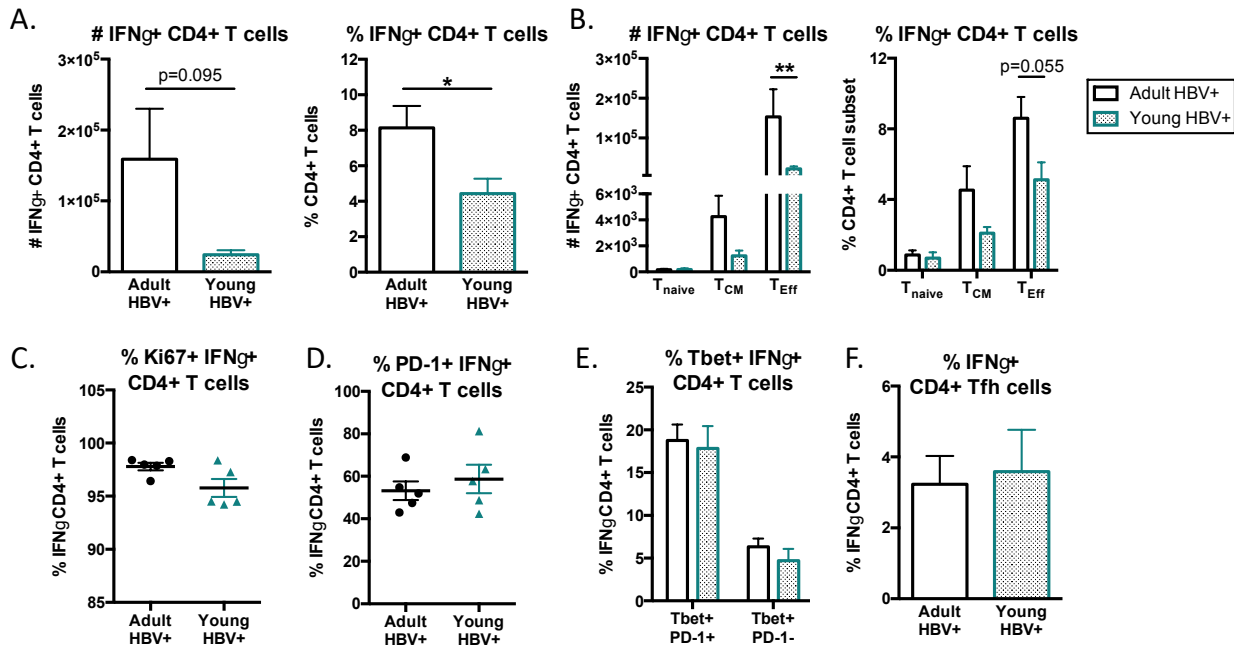
Figure 1.10. Hepatic IFNγ CD4+ T cell responses during acute HBV immunity. Hepatic leukocyte fractions were enriched from HBVtg*Rag1-/-* adult (>8 wks) and young (3 – 3.5 wks) animals eight days after adoptive transfer with HBV-naïve splenocytes and freshly stained with an IFNγ capture assay (Miltenyi) to detect secreted IFNγ, followed by antibody staining for additional surface and intracellular proteins. CD4+ T cell populations were enumerated and numbers and percentages of (**A**) total IFNγ+ (**B**) IFNγ+ T_naive, T_CM, and T_Eff, (**C**) PD-1+ IFNγ+, (**D**) Ki67+ IFNγ+, (**E**) Tbet+ IFNγ+, and (**F**) CXCR5+ PD1+ IFNγ+ T follicular helper cells were calculated. Data were analyzed using FlowJo™ Software; statistics determined by unpaired two-tailed t-test with GraphPad Prism Software; * p<0.05, ** p<0.01; n=5 per group.

Within the CD8+ T cell compartment, I also detected an increased frequency of total

IFNγ+ cells (**Fig. 1.11 A**). This increase was apparent in both CD8+ T_{Eff} and T_{CM} (**Fig. 1.11 B**).

Similar to IFNγ+ CD4+ T cells, IFNγ+ CD8+ T cells were not different in their expression of

Ki67, PD-1, Tbet, or CXCR5 at this early time point (**Fig. 1.11 C-F**).
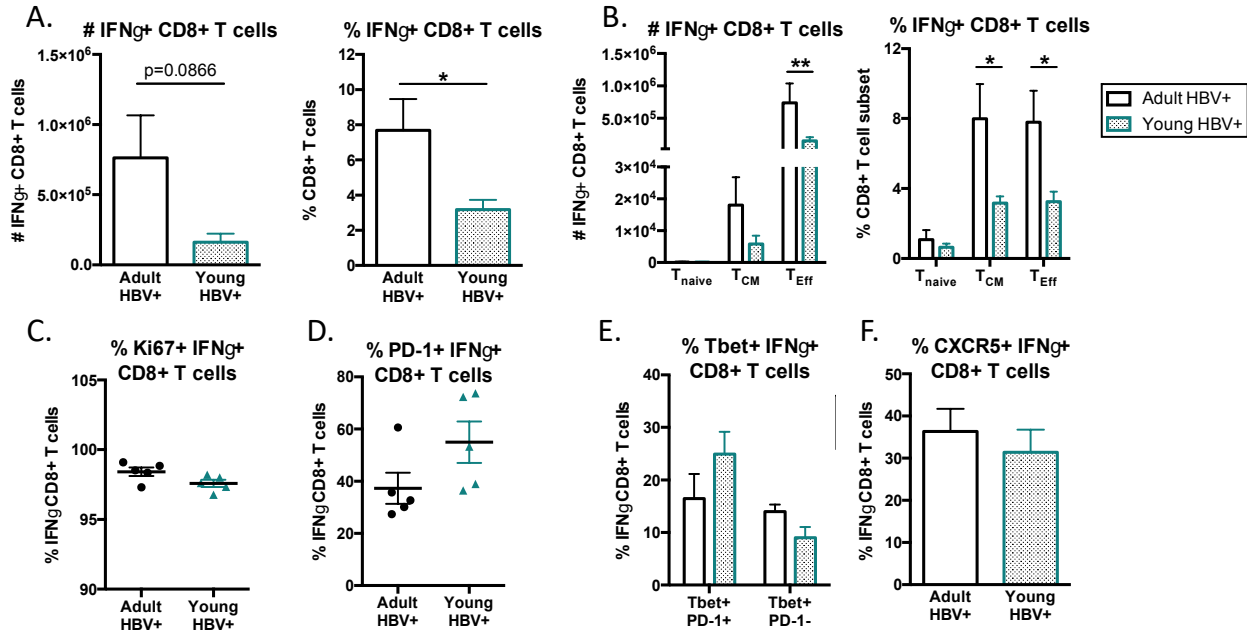
Figure 1.11. Hepatic IFNγ CD8+ T cell responses during acute HBV immunity. Hepatic leukocyte fractions were enriched from HBVtg*Rag1*-/- adult (>8 wks) and young (3 – 3.5 wks) animals eight days after adoptive transfer with HBV-naïve splenocytes and freshly stained with an IFNγ capture assay (Miltenyi) to detect secreted IFNγ, followed by antibody staining for additional surface and intracellular proteins. CD8+ T cell populations were enumerated and numbers and percentages of (**A**) total IFNγ+ (**B**) IFNγ+ T_{naive}, T_{CM}, and T_{Eff}, (**C**) PD-1+ IFNγ+, (**D**) Ki67+ IFNγ+, (**E**) Tbet+ IFNγ+, and (**F**) CXCR5+ IFNγ+ CD8+ T cells were calculated. Data were analyzed using FlowJo™ Software; statistics determined by unpaired two-tailed t-test with GraphPad Prism Software; * p<0.05, ** p<0.01; n=5 per group.

In addition to flow cytometry, I performed IFNγ ELISpot assays by co-culturing hepatic

lymphocytes together with *Rag1*-/- splenocytes as a source of APCs and exogenous HBsAg

peptides with known MHCI- and MHCII-restriction to get a sense of antigen-specific IFNγ T cell

responses. These data show that during the peak phase of inflammation – day eight post-adoptive

transfer – hepatic lymphocytes from adult mice had increased *ex vivo* baseline IFNγ production

indicated by an increased number of IFNγ spots in the absence of additional antigen (peptide "0";

Fig. 1.12). Whereas the young lymphocytes were unable to mount a significant IFNγ response to

any of the four dominant HBsAg epitopes – defined as twice the baseline (peptide "0) IFNγ

response – the adult T cells mounted a robust response to the most dominant early MHCII-

restricted CD4+ HBsAg epitope, peptide 321 (also referred to as peptide 81; **Fig. 1.12**).

Previously published work from our group shows that further differences in the strength and

diversity of T cell IFNγ responses can be measured when looking at pools of multiple HBsAg-

derived peptides that span the entire protein length (*9*).

IFNg Production by Liver Lymphocytes (Day 8)
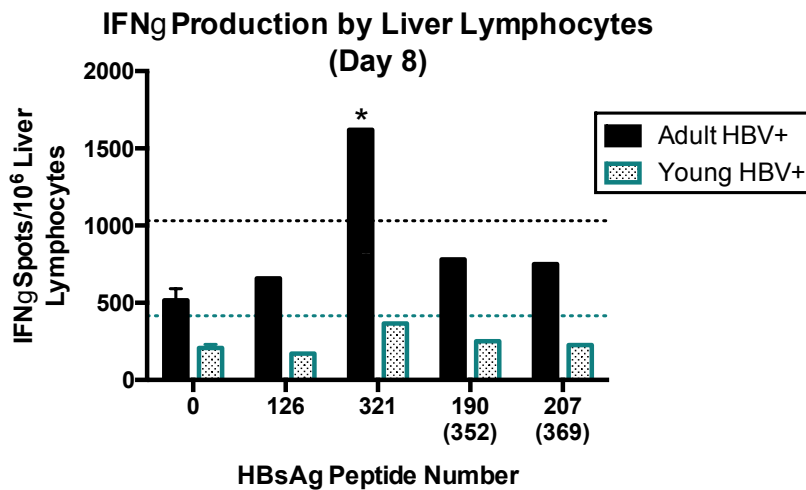
Figure 1.12. Hepatic HBV-specific IFNγ T cell responses during the early acute immune response.
Hepatic leukocyte fractions were enriched from HBVtg*Rag1-/-* adult (>8 wks) and young (3 – 3.5 wks)
animals eight days after adoptive transfer with HBV-naïve splenocytes. 10_5 liver leukocytes were mixed
in a 1:1 ratio with splenocytes from *Rag1-/-* mice as a source of APCs and stimulated overnight at 37°C
together with individual peptides derived from the HBV envelope protein (HBsAg peptides) in ELISpot
plates pre-coated with anti-IFNγ antibodies. "0" peptide denotes no peptide added. ELISpot plates were
counted and analyzed with a CTL Immunospot plate reader and software. The threshold defining a
positive response, marked with a *, is ≥2× the baseline (dashed line).

MGQNLSTSNPLGFFPDHQLDPAFRANTANPDWDFNPNKDTWPDANKVGAGAFGLGFT
PPHGGLLGWSPQAQGILETLPANPPPASTNRQSGRQPTPLSPPLRNTHPQAMQWNST
TFHQTLQDPRVRGLYFPAGGSSSGTVNPVPTTVSPISSIFSRIGDPALNMENITSGF
LGPLLVLQAGFFLLTRILTIPQSLDSWWTSLNFLGGTTVCLGQNSQSPTSNHSPTSC
PPTCPGYRWMCLRRFIIFLFILLLCLIFLLVLLDYQGMLPVCPLIPGSSTTSTGPCR
TCTTPAQGTSMYPSCCCTKPSDGNCTCIPIPSSWAFGKFLWEWASARFSWLSLLVPF
VQWFVGLSPTVWLSVIWMMWYWGPSLYSILSPFLPLLPIFFCLWVYI

$S_{126-138}$ RGLYFPAGGSSSG
$S_{321-335}$/ $S_{158-173}$ FGKFLWEWASARFSW
$S_{352-369}$/ $S_{190-197}$ VWLSVIWM
$S_{379-387}$/ $S_{207-215}$ SILSPFLPL

Figure 1.13. HBV Envelope protein sequence and dominant epitopes for CD4+ and CD8+ antigen-specific T cells. The full-length amino acid sequence of the large HBV envelope protein is shown. The start sites of the large, middle, and small HBV Envelope protein are highlighted in yellow and occur at amino acid position 1, 109, and 164, respectively. The sequence of each of the four most dominant epitopes found in our animal model are underlined and the first amino acid of each sequence is highlighted in green. The number in the subscript for each peptide name refers to the start and end amino acid positions relative to the large envelope sequence. For peptides that are also present in the large isoform, their alternative names are specified after the slash where the subscripted numbers represent the start and end positions relative to the small isoform. This is for consistency with previously identified peptides, referred to as Env190 and Env207 in publication, which correspond to peptides named above as $S_{352-369}$/ $S_{190-197}$ and $S_{369-377}$/ $S_{207-215}$, respectively (*17*).

After identifying the most common epitopes that drive IFNγ T cell responses, we were able to begin testing these peptides in tetramer format to allow for the identification of individual antigen-specific T cells by flow cytometry. The first tetramer we received from the NIH tetramer core facility was an MHCII-restricted epitope that is presented to CD4+ T cells, sequence RGLYFPAGGSSSG, starting at amino acid 126 relative to the large isoform of the hepatitis B envelope/surface protein (**Fig. 1.13**). Using this tetramer, I was able to quantitate and characterize this antigen-specific population within the liver. Adult animals on average had approximately ten times more $HBsAg_{126}$+ CD4+ T cells compared to young mice, although the $HBsAg_{126}$+ cells represented a similar proportion of total CD4+ T cells, regardless of age (**Fig. 1.14 A-B**). The difference in $HBsAg_{126}$+ cell number could be almost entirely attributed to an

expansion of HBsAg$_{126}$+ T$_{Eff}$ in adults, as there was a roughly equivalent amount of HBsAg$_{126}$+

T$_{CM}$ in adult and young livers (**Fig. 1.14 C-D**). Consistent with this, 90 – 95 percent of

HBsAg$_{126}$+ T cells in adults were of the T$_{Eff}$ phenotype, whereas only approximately 60 – 70

percent of young HBsAg$_{126}$+ T cells in young mice were T$_{Eff}$ with an increased representation of

HBsAg$_{126}$+ T$_{CM}$.
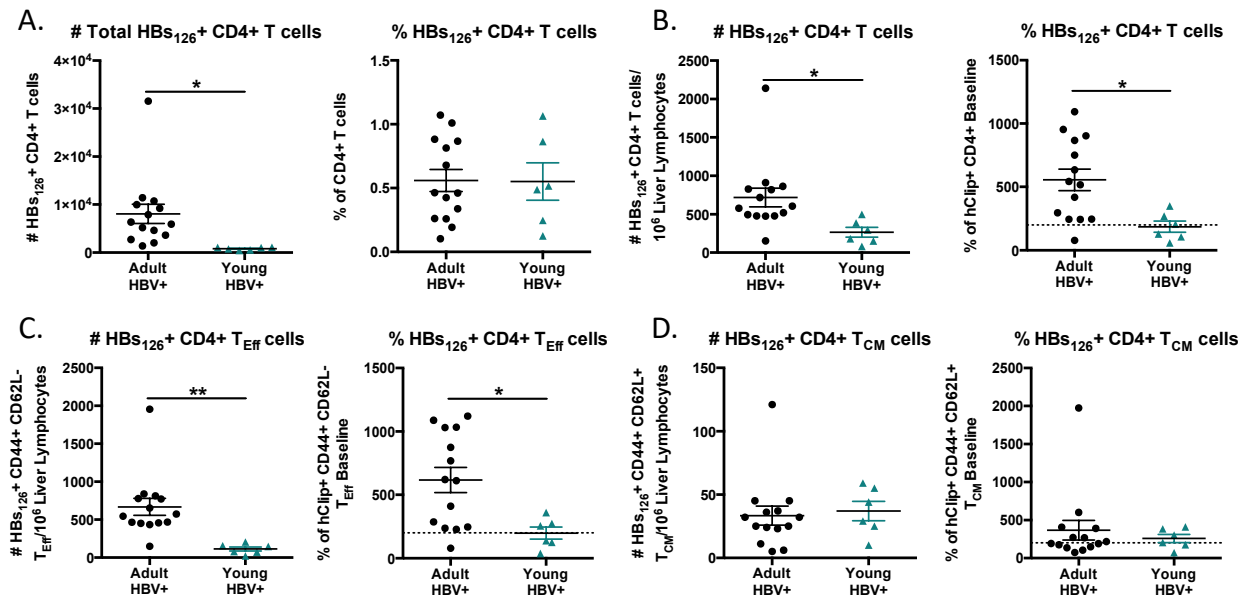
Figure 1.14. Hepatic antigen-specific CD4+ T cell responses are enriched in adults. Hepatic leukocyte fractions were enriched from HBVtg*Rag1*-/- adult (>8 wks) and young (3 – 3.5 wks) animals eight days after adoptive transfer with HBV-naïve splenocytes and stained with I-A(b)-HBs$_{126}$ (RGLYFPAGGSSSG) tetramers, followed by antibody staining for additional surface proteins. (**A**) Total HBs$_{126}$+ CD4+ T cells were measured and reported as numbers and percentage of total CD4+ T cells. (**B**) HBs$_{126}$+ CD4+ T cells per million liver lymphocytes and the percentage relative to an irrelevant peptide (I-A(b)-human CLIP, PVSKMRMATPLLMQA) baseline frequency was determined. A true antigen-specific population is defined as two-fold higher than baseline and is marked by a dotted line. Numbers per million hepatic lymphocytes and percentages above I-A(b)-hCLIP baseline of (**C**) CD44+ CD62L-T$_{Eff}$ and (**D**) CD44+ CD62L+ T$_{CM}$ were measured. Data were analyzed using FlowJo™ Software; statistics determined by unpaired two-tailed t-test with GraphPad Prism Software; * $p<0.05$, ** $p<0.01$; n≥6 per group.

To better understand the phenotypic characteristics of HBsAg$_{126}$+ cells I also evaluated

the expression of additional markers of T cell function and identity. There were no differences in

CD127 (IL-7Rα) expression, which can identify long-lived memory cells; however, this marker

is most useful after the acute inflammation phase begins to contract and eight days post-transfer

may be too soon to capture this population [**Fig. 1.15A**, (*16*)]. There were striking differences in

the expression of PD-1 and Ki67, where approximately 65% of adult $HBsAg_{126}$+ CD4+ T cells

were PD-1+ compared to approximately 25% of $HBsAg_{126}$+ CD4+ T cells in young mice and

approximately 95% of $HBsAg_{126}$+ adult T cells were Ki67+ compared to 40% in young mice

(**Fig. 1.15 B-C**). Altogether, these data suggest that the antigen-specific CD4+ T cells in adults

are more strongly activated, more proliferative, and more effector-like in their phenotype,

indicating a robust anti-viral effector T cell response is initiated in the livers of adult animals that

is significantly diminished in young animals.
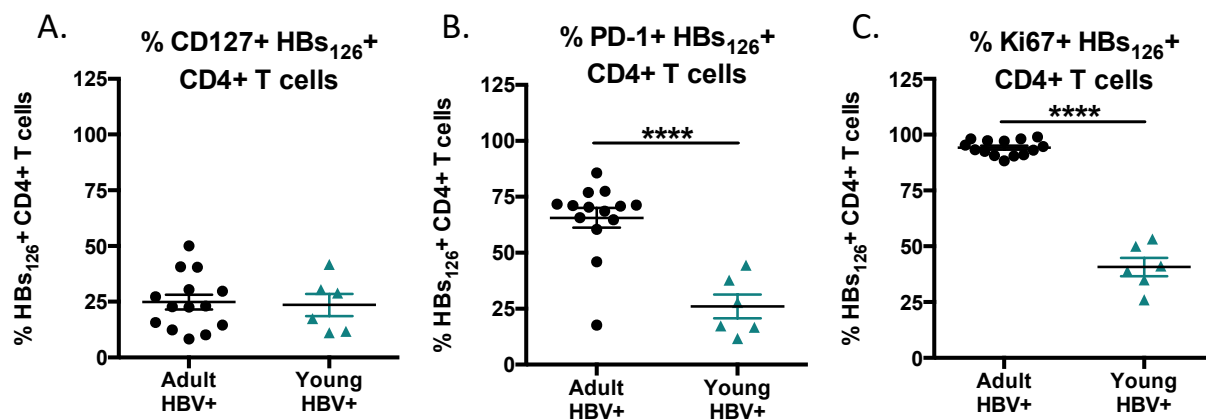
Figure 1.15. Hepatic antigen-specific CD4+ T cells express PD-1 and Ki67, but not CD127, in an age-dependent manner. Hepatic leukocyte fractions were enriched from HBVtg*Rag1-/-* adult (>8 wks) and young (3 – 3.5 wks) animals eight days after adoptive transfer with HBV-naïve splenocytes and stained with I-A(b)-HBs126 (RGLYFPAGGSSSG) tetramers, followed by antibody staining for additional surface proteins. Frequencies of CD127+ (**A**), PD-1+ (**B**), and Ki67+ (**C**) HBs126+ CD4+ T cells were measured. Data were analyzed using FlowJoᴛᴍ Software; statistics determined by unpaired two-tailed t-test with GraphPad Prism Software; **** $p<0.0001$; $n \geq 6$ per group.

The studies outlined above help provide a view into the early phase of adaptive immune

activation and the immune priming that will ultimately dictate the outcome of HBV "infection"

in these animals. Future work in our lab will continue to probe the characteristics that define a

strong and resilient effective immune response with a particular focus on identifying antigen-specific T cells and their phenotypic and functional profiles with our newly developed MHCI- and MHCII-restricted tetramers.

1.3 - Innate Immunity in HBV Infection

Another goal of my thesis work has been to carefully characterize the myeloid populations in the liver that respond to HBV. This is of critical importance to understanding the age-dependent anti-HBV immune responses, as we know these populations are primarily tissue resident and serve as an important source of antigen presentation in the liver. First, I focused on the myeloid populations during "acute HBV immunity" eight days after adoptive transfer of splenocytes and quantitated the total number and cellular frequencies of major populations including granulocytes/neutrophils, monocytes, macrophages, and dendritic cells. Just like the lymphocytes described above, myeloid cells were isolated after perfusion of the liver such that the single cell suspensions collected do not contain blood-derived, circulating mononuclear cells. It is important to note that the single cell suspensions were applied to a lymphocyte-enriching Percoll® gradient in order to efficiently remove hepatic debris and non-immune liver cells. A limitation of this approach is a likely loss of large myeloid cells such as macrophages, including liver-resident Kupffer cells, because this lymphocyte-enriching gradient is most efficient at enriching the smaller, denser cells, including lymphocytes, monocytes, and smaller monocyte-derived macrophages and dendritic cells. Nevertheless, we still observed some important age-dependent trends that are likely to impact immune priming.

There were no differences in the total number or percentages of granulocytes (CD45+ Gr1+ CD11b+), Kupffer cells (CD45+ SSC_{hi} $MHCII_{lo}$ $CD11b_{int}$ F4/80+ $Ly6c_{lo/-}$), monocyte-

derived macrophages (CD45+ CD11b$_{hi}$ Ly6c$_{hi}$ F4/80+), or dendritic cells (DCs; CD45+ CD11c+ MHCII+; **Fig. 1.16 A-E**). There was, however, a trend towards more DCs (CD45+ CD11c+ MHCII$_{hi}$), particularly of the CD11b+ type two classical dendritic cell subset (cDC2), in adult animals with no differences in the number of CD11b- cDC1 or in CD8α+ DCs (CD45+ CD11c+ MHCII$_{hi}$ CD11b- CD8α+; **Fig. 1.16 C**). Furthermore, there was also evidence of a greater than two-fold increase in MHCII expression within cDC2, suggesting that this population may play an important role in antigen presentation within the livers of adult animals (**Fig. 1.16 F**). These data are consistent with the observation that young animals have increased expansion of CD8+ T cells, as cDC1 are the subset capable of cross-presenting to CD8+ T cells and favor activation of a typical anti-viral response. On the other hand, cDC2 have been shown to play crucial roles in inducing Tfh cell priming, which may explain the increased expansion of the CD4+ T cell compartment, particularly Tfh cells, in adults that is impaired in young animals. There is also age-dependent expression of MHCII on Kupffer cells, where young animals have increased MHCII compared to adults within this macrophage subset (**Fig. 1.16 F**). Depending on the context, Kupffer cells can play a more tolerogenic role in T cell priming through their production of IL-10 and prostaglandins (*18, 19*). Therefore, it is possible that increased antigen presentation by this subset in young mice may result in more moderate lymphocyte priming as compared to other APC subsets such as dendritic cells.

Although monocytes are often considered to be a relevant peripheral cell type, it's well understood that during an ongoing immune response circulating monocytes are recruited into tissues where they can further differentiate into macrophages and dendritic cells to support immune priming. When looking at these infiltrating monocytes there are two major subsets, Ly6c$_{hi}$ CD11c- inflammatory/classical monocytes (CD45+ MHCII$_{lo/-}$ CD11b+ Ly6c$_{hi}$ CD11c-

F4/80+/-) and Ly6clo/- CD11c+ resident or patrolling monocytes, the latter of which is known to be more regulatory in its function and plays an important role in resolution of inflammation and wound healing (*20, 21*). Adult animals have increased monocyte accumulation in the liver compared to young mice, of both the inflammatory and resident subsets (**Fig. 1.16 D**).
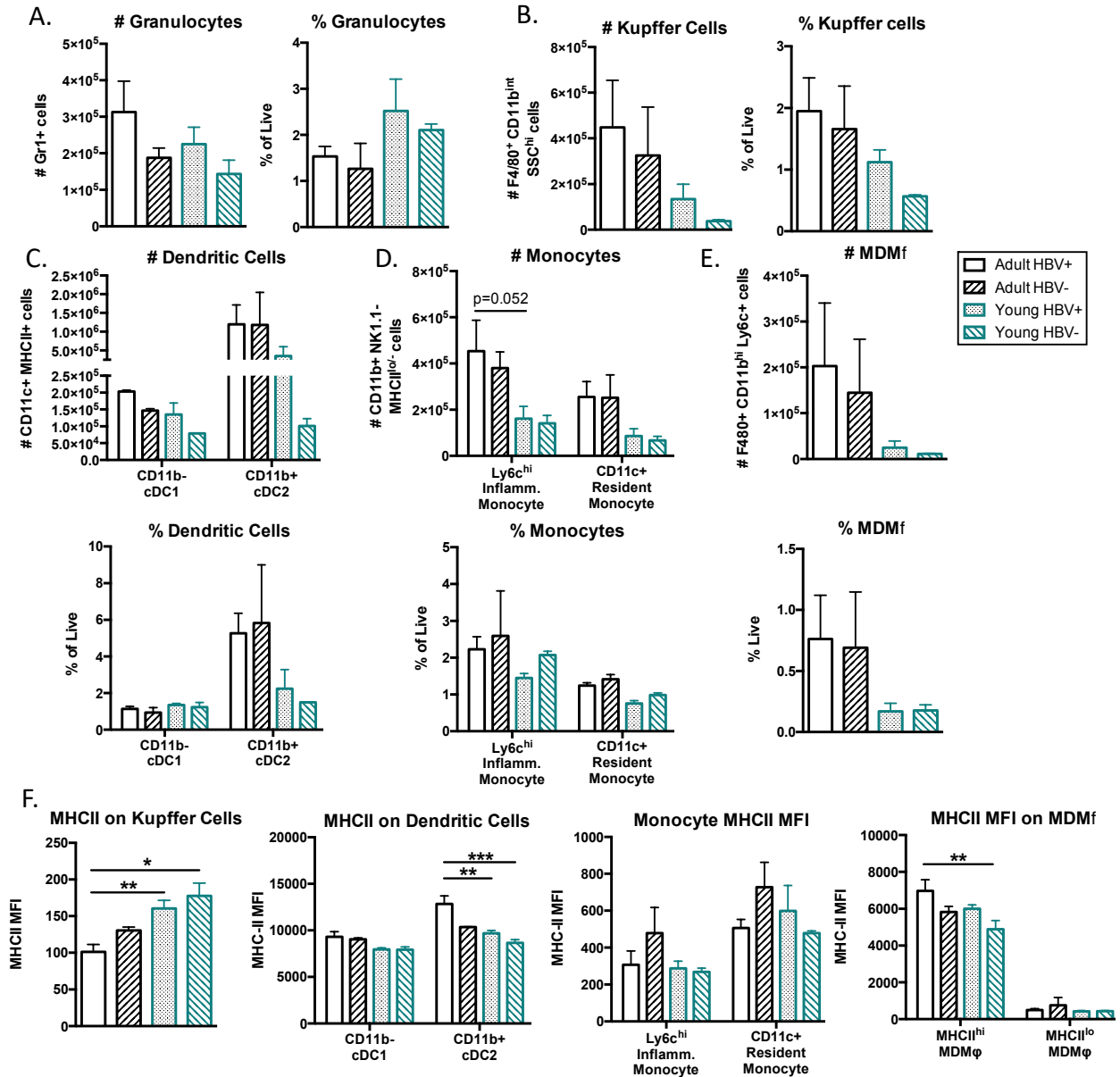
Figure 1.16. Characterization of hepatic myeloid populations during acute HBV immunity. Hepatic leukocyte fractions were enriched from HBVtg*Rag1*-/- adult (>8 wks) and young (3 – 3.5 wks) animals

eight days after adoptive transfer with HBV-naïve splenocytes. Flow cytometry was used to identify and quantitate myeloid cell populations as follows (**A**) granulocytes (Live Gr1+ CD11b+), (**B**) Kupffer cells (Live F4/80+ CD11b$_{int}$ SSC$_{hi}$ Ly6c-), (**C**) dendritic cells (DCs; Live CD11c+ MHCII+), further subdivided in to classical dendritic cell subsets 1 (cDC1; CD11b-) and 2 (cDC2; CD11b+), (**D**) monocytes (Live CD11b+ NK1.1- MHCII$_{lo/-}$ SSC$_{lo}$), and (**E**) monocyte derived macrophages (MDMφ; Live F4/80+ CD11b$_{hi}$ Ly6c$_{+/hi}$ MHCII$_{hi/+}$ or MHCII$_{+/lo}$). (**F**) MHC class II (MHCII) expression level was determined using anti-I-A(b) antibody staining and reported as median fluorescence intensity of Kupffer cells, DCs, monocytes, and MHCII$_{hi/+}$ or MHCII$_{+/lo}$ MDMφ. Data were analyzed using FlowJo™ Software; statistics determined by unpaired two-tailed t-test with GraphPad Prism Software; * $p<0.05$, ** $p<0.01$, *** $p<0.001$; n=5 for HBV+ groups and n=2 for HBV- groups.

In addition to the myeloid compartment, the liver is also home to many other innate immune cells, notably NK cells and the closely related innate lymphoid cells (ILC). ILC can be further broken up into three main subsets: ILC1, ILC2, and ILC3, which closely mimic their T cell counterparts, Th1, Th2, and Th17/22, respectively, in both their transcriptional and functional profiles. NK cells and ILC1 express the transcription factor T-bet (encoded by the gene *Tbx21*; T-box transcription factor 21), whereas NK cells additionally require eomesodermin (Eomes). Both NK cells and ILC1 are crucial for anti-viral and intracellular pathogen responses through their production of IFNγ and cytotoxic effector functions. Because of the similar phenotypic and functional profiles of ILC1 and NK cells, much of the early published literature regarding NK1.1+ TCR- cells does not distinguish between these cells. The difference between these populations can be traced back to their development, as NK cells differentiate from a dedicated NK cell precursor, while ILC1 are derived from a common ILC precursor (*22*). ILC2s are dependent on the transcription factor GATA-binding protein 3 (GATA3) and mainly produce IL-5 and IL-13 in response to IL-33 and IL-25 cytokine signals, which play critical roles in type-two immunity in the context of allergy and helminth infection. Lastly, ILC3s are dependent on the transcription factor Retinoic acid-related orphan receptor gamma t (RORγt) and respond to IL-23 and IL-1β to produce IL-17a, IL-17f, IL-22, granulocyte-macrophage colony-stimulating factor (GM-CSF), and under certain circumstances IFNγ. ILC3s can be further subdivided into

two major subsets, natural cytotoxicity receptor (NCR)+ and NCR- ILC3s, which are differentiated by their expression of NKp46 in mice and NKp44 in humans. The NCR- ILC3 subset can also be separated by CCR6 and/or CD4 expression to further identify the lymphoid tissue-inducer (LTi) and LTi-like subsets in the fetus and adult, respectively, which are positive for both CCR6 and CD4. The LTi subset was the first ILC type identified, as it plays a critical role in the development of lymphoid organs mainly through the expression of lymphotoxin, which interacts with stromal lymphoid organizer cells to generate and organize functional regions within lymphoid tissues (*23, 24*). LTi cells disappear soon after birth; however, adult bone marrow-derived LTi-like ILC3s exist and have been shown to regulate tertiary lymphoid structure formation in the context of infection and other immune insults (*24, 25*).

Our interest in ILCs was first piqued by the observation that a number of mRNA transcripts associated with genes and their products related to ILC3s were expressed at a higher level in hepatic innate immune cells from adult *Rag1*-/- animals compared to young animals at baseline, before adoptive transfer of wildtype splenocytes, as measured by microarray (**Fig. 1.17**). More specifically, analysis of this data set revealed increased expression of *Rorc* (the gene that encodes RORγt), *Il17a, Il17f, Il22, Colony-stimulating factor 2* (*Csf2*; the gene encoding GM-CSF), *Lymphotoxin α* (*Lta*) and *β* (*Ltb*), *Ccr6*, and tumor necrosis family member 11 (*Tnfsf11*, also known as RANK ligand; RANKL) and 14 (*Tnfsf14*, also known as LIGHT). These data suggested that there may be an age-dependent increase in the number or functional capacity of hepatic ILC3.
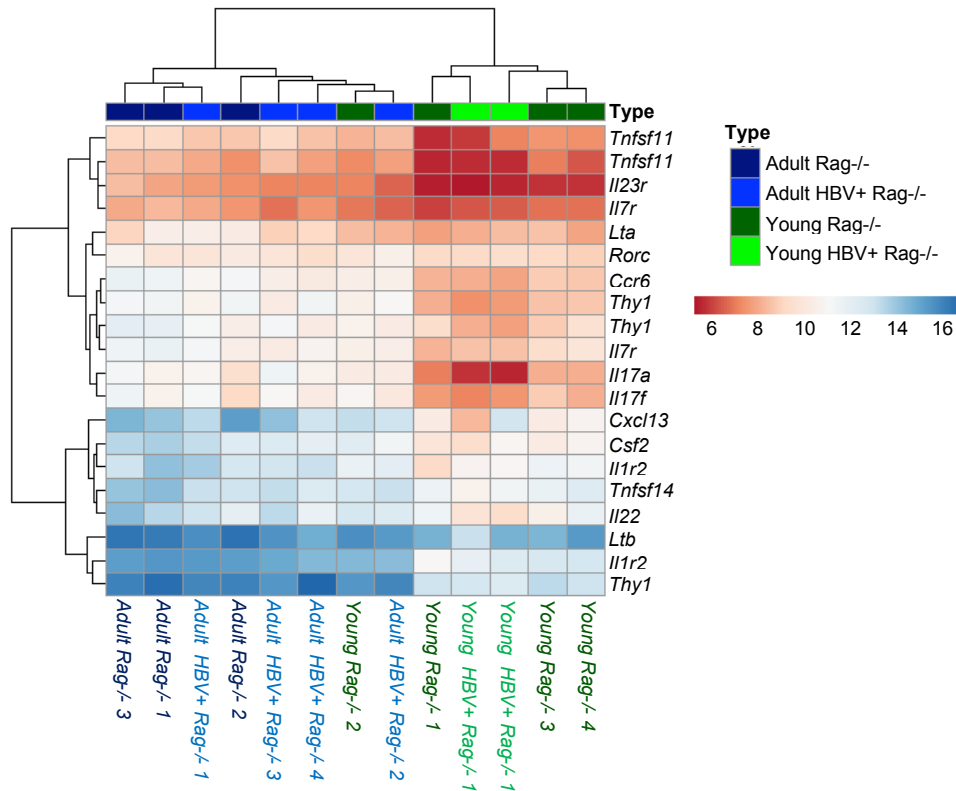
Figure 1.17. Increased expression of ILC3-associated transcripts in adult hepatic innate immune populations. Hepatic myeloid fractions were enriched from *Rag1-/-* or HBVtg*Rag1-/-* adult (8-10 wks) and young (3 wks) animals that were not adoptively transferred. RNA was isolated from frozen cell pellets and submitted to the UCSF Genomics Core for transcript analysis using the Agilent 4x44 Mouse GE platform with additional custom probes for HBV transcript recognition. The average $\log_2$ based intensity (*aveA*) of selected transcript probes across all arrays, a proxy for gene expression level, is reported in heatmap format. Individual animals are labeled on the x-axis while gene names of selected ILC3-related transcripts are on the y-axis. Color coding on the top bar represents the biological group as specified in the key while the expression level is depicted on a red/blue scale that corresponds to *aveA* levels.

In order to investigate this further, I performed flow cytometry experiments of hepatic

leukocyte populations from WT, *Rag1-/-*, and two strains of RORγt-GFP reporter mice to identify

differences in the number and frequency of liver resident NK cells, ILC1, ILC2 and ILC3.

Because ILC3s have mostly been studied in the context of the small and large intestine and the

spleen, it was critical to determine whether the markers used to identify ILC3s were similarly

expressed within the liver and to validate the robustness of the RORγt-GFP reporter by

comparing native fluorescence to intracellular RORγt staining. After careful assessment of early

experiments, we determined that the first reporter strain we were using, B6.129P2(Cg)-Rorctm2Litt/J or RORc(γt)-EGFP generated by Dr. Dan Littman (*23*), where heterozygous RORc(γt)GFP/+ animals have GFP expression within RORγt-expressing cells including ILC3, were not sufficiently bright to identify the entire hepatic population of ILC3s. Many GFP+ cells were dim and close to background levels seen in RORc(γt)GFP/GFP animals, which are RORγt-null and lack ILC3s along with other RORγt+ cell types including CD4+ T helper (Th)17, CD8+ T cytotoxic (Tc)17, and a large subset of γδ T cells. For this reason, we relied on intranuclear staining of RORγt for the data presented below. It is important to mention, however, that we have obtained a new strain of RORγt-reporter mice, designated Tg(Rorc-EGFP)1Ebe or RORc(γt)-BAC, generated in Dr. Gerard Eberl's laboratory. This RORc(γt)-BAC mouse has a much brighter and more robust GFP signal, even beyond the levels achieved with intracellular staining. This was accomplished through the use of a bacterial artificial chromosome (BAC) containing the *Rorc* gene with an EGFP construct knocked into the ATG start site of the *Rorc(γt)* isoform of the gene locus, whereby an estimated 5-10 copies of the BAC transgene were integrated at an unknown site within the genome. The resulting mouse is a bright RORγt-EGFP reporter as both a heterozygote and homozygote (*26*).

When examining the number and frequency of each hepatic NK cell and ILC subset, I found each population had a different age-dependent profile. As mentioned above, the phenotype of NK cells and ILC1s are very similar and as a result there has been inconsistency in how each of these populations is defined. For the purposes of this study, we defined NK cells as NK1.1+ CD127- CD90+/- CD49b+/- and ILC1 as NK1.1+ CD127+ CD90+ RORγt- because NK cells do not rely on the expression of CD127 (IL-7Rα) for their development, whereas ILC1s do. CD49b

(DX5) has also been used by some groups to distinguish between ILC1 and NK cells, however, in the liver we found that the majority of CD49b- NK1.1+ cells did not express CD127, inconsistent with other ILCs (*27*). Many, but not all, of these CD49b- NK1.1+ cells were also CD90+, another marker expressed by all ILC. Although CD90 expression is associated with ILCs, we also found many CD49b+ NK1.1+ cells that were CD90+, suggesting that CD90 expression alone was not sufficient to identify ILC1 nor separate CD49b+ versus CD49b- subsets. CD49b has been described to represent a marker of NK cell maturation; thus, we have evaluated CD49b+ and CD49b- NK cells separately as they are reported to be functionally distinct (*28*).

Following this gating strategy, I observed an age-dependent increased abundance of mature NK cells (NK1.1+ CD49b+ CD90+/- CD127-) at each time point, day 0 (before adoptive transfer) and day 3 and day 8 post-transfer during the acute phase of the immune response, with a clear expansion of this population over time (**Fig. 1.18**). This increase in NK cells in adults was in contrast to the age-dependent decrease in the number and percentage of immature NK cells (NK1.1+ CD49b- CD90+/- CD127-) with age, such that young animals have a greater representation of CD49b- cells within the NK cell fraction compared to adults where CD49b+ cells dominate (**Fig. 1.18**). Unlike the NK cells, there was no evidence of a major expansion of this population during the anti-HBV response. Because the differences in CD49b+ and CD49b- NK cells were reciprocal, there were no differences in the total number of NK1.1+ TCRβ- cells by age.
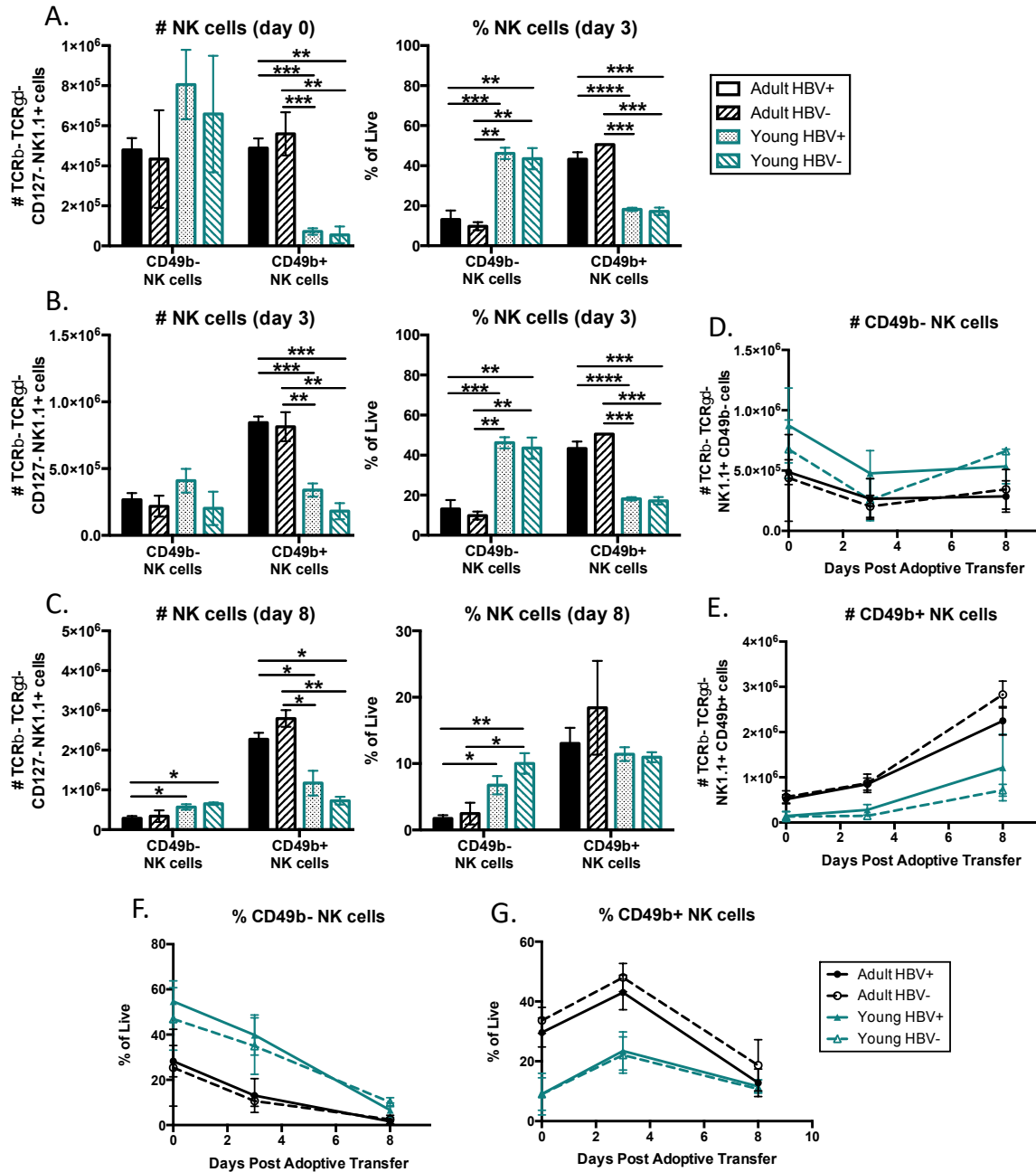
Figure 1.18. Hepatic NK cell dynamics in adult and young mice during early HBV immunity.
Hepatic leukocyte fractions were enriched from HBVtg*Rag1-/-* adult (>8 wks) and young (3 – 3.5 wks) animals eight days after adoptive transfer with HBV-naïve splenocytes. Cells were stained for surface and intracellular markers and data were collected on an LSRII flow cytometer. (**A**) The number and percentages of hepatic NK1.1+ CD127- relative to live cells were measured at day 0. NK cells at subsequent time points day 3 (**B**) and day 8 (**C**) were defined as TCRβ- TCRγδ- NK1.1+ CD127-. Total numbers of (**D**) CD49b+ and (**E**)CD49b- NK cells and percentages of (**F**) CD49b- and (**G**) CD49b+ NK cells relative to live cells is graphed as a function of time; statistics are shown in panels A-C for these data. Data were analyzed using FlowJoᴛᴍ Software; statistics determined by Tukey's ANOVA with multiple comparisons using GraphPad Prism Software; * p<0.05, ** p<0.01, *** p<0.001, **** p<0.0001; n≥4 for HBV+ groups, n ≥2 for HBV- groups.

35

I examined the number and frequency of CD127+ ILC1 during the early HBV immune response. There was a suggestion of a possible increase in ILC1 in adult HBV+ animals compared to HBV- adults and HBV+ young mice at day 0 and day 3, however this was not statistically significant (**Fig. 1.19 A-B, D-E**). By day 8 post-transfer, we could see an age-dependent increase in the number of ILC1; however, the percentage of ILC1 relative to total cells or total ILCs (CD127+ CD90+) was not different by age (**Fig. 1.19 C-F**). Together, these data suggest that age is likely not a major regulator of ILC1 differentiation or expansion during an HBV immune reponse.
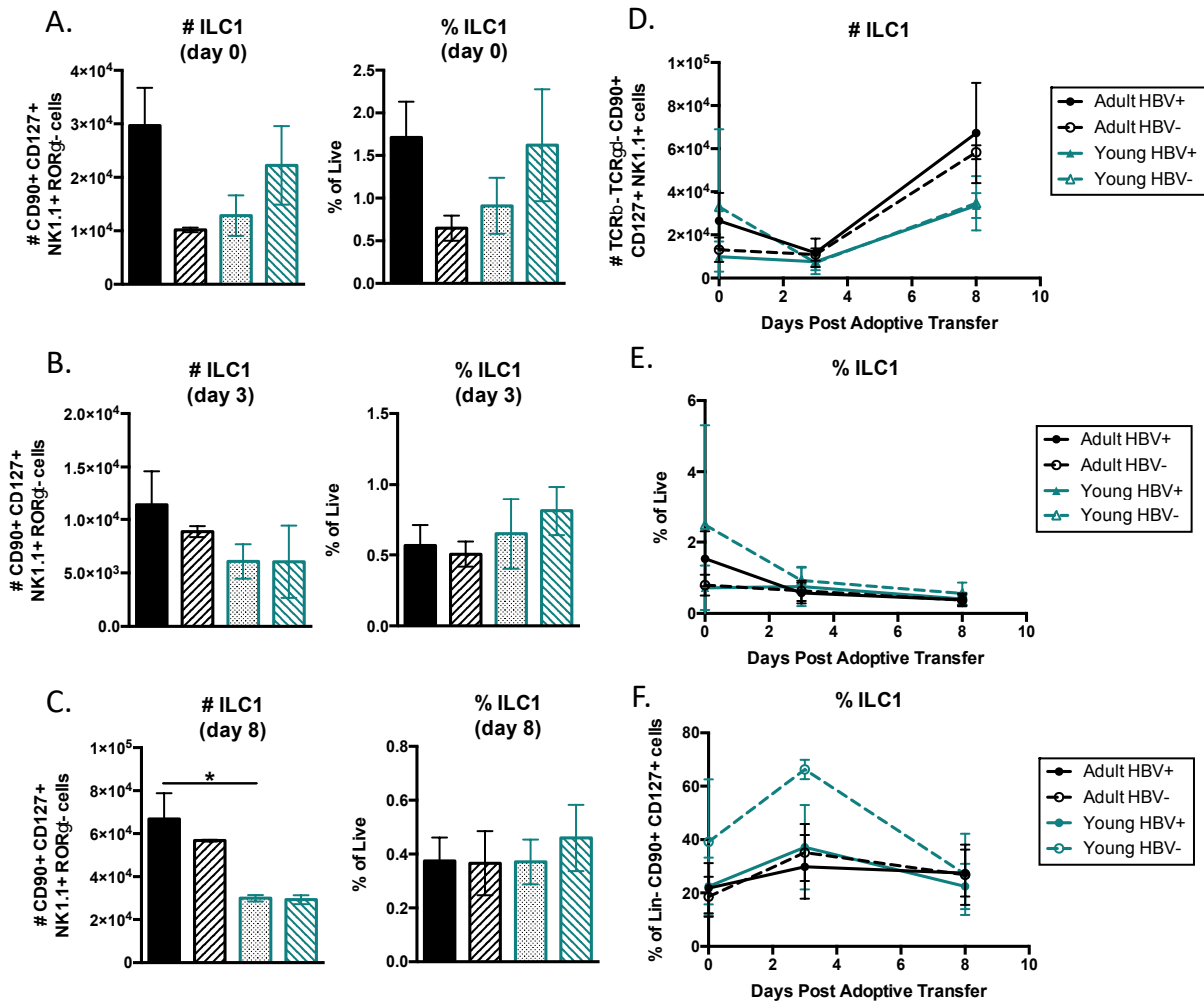
Figure 1.19. Hepatic ILC1 cell dynamics in adult and young mice during early HBV immunity.
Hepatic leukocyte fractions were enriched from HBVtg*Rag1*-/- adult (>8 wks) and young (3 – 3.5 wks)
animals eight days after adoptive transfer with HBV-naïve splenocytes. Cells were stained for surface and
intracellular markers and data were collected on an LSRII flow cytometer. The number and percentages
of hepatic NK1.1+ CD49b- relative to live cells were measured at day 0 (**A**). ILC1at subsequent time
points day 3 (**B**) and day 8 (**C**) were defined as TCRβ- TCRγδ- CD90+ CD127+ NK1.1+. (**D**) Total
numbers and (**E**) percentages relative to live cells is graphed as a function of time; statistics are shown in
panels A-C for these data. (**F**) ILC1 as a percentage of total CD90+ CD127+ cells. Data were analyzed
using FlowJoᴛᴍ Software; statistics determined by Tukey's ANOVA with multiple comparisons using
GraphPad Prism Software; * p<0.05, ** p<0.01, *** p<0.001; n≥4 for HBV+ groups, n ≥2 for HBV-
groups.

Early studies in our lab showed that NK1.1+ cells play a critical role in early liver

inflammation; however, these effects were largely attributed to NKT cells rather than NK cells as

transfer of NK1.1+ TCRβ+ cells lead to hepatic inflammation whereas transfer of NK1.1+

TCRβ- cells did not (*29*). Further investigation revealed that the presence of the HBV transgene

led to increased expression of NKG2D on NK and NKT cells and a concurrent increase in

NKG2D ligands, specifically retinoic acid inducible-1 (RAE-1), which together promoted NKT

cell activation and the production of IFNγ and IL-4, both of which play an important role in viral

control and immune priming of other lymphocytes (*30*). At the time of these studies, the

potential role of NK1.1+ TCRβ- NK cells in facilitating a productive immune priming

environment or in the eventual clearance of viral antigens had not been investigated.

Furthermore, the distinction between CD49b+ versus CD49b- NK1.1+ NK cells and their

associated functional effects was not evaluated in the context of HBV immunity. Therefore,

future studies are needed in order to determine whether the observed difference in the relative

ratios of mature and immature NK cells in adult and young mice may contribute to their age-

dependent outcomes, with a focus on which effector molecules each subset expresses and

whether these effectors can help to support antigen presentation and lymphocyte priming and

differentiation necessary for effective HBV control.

At baseline, before adoptive transfer, there were a greater number and frequency of ILC2 (CD90hi CD127+ IL-33R+ RORγt- NK1.1-) in young mice (**Fig. 1.20 A**). Interestingly, by day 8 this age-dependence was reversed and ILC2s were more abundant in adults (**Fig. 1.20 B-F**). Some recent studies have begun to uncover a role for ILC2s in non-viral liver disease contexts, particularly in relation to fibrosis (*31*). However, while we cannot rule out a role for ILC2s in anti-HBV immunity, the lack of consistent age-dependent differences throughout this early immune response suggests that these cells are likely not involved in the impaired ability of young mice to clear hepatitis B viral antigens.
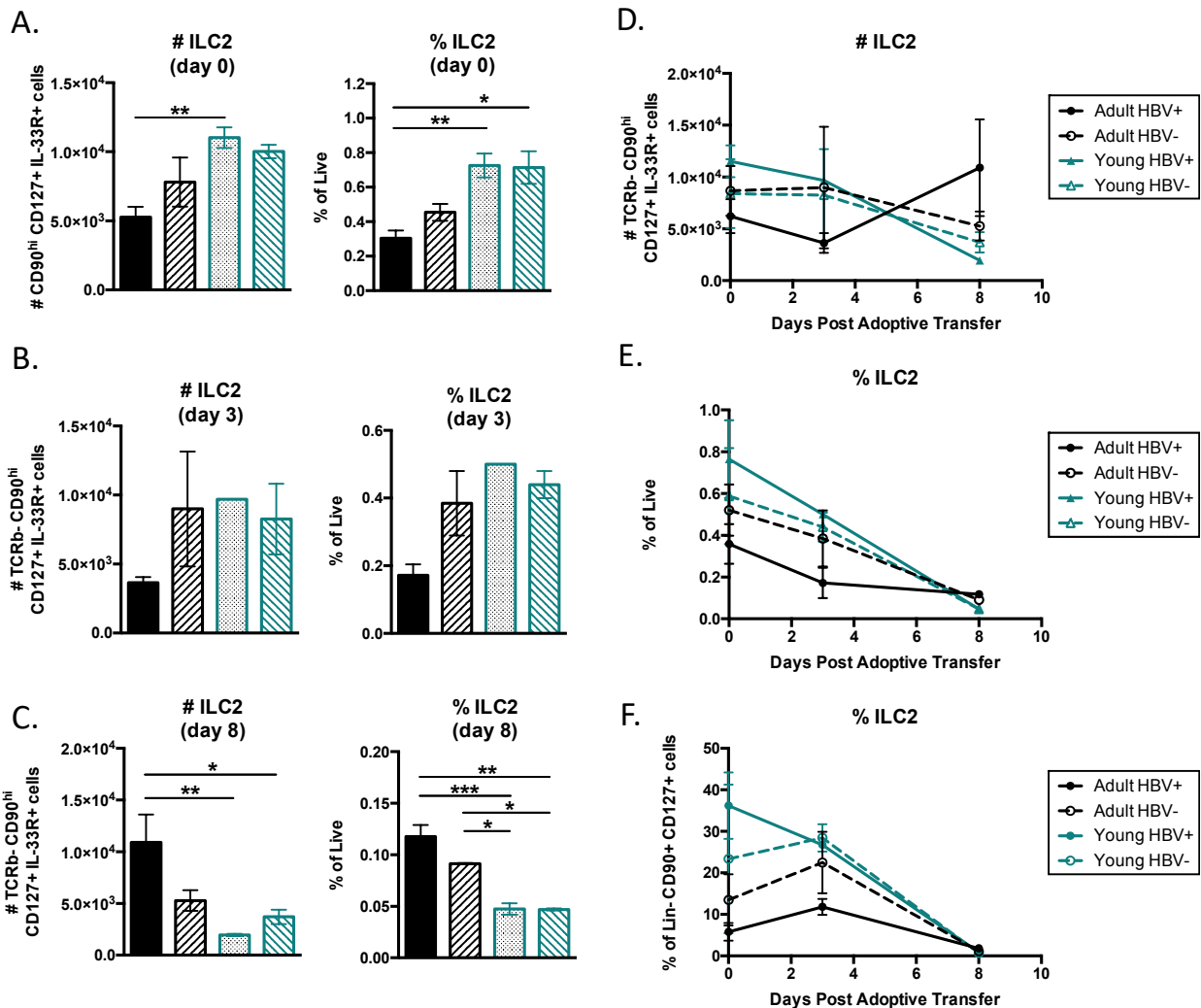
Figure 1.20. Hepatic ILC2 cell dynamics in adult and young mice during early HBV immunity. Hepatic leukocyte fractions were enriched from HBVtg*Rag1*-/- adult (>8 wks) and young (3 – 3.5 wks) animals eight days after adoptive transfer with HBV-naïve splenocytes. Cells were stained for surface and intracellular markers and data were collected on an LSRII flow cytometer. The number and percentages of hepatic CD90+/hi CD127+ IL-33R+ relative to live cells were measured at day 0 (**A**). ILC2s at subsequent time points day 3 (**B**) and day 8 (**C**) were defined as TCRβ- TCRγδ- CD90+/hi CD127+ IL-33R+. (**D**) Total numbers and (**E**) percentages relative to live cells is graphed as a function of time; statistics are shown in panels A-C for these data. (**F**) ILC2 frequency shown as a percentage of total CD90+ CD127+ cells. Data were analyzed using FlowJoTM Software; statistics determined by Tukey's ANOVA with multiple comparisons using GraphPad Prism Software; * p<0.05, ** p<0.01, *** p<0.001; n≥4 for HBV+ groups, n ≥2 for HBV- groups.

I observed that adults had an increased number of ILC3s (TCR- CD90hi CD127+ IL-33R- RORγt+ NK1.1+/-) compared to young mice at baseline and at day 3 post-adoptive transfer (**Fig. 1.21 A-B, D-F**). However, by day eight the numbers of ILC3s were roughly equivalent in adult and young animals (**Fig. 1.21 C-F**). At this later time point, we know there is a much greater infiltration of splenic donor cells, which do contain ILC3s, into the liver. Thus, it is possible that infiltrating splenic ILC3s contribute towards an equalization of numbers in young and adult mice by this time point.
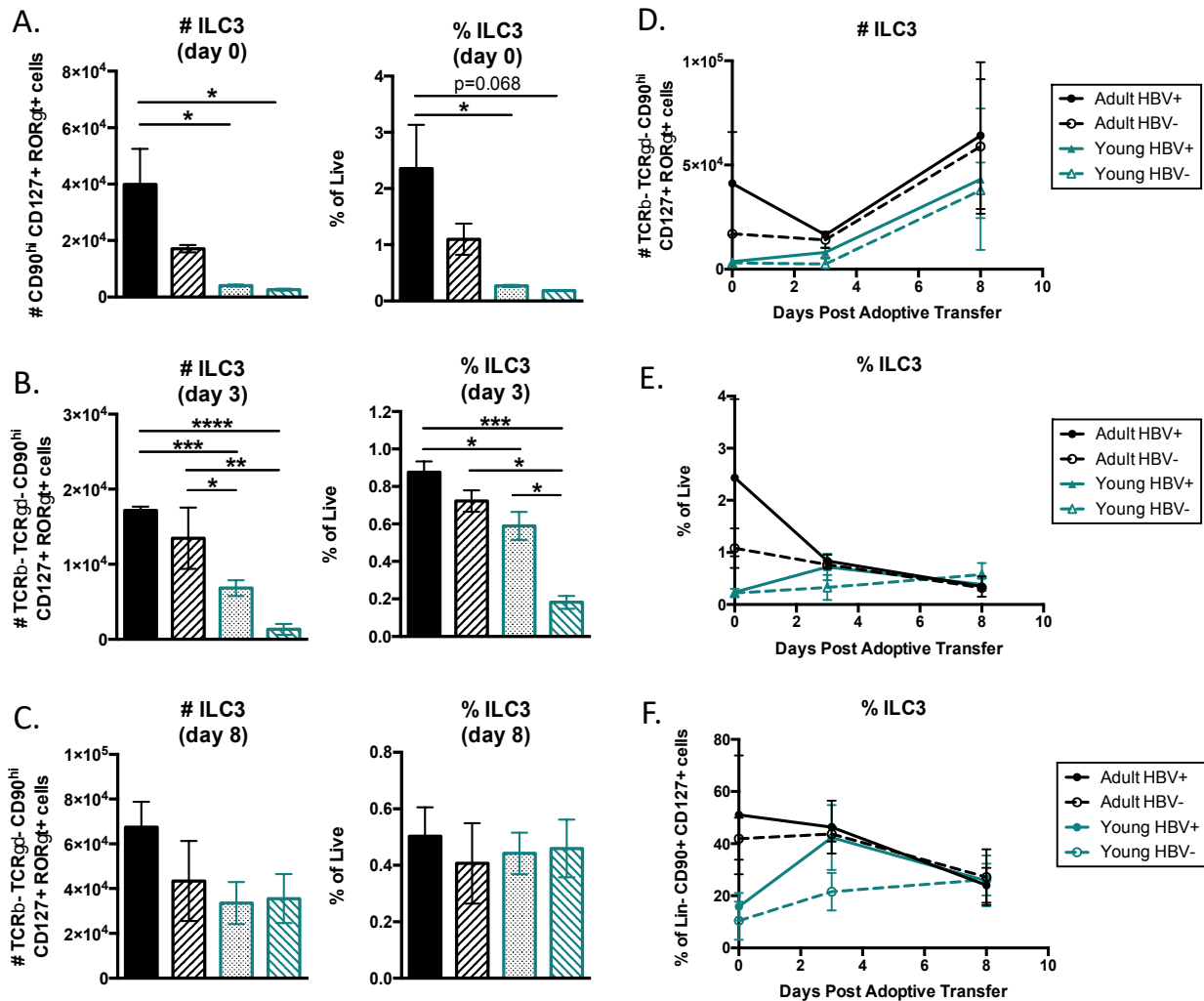
Figure 1.21. Hepatic ILC3 cell dynamics in adult and young mice during early HBV immunity.
Hepatic leukocyte fractions were enriched from HBVtg*Rag1-/-* adult (>8 wks) and young (3 – 3.5 wks) animals eight days after adoptive transfer with HBV-naïve splenocytes. Cells were stained for surface and intracellular markers and data were collected on an LSRII flow cytometer. The number and percentages of hepatic CD90+/hi CD127+ RORγt+ relative to live cells were measured at day 0 (**A**). ILC3s at subsequent time points day 3 (**B**) and day 8 (**C**) were defined as TCRβ- TCRγδ- CD90+/hi CD127+ RORγt+. (**D**) Total numbers and (**E**) percentages relative to live cells is graphed as a function of time; statistics are shown in panels A-C for these data. (**F**) ILC3 frequency shown as a percentage of total CD90+ CD127+ cells. Data were analyzed using FlowJo™ Software; statistics determined by Tukey's ANOVA with multiple comparisons using GraphPad Prism Software; * p<0.05, ** p<0.01, *** p<0.001, **** p<0.0001; n≥4 for HBV+ groups, n ≥2 for HBV- groups.

Intriguingly, the differences I observed in the number and frequency of hepatic ILC3s

correlates with the microarray dataset and suggests these cells may have important age-

dependent roles in the liver. In fact, several groups have uncovered an age-dependent accumulation of ILC3s within the gut, particularly the small intestine, as well as a phenotypic switch that correlates with a parallel increase in the commensal microbial burden that occurs in early life (*24, 32*). These studies illustrate that ILC3s are particularly well suited to respond to environmental signals that have the potential to govern global shifts in the type and strength of a given immune response.

A more in-depth characterization of this immune population revealed that there are not only differences in the abundance of ILC3s, but also changes in their phenotypic profiles. The major ILC3 subsets in mice and humans include the NCR+ and NCR- subsets. In mice, NCR+ ILC3s are defined by the expression of NKp46 alone, while in humans NCR+ ILC3s are defined by the expression of NKp44. In our mouse experiments, the most obvious difference in ILC3s was the greater number and frequency of NKp46- ILC3s in adult liver (**Fig. 1.22 A-B**). Although the majority of ILC3s were of the NKp46- subset in both young and adult livers, there was a stronger skewing towards NKp46- within the adults. This subset is believed to be more plastic than the NKp46+ subset, having the potential to differentiate into NKp46+ ILC3s, ILC1-like, or ILC2-like cells (*33*). By day three I observed a shift towards an increased frequency in the NKp46+ subset, which, in young mice, led to more NKp46+ versus NKp46- ILC3s, indicating that the early immune environment in the liver supports expansion of this NKp46+ subset (**Fig. 1.22 B**). By day eight we see a return to an increased percentage of NKp46- ILC3s compared to NKp46+ ILC3s with similar frequencies by age (**Fig. 1.22 C**).
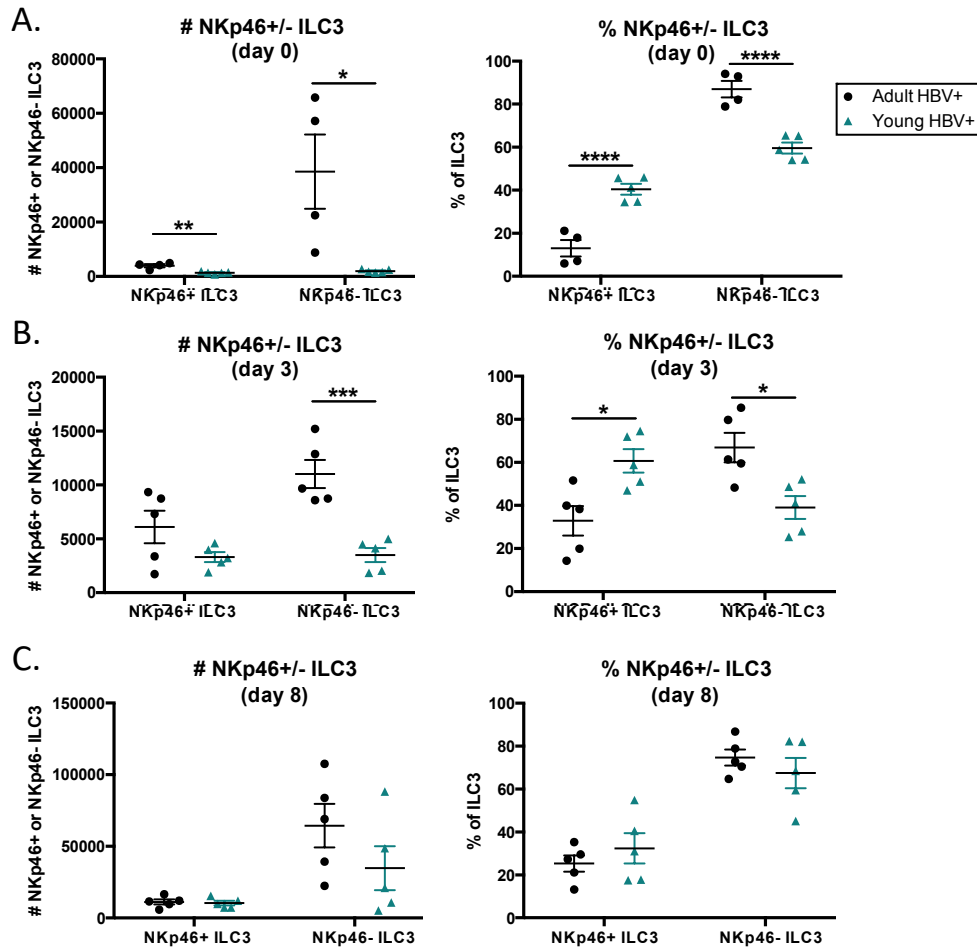
Figure 1.22. Dynamics of major ILC3 subsets in the liver during early HBV immunity in adult and young mice. Hepatic leukocyte fractions were enriched from HBVtg*Rag1*-/- adult (>8 wks) and young (3 – 3.5 wks) animals eight days after adoptive transfer with HBV-naïve splenocytes. Cells were stained for surface and intracellular markers and data were collected on an LSRII flow cytometer. The number and percentages of hepatic NKp46+ and NKp46- CD90+/hi CD127+ RORγt+ relative to total ILC3 were measured at day 0 (**A**). NKp46+ and NKp46- ILC3s at subsequent time points, day 3 (**B**) and day 8 (**C**) were defined as TCRβ- TCRγδ- CD90+/hi CD127+ RORγt+. Data were analyzed using FlowJoTM Software; statistics determined by unpaired two-tailed t-test using GraphPad Prism Software; * p<0.05, *** p<0.001, **** p<0.0001; n≥4.

The markers CCR6 and CD4 have been shown to mark the LTi-like subset of ILC3s. We found that the commercially available CCR6 antibodies were positively staining hepatic leukocytes in *Ccr6*-/- mice suggesting there was non-specific staining, at least within liver tissue. For this reason, I focused on using CD4 to identify this LTi-like subset. The CD4+ subset was a small fraction of the initial hepatic ILC3 population and was mostly found only within NKp46-

ILC3s; however, there was a small but trustworthy subset of CD4+ NKp46+ ILC3 that was slightly increased at baseline in adults but was small and equivalent by age at day three and eight (**Fig. 1.23**). It is unclear whether this population retains any LTi-like properties. Within the NKp46- subset, there was an overall greater number of adult CD4+ LTi-like ILC3; however, the percentage of NKp46- ILC3s which have an LTi-like phenotype was increased within the young animals (**Fig. 1.23 A-B**). These observations are consistent with LTi cells playing a critical role in early development of primary and secondary lymphoid organs and may explain why a greater proportion of young ILC3s have this phenotype. At the same time, the increase of total CD4+ NKp46- ILCs, is consistent with age-dependent increases of total ILC3s across various tissues, with a shift away from a lymphoid-organizing phenotype and poised to differentiate into other ILC effector functions depending on changes in the microenvironment.
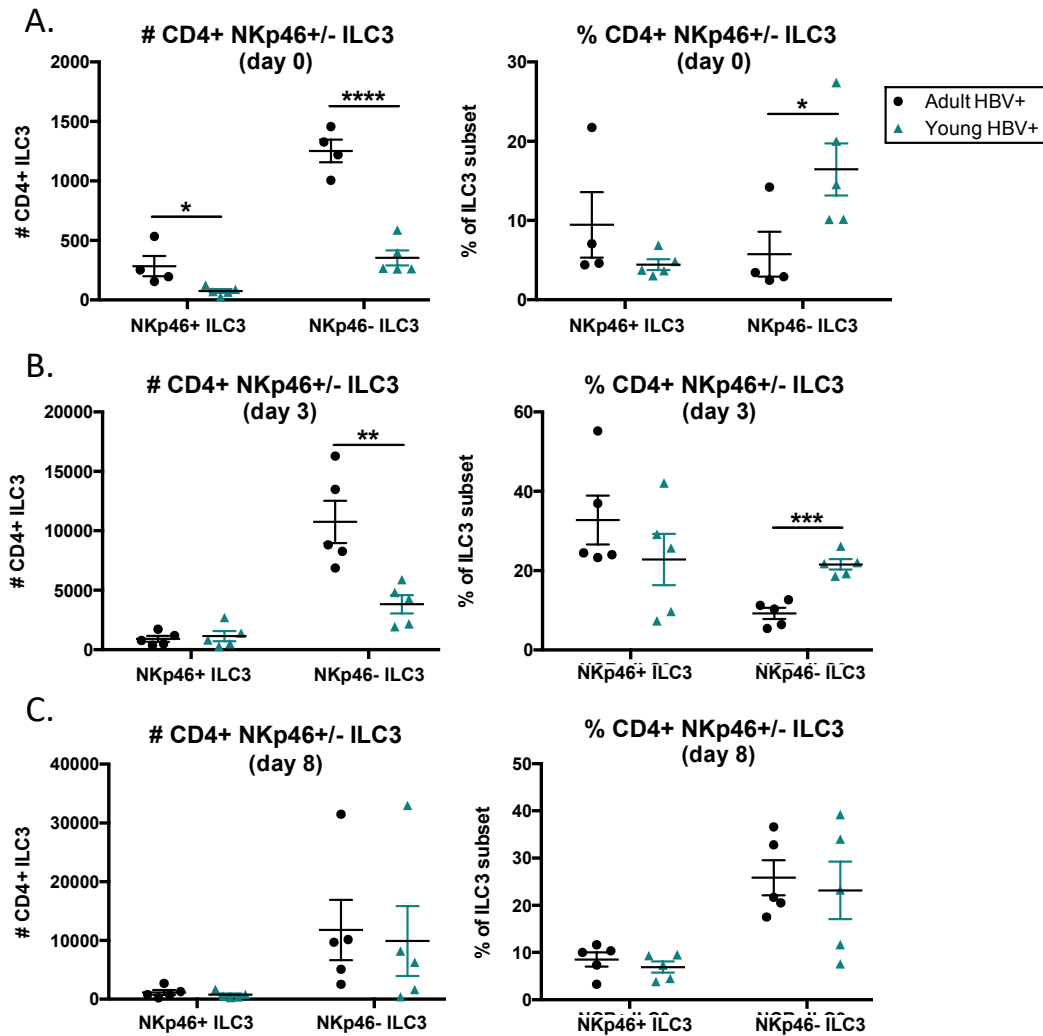
Figure 1.23. CD4 expression within hepatic NKp46+ and NKp46- ILC3 subsets during early HBV immunity in adult and young mice. Hepatic leukocyte fractions were enriched from HBVtg*Rag1*-/- adult (>8 wks) and young (3 – 3.5 wks) animals eight days after adoptive transfer with HBV-naïve splenocytes. Cells were stained for surface and intracellular markers and data were collected on an LSRII flow cytometer. The number and percentages of hepatic CD4+ NKp46+/- CD90+/hi CD127+ RORγt+ relative to total ILC3 were measured at day 0 (**A**). CD4+ NKp46+ and NKp46- ILC3s at subsequent time points, day 3 (**B**) and day 8 (**C**) were defined as TCRβ- TCRγδ- CD90+/hi CD127+ RORγt+-. Data were analyzed using FlowJo™ Software; statistics determined by unpaired two-tailed t-test using GraphPad Prism Software; * $p < 0.05$, ** $p < 0.01$, *** $p < 0.001$, **** $p < 0.0001$; n≥4.

Recent work by several groups has nicely shown that ILC3s in the gut and spleen express MHCII and are capable of presenting antigen to CD4+ T cells (*34-38*). The tissue environment is critical in directing the role of this antigen presentation towards T cell activation or tolerance. In the spleen, ILC3s express high levels of MHCII and have a higher percentage of costimulatory

molecule expression, particularly OX40L, CD80, and CD86, making them efficient antigen presenting cells, in some respects performing nearly as well as *bona fide* antigen-presenting dendritic cells (*37, 38*). In the small intestine, however, ILC3s express MHCII at a lower level and have greatly reduced co-stimulatory molecule expression resulting in severely blunted T cell priming and prevention of commensal microbe-driven inflammation (*35, 37*). Similar to the gut, the liver is exposed to a large antigenic burden, as 70 percent of its blood supply comes via the portal vein, which transport blood directly from the small intestine. Because of this, one might expect that the phenotype of hepatic ILC3s (livILC3) might be more similar to the small intestine ILC3s (siILC3) compared to splenic ILC3s (spILC3) – particularly in the young animals as they are experiencing colonization by commensal microbiota. In fact, I did find that a minority of hepatic ILC3s were MHCII+, approximately 10-20 percent; interestingly, I detected both NKp46+ and NKp46- subsets expressing MHCII+ (**Fig. 1.24**). In both the spleen and gut MHCII expression is mostly, but not exclusively, limited to the NKp46- subset. There was an age-dependent increase in the MHCII+ NKp46+ subset at all time points (**Fig. 1.24 A-C**). In the NKp46- subset, there was a trend towards young mice having a greater percentage of MHCII+ NKp46- ILC3s, consistent with a potential role for these cells in modulating T cell responses during this window of microbial colonization. At baseline, there was a greater total number of MHCII+ NKp46- ILC3s in adults despite the aforementioned trend, likely reflecting the total increased number of this subset in adults. These data suggest that hepatic ILC3s are more similar to the small intestine ILC3s with respect to MHCII expression, though they interestingly differ in having a more prominent MHCII+ NKp46+ subset. Future studies are required in order to assess the antigen presentation capacity of each MHCII+ subset. When examining expression of the co-stimulatory molecule OX40L by flow cytometry, there were very few OX40L+ ILC3 by flow

cytometry in the liver, suggesting that these cells are less likely to be efficient antigen presenting cells. However, it is important to note that TNF family members are subject to cleavage by metalloproteinases and others have reported challenges detecting OX40L after certain cell isolation protocols. For this reason, we plan to confirm OX40L expression patterns within hepatic ILCs by measuring *Tnfsf4* (OX40L) mRNA transcript levels.
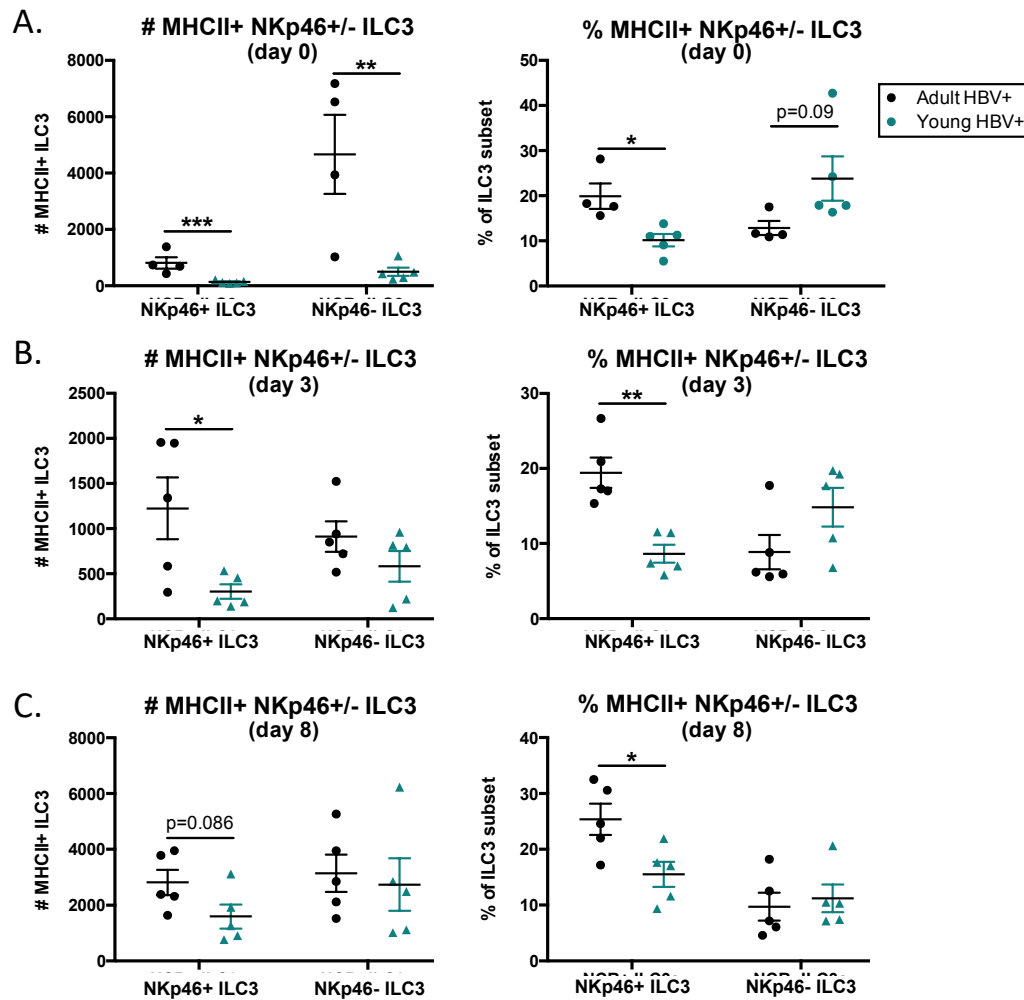
Figure 1.24. MHC class II expression within hepatic NKp46+ and NKp46- ILC3 subsets during early HBV immunity in adult and young mice. Hepatic leukocyte fractions were enriched from HBVtg*Rag1*-/- adult (>8 wks) and young (3 – 3.5 wks) animals eight days after adoptive transfer with HBV-naïve splenocytes. Cells were stained for surface and intracellular markers and data were collected on an LSRII flow cytometer. The number and percentages of hepatic MHCII+ NKp46+/- CD90+/hi CD127+ RORγt+ relative to total ILC3 were measured at day 0 (**A**). MHCII+ NKp46+ and NKp46- ILC3s at subsequent time points, day 3 (**B**) and day 8 (**C**) were defined as TCRβ- TCRγδ- CD90+/hi

CD127+ RORγt+. Data were analyzed using FlowJo™ Software; statistics determined by unpaired two-tailed t-test using GraphPad Prism Software; * p<0.05, ** p<0.01; n≥4.

I also examined expression of CD69 on ILC3 subsets. CD69 plays an important role in tissue residency and can also be a marker of recently activated cells. At baseline, CD69 is probably most relevant as a marker of tissue retention. We observed that 75 percent of both adult and young NKp46+ ILC3s are CD69+, suggesting most of these cells lack the ability to exit the liver and circulate (**Fig. 1.25 A**). Within the NKp46- subset, which is believed to be more plastic in its differentiation status, I observed that the young mice had a 20-25 percent decrease in the percentage of CD69+ cells, suggesting that these cells were more capable of leaving the liver and potentially still functioning to seed other tissues with ILCs. By day three and eight I see noted that CD69 expression within the NKp46- subset increased in young animals while slightly decreasing in adults (**Fig. 1.25 B-C**). This may either reflect a more rapid expansion of adult ILC3s that have yet to upregulate CD69, or instead suggest that young ILC3s are more sensitive to activation. At day eight I observed that there was an overall decrease in the percentage of CD69+ ILC3s, perhaps reflecting an influx of splenic CD69- ILC3s from the adoptive transfer, particularly of the NKp46- subset, which is known to be more abundant in the spleen compared to NKp46+ ILC3 (**Fig. 1.25 C**).
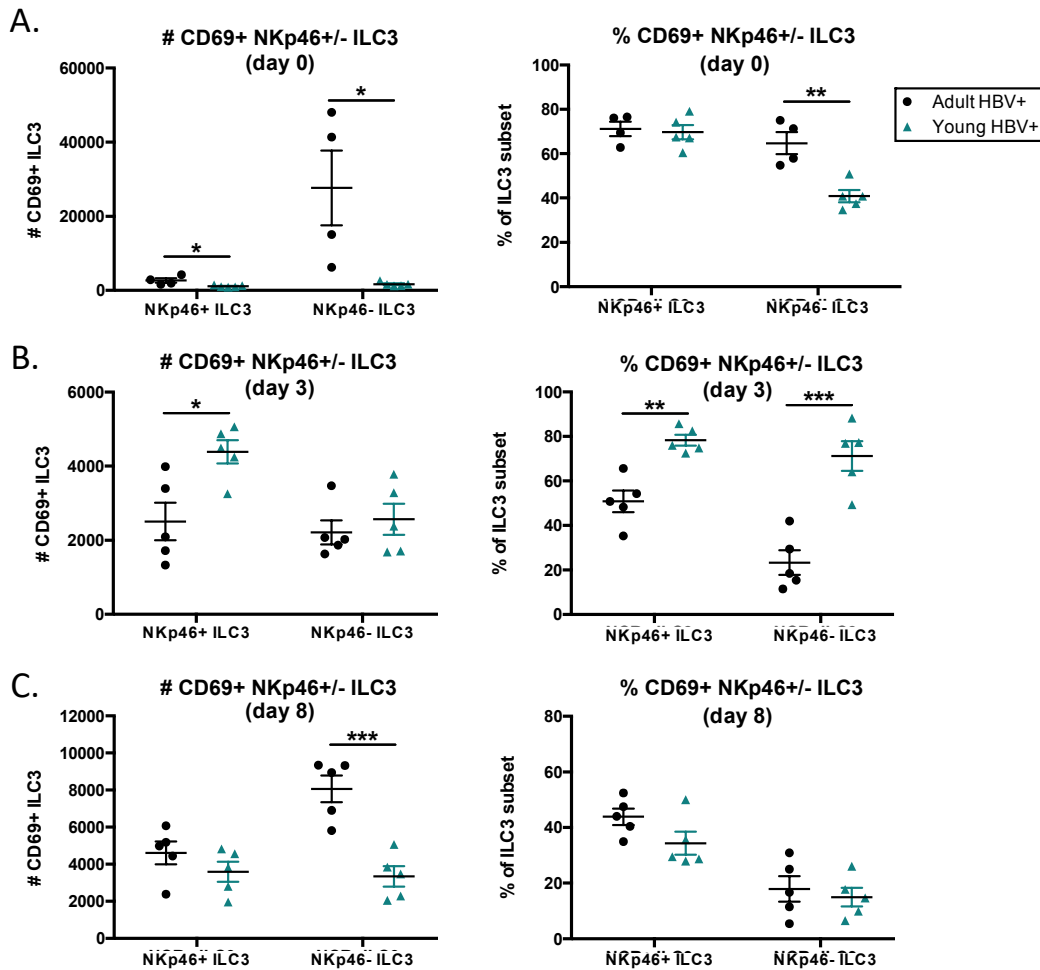
Figure 1.25. CD69 expression within hepatic NKp46+ and NKp46- ILC3 subsets during early HBV immunity in adult and young mice. Hepatic leukocyte fractions were enriched from HBVtg*Rag1*-/- adult (>8 wks) and young (3 – 3.5 wks) animals eight days after adoptive transfer with HBV-naïve splenocytes. Cells were stained for surface and intracellular markers and data were collected on an LSRII flow cytometer. The number and percentages of hepatic CD69+ NKp46+/- CD90+/hi CD127+ RORγt+ relative to total ILC3 were measured at day 0 (**A**). CD69+ NKp46+ and NKp46- ILC3s at subsequent time points, day 3 (**B**) and day 8 (**C**) were defined as TCRβ- TCRγδ- CD90+/hi CD127+ RORγt+ NKp4. Data were analyzed using FlowJo™ Software; statistics determined by unpaired two-tailed t-test using GraphPad Prism Software; * $p < 0.05$, ** $p < 0.01$, *** $p < 0.001$; n≥4.

To determine if cytokine production by ILC3s was different by age, I measured *ex vivo*

cytokine production without additional stimulation in an effort to minimize cell manipulation.

When examining IL-22, there was a larger percentage of IL-22+ ILC3s within the NKp46- subset

compared to the NKp46+ subset (**Fig. 1.26**). This population was increased in adults at baseline

but was equivalent by age at the later time points, arguing against a major role for this cytokine

in age-dependent ILC3 responses, perhaps suggesting a homeostatic role of ILC3s in the liver.
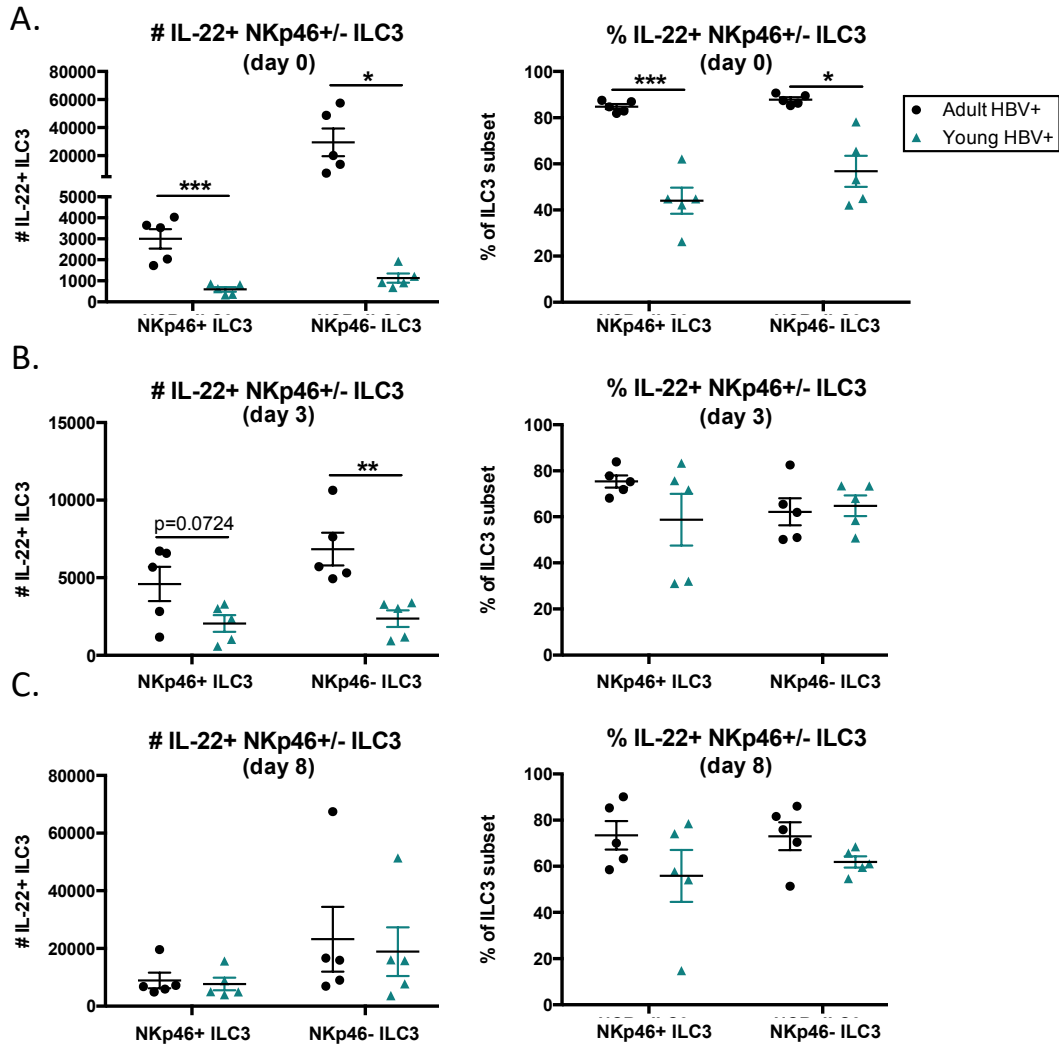
Figure 1.26. IL-22 expression within hepatic NKp46+ and NKp46- ILC3 subsets during early HBV immunity in adult and young mice. Hepatic leukocyte fractions were enriched from HBVtg*Rag1*-/- adult (>8 wks) and young (3 – 3.5 wks) animals eight days after adoptive transfer with HBV-naïve splenocytes. Cells were cultured *ex vivo* for 4 hrs in the presence of brefeldin A, without stimulation, and subsequently stained for surface and intracellular markers and data were collected on an LSRII flow cytometer. The number and percentages of hepatic IL-22+ NKp46+/- CD90+/hi CD127+ RORγt+ relative to total ILC3 were measured at day 0 (**A**). IL-22+ NKp46+ and NKp46- ILC3s at subsequent time points, day 3 (**B**) and day 8 (**C**) were defined as TCRβ- TCRγδ- CD90+/hi CD127+ RORγt+-. Data were analyzed using FlowJoᴛᴍ Software; statistics determined by unpaired two-tailed t-test using GraphPad Prism Software; * p<0.05, ** p<0.01, *** p<0.001; n≥4.

When examining GM-CSF production within ILC3s, I found no major differences in the percentage of GM-CSF+ ILC3s. Only a small percentage of ILC3s expressed GM-CSF, which was lowest at day three (**Fig. 1.27**). While at baseline there was significant GM-CSF production by both NKp46+ and NKp46- ILC3 subsets, later on this became more associated with the NKp46+ subset.
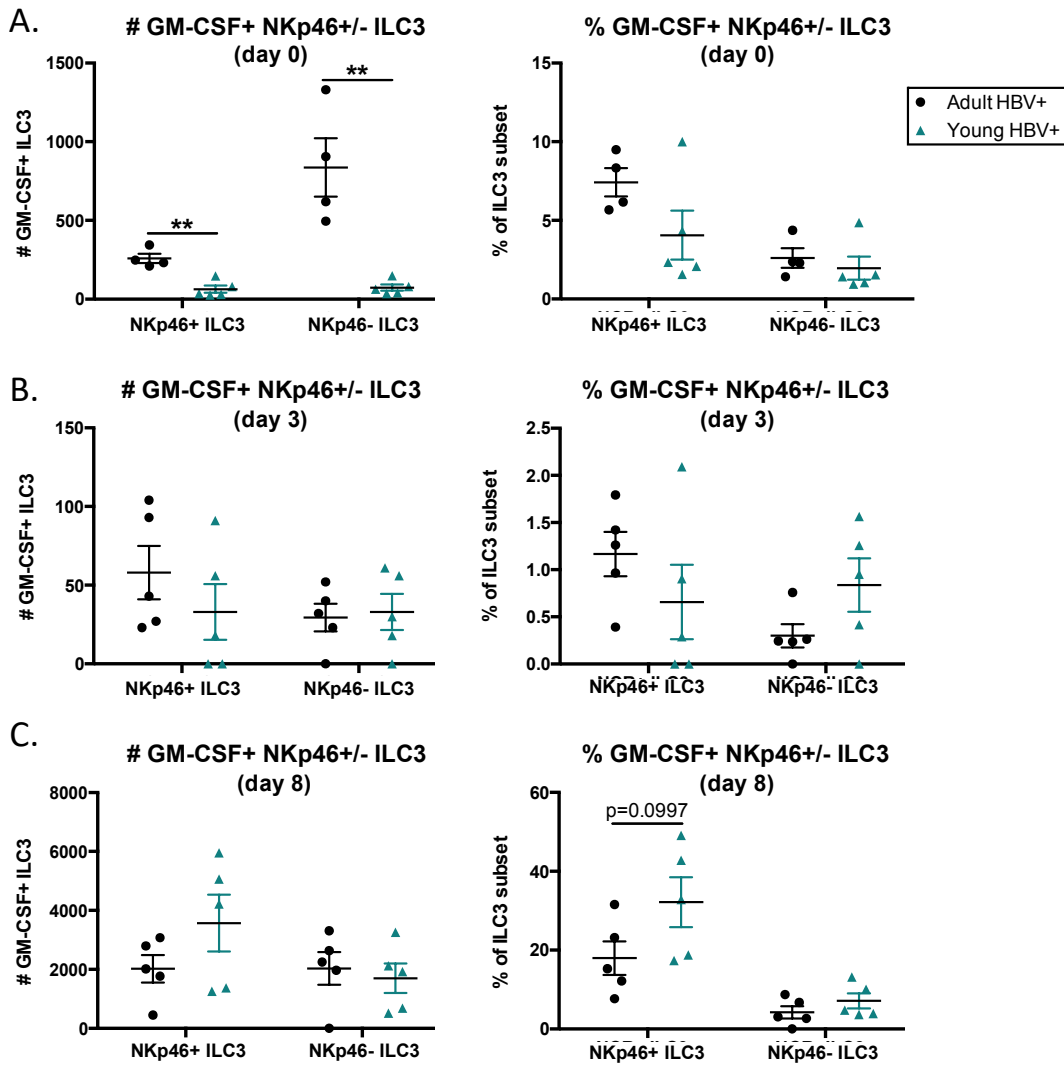
Figure 1.27. GM-CSF expression within hepatic NKp46+ and NKp46- ILC3 subsets during early HBV immunity in adult and young mice. Hepatic leukocyte fractions were enriched from HBVtg*Rag1-/-* adult (>8 wks) and young (3 – 3.5 wks) animals eight days after adoptive transfer with HBV-naïve splenocytes. Cells were cultured *ex vivo* for 4 hrs in the presence of brefeldin A, without stimulation, and subsequently stained for surface and intracellular markers and data were collected on an LSRII flow

cytometer. The number and percentages of hepatic GM-CSF+ NKp46+/- CD90$_{+/hi}$ CD127+ RORγt+ relative to total ILC3 were measured at day 0 (**A**). GM-CSF+ NKp46+ and NKp46- ILC3s at subsequent time points, day 3 (**B**) and day 8 (**C**) were defined as TCRβ- TCRγδ- CD90$_{+/hi}$ CD127+ RORγt+. Data were analyzed using FlowJo$_{TM}$ Software; statistics determined by unpaired two-tailed t-test using GraphPad Prism Software; * p<0.05, ** p<0.01, *** p<0.001; n≥4.

Finally, I measured IL-17a cytokine production using a cytokine secretion assay that allows for detection of actively secreted IL-17a by incubating the cells for a short period in the presence of an anti-IL-17a "capture" antibody that functions to tether the secreted cytokine to the cell surface for subsequent detection. I did not measure IL-17a secretion at baseline and had a limited sample size at day 3 preventing me from drawing any conclusions about age-dependent IL-17a production by hepatic ILC3s at these early time points (**Fig. 1.28 A**). Despite this, I observed that IL-17a is mostly produced by the NKp46- subset, consistent with ILC3s in other tissues; however, there was still some IL-17a production by NKp46+ ILC3. At day eight, I did not find any age-dependent differences but there was a trend towards increased numbers and percentages of IL-17a+ ILC3s in adult animals (**Fig. 1.18 B**). Future studies are required to more carefully assess this population.
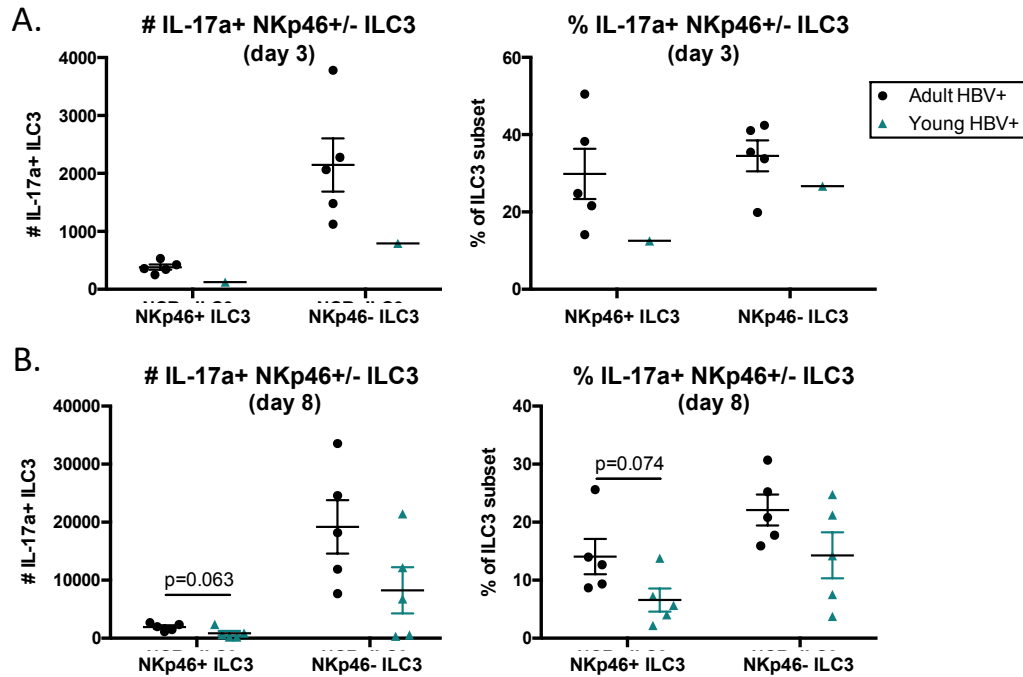
Figure 1.28. IL-17a expression within hepatic NKp46+ and NKp46- ILC3 subsets during early HBV immunity in adult and young mice. Hepatic leukocyte fractions were enriched from HBVtg*Rag1*-/- adult (>8 wks) and young (3 – 3.5 wks) animals eight days after adoptive transfer with HBV-naïve splenocytes. Cells were cultured *ex vivo* for 45 minutes with anti-IL-17a capture antibodies (Miltenyi IL-17a secretion assay), without stimulation, and subsequently stained for surface and intracellular markers and data were collected on an LSRII flow cytometer. The number and percentages of hepatic IL-22+ NKp46+/- CD90+/hi CD127+ RORγt+ relative to total ILC3 were measured at day 0 (**A**). IL-17a+ NKp46+ and NKp46- ILC3s at subsequent time points, day 3 (**B**) and day 8 (**C**) were defined as TCRβ- TCRγδ- CD90+/hi CD127+ RORγt+. Data were analyzed using FlowJo™ Software; statistics determined by unpaired two-tailed t-test using GraphPad Prism Software; n=5 for all groups, except n=1 for day 3 young HBV+.

Discussion

The age-dependent outcome of HBV infection has long been of interest in understanding what immunologic features lead to effective control of the infection. Despite the enormous global burden of HBV, the only therapies currently available for treating chronic HBV – nucleot(s)ide analogs that inhibit viral replication – do not lead to viral clearance. As a result, patients often take these anti-viral drugs indefinitely in order to minimize clinical and subclinical inflammation that contributes to the development of cirrhosis and hepatocellular carcinoma.

Thus, the identification of immune mechanisms that are deficient or impaired during the immune response of young individuals, who go on to develop a persistent infection and chronic disease, provides the opportunity for therapeutic intervention to reverse these effects.

The goal of my work discussed in this chapter was to further characterize these age-dependent differences in an effort to uncover critical pathways that might be targetable and lead to improved immune outcomes. Indeed, the first part of this chapter describes a body of work that led to the identification of a critical OX40/OX40L interaction in supporting effective HBV immunity (*15*). A recent study highlighted the relevance of these findings in humans, showing that augmentation of OX40 signaling and blockade of PD-1 can lead to increased effector responses by antigen-specific cells, similar to our studies in mice (*39*).

My characterization of T cell populations also revealed a general defect in the priming of CD4+ effector T cells in young mice, suggesting that other regulators of CD4+ T cell priming, including efficient MHCII antigen presentation by cDC2 and other cells such as ILC3s – discussed in more detail below – may represent additional targetable pathways to improve immune outcomes in young animals. One future goal inspired by this project is a careful evaluation of the immune priming capabilities of the various antigen-presenting cells present in the liver of adult and young animals. These experiments would most simply be carried out by *in vitro* culturing of flow cytometry-sorted hepatic APC populations with OT-I and OT-II T cells in the presence of OVA antigens followed by measuring T cell proliferation and production of effector cytokines. The increased expression of MHCII on cDC2 and monocyte-derived macrophages of adult animals suggests these cells may represent a potent source of antigen presentation compared to their young counterparts expressing low amounts of MHCII.

The difference in mature and immature hepatic NK cell populations by age was also notable and has been previously described to be a unique feature of this organ (*27*). Whether and how these cells support and interface with other innate and adaptive immune cells in particularly relevant due to their high frequency in the liver and reported contributions of these cells in HBV immunity. Finally, the observation of age-dependent differences in the number and phenotype of hepatic ILC3s, including their expression of antigen presenting molecules, is interesting and unique compared to other hepatic ILC populations. We know that age-dependent deficits in the hepatic innate immune environment of young mice are sufficient to result in impaired immunity, even with the transfer of adult splenocytes. These data strongly suggest that innate immune populations play a critical role in the early events that dictate immune outcomes to HBV. Thus, the identification of differences in a tissue-resident immune cell with previously described functions involved in age-dependent immunity in the gut seem highly relevant and worthy of further investigation. Studies directed at addressing the role of these cells are discussed in more detail in the subsequent chapters of this thesis.

Chapter 2. Age-dependent differences in hepatic lymphoid organization influence hepatitis B immunity

Introduction

Recent studies over the past decade have revealed that in addition to secondary lymphoid organs, immune priming against hepatitis B viral antigens first occurs within the liver (*14, 40*). When visualizing the immune populations within the liver during early immunity, it is possible to observe various different immune cells clustering together around hepatic portal vasculature as well as within the liver parenchyma. Work from our laboratory in a mouse model of HBV infection has shown that hepatic macrophages reorganize within the tissue within the first few days during HBV immunity and anchor these leukocyte clusters, allowing for further immune cell recruitment (*14*). Disruption of the macrophage-based clusters with clodronate liposome treatment – known to target and kill phagocytic cells including Kupffer cells – completely ablates immune clustering in the liver, indicating that clustering of other cell types including T and B cells is dependent on macrophages. By day eight after adoptive transfer, these macrophage-based clusters were found to include a diversity of innate and adaptive immune cells including CD11c+ dendritic cells, CD4+ and CD8+ T cells, and B220+ B cells.

Interestingly, robust formation of these hepatic leukocyte clusters is age-dependent. Adult animals that go on to clear HBV antigens form numerous small- and moderately-sized immune aggregates with diverse cell composition within each cluster. In comparison, young animals that fail to control HBV form fewer hepatic immune clusters, and the clusters that do form are smaller and less diverse. These observations suggest that aggregation of immune cells may be an important step in facilitating the priming of an effective immune response, as priming is

impaired in animals that lack these clusters. In further support of this hypothesis, cluster

disruption by clodronate liposome treatment resulted in blunted liver inflammation and impeded

viral clearance, dramatically reducing antigen-specific IFNγ T cell responses and impairing *Il21*

transcript expression – both of which have previously been shown to play a crucial role in viral

control (*9, 14*).

Efforts to identify molecular regulators of cluster formation were initially focused on the

chemokine CXCL13 and its receptor, CXCR5, which is present on both T follicular helper cells

and B cells. Both the chemokine and the receptor were found to be expressed in an age-

dependent fashion; there was an increase in expression of both molecules within the hepatic

immune populations of adult compared to young mice (*14*). Indeed, this study showed that

CXCL13 and CXCR5 do play an essential role in viral clearance, as neither *Cxcl13-/-* nor *Cxcr5-/-*

mice were capable of clearing viral antigens. Surprisingly, the number of macrophage clusters

was not impaired in these knockout mice, suggesting that the role of CXCL13 and CXCR5 is

downstream of cluster formation, likely with a specific role in Tfh and B cell responses.

These early experiments in our lab led us to wonder what other cells and molecules may

be regulating cluster formation. In order to address this question, we first focused on developing

a robust and high-throughput way to characterize the hepatic immune clusters. Efforts in our lab

initially relied on fluorescent microscopy for the staining and visualization of the immune

clusters. Unfortunately, several limitations of this approach including the high autofluorescence

within the liver due to the metabolite-rich environment of this organ, together with tissue

integrity and technical variations from experiment-to-experiment led us to reconsider the utility

of this approach for large-scale projects. For these reasons, we turned to a chromogenic-based

immunohistochemistry (IHC) approach in close collaboration with the UCSF Biotechnology and

Biomarker Tissue Core (BTBTC). The benefits of this approach include a lack of

autofluorescence, because we are not detecting fluorescent probes, extremely stable tissue

storage and integrity after formalin-fixation and paraffin embedding of liver tissue using an

optimized collection approach (*41*), and the ability to use automated slide staining on the

Ventana Discovery Ultra platform followed by automated whole-slide imaging using the Zeiss

Axioscanner Z1.

Results

     Despite initial optimism about overcoming autofluorescence limitations of the liver, we

experienced similar obstacles when first developing our IHC staining approach. Early rounds of

tissue staining repeatedly showed that while sensitivity, specificity, and chromogen dye color

profiles were robust in spleen and thymus, staining liver tissue presented unique challenges (**Fig.**

2.1). Working closely with Jennifer Bolen of the BTBTC, overseen by Dr. Scott VandenBerg,

we went through iterative rounds of tissue staining varying the times, temperatures, and reagents

used for antigen retrieval, blocking, conditioning, and cell stripping between staining with each

antibody. We found that the yellow dyes were most likely to cause blushing of the tissue,

resulting in background staining and similar signal:noise complications caused by

autofluorescence. We also found that some antibodies led to more problematic background

blushing than others, highlighting the importance of testing multiple antibody-dye combinations

with various staining conditions in order to identify the most robust protocol for each single,

duplex, and triplex combination of markers of interest, especially within liver tissue. Ultimately,

we were able to optimize protocols for three triplex stains, using hematoxylin counterstaining to

identify individual cell nuclei.
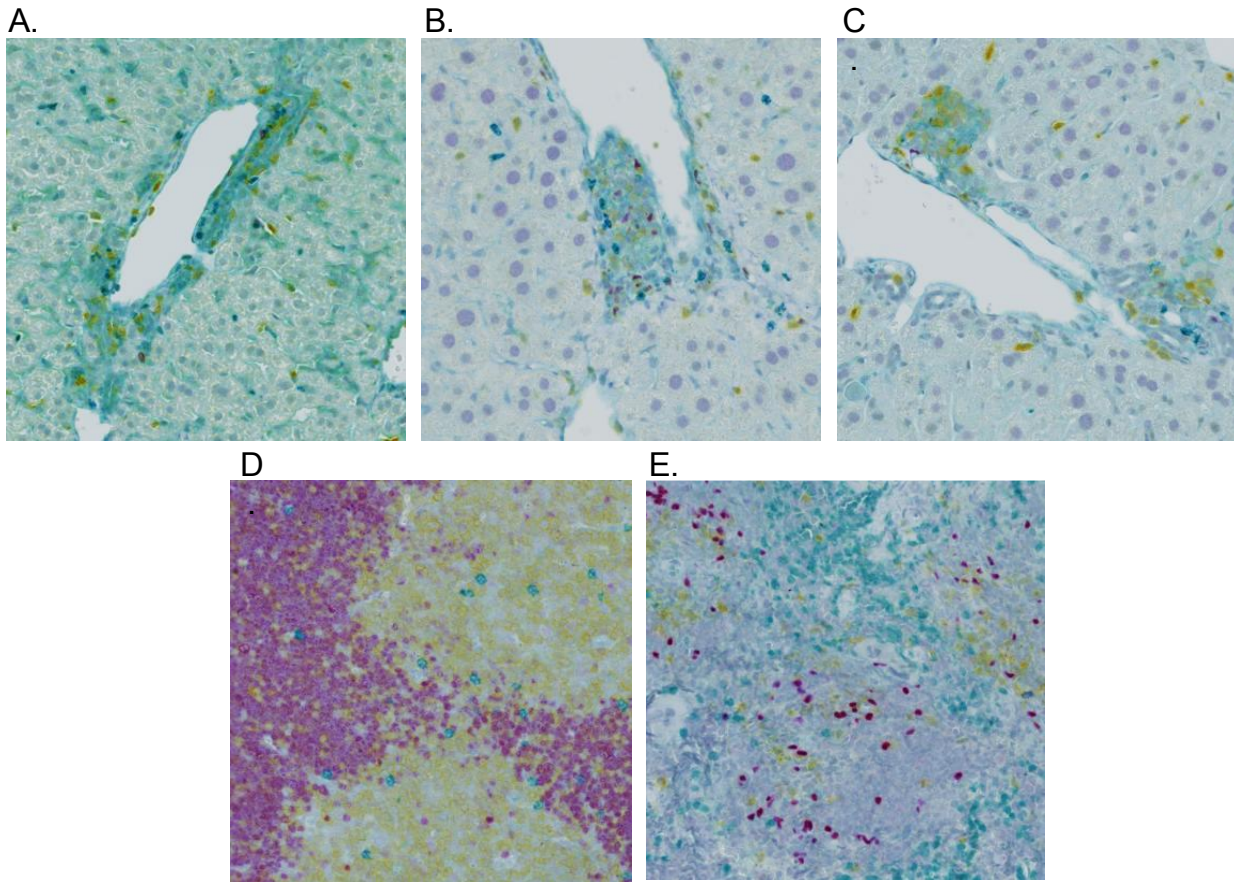
Figure 2.1. Liver tissue presents unique challenges when developing multiplexed chromogenic-based immunohistochemistry staining protocols. (**A-C**) Liver, (**D**) thymus, and (**E**) spleen were isolated from mice and drop-fixed in formalin for 24 hours, followed by ethanol dehydration and embedding into paraffin wax blocks. Formalin-fixed paraffin-embedded (FFPE) tissue blocks were sectioned at 4 µm and stained with anti-RORγ (purple), anti-CD11b (teal), and anti-CD3 (yellow), under variable conditions using the Ventana Discovery Ultra platform. Stained sections were imaged at 20X resolution with the Zeiss Axioscanner Z1. Scale bars represent 50 µm.

As we were optimizing conditions for the triplex stains, we had early success with a duplex stain using anti-CD8α with a purple chromogenic dye and anti-CD4 with a yellow dye. While these markers are most useful in identifying T cells, it's worth noting that other cell types including dendritic cells can also express lower levels of these surface proteins. Assessment of the scanned images from adult and young tissue sections stained with anti-CD4, anti-CD8α, and hematoxylin showed that there were distinct patterns of CD4+ and CD8+ cell localization. Adult animals had prominent periportal and parenchymal inflammation with clusters of CD4+ and

CD8+ cells mixed together (**Fig. 2.2 A-B**). Alternatively, young animals had some smaller cell

clusters that were predominantly comprised of CD8+ cells. Based on flow cytometry at this same

time point, we know that the vast majority of CD8+ cells in the liver are T cells; however, it is

possible that some of these CD8+ cells include DCs. These clusters in young mice were most

often associated with portal tracts with few parenchymal cell clusters present (**Fig. 2.2 C-D**).

Young animals in general also had fewer CD4+ cells but had many individual single CD8+ cells

spread throughout the liver parenchyma (**Fig. 2.2 C-D**).
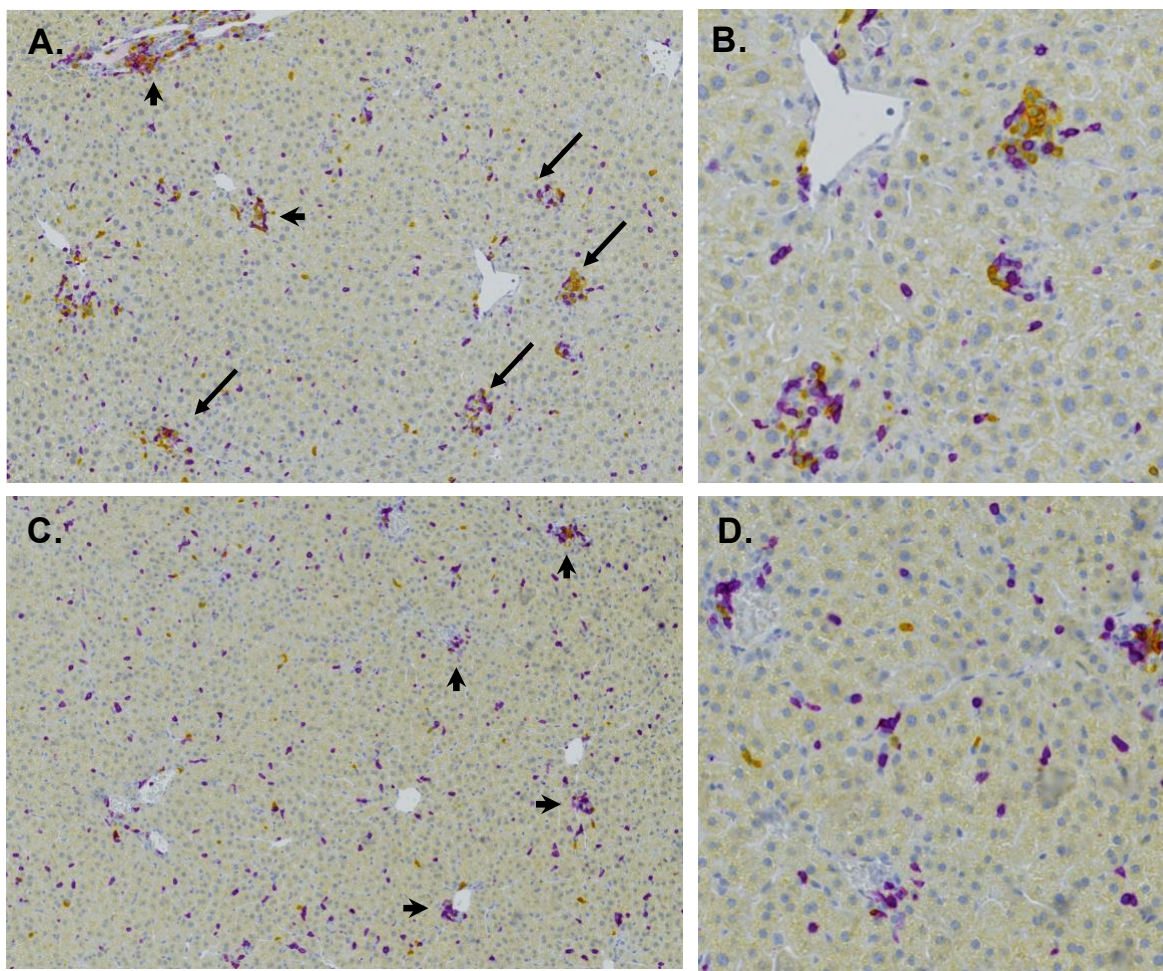
Figure 2.2. CD4 and CD8 staining patterns in adult and young liver during acute HBV immunity.
Liver tissue was isolated from adult (**A-B**) and young (**C-D**) HBVtg*Rag1-/-* mice eight days post-adoptive
transfer and drop-fixed in formalin for 24 hours, followed by ethanol dehydration and embedding into
paraffin wax blocks. FFPE tissue blocks were sectioned at 4 μm and stained with anti-CD4 (yellow), anti-
CD8 (purple) using the Ventana Discovery Ultra platform. Stained sections were imaged at 20X
resolution with the Zeiss Axioscanner Z1. Scale bars for (**A, C**) represent 100 μm., scale bars for (**B, D**)
represent 50 μm. Long arrows point to intraparenchymal clusters, short arrows point to periportal clusters.

We added an additional marker, RORγ, for a triplex stain with CD4, CD8α, and RORγ, together with hematoxylin. The first two colors used, yellow and purple, are both very bright and have distinct color profiles, blending into a brick red color when there is overlap. The options for a third color at the time when we designed these staining panels were red and teal, a light blueish color. Because yellow and purple overlap to form a red color, we did not choose this option to simplify interpretation of the data. This left us with teal for the third dye. Unfortunately, this color is not bright enough for proteins expressed in low amounts in the liver. It does, however, work well on all markers tested in spleen and thymus, again highlighting unique challenges within the liver. Another limitation with teal is the similar color profile it shares with hematoxylin, which is a darker blue color. Although these two dye colors can be differentiated, we found it was best practice to use teal with membrane-restricted markers rather than nuclear-localized markers that would spatially overlap with hematoxylin. Thus, for the RORγ, CD8α, CD4 triplex stain we opted to move RORγ to purple, which provides the brightest and strongest signal, CD8α to teal, as CD8α seemed to be the most highly expressed marker of the three and is very clearly membrane-localized, leaving CD4 on yellow, also with strong membrane localization. We initially sought to find a RORγt-specific antibody; however, all of the antibodies we tested detected both RORγ isoforms – RORγ itself and RORγt. While RORγt expression is restricted to the hematopoietic compartment, RORγ is expressed uniformly by hepatocytes, the main parenchymal cell of the liver. Fortunately for our purposes, this antibody has a much higher affinity for the RORγt isoform, which leads to brighter staining within hematopoietic cells relative to hepatocytes. Furthermore, nuclei of hepatocytes are much larger than lymphocyte and ILC nuclei, and as such are easy to differentiate accordingly.

Once we had the RORγ, CD8α, CD4 triplex stain optimized on liver tissue sections, we stained a cohort of sections from adult and young HBVtg*Rag1-/-* animals eight days post-adoptive transfer during the peak acute immune response (**Fig. 2.3**). Our goal with this stain was to identify five major populations of immune cells: CD4+ T cells (CD4+ CD8α- RORγ-), CD8+ T cells (CD4- CD8α- RORγ-), T helper 17 cells (Th17; CD4+ CD8α- RORγ+), type 17 CD8+ T cells (Tc17; CD4- CD8α+ RORγ+), and ILC3 (CD4-/low CD8α- RORγ+) (**Fig. 2.3 G-N**). Due to limitations in the number of markers we can include in one stain, there are some noteworthy caveats to point out when identifying cell types by these parameters. As mentioned above, CD4 and CD8α can be expressed on some innate immune populations, particularly some subsets of dendritic cells, so it is likely that a portion of the cells determined to be CD4+ T cells and CD8+ T cells are actually dendritic cells; however, we know by flow cytometric analysis that this is a very small portion of total CD4+ and CD8+ events and the vast majority are indeed TCRβ+ T cells. Another important caveat is the use of CD4 to differentiate between Th17 and ILC3s. While all Th17 cells are CD4+, the LTi-like subset of ILC3s also expresses CD4+. We know from earlier flow cytometry experiments that CD4 is expressed by a minority of total ILC3 and that most CD4+ RORγ+ cells are TCRβ+ Th17 cells. For this reason, we decided to classify CD4+ RORγ+ cells as Th17 in instances where CD4 staining is definitive; however, in instances where CD4 staining is exceptionally dim or not clearly encompassing the circumference of the identified RORγ+ cell we defaulted to classifying these cells as ILC3s. Interestingly, most of the ILC3s we found were associated with immune cell clusters and often positioned near portal tracts; however, isolated ILC3s within the liver parenchyma could be identified, particularly in young mice (**Fig. 2.3 F**). There were numerous examples of RORγ+ ILC3s directly contacting

CD8+ cells, raising the possibility that ILC3s may exert a direct effect on CD8+ cell activities

(**Fig. 2.3 K-M**).
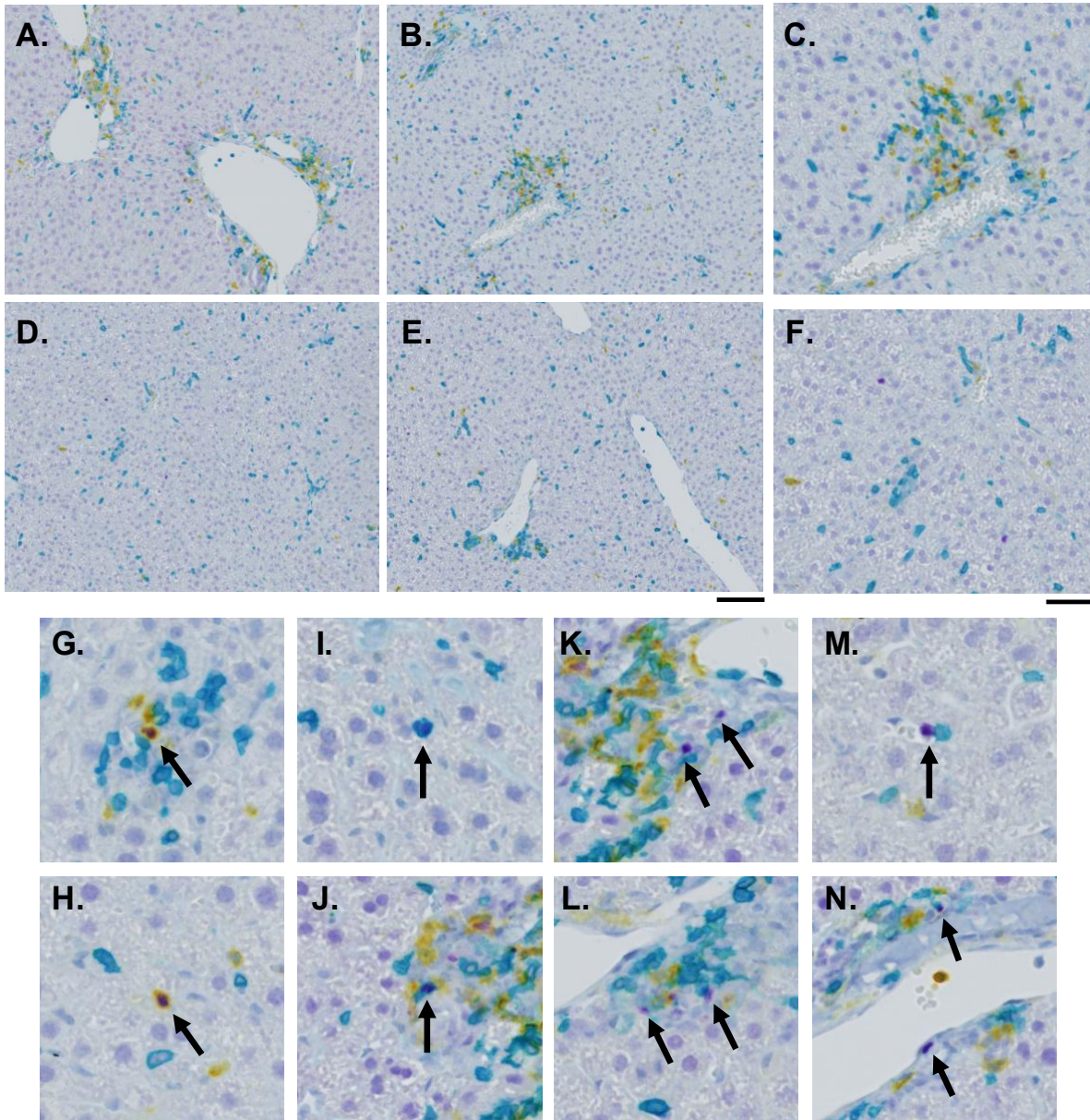
Figure 2.3. RORγ, CD4, and CD8 staining patterns in adult and young liver during acute HBV immunity. Liver tissue was isolated from adult (**A-C**) and young (**D-F**) HBVtg*Rag1*-/- mice eight days post-adoptive transfer and drop-fixed in formalin for 24 hours, followed by ethanol dehydration and embedding into paraffin wax blocks. FFPE tissue blocks were sectioned at 4 μm and stained with anti-RORγ (purple), anti-CD8 (teal), and anti-CD4 (yellow) using the Ventana Discovery Ultra platform. Stained sections were imaged at 20X resolution with the Zeiss Axioscanner Z1. (**G-H**) Arrows point to CD4+ RORγ+ Th17, (**I-J**) CD8+ RORγ+ Tc17 and (**K-N**) RORγ+ CD4- CD8- ILC3. Scale bars represent 100 μm for (**A-B, D-E**), 50 μm for (**C, F**), and 25 μm for (**G-N**).

We had previously relied on a pathologist blinded to sample identity to review tissue staining images and to count and score various parameters by eye. However, there are limitations to this approach; the major factor being sample size and the ability to now review whole slide scanned images that cover several millimeters of tissue area as opposed to five to ten 10X or 20X view frames from traditional wide-field microscopes. Thus, in order to expand our bandwidth to accommodate these >100x larger data sets, I partnered with Austin Edwards, a bioinformatics programmer in UCSF's Biological Imaging Development Center (BIDC). Through this collaboration we aimed to measure both quantitative and qualitative parameters from our stained tissue sections using automated machine learning. In short, this analysis pipeline using Ilastik software [interactive machine learning for (bio)image analysis; (*42*)] involves first segmenting the image into two main object groups: cells and stroma, using nuclear hematoxylin staining to identify individual cells, followed by classification of the individual cell objects based on the staining patterns with the antibodies and chromogenic dyes (**Fig. 2.4 A-B**). Beyond these basic steps we have added additional filters that allow us to identify vasculature structures and immune cell clusters, with adjustable parameters that allow us to fine-tune the analysis as appropriate based on the samples and specific stains used (**Fig. 2.4 C**).
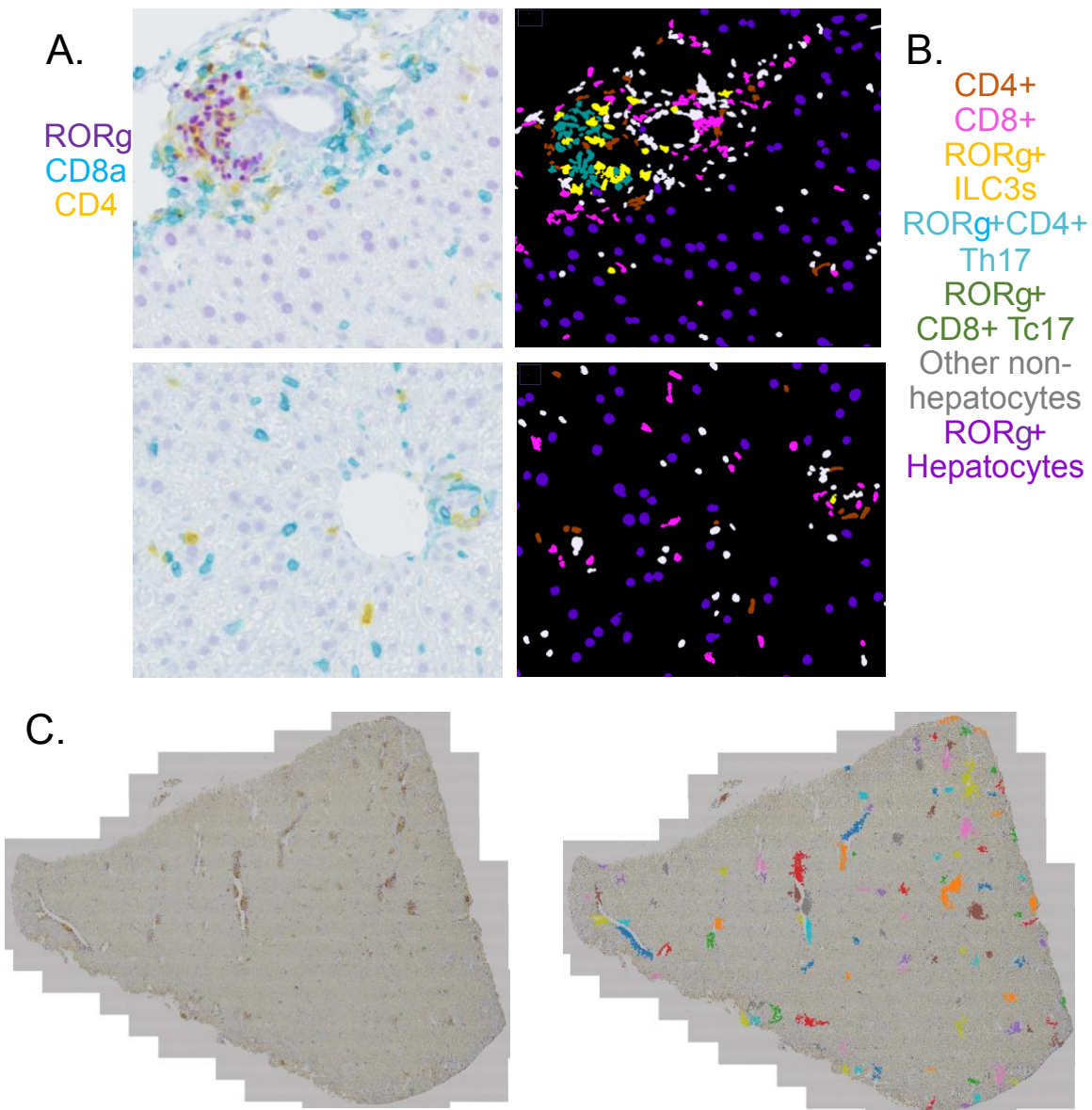
Figure 2.4. Immunohistochemistry image analysis workflow. Images files are converted from the native czi format into TIFF and ultimately HDF5 for compatibility with ilastik software. Images were first segmented to identify and separate cellular nuclei, defined by the presence of hematoxylin staining, from the stromal regions of the tissue which allows individual cells to be separated into single "objects." Objects were then classified into one of several groups: CD4+, CD8+, RORγ+ ILC3, RORγ+ CD4+ Th17, RORγ+ CD8+ Tc17, RORγ+ Hepatocytes, or "other" based on the staining with the four dyes present: purple (RORγ+), teal (CD8+), yellow (CD4+), and hematoxylin. (**A**) Original images prior to processing are transformed into (**B**) prediction files with segmented and classified cellular objects based on staining patterns in (**A**) such that each colored object represents a different cells class: CD4+ T cells (orange), CD8+ T cells (pink), ILC3 (yellow), Th17 (teal) green (Tc17), white ("other" non-hepatocytes), and purple (hepatocytes). (**C**) A clustering filter is applied to the left image by setting parameters such that a minimum number of 5 cells must be less than or equal to a maximum pixel distance between each cell; groups of cells that meet both criteria are grouped together and identified as "clusters" (right). Colors in the right panel are arbitrary and are shown to illustrate the number and variety of cluster sizes and distribution.

After developing this analysis pipeline, we analyzed a small preliminary dataset to identify age-dependent patterns of CD4+ and CD8α+ T cell localization relative to ILC3s. From this analysis we were able to reveal an increased proportion of CD4+ T cells relative to CD8+ T cells in adult liver sections compared to young mice (**Fig. 2.5 A**). We also detected a small but significant increase in the percentage of identified cells that were participating in an immune cluster, defined as five or more cells in close proximity, such that approximately 40% of identified cells (which includes any cell that was CD4+, CD8α+ and/or RORγ+) were cluster-associated in adults compared to only 25 percent of identified cells being cluster-associated in young animals (**Fig. 2.5 B**). Despite the difference in the frequency of cells that are cluster associated, I did not find a significant difference in the number of cells that were found in each identified cluster, with adult clusters averaging 12.45 ± 0.598 SEM cells per cluster, while clusters in young mice averaged 11.24 ± 0.862 SEM cells per cluster (**Fig. 2.5 C**). Notably, there were 16 clusters that had greater than 50 cells per cluster in adults compared to only one cluster in young mice with greater than 50 cells per cluster. These data suggest that the clusters that do form in young mice are similar in size to the clusters that form in adults, but that adult mice appear to have an increased capacity to form very large T cell clusters. We further optimized the prediction algorithm and are currently running a larger dataset through this same pipeline to validate these initial findings.
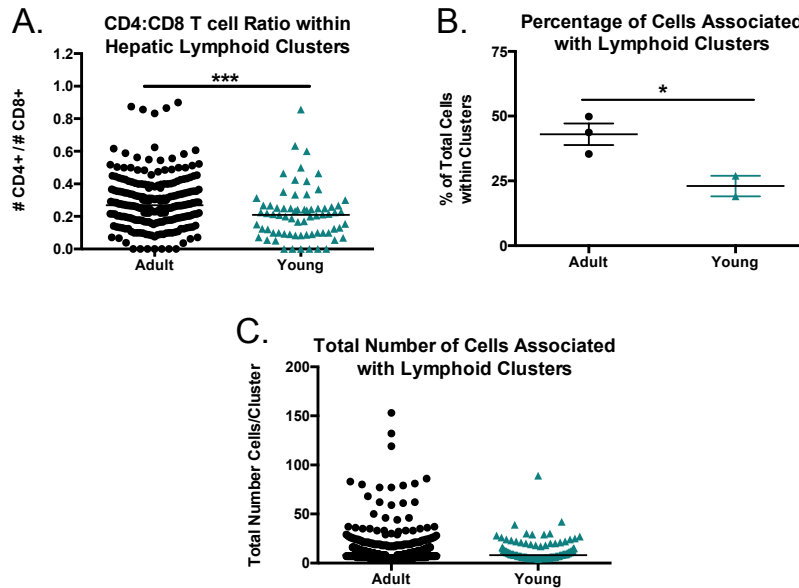
Figure 2.5. Preliminary analysis of RORγ/CD8/CD4 triplex staining via ilastik pipeline in adult and young livers during acute HBV immunity. Liver tissue from three adults and two young mice were sectioned and stained with anti- RORγ, CD8, and CD4 and scanned 20X resolution images were analyzed using our customized ilastik analysis pipeline to segment and classify individual cells. (**A**) Total numbers of CD4+ and CD8+ T cells were counted within every cluster identified within adult and young livers. The number of CD4+ cells was divided by the number of CD8+ cells within every cluster such that each dot represents the ratio of CD4+:CD8+ cells within a specific cluster. (**B**) The percentage of objects classified as CD4+, CD8+, or RORγ+ that are within a cluster is shown as a percentage of the total number objects classified as CD4+, CD8+ or RORγ+. (**C**) The number of CD4+, CD8+, or RORγ+ objects found in each cluster such that each dot represents an individual cluster. Data were analyzed using FlowJoTM Software; statistics determined by unpaired two-tailed t-test using GraphPad Prism Software; n=3 adults, n=2 young.

We also measured the ratio of CD4+ to CD8+ T cells in clusters in which one or more ILC3s were present in the cluster (ILC3+) compared to clusters without ILC3s (ILC3-) in both young and adult animals. Adults had a greater frequency of CD4+ T cells in both ILC3+ and ILC3– clusters relative to young mice (**Fig. 2.6 A**). There was no difference between the relative frequencies of CD4+ and CD8+ T cells within adults, nor within young mice suggesting that ILC3 presence in a cluster does not affect the accumulation of CD4+ versus CD8+ cells within that cluster. There was a trend towards a greater number of clusters that contained one or more ILC3s in adults compared to young mice; however, greater numbers of mice in each group are

needed to validate this observation (**Fig. 2.6 B**). We did find that ILC3+ clusters in adults had a

higher number of total CD4+ and CD8+ cells compared to ILC3– clusters as well as both ILC3+

and ILC3– clusters in young mice (**Fig. 2.6 C**). These data suggest that in adults, ILC3 may

facilitate clustering of more cells, or alternatively, that ILC3s are recruited to larger – and likely

more inflammatory – clusters rather than small, more contained clusters. Because these cells are

present in the tissue before T cells, it is reasonable to hypothesize that ILC3s may associate with

the macrophages we know to anchor these clusters as early as, or earlier than, the T cells.
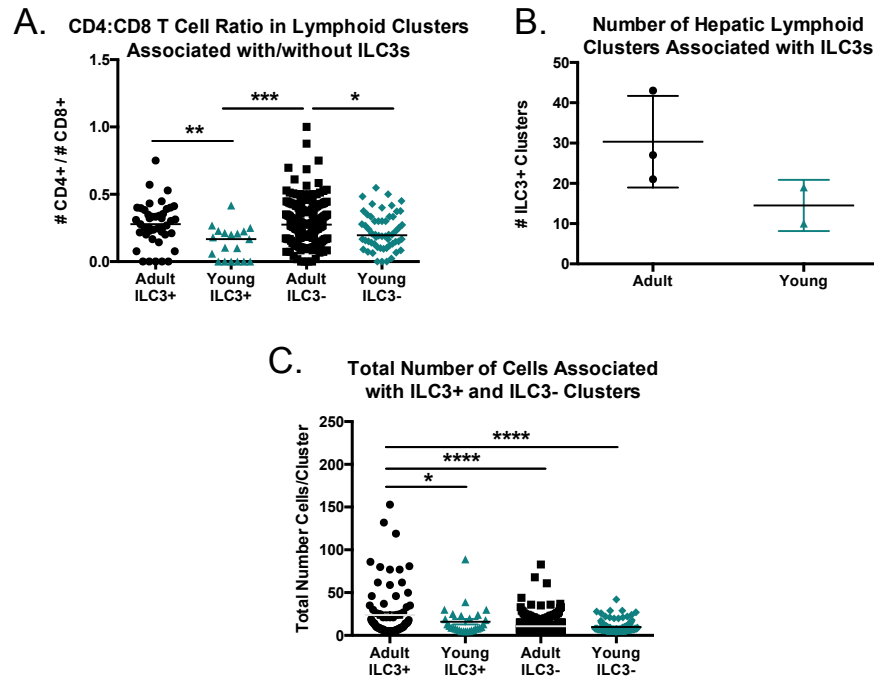
Figure 2.6. Preliminary analysis of ILC3-associated clusters from RORγ/CD8/CD4 triplex stained liver tissue via the ilastik pipeline by age during acute HBV immunity. Liver tissue from three adults and two young mice were sectioned and stained with anti- RORγ, CD8, and CD4 and scanned 20X resolution images were analyzed using our customized ilastik analysis pipeline to segment and classify individual cells. (**A**) Total numbers of CD4+ and CD8+ T cells were counted within every cluster identified within adult and young livers. The number of CD4+ cells was divided by the number of CD8+ cells within every cluster such that each dot represents the ratio of CD4+:CD8+ cells within a specific cluster that contains one or more RORγ+ ILC3 (ILC3+) versus clusters with no ILC3s (ILC3-). (**B**) The number of clusters that are associated with ≥1 ILC3. (**C**) The number of CD4+, CD8+, or RORγ+ objects found in each cluster such that each dot represents an individual ILC3+ or ILC3- cluster. Data were analyzed using FlowJoTM Software; statistics determined by unpaired two-tailed t-test using GraphPad Prism Software; n=3 adults, n=2 young.

In addition to evaluating T cell and ILC3 localization, we also have great interest in better understanding the tissue distribution of macrophage and other myeloid populations relative to immune clusters and other immune cell populations. We first attempted to use F4/80, a marker of macrophages, including Kupffer cells, which is mostly macrophage-specific, although can be expressed by a subset of monocytes and dendritic cells. Although we have been able to observe reproducible and clear tissue staining with this marker by fluorescent imaging, we were unable to find an F4/80 antibody with specific staining that was compatible with the Ventana automated slide staining system. As a result, we opted for a different myeloid marker, CD11b (integrin alpha M, encoded by *Itgam*). CD11b is much less specific to macrophages; however, all macrophages are CD11b+, though to varying levels. In addition, CD11b also marks other myeloid cells including monocytes, granulocytes, and subsets of dendritic cells (cDC2) as well as mature NK cells and some activated T cells. Although this marker is less specific, it is useful in identifying the base of the immune cell clusters that form, and is especially informative due to the high abundance of CD11b+ cells in the liver, particularly Kupffer cell macrophages, that allow us to broadly observe the immune landscape during HBV immunity. Due to its high prevalence and variable expression across different cell types, we did find CD11b to be one of the more challenging markers to optimize within liver. This antibody, when paired with a yellow dye, led to high background blushing of the tissue, which both obscured teal staining patterns of other markers by shifting the teal color profile, as well as masked specific but dim signals from CD11b$_{low}$ cells. Moving forward, we learned that CD11b was best paired with teal or purple dyes. We worked up two triplex stains that include CD11b: (1) RORγ, CD11b, and CD3 and (2) CD45R (B220), CD11b, and CD3. The first stain allows us to identify CD11b+ myeloid and NK cell populations, CD3+ T cells (including both αβ T cells and γδ T cells), CD3+ RORγ+ T cells,

and RORγ+ CD3- ILC3 (**Fig. 2.7**). Compared to the RORγ, CD8, CD4 triplex stain, the RORγ, CD11b, CD3 stain enables complete discernibility between RORγ+ CD3+ T cells and RORγ+ CD3- ILC3s and eliminated the ambiguity of CD4+ RORγ+ cells with the possible Th17 versus ILC3 identity. A limitation of this stain, however, is the inability to differentiate between Th17, Tc17, and RORγ+ γδ T cells, as all three of these populations will appear CD3+ RORγ+. Because of limitations of CD11b on yellow, this stain was best optimized with RORγt on purple, CD11b on teal, and CD3 on yellow. Although CD3 staining in spleen and thymus was crisp (**Fig. 2.1 D-E**), we found the membrane staining pattern of CD3 in the liver was very dependent on cell conditioning and striping conditions and even when fully optimized was often much more "fuzzy" and less discrete compared to spleen and thymus and compared to CD4 and especially CD8 in the liver. Nevertheless, we were able to identify striking differences between adult and young liver sections, particularly related to the CD11b staining. In adult liver we noted that there was a reorganization of CD11b$_{dim}$ cells, which are likely sinusoidal Kupffer cells, and other CD11b$_{bright}$ cells into distinct clusters that associate with CD3+ and RORγ+ cells, with visible "spindle"-like CD11b+ processes reaching out into the parenchyma (**Fig. 2.7 A-C**). Young animals had fewer clusters present and tended to be either CD3-dominant or CD11b-dominant, with less co-clustering of both cell types (**Fig. 2.7 D-F**). We also observed a number of RORγ+ CD3- ILC3s, marked by arrows, which were often associated with immune cell clusters around portal tracts and were found in direct contact with both CD11b+ and CD3+ cells.
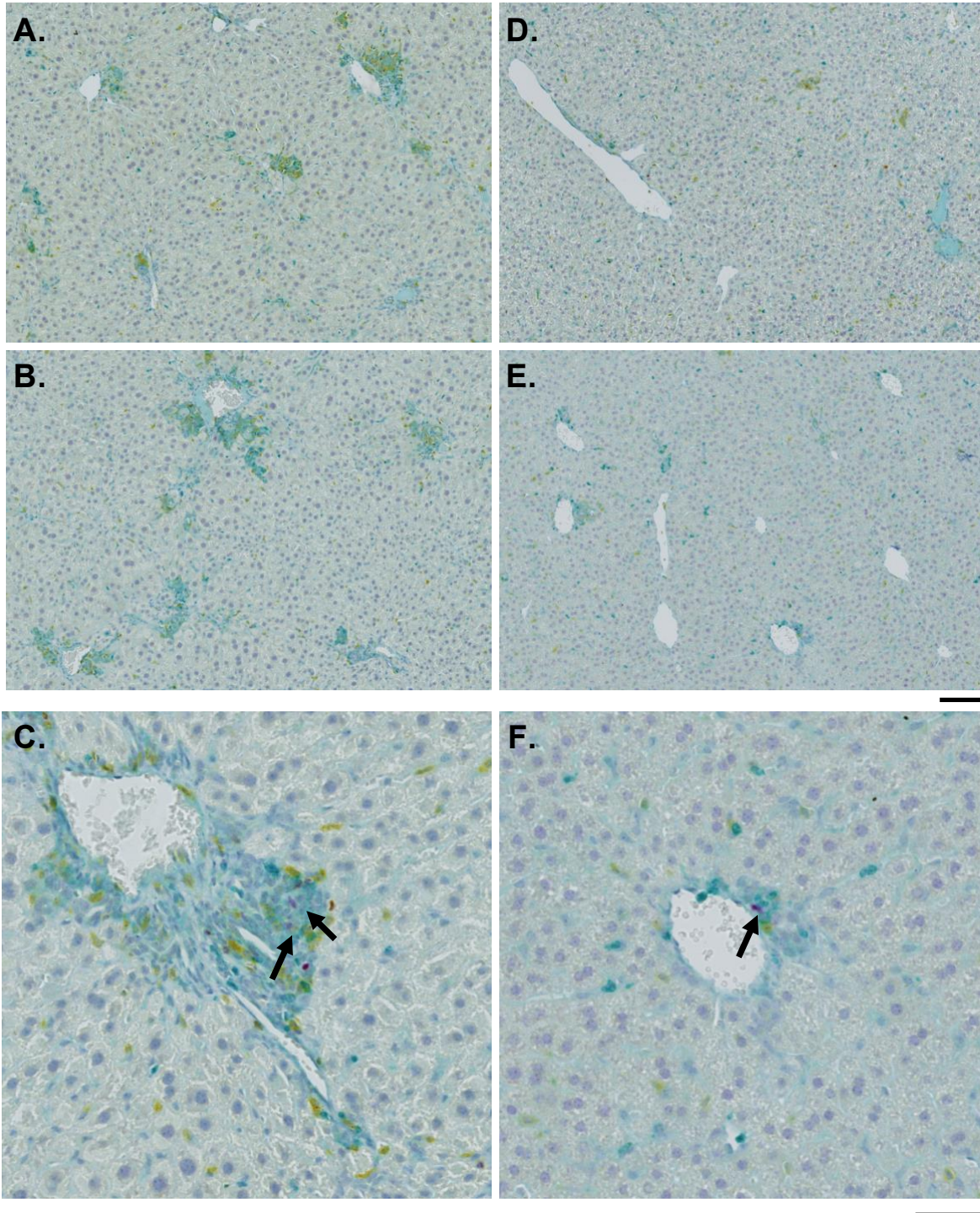
Figure 2.7. RORγ, CD11b, and CD3 staining patterns in adult and young liver during acute HBV immunity. Liver tissue was isolated from adult (**A-C**) and young (**D-F**) HBVtg*Rag1-/-* mice eight days post-adoptive transfer and drop-fixed in formalin for 24 hours, followed by ethanol dehydration and embedding into paraffin wax blocks. FFPE tissue blocks were sectioned at 4 μm and stained with anti-RORγ (purple), anti-CD11b (teal), and anti-CD3 (yellow) using the Ventana Discovery Ultra platform. Stained sections were imaged at 20X resolution with the Zeiss Axioscanner Z1. Arrows point to RORγ+ CD3- ILC3. Scale bars represent 100 μm for **(A-B, D-E)** and 50 μm for (**C, F**).

The second CD11b stain, CD45R (B220), CD11b, and CD3 allows us to discriminate between B cells (B220+), myeloid and NK cell populations (CD11b+), and T cells (CD3+, includes αβ T cells and γδ T cells; **Fig. 2.8**). Once again, an important caveat is that while B220 is mostly found on B cells, it can also be upregulated on other immune populations, including some myeloid cells, NK cells, and T cells. Differences in the morphology and staining intensity patterns between B cells and myeloid cells can lend increased confidence to B cell identification, as B cells are rounder and brighter for B220 compared to other myeloid populations. For this stain we opted for similar conditions to the other CD11b and CD3 stain due to the limitations discusses above for these antibodies, leaving CD11b on teal, CD3 on yellow, and swapping out RORγ on purple for B220. In adult animals, we found most of the B220+ cells to be localized within immune cell clusters, both periportal and parenchymal types (**Fig. 2.8 A-C**). On the other hand, while there were abundant B220+ cells present in the young livers, most of these cells were isolated or in contact with only one or two other cells and usually not present in the few clusters present in these animals (**Fig. 2.8 D-E**). These data suggest that B cells in adult animals are either supported by the immune cluster environment, or instead help contribute to the priming and activation of other T cells present in the clusters. Thus, the absence of B cell-cluster association in young mice may contribute to their impaired ability to prime T cells and produce high affinity and class-switched B cells necessary for HBV control.
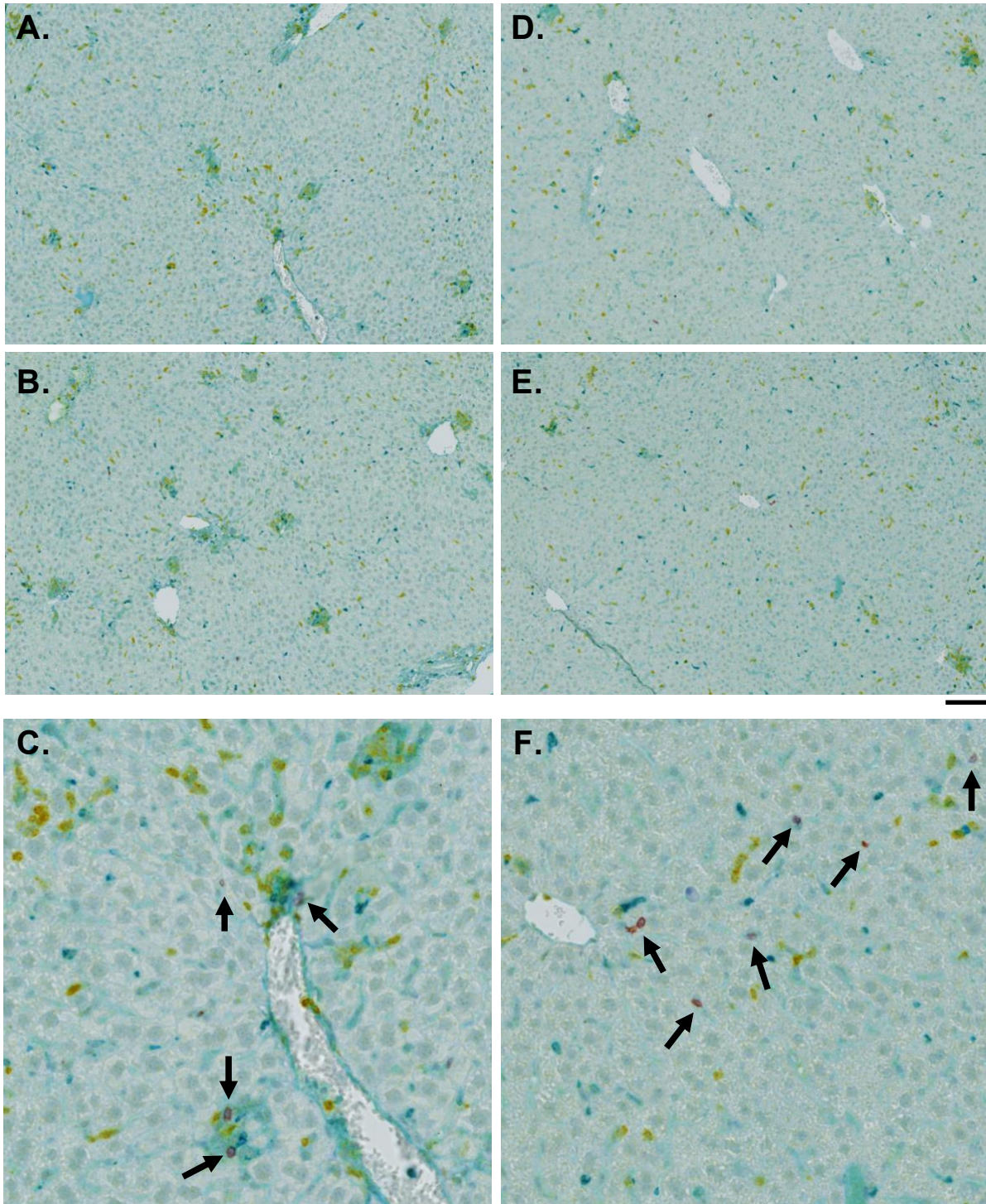
Figure 2.8. B220, CD11b, and CD3 staining patterns in adult and young liver during acute HBV immunity. Liver tissue was isolated from adult (**A-C**) and young (**D-F**) HBVtg*Rag1^{-/-}* mice eight days post-adoptive transfer and drop-fixed in formalin for 24 hours, followed by ethanol dehydration and embedding into paraffin wax blocks. FFPE tissue blocks were sectioned at 4 μm and stained with anti-CD45R/B220 (purple), anti-CD11b (teal), and anti-CD3 (yellow) using the Ventana Discovery Ultra platform. Stained sections were imaged at 20X resolution with the Zeiss Axioscanner Z1. Arrows point to B220+ B cells. Scale bars represent 100 μm for **(A-B, D-E)** and 50 μm for **(C, F)**.

We have completed staining and imaging of liver sections from several groups of adult and young HBV transgenic animals at day eight post-adoptive transfer with all three of these fully optimized and automated triplex stains and are currently working on analyzing these datasets with the same pipeline developed for the RORγt, CD8, CD4 stain. Despite the data analysis being computationally intensive, it is possible to upload image files into the ilastik program and run the algorithm with little to no oversight. Thus, after a time and effort-intensive process that took over three years to develop, we have now created a high-throughput system to stain, image, and analyze large datasets in order to generate highly powered and meaningful data that will contribute to understanding immune cell biology within the liver. The stains we developed with the BTBTC are available for other researchers to use, and while strategically optimized for liver, also work equally well or better in three other tissues we tested, spleen, thymus, and lymph nodes. We have also developed a parallel human panel with anti-RORγt, -CD3, and -CD68 to enable the visualization of ILC3s, T cells, and myeloid cells within human liver specimens.

Discussion

Recent advances in microscopy and computational technologies have greatly increased the amount of information that can be obtained from staining and imaging of tissue sections. Limitations in the numbers of markers used in tissue staining can restrict the ability to clearly identify specific cell populations with the same confidence level one would achieve with flow cytometry or mass cytometry; however, the ability to directly evaluate immune cell organization *in situ* can provide a wealth of information that is lost once that tissue is turned into a single-cell suspension. Our goals in developing these stains were to create a robust platform to evaluate the

dynamics of immune cell reorganization during an anti-viral immune response. While approaches such as live imaging with multi-photon microscopy can enable visualization of motile cells over a one- or two-day window, this approach is limited in the number of individual animals that can be observed. On the other hand, the platform we have now developed with our collaborators in the BTBTC and BIDC allows us to generate and evaluate large datasets to understand how hepatic immune cell organization is affected by experimental intervention at a population-level, rather than within a single individual.

The datasets we have already collected contain tens of thousands of data points for each tissue section collected. When multiplied by the number of individual animals for which we have stained, we have millions, if not billions, of data points that will enable us to draw conclusions that are much more representative of the true biology compared to earlier approaches that rely on selecting small regions of tissue. Thus far, we have already uncovered exciting observations that show differences between CD4+ and CD8+ T cell localization within the liver of adult and young animals. These data support early observations by flow cytometry, but also allow for deeper insights we would never have understood by using flow cytometry alone. Specifically, we can see that the increase in CD4+ T cells in adult livers is not just a global increase, but that these cells are associating with aggregates of other immune cells in adults. In the young mice, the reduced number of hepatic CD4+ T cells is most notably lacking from the few clusters that do form. These data highlight an inability of young mice to recruit CD4+ helper T cell support to the limited number of CD8+ T cell clusters that do form, and identify a potential mechanism that could explain why the abundance of CD8+ T cells in young mice is not sufficient to effect viral antigen clearance.

The focus of our ongoing imaging-related efforts is to complete the computational analysis of already stained liver sections using the customized analysis pipeline we have developed with

Austin Edwards within Ilastik machine learning. We are specifically interested in quantitating the numbers and types of immune cells that are cluster-associated or not, the size of clusters, whether and how close immune clusters are to portal tracts and vascular regions of the liver, as well as the diversity and composition of immune clusters that are or are not associated with individual immune cells including ILC3s and B cells. We aim to identify characteristics of immune clusters and immune cell distribution that are present in adult animals that clear HBV antigens, but are diminished or absent in young animals that are unable to control HBV "infection" in order to identify mechanisms of immunity that could potentially be boosted in young animals to support an immunological switch towards effective anti-HBV immunity. In the future, once we have identified specific features of immune organization that we hypothesize to contribute to effective immune priming, we will test these hypotheses with additional imaging techniques such as targeted confocal microscopy and live imaging to understand how individual cell-to-cell interactions support the population level dynamics observed in large tissue sections.

Chapter 3. *RORc*(γt)-deficient mice have impaired anti-HBV immunity

Introduction

Mouse models to study ILC3s

After identifying age-dependent differences between hepatic ILC3 populations in adult and young mice, we hypothesized that these cells may play an important role in facilitating effective HBV immunity. Therefore, we decided to study animals deficient in the transcription factor required for their development and differentiation, RORγt, to monitor the effect of ILC3-deficiency on HBV immune outcome. In 2004, Gérard Eberl *et al.*, of Dr. Dan Littman's laboratory generated a RORγt reporter and knock-out mouse by inserting the EGFP coding sequence within the first exon of the *Rorc*(γt) isoform locus (exon 1γt), which is nested within the *Rorc*(γ) locus (*23*). Insertion of the EGFP coding sequence disrupts the coding sequence of *Rorc*(γt) but does not affect *Rorc*(γ), which is widely expressed in many adult tissues including liver, lung, muscle, heart, and brain and has a separate ATG start site upstream of exon 1γt. The resulting *Rorc*(γt)+/GFP heterozygous mouse is a reporter of RORγt-expressing cells, whereas the *Rorc*(γt)GFP/GFP homozygous mice are complete RORγt knock-outs, resulting in deficiency of RORγt-dependent cells. Initial characterization of these mice revealed that in fetal mice, EGFP expression was restricted to LTi cells that were CD127 (IL-7Rα)+, and mostly CD4+, which were not present in the thymus. By adulthood, GFP expression was observed within CD4+ CD8+ double-positive thymocytes and was weakly present in single-positive thymocytes, which was attributed to the long half-life of EGFP (>24 h), rather than active RORγt expression at the single positive stage as no *Rorc*(γt) mRNA was detected in these cells. Consistent with previous

reports, RORγt-deficient thymocytes had reduced survival in culture and $Rorc(\gamma t)_{GFP/GFP}$ mice had 30-50% fewer double-positive thymocytes compared to wild-type mice, showing an important role for RORγt in thymocyte survival at this stage. In an earlier report by the same group, researchers described a similar phenotype in the thymus of $Rorc(\gamma)_{-/-}$ mice and further showed that beyond the double-positive stage, there is also a dramatic reduction in the total number of single-positive T cells within the thymus, likely as a result of the survival defects during the double-positive stage (*43*).

The role of fetal LTi cells in lymphoid organization

The most striking phenotype of these mice, however, is the complete lack of peripheral lymph nodes and Peyer's patches, which are organized lymphoid follicles within the mucosa and submucosa of the small intestine that play an essential role in regulating gut immunity and homeostasis (*23*). The absence of these lymphoid tissues highlights the essential role that fetal LTi cells play in lymphoid organization and ontogeny. Notably, splenic architecture and cellularity is maintained in $Rorc(\gamma)$- and $Rorc(\gamma t)$-deficient animals, illustrating a lack of LTi-dependency in this organ. Further experimentation showed that LTi cell expression of $LT\alpha_1\beta_2$ is critical for induction of adhesion molecules VCAM-1 and ICAM-1 by mesenchymal cells in the lymph node and Peyer's patch anlagen, designated stromal "organizer" cells (*23*). The requirement of LTi expression of lymphotoxins could be bypassed by treating mice with an agonistic antibody against the $LT\alpha_1\beta_2$ receptor, LTβR, which led to the direct upregulation of VCAM-1 and ICAM-1 expression. These adhesion molecules play a critical role in organizing the architecture of the lymphoid tissues. The authors also showed that CXCL13 was required for early LTi recruitment to all lymph nodes and Peyer's patch anlagen except for mesenteric and

cervical lymph nodes, which had normal numbers of LTi cells in CXCL13-deficient mice. Furthermore, they also identified IL-7 to be critical for early LTi cell recruitment to lymphoid tissues as blockade of the IL-7Rα (CD127) with an antagonistic antibody at embryonic day 12 (E12) and E15 led to a decreased or complete loss of LTi cell clusters at lymph node and Peyer's patch anlagen. The blockade of IL-7Rα at only E15, however, had no impact on LTi accumulation at these sites, demonstrating the role of IL-7 in very early LTi recruitment, which later becomes dispensable. The authors concluded that while IL-7 and CXCL13 both play some role in fetal LTi cell recruitment, there are additional factors that contribute to this process. At the time when these papers were published, the field of ILC biology was still in its infancy and it was not yet appreciated that LTi cells represented only a subset of ILC3s and that these cells have many functions later in life beyond their early requirement for lymph node development.

Adult LTi-like cells retain lymphoid organizing capabilities

While these studies outlined a clear role for LTi cells during fetal lymphoid organogenesis, it remained unclear what role these cells played in adulthood. Researchers hypothesized that since these cells remain in secondary lymphoid organs in adults, perhaps they continue to play a role maintaining lymph node organization important for efficient immune priming during infection. Elke Scandella *et al.*, showed that after experimental lymphocytic choriomeningitis virus (LCMV) infection, splenic architecture was disrupted. Specifically, the network of gp38+ fibroblastic reticular cells (FRC) was dramatically reduced and marginal zones, T cell zones, and B cell zones were completely disrupted, coinciding with the peak activation of CD8+ cytotoxic lymphocytes (CTL) (*25*). Overtime, gp38+ cells that play an essential role in T cell zone architecture were repopulated and splenic cellular organization was

recovered by day 25 post-infection. During this recovery period, mice displayed an impaired ability to mount an immune response after immunization with recombinant glycoprotein from vesicular stomatitis virus (VSV-G). Animals immunized at day eight post-LCMV infection failed to produce antibodies against VSV-G and animals immunized at day 16 post-infection produced greatly reduced antibody titers, illustrating the essential role that lymphoid organization plays in immune priming. The authors found that the number of LTi cells increased within these tissues, reaching peak accumulation by day eight to twelve post-infection. They generated bone marrow chimeras with *Rorc*(γ)-/- bone marrow transferred into irradiated wild-type recipients and observed that splenic architecture recovery was delayed – though not fully blocked – suggesting RORγ+ cells contribute to the reorganization of lymphoid tissue after virus-mediated disruption. Indeed, when they adoptively transferred enriched LTi cell preparations into the chimeras, they observed restoration of the gp38+ FRC network at day 16, similar to that seen in WT animals, showing the potential of these cells to support cellular reorganization. These experiments showed for the first time that LTi-like cells in adult lymphoid organs retained some of their lymphoid-organizing capabilities.

Another study published two months later went on to show a *bona fide* role of adult LTi-like cells in the development of cryptopatches (CP) into mature isolated lymphoid follicles (ILF) (*24*). Unlike Peyer's patches, the formation and maturation of ILF occurs after birth and is dependent on microbial colonization of the gut. These structures consist primarily of clusters of B cells, stromal cells, and dendritic cells and play a critical role in the production of mucosal IgA antibodies. This study showed that CD3- CD11c- Gr1- B220- CD19- IgA- lineage (Lin)- RORγt+ LTi-like cells isolated from two-month-old mice were capable of inducing ILF formation in *Rorc*(γt)-/- adult recipient mice. They went on to show that this was dependent on

the signaling downstream of LTβR, similar to the dependency of fetal lymphoid organogenesis on LTβR signaling. They characterized the differences between embryonic LTi cells and adult LTi-like cells and found that the adult cells expressed less LTα compared to fetal LTi cells, but similar levels of LTβ and increased expression of RANKL (encoded by *Tnfsf11*) and LIGHT (encoded by *Tnfsf14*), the latter of which is also an LTβR ligand. The authors concluded that adult LTi-like cells maintain ligand expression that allows them to interact with stromal "organizer" cells and facilitate immune cell organization beyond the window of embryonic development and into adulthood.

In addition to expression of lymphotoxins, researchers recognized early on that like RORγt+ Th17 cells, RORγt+ LTi-like cells were capable of producing IL-17, as well as IL-22 (*44*). Studies have shown a role for IL-17 production in supporting the formation of inducible bronchus-associated lymphoid tissue (iBALT), consistent with an effector function of promoting lymphoid organization. In this study, however, it was CD4+ T cell-derived IL-17 production rather than ILC3-derived IL-17 production that was essential (*45*). To my knowledge, no other studies have shown a direct role for ILC3-derived IL-17 exclusively playing an essential role in lymphoid structure formation. Given the role that IL-17 plays in lymphotoxin-independent induction of chemokines – including CXCL13 and CCL19, which attract CXCR5+ and CCR7+ lymphocytes, respectively – and a role for IL-17 in the formation of germinal centers, it is likely that IL-17 production by LTi-like cells can synergistically contribute to lymphoid structure organization (*45, 46*).

Functional effects of ILC3-derived cytokines beyond lymphoid organization

Beyond lymphoid organization, IL-23-driven IL-17A and IL-17F production by ILC3s in the oral mucosa was demonstrated to play an essential role in control of mucosal *Candida albicans* infection (*47*). In addition, IL-17F, and to a lesser degree IL-17A, were also shown to be critical in a model of experimental *Citrobacter rodentium* infection; mice that were deficient in either or both cytokines had increased bacterial burden and increased intestinal inflammation (*48*). In this study, T cells seemed to be the major source of IL-17A while an unidentified population, likely ILC3s, was the primary IL-17F source. The authors showed both IL-17A and IL-17F played important roles in the production of β-defensin anti-microbial peptides in response to *C. rodentium* infection and hypothesized that a decreased abundance of these molecules in the absence of IL-17 contributes to the observed phenotypes. These studies expanded the understanding of ILC3 effector functions beyond lymphoid organization.

ILC3s have also been shown to secrete GM-CSF, which has varying roles depending on the context. One group showed that GM-CSF production by ILC3s was required for efficient induction of oral tolerance against commensal microbes (*49*). In this study, microbes drove IL-1β production by macrophages, which in turn stimulated NKp46- ILC3s, and to a lesser degree NKp46+ ILC3s, to produce GM-CSF that ultimately supported Treg differentiation. In *Csf2-/-* mice, which lack expression of the gene encoding GM-CSF, Treg numbers were greatly reduced in the gut, leading to loss of oral tolerance to dietary antigens and dysbiosis of the gut immune environment, which the authors hypothesized was a result of decreased retinoic acid and IL-10 production by macrophages and DCs. In a separate study, ILC3-derived GM-CSF was described as having a pro-inflammatory role, which functioned by promoting recruitment of inflammatory

Ly6c+ monocytes in a model of anti-CD40-induced innate colitis (*50*). In this study, GM-CSF was important for induction of CCL2, and to a lesser degree CCL19, resulting in trafficking of CCR2+ and CCR7+ cells, as well as movement of ILC3s out of cryptopatches, prior to the formation of immune clusters elsewhere in the tissue, indicating that GM-CSF from ILC3s may be another mechanism by which ILC3s can regulate lymphoid organization.

Discovery of NCR+ ILC3 and clarification of their ontogeny

The shift in focus away from canonical LTi-associated functions of ILC3s was further expanded when researchers discovered a population of NK-like cells that were also RORγt+. Further investigation showed that these cells were NKp46+ in mice and NKp44+ in humans. The literature from this period can be confusing, as there was no consensus on the origin of these cells or nomenclature. As a result, disparate groups of researchers began referring to these cells by different names, including NKR-LTi, NKR+ RORγt+ ILC, NCR-22, NK22, and ILC22 – as people also discovered these cells to be a major source of IL-22.

Two publications helped to clarify that RORγt+ ILCs are in fact distinct from NK cells. First, an earlier study from Dr. Gérard Eberl in 2004 used RORγt fate-mapping to track which cells RORγt-expressing precursors are capable of differentiating into. They carried out these studies by crossing *Rorc*(γt)-Cre_TG mice that express Cre recombinase under the control of the *Rorc*(γt) locus via a bacterial artificial chromosome transgene, to R26R mice that express GFP under the control of the *Rosa26* locus (which is constitutively expressed) only after Cre-mediated recombination and excision of a LoxP-flanked STOP cassette that prevents translation of GFP before its removal (*51*). In these mice, once RORγt has been expressed at any point GFP

expression is induced and maintained due to the constitutive nature of *Rosa26* expression. Thus, any cell that is GFP- has never previously expressed RORγt because it was unable to remove the STOP cassette and permit GFP expression due to a lack of Cre expression. The data presented in this study showed that splenic NK cells, identified as CD3- DX5(CD49b)+ and/or NK1.1+, had no GFP expression, indicating that NK cells are not dependent on the transcription factor RORγt. Therefore, the authors concluded that NK cells do not develop from a RORγt+ progenitor or precursor population.

The second study to clarify the origin of ILC3s asked the converse question: whether the NK-like NKp46+ RORγt+ ILC3s differentiate from the NK cell lineage, or instead from the LTi/LTi-like RORγt+ lineage. In these experiments the authors sorted 2 x 10⁴ NK cells (NKp46+ RORγt-), LTi-like cells (NKp46- RORγt+), or NKp46+ RORγt+ from small intestine, large intestine, and spleen of *Rorc*(γt)GFP/+ mice and transferred them into recipient *Rag2-/-Il2rg-/-* mice, which lack all mature T cells and ILC populations (*52*). Twenty-eight days after adoptive transfer, the authors found that only the LTi-like and NKp46+ RORγt+ cells, and not the NK cells, gave rise to a population of NKp46+ RORγt+ cells. Interestingly, many of the RORγt GFP+ cells from the LTi-like and NKp46+ RORγt+ subsets lost their GFP expression by day 28, suggesting the possibility of additional plasticity in these cells beyond NKp46 expression. These results were replicated *in vitro*, again showing an inability of NK cells to differentiate into a RORγt+ population. Taken together, these two studies show that multiple ILC3 subsets come from a common RORγt-dependent precursor that is separate from NK cells, and that NK cells do not differentiate from a RORγt+ precursor.

Functional roles and plasticity of NCR+ and NCR- ILC3

The latter group went on to characterize this NKp46+ subset of ILC3s (now called NCR+ ILC3) using a similar fate mapping approach as Eberl and Littman, except with EYFP instead of EGFP, termed RORγtfm (*52*). They, and others, showed that in addition to being a major source of IL-22 production, mouse and human NCR+ ILC3 can progressively lose RORγt expression while upregulating T-bet and switching towards an IFNγ-producing ILC1-like phenotype (*52, 53*). This population was later termed "ex-ILC3" due to their former expression of RORγt. Subsequent studies were completed to clarify that in addition to ex-ILC3s, there are *bona fide* ILC1 that are RORγtfm– and develop from a common ILC precursor in the bone marrow identified as Lin- (CD3- CD5- CD19- B220- Gr1- NK1.1- TER-119-) Id2+ IL-7Rα+ CD25- α4β7+ (termed CHILP – common progenitor to all helper-like ILC) (*22*). Furthermore, this CHILP does not give rise to Eomes+ NK cells, further illustrating the distinction between NK cells and not only ILC3s but also ILC1s and ILC2s (*22*).

After clarifying the origin and identity of these NK-like IL-22+ ILC3, several independent groups went on to show critical functional roles for IL-22-producing NKp46+ and NKp46- ILC3s in regulating tissue homeostasis and disease, most prominently within the intestine. In the context of *C. rodentium* infection in mice, IL-23 expression is highly induced resulting in expression of IL-22 from both NKp46+ and NKp46- ILC3 subsets. While IL-6 was required for the induction of IL-17A by ILC3, a loss of IL-6 did not affect IL-22 production but a loss of IL-23 completely abrogated the early induction of IL-22 by ILC3 (*54*). In the absence of IL-23, IL-22, or ILC3s, animals succumb to the infection more rapidly and with greatly increased intestinal pathology, highlighting a protective role of IL-22 (*54-56*).

Although it was first reported that the important subset of IL-22-producing ILC3s was NKp46+, careful follow-up studies revealed that although NKp46+ ILC3 do produce significant amounts of IL-22, that subset was dispensable for protection from *C. rodentium* infection, whereas the CD4+ NKp46- ILC3 subset was required for bacterial control (*55, 56*).

Activated dendritic cells are an important source of IL-23 and contribute to the ability of IL-23R+ ILC3s to induce IL-22 secretion. IL-22R expression is restricted to non-hematopoietic cells and is mostly found on epithelial and other stromal cells, including hepatocytes within the liver. Signaling via IL-22R can trigger secretion of antimicrobial peptides including regenerating islet-derived III (REGIII)β and REGIIIγ and β-defensins, which can both directly kill bacteria as well as modulate microbial colonization of tissues (*54, 57, 58*). IL-22 can also induce expression of enzymes important for fucosylation. This process plays an important role in shaping commensal microbial communities and can protect against pathogenic infection by *Salmonella typhimurium* (*59*). IL-22R signaling via STAT3 also induces epithelial cell proliferation and upregulation of gene pathways associated with wound healing and tissue repair (*60, 61*). On the other hand, IL-22 can also act as a pro-inflammatory mediator, stimulating expression of chemokines including CXCL10 and CCL20 and promoting recruitment of CXCR3+ and CCR6+ cells, particularly with a helper 17-like phenotype (*62-64*).

ILC3s are important antigen-presenting cells

A more recent body of work by several groups has focused on understanding the role MHC class II (MHCII) expression on a subset of ILC3s. Matthew Hepworth *et al.*, first showed in 2013 that ILC3s regulate adaptive immunity not through their expression of cytokines, but instead through their expression of MHCII and direct modulation of CD4+ T cell responses (*35*).

The authors first observed that *Rorc*(γt)GFP/GFP knock-out mice have increased frequencies of circulating CD44+ CD62Llow CD4+ effector T cells and increased Ki67+ CD4+ T cells; these mice also exhibited splenomegaly and elevated levels of commensal bacteria-specific IgG compared to control mice, indicative of increased basal inflammation in the absence of RORγt. Oral administration of broad-spectrum antibiotics reversed this phenotype, providing a link between microbial dysbiosis and immune dysregulation. The authors observed high levels of MHCII expression within small intestine ILC3s that was greatest in NKp46- T-bet- ILC3s but could also be observed in a small subset of NKp46- T-bet+ and NKp46+ T-bet+ ILC3s. The authors tested the ability of MHCII+ ILC3s from the small intestine to prime OT-II CD4+ T cells, which have a TCR specific for OVA peptide, and found that unlike dendritic cells, ILC3s lacked expression of CD40, CD80, and CD86 costimulatory molecules and were unable to induce T cell proliferation, as marked by CFSE dilution. They went on to generate mice with MHCII deleted within ILC3s by crossing *H2-Ab1*fl mice with *Rorc*Cre mice. Because RORγt expression is limited to ILCs and T cells – and T cells do not express MHCII – this deletion only functionally affects ILC3s. In these MHCΔILC3 mice, deletion of MHCII from ILC3s alone was sufficient to recapitulate the CD4+ T cell dysregulation phenotype of *Rorc*(γt)GFP/GFP mice. Furthermore, they again showed that this immune dysregulation in MHCΔILC3 mice could be ameliorated by oral antibiotic administration.

While the above study highlighted a role for ILC3s in promoting T cell tolerance to microbial antigens, additional studies revealed a role for MHCII+ ILC3s in productive antigen presentation and immune priming. Nicole von Burg *et al.,* generated a similar mouse model with MHCII deleted in RORγt-expressing cells that they term *I-ab*ΔILC3 (*38*). Interestingly, the authors reported that these mice did not show signs of spontaneous inflammation or CD4+ T cell

expansion as was described in the Hepworth *et al.* report. These observations highlight the role that commensal microbiota play in this process, as it is now well accepted that animals housed in different facilities can have dramatically different commensal microbial communities that affect immunity during both homeostasis and disease (*34, 38*). Nevertheless, the authors went on to show that *I-ab*ΔILC3 mice had an impaired ability to produce OVA-specific IgG1, IgG2a, IgG2b, and IgG3 antibodies after immunization, similar to the impairment seen in complete RORγt-/- mice. They also found a reduced number of proliferating CD4+ OT-II cells in these immunized *I-ab*ΔILC3 mice. They confirmed that splenic ILC3s could efficiently uptake antigen, albeit with reduced kinetics compared to bone marrow-derived macrophages. They also identified IL-1β as an important positive regulator of the expression of MHCII; co-stimulatory molecules CD80, CD86, and CD40; and the activation marker CD69 on ILC3s. IL-1β treatment also increased the functional ability of ILC3s to activate antigen-specific OT-II CD4+ T cells in culture measured by CFSE dilution.

Although these two studies showed conflicting results, there are two important considerations that may explain these findings. First, as previously mentioned, these studies were carried out in different facilities and as a result, the microbial communities that colonized the animals in each facility were likely very different and might have contributed to the presence of basal inflammation in the Hepworth model that was absent in the von Burg study. Secondly, Hepworth *et al.*, mainly studied the role of *intestinal* ILC3s in their ability to prime T cells, whereas von Burg *et al.*, studied *splenic* ILC3s. A major distinction between these two populations was the difference in expression of co-stimulatory molecules on splenic ILC3s that was not present on intestinal ILC3s. It is important, however, to note that expression of co-stimulatory molecules was also very low at baseline in splenic ILC3s and these were only

induced in the presence of IL-1β. This suggests that while tissue-specific differences in ILC3s likely contribute to their functional profiles, the presence of IL-1β can have profound effects on the activity of ILC3s. Furthermore, local differences in IL-1β irrespective of tissue origin may contribute to these functional differences.

Early reports highlighted a role for co-stimulation by splenic ILC3s independent of MHCII-antigen presentation such that OX40L+ ILC3s were able to increase survival of already primed or activated OX40+ CD4+ Th2 cells, and could be seen in close contact with these cells *in vivo* (*36*). Together these experiments highlight the importance of co-stimulatory molecule expression on ILC3s in directly and indirectly supporting effector CD4+ T cell and T-dependent B cell responses.

Another recent study nicely showed that abundant IL-23 in the small intestine leads to decreased MHCII expression on NKp46- ILC3, while IFNγ – which is more abundant in the spleen relative to the gut – increases MHCII on NKp46- ILC3, in part through the regulated expression of CIITA, a major transcriptional regulator of MHCII (*37*). Perhaps most interestingly, the authors showed that small intestine ILC3s (siILC3) adoptively transferred into mice and recovered from the spleen acquire a splenic ILC3 (spILC3) phenotype, and vice versa, illustrating the plasticity of these populations and the ability to adjust to their microenvironment. They also noticed that there was no tissue-specific bias imprinted upon the NKp46- ILC3s such that siILC3 and spILC3 did not preferentially home to their origin tissue. Consistent with the earlier reports, the enriched MHCII-positivity within the spleen and parallel increase in co-stimulatory molecule expression enabled these cells to prime T cells much more efficiently than their siILC3 counterparts.

Plasticity of ILC3s; a spectrum of phenotypes and functions

As reviewed above, there is now a significant body of literature supporting the notion that ILC3s are a highly plastic population capable of differentiating and de-differentiating into different subsets. On one end of the spectrum are the CD4+ CCR6+ LTi-like ILC3s that express lymphotoxins and can produce IL-17 and IL-22 (*44*). On the other end of the spectrum are the NKp46+ ILC3s which express T-bet and mainly produce IL-22 and IFNγ (*52, 53*). This subset is further able to completely lose RORγt expression in the presence of IL-12, acquiring an "ex-ILC3", ILC1-like phenotype. In the middle of the spectrum lies the NKp46- ILC3s that lack CCR6 and CD4 expression. These cells have the potential to upregulate NKp46 in the presence of IL-1β and IL-23, or instead can acquire CCR6 expression and an LTi-like identity (*53, 65-67*). This NKp46- subset, in addition to serving as a more immature subset capable of differentiating towards LTi-like or NKp46+ subsets, is a potent producer of IL-17, IL-22, and GM-CSF cytokines upon stimulation (*49, 65, 68*). A portion of these NKp46- ILC3 also express MHCII and can act as antigen-presenting cells, leading either to immune priming or immune tolerance depending on context (*35, 38, 69*). The extreme variability of ILC3s is likely in part because they are well-suited to respond to environmental signals through their expression of IL-23R, whose ligand, IL-23, is highly inducible by microbial stimuli; their ability to respond to retinoic acid produced in the gut; and their dependency on aryl hydrocarbon receptor (Ahr), a transcription factor that senses soluble aromatic hydrocarbons produced by commensal microbes (*70-72*).

ILC3 are primarily tissue-resident

Although ILC3s can be found within circulation, it is well accepted that ILCs are primarily tissue-resident. The most compelling support for this comes from a study that used

parabiosis experiments to show that greater than 95 percent of lineage- (CD3ε, CD5, CD8α, CD19, TCRγδ, TCRβ and FcεR1) ILC1 (RORγt- Eomes- NK1.1+), ILC2 (RORγt- GATA3+), ILC3 (RORγt+ CD4-), and LTi cells (RORγt+ CD4+) were host-derived rather than of donor origin after 30 days, and up to 130 days, of shared circulation between congenically marked CD45.1 and CD45.2 animals when looking in the small intestine lamina propria, salivary gland, lung, and liver (73). In humans, a population of lineage- (CD3- CD4- CD5- TCRαβ TCRγδ CD14- CD19-) CD7+ CD56- CD127+ cells were found in circulation that lacked expression of transcription factors associated with specific ILC lineages. These cells were mostly CD117 (cKit)+ and when cultured *ex vivo* within a stromal cell-based culture system displayed unipotent and multipotent features, leading the authors to conclude this population acts as a circulating committed ILC precursor capable of differentiating into each of the ILC subsets and potentially re-seeding tissues (74).

Modification of our HBV transgenic mouse model to study effects of ILC3-deficiency on HBV immunity

As mentioned in earlier chapters, our laboratory became interested in ILC3s when we discovered an age-dependent transcriptional immune signature, later confirmed by flow cytometry, indicating that ILC3s were more enriched within the liver of adults compared to young mice. This observation together with the known roles of ILC3s in regulating immune cell organization, recruitment, and priming, led us to hypothesize that the age-dependent accumulation of these cells may contribute to age-dependent outcomes in HBV. At the time when we first started our studies in early 2015, the most accessible mouse model available was the previously described *Rorc*(γt)GFP/GFP reporter/knockout mouse generated in Dr. Dan

Littman's laboratory (*23*). Dr. Richard Locksley kindly provided these *Rorc*(γt)GFP/GFP mice to us to cross onto our HBVtg*Rag1*-/- mouse model background generating HBVtg*Rag1*-/--*Rorc*(γt)GFP/GFP mice or HBVtg*Rag1*-/--*Rorc*(γt)GFP/+ reporter mice. Despite some limitations of these mice described above, this model provided a reliable way to completely ablate ILC3s in HBVtg*Rag1*-/- recipient mice, enabling us to ask the critical question: can mice that lack ILC3s mount an effective anti-HBV immune response?

Results

In order to test the hypothesis that the age-dependent increase in ILC3s contributes towards effective immunity against HBV in adult animals, we adoptively transferred 10_8 HBV-naïve WT splenocytes into HBVtg*Rag1*-/- and HBVtg*Rag1*-/--*Rorc*(γt)GFP/GFP mice, hereafter referred to ILC3-sufficient and ILC3-deficient mice, respectively, and monitored disease outcome. Importantly, since recipient animals are on a *Rag1*-/- background, RORγt-deficiency does not impact the T cell compartment, which is reconstituted from a RORγt-replete donor animal allowing for normal differentiation of Th17 and RORγt+ γδ T cells. I observed striking differences in immune outcomes of ILC3-sufficient and ILC3-deficient animals. ILC3-deficient animals displayed increased early liver inflammation, as measured by alanine aminotransferase (ALT) rise, compared to ILC3-sufficient animals, with peak differences occurring around day seven post-adoptive transfer (**Fig. 3.1 A**). This increased inflammation could also be observed histologically, with dramatically increased portal inflammation in ILC3-deficient animals (**Fig. 3.1 B**). Despite increased inflammation, 75 percent of ILC3-deficient animals were unable to clear HBsAg or make anti-HBs antibodies, indicating these animals are severely impaired in

their ability to control HBV (**Fig. 3.1 C-D**). Of the animals screened for anti-HBs antibodies,

only two ILC3-deficient mice produced a response, with very low antibody titers (**Fig. 3.1 E**).
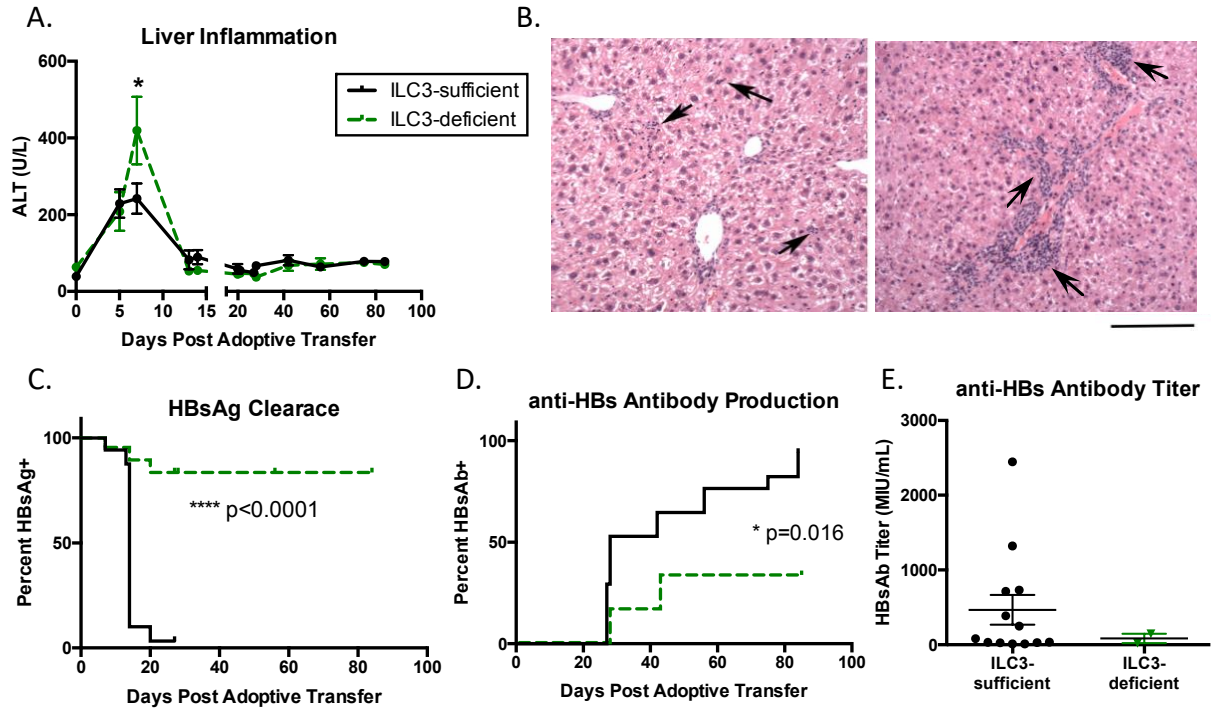
Figure 3.1. HBV immunity is strongly impaired in ILC3-deficient *Rorc*(γt)GFP/GFPHBVtg*Rag1*-/- mice. Adult (>8wks) HBVtg*Rag1*-/- (ILC3-sufficient) or *Rorc*(γt)GFP/GFPHBVtg*Rag1*-/- (ILC3-deficient) animals were adoptively transferred with HBV-naïve splenocytes. (**A**) Liver disease was monitored by plasma alanine aminotransferase (ALT). (**B**) Hematoxylin and Eosin (H&E) staining of representative FFPE liver tissue sections from ILC3-sufficient (left) and ILC3-deficient (right). Scale bar represent 150 μm; arrows point to clusters of immune cells in the liver parenchyma and next to portal tracts. (**C**) Clearance of circulating HBsAg and (**D**) production of anti-HBs antibodies were monitored over time by qualitative and quantitative ELISAs, respectively. (**E**) Quantitative antibody titers are shown at day 84 post-adoptive transfer for animals that produced a positive anti-HBs result. Data were analyzed using FlowJoTM Software; statistics determined by a log-rank (Mantel-Cox) Chi square survival test or unpaired two-tailed t-test with GraphPad Prism Software; * p<0.05, *** p<0.001, n≥21 per group for ALT and HBsAg clearance data, pooled from five independent experiments; n≥6 per group for anti-HBs antibody data pooled from two independent experiments.

I performed a series of experiments to pinpoint the underlying differences within the

hepatic immune compartment that might explain the impaired HBV clearance in ILC3-deficient

animals. I examined immunity at day 8 post-transfer during the early window of immune

priming, as well as later at day 29 to determine the effect of ILC3-deficiency on sustained

immune responses. When grossly examining the composition of the hepatic immune compartment I observed similar numbers of total CD45+ hepatic immune cells in ILC3-deficient animals on day 8 and on day 29 (**Fig. 3.2 A**). T cells comprised approximately half of the hepatic immune cells both time points and I noted that ILC3-deficient mice had a small reduction in the frequency of TCRβ+ T cells at both time points (**Fig. 3.2 B**). I observed that NK cells made up about 20 percent of the hepatic immune cells in ILC3-sufficient mice and that ILC3 deficiency reduced the frequency of NK cells slightly at day 8 and dramatically at day 29 to 4-fold less than control mice (**Fig. 3.2 C**). These data suggest that ILC3s play a critical role in supporting NK cell responses throughout the course of disease and highlight a potential defect that may contribute to the impaired HBV immunity of these animals. I also observed a reduction of NK1.1+ T cells in ILC3-deficient mice at the later time point only; though, this population was reduced over time and only made up a small fraction of total hepatic lymphocytes (**Fig. 3.2 F**). The reduction in frequency of T cells, NK cells, and NK1.1+ T cells was partially offset by an increase in the percentage of B cells in ILC3-deficient mice at day 8, but by day 29 the frequency of B cells was equivalent between groups (**Fig. 3.2 D**). Although there were similar numbers of Gr-1$_{hi}$ granulocytes, mostly neutrophils, at day 8, that number greatly expanded by day 29 and I observed a 5-fold increase in the percentage of granulocytes in ILC3-deficient mice (**Fig. 3.2 E**). Taken together, these data suggest that the loss of ILC3s results in impaired T cell and NK cell responses shown to be critical in control of HBV infection and instead favors an inflammatory and neutrophil-rich response, most often associated with bacterial infections, wound healing, and tissue remodeling.
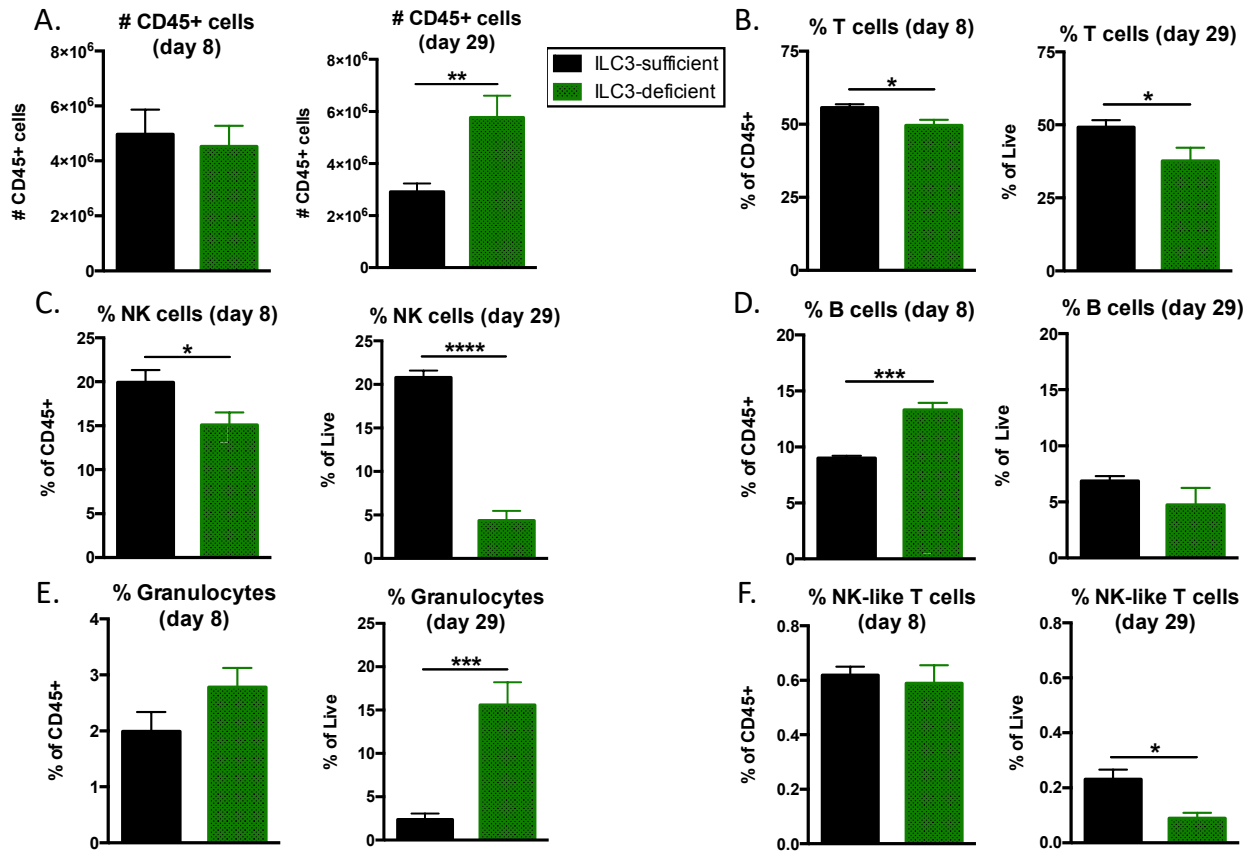
Figure 3.2. Hepatic immune cell composition changes over time and is disrupted in ILC3-deficient mice. Hepatic leukocyte fractions were enriched from adult (>8 wks) HBVtg*Rag1*-/- (ILC3-sufficient) and *Rorc*(γt)GFP/GFPHBVtg*Rag1*-/- (ILC3-deficient) animals 8 days and 29 days after adoptive transfer with HBV-naïve splenocytes. Total numbers of CD45+ lymphocytes (**A**) were measured on day 8 and 29 and the percentages of the follow populations relative to CD45+ or Live cells were measured and defined as follows: (**B**) T cells (CD45+ TCRβ+ CD90+), (**C**) NK cells (CD45+ TCRβ- CD90- NK1.1+), (**D**) B cells (CD45+ TCRβ- B220+), (**E**) granulocytes (CD45+ Gr1hi), and (**F**) NK-like T cells (CD45+ TCRβ+ CD90+ NK1.1+). Data were analyzed using FlowJoTM Software; statistics determined by unpaired two-tailed t-test with GraphPad Prism Software; * $p<0.05$, *** $p<0.001$, **** $p<0.0001$; n≥4 per group.

I examined the composition of αβ T cells to determine if there were any differences within T cell populations previously identified to play a role in productive HBV immune responses. I discovered a striking phenotype of dramatically increased numbers of CD4+ T cells relative to CD8+ T cells in ILC3-deficient mice. In adult ILC3-sufficient mice that mount an effective immune response, I found that a majority of their hepatic T cells were CD8+ (~70-80 percent) while a minority were CD4+ (~20-25 percent) (**Fig. 1.8 and Fig. 3.3 A-B**). In the ILC3-

94

deficient mice, however, I observed that this CD4/CD8 T cell skewing was completely reversed at day eight, with CD4+ T cells now comprising 75 percent of the hepatic αβ T cell compartment and CD8+ T cells only making up 20 percent of total T cells (**Fig. 3.3 A**). By day 29 I still observed T cell skewing towards CD4+ T cells compared to ILC3-sufficient animals; however, the effect was not as dramatic as day 8 and instead I observed that αβ T cells were roughly equally split between CD4+ and CD8+ T cell subsets in ILC3-deficient mice (**Fig. 3.3 B**). Interestingly, the number of CD8+ T cells in the liver of ILC3-deficient mice at day 29 had caught up to that of control mice, such that the increase of CD4+ T cells in the absence of ILC3s was the sole driver of the skewing towards CD4+ T cells compared to ILC3-sufficient mice. I had previously identified a small, but significant, defect in the ability of young mice to mount an effective CD4+ T effector response compared to adults. Although these ILC3-deficient mice had abundant CD4+ T cells, they were still unable to clear HBV. This strongly suggests that the quality of the CD4+ T cell response in ILC3 mice was impaired, and further, that the loss of CD8+ T cells may also have limited the ability of these mice to effectively clear HBsAg.

I addressed whether the CD4+ T cell skewing was liver specific, or instead reflected a systemic shift in T cell responses. I measured the number of CD4+ and CD8+ T cells in the liver, spleen, and circulating peripheral blood mononuclear cells (PBMCs) to address this question. Similar to the liver, I observed an expansion of CD4+ T cells in the spleen, as well as in circulating PBMCs (**Fig. 3.3 E-F**). However, unlike the liver, I detected no restriction on CD8+ T cell accumulation in the spleen in the absence of ILC3s, as there were a similar number of CD8+ T cells regardless of ILC3 deficiency (**Fig. 3.3 E**). In circulation, I measured an increase in CD8+ T cells similar to that seen for CD4+ T cells (**Fig. 3.3 F**). Taken together these data suggest that ILC3s may normally play a role in restricting CD4+ T cell expansion, particularly in

the context of an adoptive transfer model whereby transferred T cells are recognizing new HBV

antigens, as well as potentially new commensal antigens not present in the donor's microbial

communities. Furthermore, the loss of ILC3s in recipient animals seems to restrict the early

ability of CD8+ T cells to accumulate within the liver, despite an abundance of these cells in

circulation and secondary lymphoid organs. This observation suggests that ILC3-deficiency

results in either a defect in the local priming or differentiation of CD8+ T cells within the liver,

and/or that there is an impaired ability to recruit or maintain CD8+ T cells within the tissue

during early immune priming, which can eventually be overcome with time.
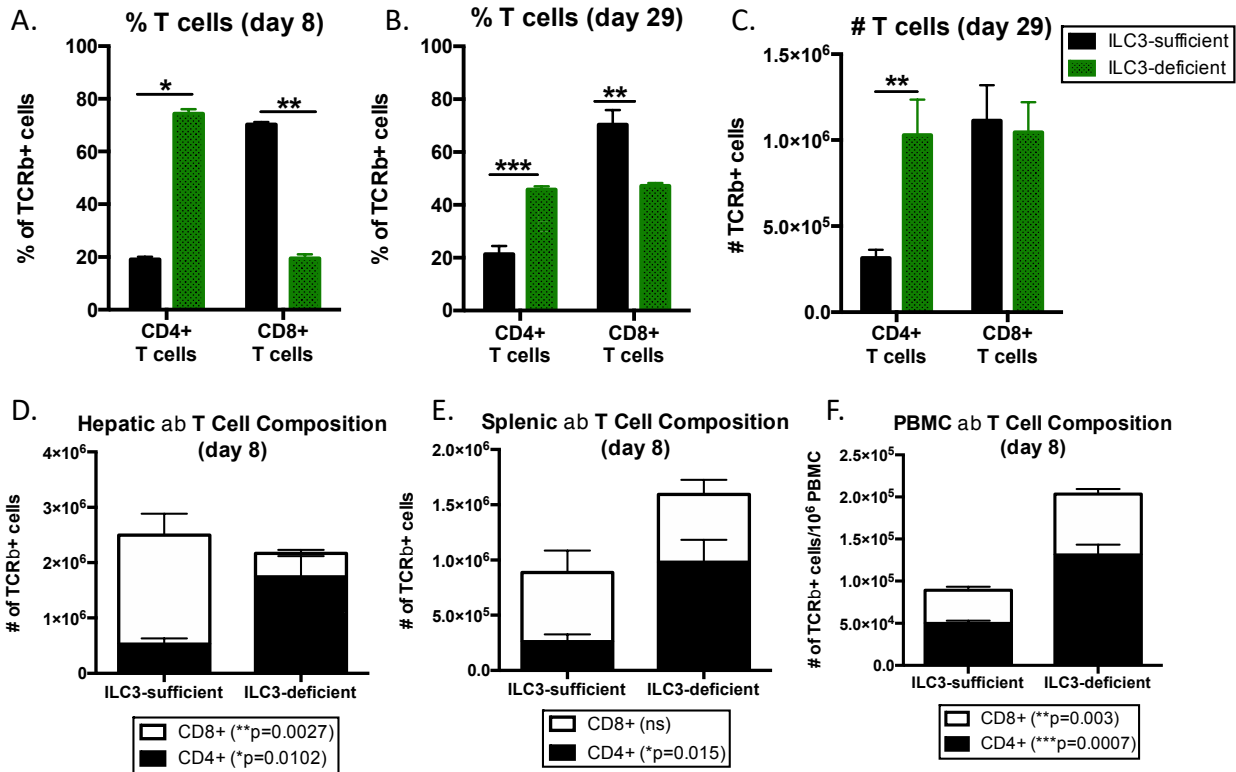
Figure 3.3. ILC3 deficiency causes global CD4+ T cell expansion and restricts hepatic CD8+ T cell accumulation. Hepatic leukocyte fractions were enriched from adult (>8 wks) HBVtg*Rag1-/-* (ILC3-sufficient) and *Rorc*(γt)GFP/GFPHBVtg*Rag1-/-* (ILC3-deficient) animals 8 days and 29 days after adoptive transfer with HBV-naïve splenocytes. Percentage of CD4+ T cells (CD45+ TCRβ+ CD90+ CD4+) and CD8 T cells (CD45+ TCRβ+ CD90+ CD8+) of total TCRβ+ cells on day 8 (**A**) and day 29 (**B**) post-adoptive transfer. (**C**) Number of CD4+ and CD8+ T cells on day 29 post-transfer. (**D-F**) Numbers of

CD4+ and CD8+ TCRβ+ T cells from liver (**D**), spleen (**E**), and peripheral blood mononuclear cells (PBMC) (**F**) were quantified as absolute numbers within the given tissue, or as a frequency per 10_6 PBMC. Data were analyzed using FlowJo™ Software; statistics determined by unpaired two-tailed t-test with GraphPad Prism Software; * p<0.05, *** p<0.001, **** p<0.0001; n≥4 per group.

We confirmed the CD4+ T cell skewing of ILC3-deficient animals through tissue staining with anti-CD8α and anti-CD4, as described in Chapter 2, on both day 8 and day 29 post-splenic reconstitution. During early inflammation, adult ILC3-sufficient animals had numerous periportal and parenchymal T cell clusters, with similar representations of CD4+ and CD8+ T cells within the clusters, along with many individual CD8+ and some CD4+ T cells distributed throughout the parenchyma (**Fig. 3.4 A-C**). Consistent with the H&E staining results and the flow cytometry data, we could very clearly observe much greater periportal inflammation in ILC3-deficient mice on day 8, with large T cell clusters encompassing many of the portal tracts within the liver (**Fig. 3.4 D-F**). These clusters tended to either have similar proportions of CD4+ and CD8+ T cells or were heavily dominated by CD4+ T cells, particularly the intra-parenchymal clusters, with very few CD8+ T cell-dominant clusters. We also observed a much greater number of individual CD4+ T cells distributed throughout the parenchyma compared to ILC3-sufficient mice. Notably, the total number of CD45+ cells and T cells recovered from both ILC3-sufficient and ILC3-deficient mice as determined by flow cytometry was not different, suggesting that there was a profound difference in the distribution of these cells (**Fig. 3.2 A-B, Fig. 3.3 D**). These data strongly implicate a role for ILC3s in regulating T cell distribution and localization throughout the tissue.
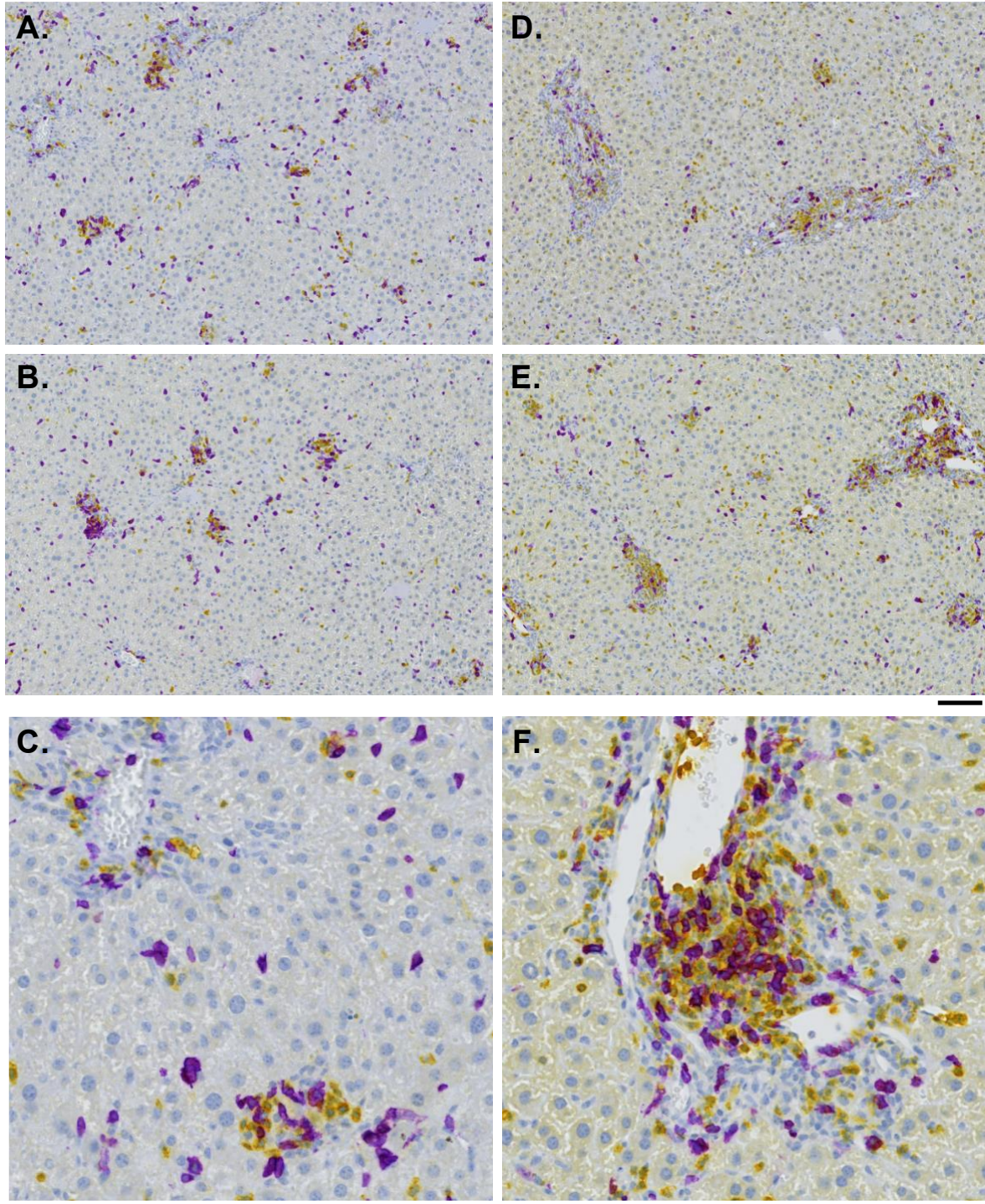
Figure 3.4. CD4 and CD8 staining patterns in ILC3-suffcient and ILC3-deficient liver during acute HBV immunity. Liver tissue was isolated from HBVtg*Rag1*-/- ILC3-sufficient (**A-C**) and *Rorc*(γt)GFP/GFPHBVtg*Rag1*-/- ILC3-deficient (**D-F**) mice eight days post-adoptive transfer and drop-fixed in formalin for 24 hours, followed by ethanol dehydration and embedding into paraffin wax blocks. FFPE tissue blocks were sectioned at 4 μm and stained with anti-CD4 (yellow), anti-CD8a (purple) using the Ventana Discovery Ultra platform. Stained sections were imaged at 20X resolution with the Zeiss Axioscanner Z1. Scale bars for (**A-B, D-E**) represent 100 μm, scale bars for (**C, F**) represent 50 μm.

By day 29 post-transfer, we observed that the majority of the inflammation present on day 8 had resolved in the ILC3-sufficient mice, with few T cell clusters remaining that were mostly intra-parenchymal or loosely associated with portal tracts (**Fig. 3.5 A-C**). This observation is consistent with the loss of circulating HBsAg in all of these ILC3-sufficient mice by this time point. The few remaining immune cell aggregates observed likely serve as a hub for continued activation of antigen-specific T cells needed to maintain prolonged clearance of HBsAg in the context of a transgenic HBV model. The ILC3-deficient mice, which had all failed to clear HBsAg by day 29, however, did not resolve the high levels of hepatic inflammation and immune cell infiltration observed on day 8. In the absence of ILC3s, there was a substantial amount of inflammation still present in the liver at this later time point, with numerous periportal and parenchymal T cell clusters, some of which were extremely large and encompassed the entire area around a given portal tract (**Fig. 3.5 D-F**). ILC3-deficient mice also still had an increased representation of CD4+ T cells relative to ILC3-sufficient animals; however, we observed that unlike day 8, there were many fewer CD4+ only, or CD4+ T cell-dominant, clusters and a greater influx of CD8+ T cells was observed, consistent with the flow cytometry data (**Fig. 3.3 C**). These data suggest that the persistent inflammation present in ILC3-deficient mice may result from an inability of these mice to clear viral antigens, which can continue to stimulate an inflammatory response. This observation is reminiscent of ectopic lymphoid structures that can be found in patients with chronic viral infection, which, similar to aggregates found in ILC3-deficient mice, do not to lead to effective immune priming and viral clearance. Thus, it is important to better understand how the immune aggregates that form in ILC3-sufficient mice and lead to productive immunity differ from both the aggregates found in ILC3-deficient mice and those found in patients with CHB, which lead to unproductive inflammation.

As discussed in Chapter 2, we will use Ilastik software and machine learning, to complete this

analysis in a quantitative and qualitative manner to characterize these differences.
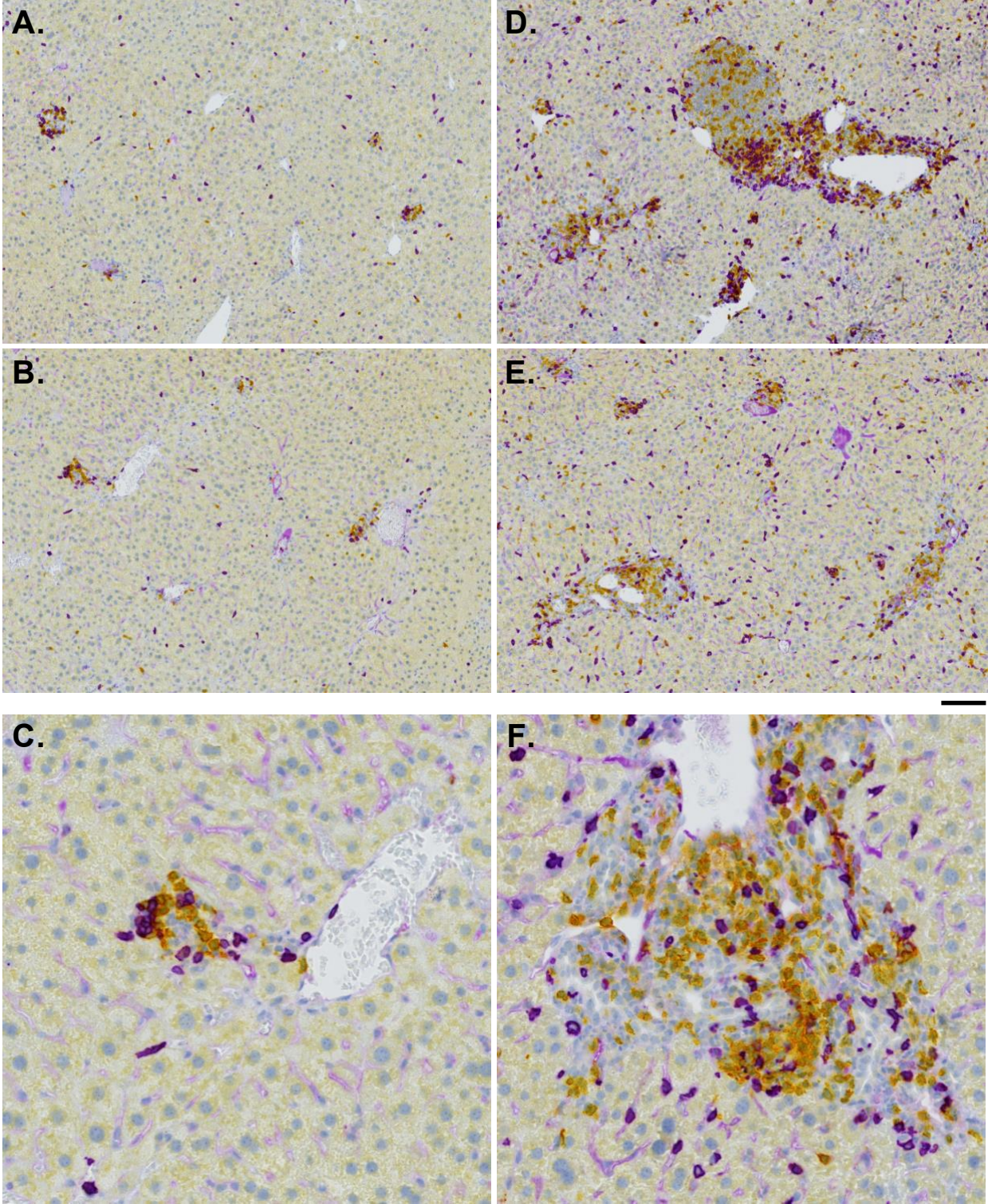
Figure 3.5. CD4 and CD8 staining patterns in ILC3-suffcient and ILC3-deficient liver during sustained HBV immunity. Liver tissue was isolated from HBVtg*Rag1*-/- ILC3-sufficient (**A-C**) and *Rorc*(γt)GFP/GFPHBVtg*Rag1*-/- ILC3-deficient (**D-F**) mice 29 days post-adoptive transfer and drop-fixed in formalin for 24 hours, followed by ethanol dehydration and embedding into paraffin wax blocks. FFPE tissue blocks were sectioned at 4 μm and stained with anti-CD4 (yellow), anti-CD8a (purple) using the Ventana Discovery Ultra platform. Stained sections were imaged at 20X resolution with the Zeiss Axioscanner Z1. Scale bars for (**A-B, D-E**) represent 100 μm, scale bars for (**C, F**) represent 50 μm.

After identifying substantial differences in CD4+ and CD8+ T cell composition of the liver, I measured the frequencies of naïve, central memory, and effector/effector memory subsets of T cells to understand how ILC3 loss might affect T cell differentiation, as I previously identified a defect in CD4+ TEff cells in young mice at day 8 that also fail to control HBV. When first focusing on CD4+ T cells, I observed that the increased number of these cells in ILC3-deficient mice occurred almost entirely within the CD44+ CD62L- TEff/TEM subset as there were no differences in the number of TCM or TNaïve CD4+ cells in ILC3-deficient mice at day 8 (**Fig. 3.6 A**). By day 29, when the T cells have had more time to establish their phenotypes after the initial period of acute inflammation subsided, I noted that there was a reduction in the frequency of CD4+ T cells with a central memory phenotype, again with an abundance of TEff cells (**Fig. 3.6 B**). I also examined expression of PD-1 and found that there was no difference in the frequency of PD-1+ cells at day 8 but there was a decreased percentage of PD-1+ CD4+ T cells at day 29, with an overall decrease in the percentage of PD-1+ cells in both groups relative to day 8 (**Fig 3.6 C**). Although PD-1 is often regarded for its role in T cell exhaustion in settings of chronic disease, it is also a well-known activation marker whose expression is increased in response to TCR stimulation and T cell activation. One potential explanation for the decrease in PD-1 expression in CD4+ T cells in ILC3-deficient mice that do not clear HBV antigens may be that the dramatic CD4+ T cell expansion we observe is partially a result of bystander activation rather than an antigen-driven response and thus, less PD-1 is upregulated in this pool of non-TCR stimulated CD4+ T cells. The best way to address this question is to identify the frequency

of antigen-specific T cells in each animal with MHCII tetramers. We are currently in the process of generating these tetramers with the NIH Tetramer Core Facility and plan to evaluate this both at day 8, and especially at a later time point such as day 29. In the absence of tetramers, I attempted to assess the functional role of these cells by measuring IFNγ and IL-17A cytokine production by CD4+ T cells. Thus far, I have only examined an early time point. I observed an increased number of IFNγ+ and IL-17A+ CD4+ T cells in ILC3-deficient mice, without a difference in the frequency of either population, indicating the increase in these populations is reflective of the increase in total CD4+ T cells, rather than a skewed differentiation towards the production of one or the other cytokines (**Fig. 3.6 D-G**). Interestingly, I observed that there was much more expression of PD-1 on ILC3-sufficient IFNγ+ CD4+ T cells compared to IFNγ+ CD4+ T cells from ILC3-deficient mice, although the opposite was true for IL-17A+ CD4+ T cells (**Fig. 3.6 H**). Again, if we consider PD-1 as a marker reflective of recent antigen experience and TCR engagement, this may suggest that a large portion of the IFNγ-producing CD4+ T cells in ILC3-deficient mice might be HBV non-specific bystander cells, while the opposite may be true for the IL-17A+ subset. This also makes some sense in the context of microbially driven expression of IL-23 and its support of RORγ+ and IL-17A+ cell differentiation. Thus, if there were microbial dysbiosis due to ILC3 loss in these mice, it is possible that IL-23 may be locally increased near portal tracts where an influx of intestinal blood flow – carrying microbes and/or microbial products – could lead to increased IL-23 secretion by DCs and other myeloid cells that promote Th17 skewing of antigen-specific cells. Careful experiments with a panel of HBV-specific tetramers will be necessary to clarify these hypotheses and determine whether there is a decrease in HBV-specific IFNγ+ cells and/or an increase of HBV-specific IL-17A+ cells, which are likely to be less effective at controlling viral pathogens than their IFNγ+ Th1 counterparts.
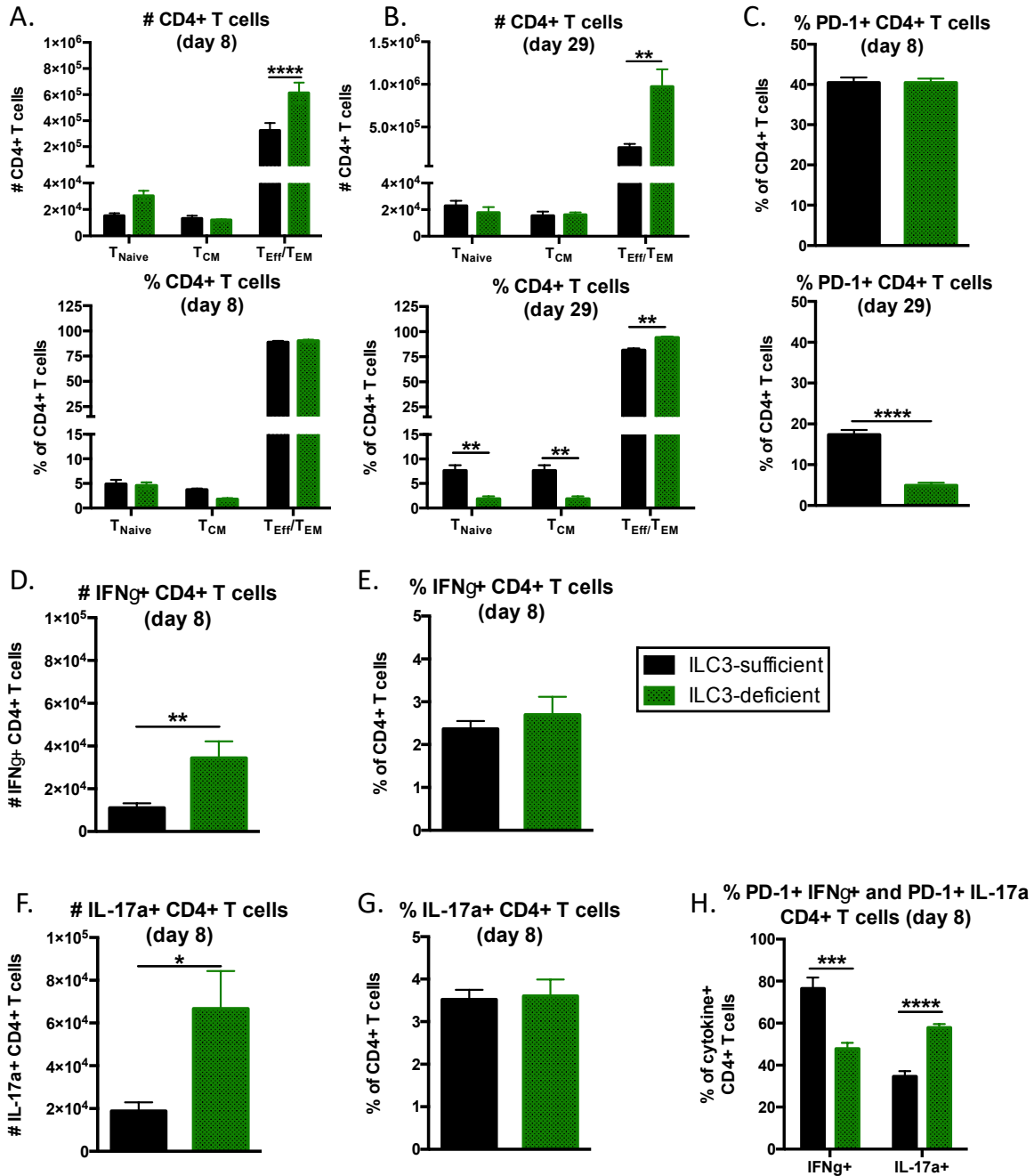
Figure 3.6. ILC3 deficiency impairs CD4+ central memory T cell responses and favors effector differentiation. Hepatic leukocyte fractions were enriched from adult (>8 wks) HBVtg*Rag1*-/- (ILC3-sufficient) and *Rorc*(γt)GFP/GFPHBVtg*Rag1*-/- (ILC3-deficient) animals 8 days and 29 days after adoptive transfer with HBV-naïve splenocytes. The number (**A**) and percentage (**B**) of CD44- CD62L+ Tnaive, CD44+ CD62L+ TCM (central memory) and CD44+ CD62L- TEff/TEM (effector/effector memory) CD4+ T cells on day 8 (left) and day 29 (right). (**C**) Percentage of PD-1+ CD4+ T cells. The number (**D, F**) and percentage (**E, G**) of IFNγ+ (**D-E**) and IL-17A+ (**F-G**) CD4+ T cells. (**H**) Percentage of PD-1+ IFNγ+ and PD-1+ IL-17A+ CD4+ T cells. Data were analyzed using FlowJoᴛᴍ Software; statistics determined by unpaired two-tailed t-test with GraphPad Prism Software; * p<0.05, ** p<0.01, *** p<0.001, **** p<0.0001; n≥4 per group (**A-C**) n=6 per group (**D-H**).

When examining CD8+ T cells, I observed that at the early time point the major loss of CD8+ T cells in ILC3-deficient mice is due to a reduction of CD44+ CD62L- T$_{Eff}$ subset (**Fig 3.7 A**). Because of the loss of T$_{Eff}$, there is a relative increase in the frequencies of T$_{CM}$ and T$_{Naive}$ CD8+ cells relative to total CD8+ T cells. At day 29, however, I observed that similar to the CD4+ T cells, there was a marked reduction in the frequency as well as the number of central memory CD8+ T cells, suggesting an inability to sustain T$_{CM}$ more globally (**Fig. 3.7 B**). Unlike the CD4+ T cells, I noted that at the early time point there was an increased percentage of PD-1+ CD8+ T cells (**Fig. 3.7 C**). Similar to the CD4+ T cells, it's possible that this could represent an increased frequency of recently TCR-activated CD8+ T cells. Alternatively, a recent study in a model of acute LCMV infection showed that CD8+ effector T cells rapidly upregulate PD-1 on their surface and that it plays a functional inhibitory role within these cells at an early time point, such that blockade of PD-L1 (one of the ligands of PD-1) results in increased granzyme B production, enhanced viral clearance, and increased generation of memory-like T cells, which was only apparent after day 14 post-infection (*75*). This study suggests that the increased expression of PD-1 on CD8+ T cells in the liver of ILC3-deficient mice may similarly play a functional role in suppressing cytotoxic activities and memory cell formation of CD8+ T cells, and perhaps contribute to the impaired clearance of HBV viral antigens in our model. When measuring cytokine production within CD8+ T cells during early immunity, I observed a decreased number of IFNγ+ and IL-17A+ CD8+ T cells in the ILC3-deficient mice; however, the percentage of IFNγ+ and IL-17A cells was not changed (**Fig 3.7 D-G**). Like CD4+ T cells, these findings again indicate there is not an early defect in cytokine production, and differences in total numbers of cytokine-producing cells reflects a defect in total CD8+ T cell accumulation. Similar to total CD8+ T cells, I also noted that IFNγ-producing CD8+ T cells in ILC3-deficient mice

have more PD-1 expression, though there were no differences in the percentage of PD-1+ IL-17A-producing CD8+ T cells. Finally, I also assessed the expression of CXCR3 on CD8+ T cells, as this chemokine receptor has been shown to play a critical role in both homing and retention of tissue resident memory T cells, as well as in the activation of Th1 and CTL responses (*76*). Indeed, I observed that ILC3-deficiency led to a reduced frequency of CXCR3+ CD8+ T cells, suggesting that trafficking of these T cells may be impaired in the absence of ILC3s, and may partially explain their reduced numbers in the liver at this time despite abundant circulating CD8+ T cells (**Fig. 3.7 I**).
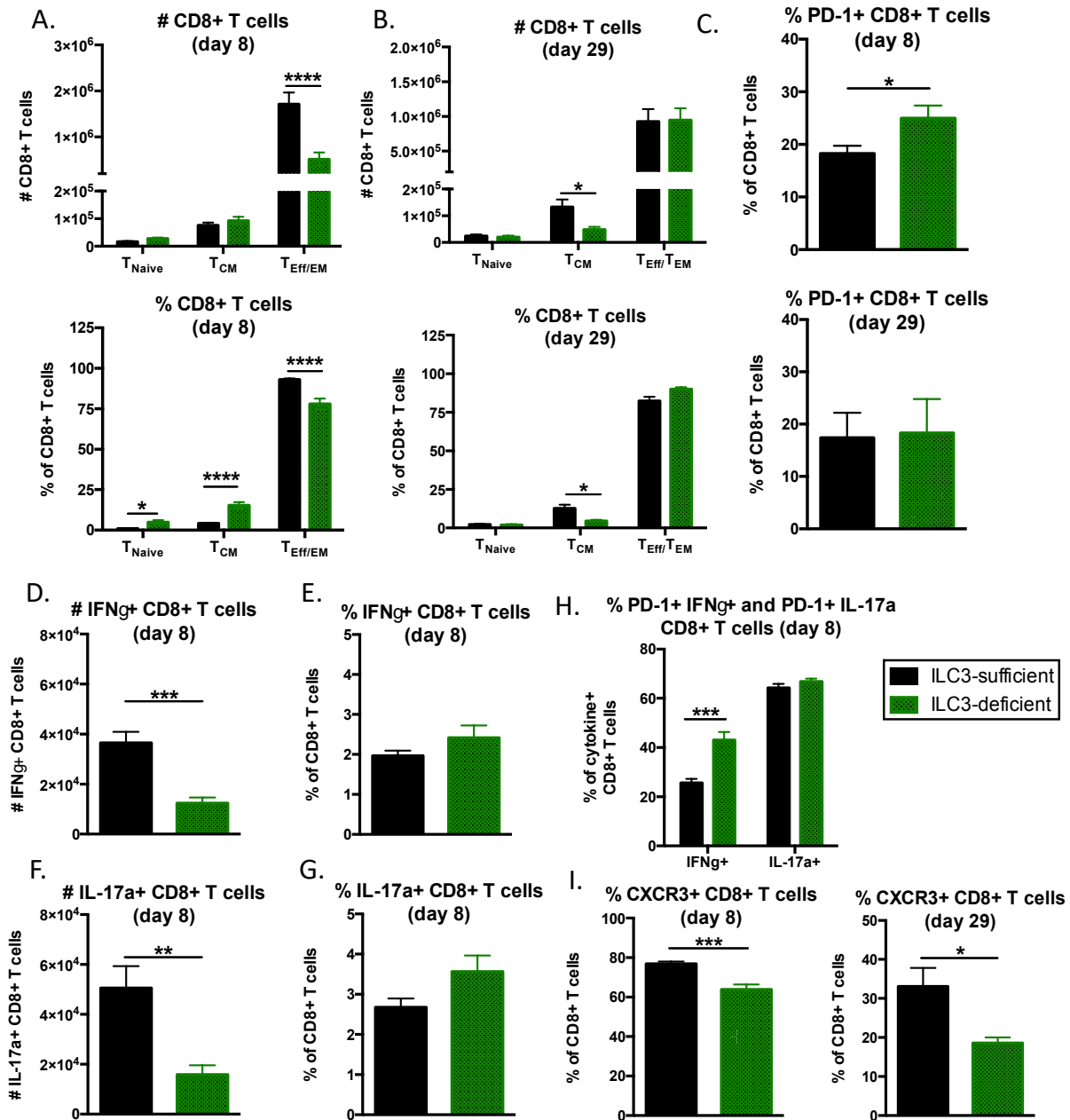
Figure 3.7. ILC3 deficiency impairs early CD8+ effector T cell and late central memory responses. Hepatic leukocyte fractions were enriched from adult (>8 wks) HBVtg*Rag1*-/- (ILC3-sufficient) and *Rorc*(γt)GFP/GFPHBVtg*Rag1*-/- (ILC3-deficient) animals 8 days and 29 days after adoptive transfer with HBV-naïve splenocytes. The number (**A**) and percentage (**B**) of CD44- CD62L+ Tnaive, CD44+ CD62L+ TCM (central memory) and CD44+ CD62L- TEff/TEM (effector/effector memory) CD8+ T cells on day 8 (left) and day 29 (right). (**C**) Percentage of PD-1+ CD8+ T cells. The number (**D, F**) and percentage (**E, G**) of IFNγ+ (**D-E**) and IL-17A+ (**F-G**) CD8+ T cells. (**H**) Percentage of PD-1+ IFNγ+ and PD-1+ IL-17A+ CD8+ T cells. (**I**) Percentage of CXCR3+ CD8+ T cells on day 8 (left) and day 29 (right). Data were analyzed using FlowJoTM Software; statistics determined by unpaired two-tailed t-test with GraphPad Prism Software; * p<0.05, ** p<0.001, *** p<0.001, **** p<0.0001; n≥4 per group (**A-C**), n=6 per group (**D-H**) n≥3 per group (**I**).

Although I have not yet had the opportunity to assess the prevalence of antigen-specific T

cells in ILC3-deficient animals, as we have only very recently identified the dominant HBV

epitopes and their MHC-restriction required to create MHC class I (MHCI) and MHCII

tetramers, I have been able to use IFNγ ELISpot assays to gain some insights into antigen-

specific responses. Over time, as we have learned more about the individual peptides, and now

specific epitopes within those peptides, we have refined the assay to focus on the most common

epitopes that drive antigen-specific IFNγ production. In short, the assay is performed by

culturing hepatic lymphocytes together with an equivalent number of splenocytes from a *Rag1*-/-

animal that does not express the HBV transgene, as a source of antigen presenting cells (APCs),

in the presence of peptides derived from the HBV envelope protein (surface antigen) overnight

followed by detection of secreted IFNγ. Importantly, because lymphocytes are taken directly

from the liver where HBV antigen is abundant, particularly at early time points, it is possible that

IFNγ spots detected in the "0" peptide wells, which are not stimulated with HBV peptides, may

still represent recently activated cells that are HBV-specific. Another consideration when

interpreting results from the assay is that I have not separated T cells from other IFNγ-producing

cells, so while peptide-boosted responses do represent antigen-specific responses, "baseline"

IFNγ production may also include innate sources of the cytokine that are not antigen-specific.

Nonetheless, for the purposes of these assays I have defined a positive antigen-specific response

as a response with ≥2-fold baseline IFNγ. Data from these experiments were mixed, suggesting

complex regulation of IFNγ, likely within multiple cellular compartments. At day eight, during

peak inflammation and at a time when the antigenic burden is high, I observed that ILC3-

deficient mice had an increased baseline IFNγ response, approximately 2-4-fold higher than that

of ILC3-sufficient mice. As a result, ILC3-deficient mice had a greater number of IFNγ spots

compared to ILC3-sufficient mice in nearly every peptide assessed; however, these responses only crossed the 2-fold threshold of a positive response for peptides 81[1] and 92, which correspond to the HBs$_{321-335}$ and HBs$_{207-215}$ peptides described in Chapter 1, the former being MHCII-restricted and the latter a previously published MHCI-restricted epitope (*17*) (**Fig. 3.8 A**). Notably, the CD4+ T cell IFNγ response to peptide 81 was greatly diminished in ILC3-deficient mice compared to ILC3-sufficient mice, while the CD8+ T cell response to 92 was proportionally equivalent to baseline (256% ILC3-deficient vs. 264% ILC3-sufficient). These data suggest that while there were more IFNγ+ CD4+ T cells detected by flow cytometry (**Fig 3.7 B**), there were not more IFNγ+ cells responding to MHCII-restricted epitopes, indicating a portion of the IFNγ+ CD4+ T cells detected by flow cytometry are likely HBV non-specific. These two peptides, 81 and 92, are by far the most common responses we detect in our model, with 81 (FGKFLWEWASARFSW) often appearing earlier and stronger than 92 (VWLSVIWM), while 92 persists longer and usually elicits its strongest responses at later time points. Peptide 82 is partially overlapping with 81 and Jean Publicover in our laboratory has since shown that the shared sequence between both peptides contains a portion of the dominant epitope that is completely contained within peptide 81 and explains why 81 is a stronger CD4+ T cell activator than 82. ILC3-sufficient animals also showed a positive response for peptide 32, which contains the MHCII-restricted epitope referred to as HBs$_{126}$ and described in Chapter 1. ILC3-sufficient mice also had a response to peptide 47, which we have occasionally seen come up as the source

---

[1] Peptides were originally numbered when 15-mers with 11 amino acid overlapping sequences were created spanning the entire HBV envelope coding sequence such that peptide 1 began at the N-terminus and 95 ended at the C-terminus.

of a sub-dominant epitope during earlier responses (<30 days); however, we do not know the MHC restriction or specific sequence of the epitope.

Two weeks later on day 22, we observed that ILC3-deficient mice still had an elevated basal IFNγ response without stimulation, which may reflect a continued response to HBV antigens *in vivo* (**Fig. 3.8 B**). However, by this time we noted that ILC3-deficient mice begin to have stronger responses to more peptides, including 72 and 190. Peptide 190 is very similar to peptide 88 and represents the fourth dominant epitope that we often find strong IFNγ responses against in our model; it was previously published to be a MHCI-restricted epitope (SILSPFLPL) (*17*). We have limited evidence that peptide 72 IFNγ responses are likely due to CD4+ T cells and thus presumably a MHCII-restricted epitope, but it does not appear as often as some of the other responses and we have not validated this. Notably, the strength of the CD4+ T cell MHCII-restricted peptide 81 response is still greatly diminished at this day 22 time point.

One week later, by day 29, we observed that the baseline IFNγ response that was elevated initially in ILC3-deficient mice was reduced (**Fig. 3.8 C**). In this experiment we found ILC3-deficient mice mounted a robust HBV antigen-specific response to multiple MHCII- and MHCI-restricted epitopes. Consistent with earlier time points, however, we observed that ILC3-deficient mice still have a blunted response to three of the four dominant peptides, 32, 81, and 92. Finally, five months out, we noted that both groups mounted proportionally similar IFNγ responses with peptide 92 being the only antigen-driven IFNγ response observed in both groups (**Fig. 3.8 D**).
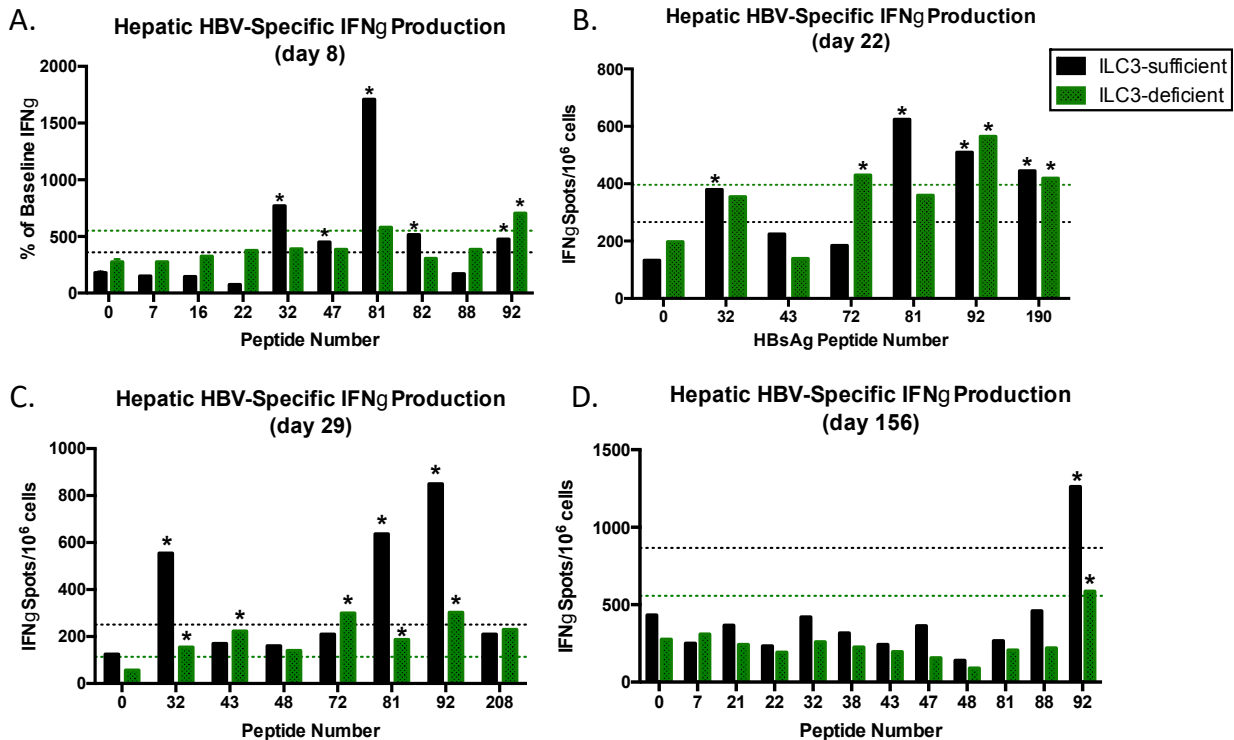
Figure 3.8. ILC3-deficient mice have blunted early antigen-specific IFNγ T cell responses and a sustained impaired CD4+ T cell response to the dominant MHCII-restricted epitope. Hepatic leukocyte fractions were enriched from adult (>8 wks) HBVtg*Rag1*-/- (ILC3-sufficient) and *Rorc*(γt)GFP/GFPHBVtg*Rag1*-/- (ILC3-deficient) animals (**A**) eight days, (**B**) 22 days, (**C**) 29 days, and (**D**) 156 days after adoptive transfer with HBV-naïve splenocytes. 10_5 liver leukocytes were mixed in a 1:1 ratio with splenocytes from *Rag1*-/- mice as a source of APCs and stimulated overnight at 37°C together with individual peptides derived from the HBV envelope protein (HBsAg peptides) in ELISpot plates pre-coated with anti-IFNγ antibodies. "0" peptide denotes no peptide added. ELISpot plates were counted and analyzed with a CTL Immunospot plate reader and software. The threshold defining a positive response, marked with a *, is ≥2× the baseline (dashed line). N=pooled from ≥4 mice per group.

Taken together, the IFNγ ELISpot data suggest that IFNγ-producing hepatic immune cells from ILC3-deficient mice may be overall more sensitized to produce IFNγ, but with a diminished contribution from antigen-specific cells, particularly CD4+ T cells illustrated by the blunted 32 and 81 peptide responses. As time progressed the amount of basal IFNγ produced by *ex vivo* hepatic lymphocytes decreased and a more robust antigen-specific T cell response was observed. Interestingly, at each time point there was a notable decrease in peptide 81 responses both in total number and as a percentage of baseline indicating a significant defect in priming or survival

of this dominant HBV antigen-restricted CD4+ T cell subset. This highlights a major defect in ILC3-deficient mice that may contribute to the inability of these mice to clear HBV antigens.

We know that Tfh cells and their production of IL-21 are essential for effective immunity against HBV, so I examined whether Tfh differentiation was defective in ILC3-deficient animals to help explain their impaired antigen clearance. To my surprise, I initially found that not only were there a greater number of CXCR5+ PD1+ ICOS+ CD4+ Tfh in ILC3-deficient mice at day 8 during early immunity, but a similar percentage of CD4+ T cells had a Tfh phenotype (**Fig. 3.9 A-B**). Additionally, I also detected significantly higher expression of *Il21* mRNA transcripts in RNA isolated from hepatic lymphocytes (**Fig. 3.9 C**). Together these data showed that ILC3-deficient animals had enhanced, rather than impaired, early Tfh responses. However, this response was not durable. When I examined a later time point, one month out, I observed that there was a marked reduction in the frequency of CD4+ Tfh cells in ILC3-deficient mice (**Fig. 3.9 D-E**). ILC3-sufficient mice showed a distinct expansion of their hepatic Tfh population by both total number and percentage of total CD4+ T cells between day 8 and day 29; however, this expansion did not occur in ILC3-deficient animals (**Fig. 3.9 D-E**). These data fit with the earlier assessment of CD4+ T cells, such that there seems to be an early robust response of CD4+ T cells, which is likely in part HBV non-specific, followed by a reduction in overall inflammation that gives way to a CD4+ T cell compartment that is lacking in its ability to respond to selected HBV antigens and maintain memory populations. Thus, I hypothesize that the earlier burst of hepatic Tfh cells in ILC3-deficient mice is possibly directed towards non-HBV antigens, while the HBV-specific Tfh response that normally develops over time in the presence of ILC3s does not occur when these cells are lost, ultimately resulting in impaired Tfh differentiation, which we know to be an essential population in hepatitis B viral control.
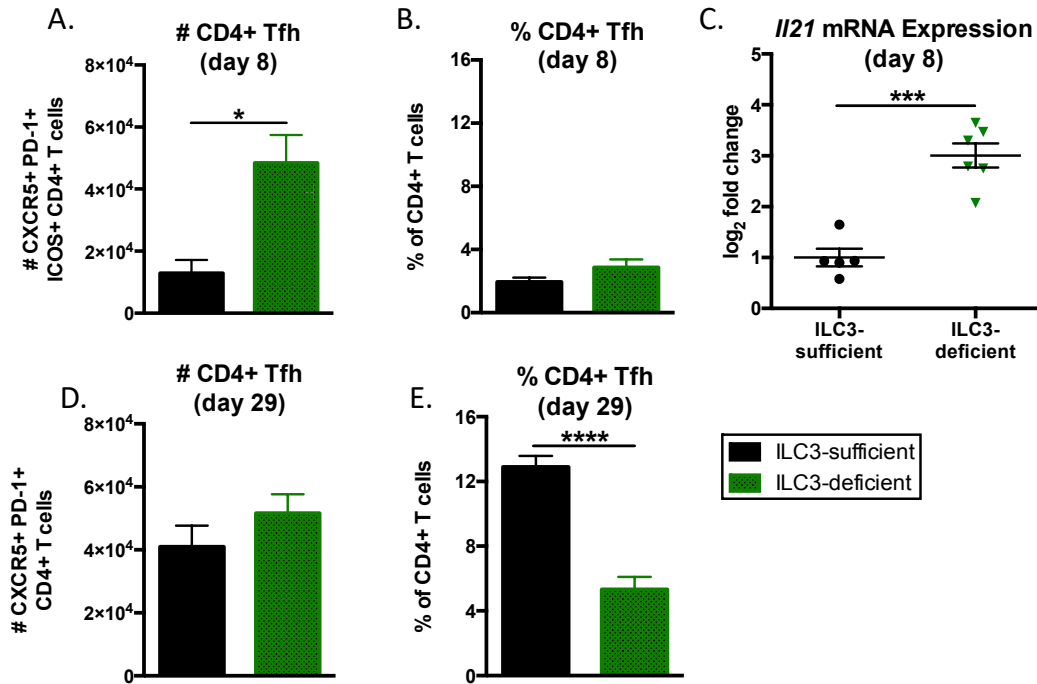
Figure 3.9. ILC3-deficient mice have robust early hepatic Tfh response with an impaired ability to sustain the response. Hepatic leukocyte fractions were enriched from adult (>8 wks) HBVtg*Rag1*-/- (ILC3-sufficient) and *Rorc*(γt)GFP/GFPHBVtg*Rag1*-/- (ILC3-deficient) animals 8 days and 29 days after adoptive transfer with HBV-naïve splenocytes. Total numbers (**A, D**) and percentage (**B, E**) of CD4+ T follicular helper cells (CD45+ TCRβ+ CD4+ CXCR5+ PD-1+) on day 8 (**A-B**) and day 29 (**D-E**). (**C**) Fold-change expression of *Il21* mRNA transcripts relative to *Gapdh* in RNA isolated from hepatic leukocyte-enriched cell preparations on day 8. Data were analyzed using FlowJoᴛᴍ Software; statistics determined by unpaired two-tailed t-test with GraphPad Prism Software; * p<0.05, n≥5 per group.

Considering ILC3-deficient animals were impaired in their ability to produce anti-HBs antibodies (**Fig 3.1 D-E**), I wondered whether there might be a general impairment in their B cell responses to HBV. Despite seeing increases in percentages of B cells at an early time point (**Fig 3.2 D**), we know that this response often takes several weeks to develop. For these experiments I chose to evaluate B cell responses at day 22 rather than day 8. Similar to day eight, I detected an increase in the total number and percentage of B cells in ILC3-deficient mice at day 22 (**Fig 3.10 A-B**). I went on to characterize the expression of IgM and several IgG isotypes to determine if class-switching was impaired, as our group previously demonstrated class-switching correlated with Tfh cell responses and HBV clearance (*9*). I noted that while there was an increase in the

number of non-class-switched IgM+ CD44$_{hi}$ B cells, there were also increases in the IgG1+ and IgG3+ B cells with a similar trend towards increased IgG2b+ B cells, suggesting that class-switching in general was not impaired by ILC3-deficiency (**Fig 3.10 C**). In the B cell fraction of these ILC3-deficient mice, there was a trend towards more IgM and less IgG subtypes, supporting the idea that there is enhanced expansion of less functionally mature B cells in these mice compared to controls. An important caveat of this staining experiment is that I did not determine the antigen-specificity of these B cells, and thus it remains possible that class-switching of HBV-specific B cells could be limited. Indeed, it wasn't until day 29 that I detected defects in Tfh cell accumulation and thus, it is reasonable to predict that a delayed defect in B cell activity may also coincide with a loss of Tfh cells. A colleague in the lab is currently working on developing an assay to detect antigen-specific B cells by flow cytometry and ELISpot according to recently published protocols and we hope to use these methods to assess the frequency of HBV-specific B cells (*77, 78*). These data will help us better understand whether the B cell immunoglobulin class switching that occurs in ILC3-deficient mice is occurring within HBV-specific B cells. We know from anti-HBs antibody titer ELISAs that ILC3-deficient mice are impaired in production of total anti-HBs antibodies, and so it will be important to understand whether the defect in antibody is a result of fewer antigen-specific B cells, their ability to class-switch, or their ability to functionally secrete antibody.

We also performed immunohistochemistry tissue staining with anti-B220, -CD3, and -CD11b antibodies to visualize the distribution of B cells within the liver relative to T cells and myeloid cells. In ILC3-sufficient mice, we detected B cells dispersed throughout the tissue and often associating with small clusters of other CD3+ and CD11b+ immune cells (**Fig. 3.10 D-E**). In the ILC3-deficient mice, however, we observed distinct and well-organized clusters of B cells,

both alone and with other CD11b+ cells and CD3+ T cells (**Fig. 3.10 F-G**). These clusters were often associated with portal tracts, rather than distributed throughout the parenchyma, and were reminiscent of organized tertiary lymphoid structures. We will use the Ilastik imaging pipeline discussed earlier to more specifically characterize these differences. The absence of these B cell structures in ILC3-sufficient mice that are capable of anti-HBs seroconversion, suggests that these structures are not required for effective HBV immunity and may be counterproductive. Furthermore, the presence of increased B cells and IgG+ cells in the ILC3-deficient animals may indicate that the B cell structures that do form do not represent an HBV-specific response, as we cannot detect anti-HBs antibodies in mice that form the B cell aggregates.

B220 CD3 CD11b
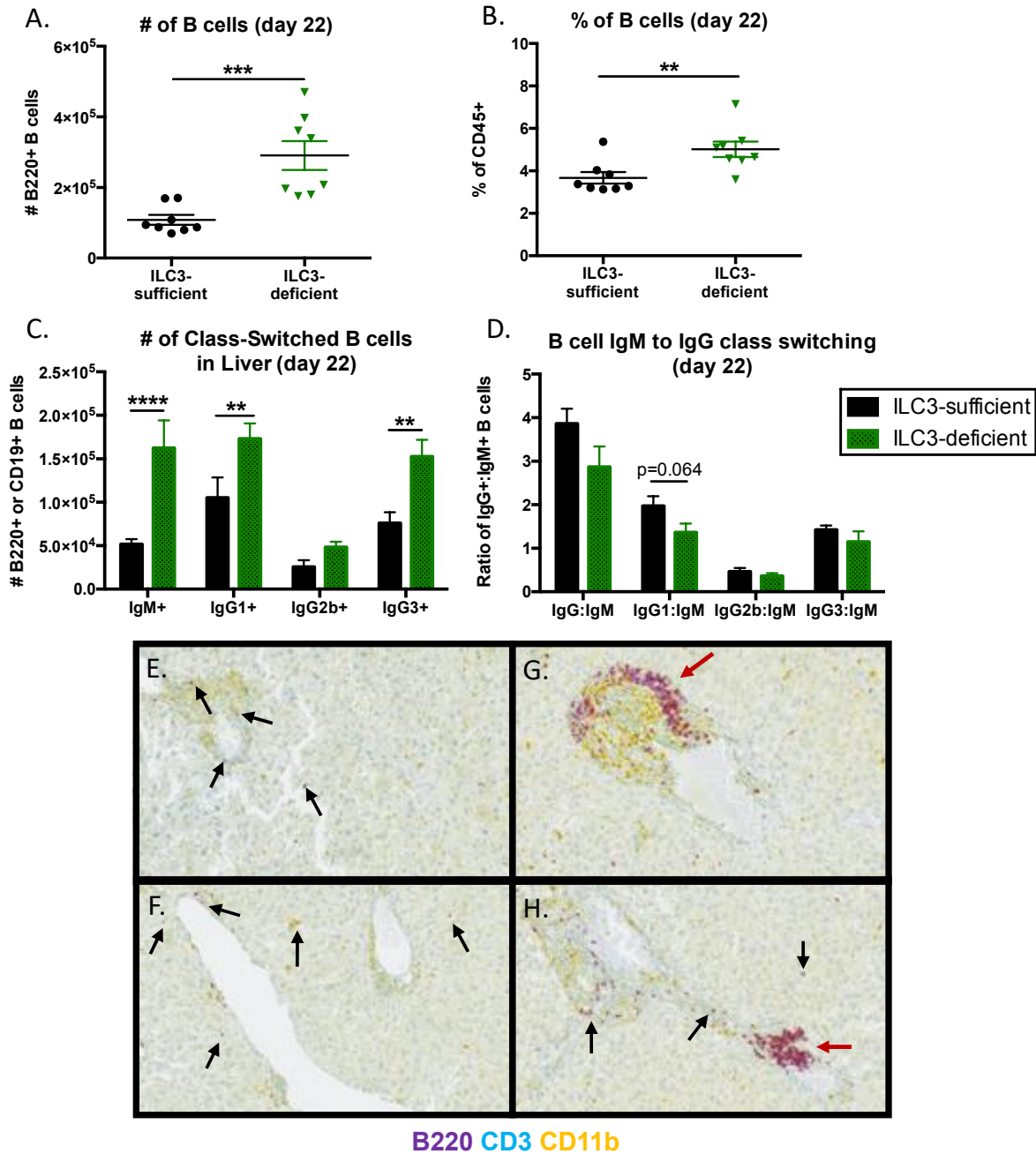
Figure 3.10. ILC3-deficient mice have robust early hepatic B cell responses with evidence of organized lymphoid structures. Hepatic leukocyte fractions were enriched from HBVtg*Rag1-/-* adult (>8 wks) HBVtg*Rag1-/-* (ILC3-sufficient) and *Rorc*(γt)GFP/GFPHBVtg*Rag1-/-* (ILC3-deficient) animals 22 days after adoptive transfer with HBV-naïve splenocytes. Total numbers (**A**) and percentage (**B**) of B cells (CD45+ TCRβ- CD11c- Gr1-+ B220+). (**C**) Total numbers of IgM+ and IgG1+, IgG2b+, and IgG3+ class-switched B cells of unidentified antigen-specificity. ILC3-sufficient (**D-E**) and ILC3-deficient (**F-G**) 4 μm FFPE liver sections were stained with anti-CD45R (B220; purple), anti-CD3e (teal), and anti-CD11b (yellow). Black arrows point to individual or small clusters of B220+ cells; red arrows point to large B cell clusters. Data were analyzed using FlowJoᴛᴍ Software; statistics determined by unpaired two-tailed t-test with GraphPad Prism Software; * p<0.05, n=8 per group.

After noticing a profound amount of inflammation within the ILC3-deficient mice that are unable to clear HBV antigens, I suspected that a portion of the inflammation we observed might be due to HBV non-specific responses. I became aware of a handful of studies that suggested other groups have observed some similar phenotypes within *Rorc*(γt)-/- and *Rorc*(γt)-/- Rag-/- mice, which manifested as splenomegaly, increased CD4+ T cell frequency, and disrupted gut microbial communities leading to increased colitis susceptibility and pathology (*35, 69, 79*). We also know that changes within the innate immune compartment are sufficient to drive an effective or ineffective response, as the age of the recipient hepatic immune environment in HBVtg*Rag1*-/- mice dictates disease outcome, regardless of the age of the donor adaptive immune cells. Thus, in addition to the possibility of indirect effects due to changes in the microbiota of ILC3-deficient mice, we also wondered whether the loss of ILC3s may directly impair the maturation of innate lymphocytes and myeloid cells that play a critical role in priming the adaptive immune response.

In order to identify changes in the innate immune compartment within ILC3-deficient mice, I performed flow cytometry and qPCR to assess myeloid populations and their expression of relevant genes at baseline (day "0") in *Rorc*(γt)GFP/GFP*Rag1*-/- and *Rag1*-/- mice in the absence of the HBV transgene and without adoptive transfer of WT splenocytes. I observed a total increase in the number of hepatic CD45+ immune cells in ILC3-deficient mice **(Fig. 3.11 A)**. This increase was due to an increase in most myeloid lineage cells without an increase in NK cells **(Fig. 3.11 B-H)**. When looking proportionally at the differences in the percentage of each population relative to the total pool of CD45+ cells in the liver, there was a decrease in both mature CD11b+ and immature CD11b- NK cells **(Fig. 3.11 B)** and an increase in dendritic cells **(Fig 3.11 D)**, monocytes **(Fig. 3.11 G-H)**, and monocyte-derived macrophages **(Fig. 3.11 E)**.

These data indicate that there is a substantial expansion of myeloid populations in the liver in the absence of ILC3s, with a notable lack of NK cell expansion and/or recruitment to the liver.
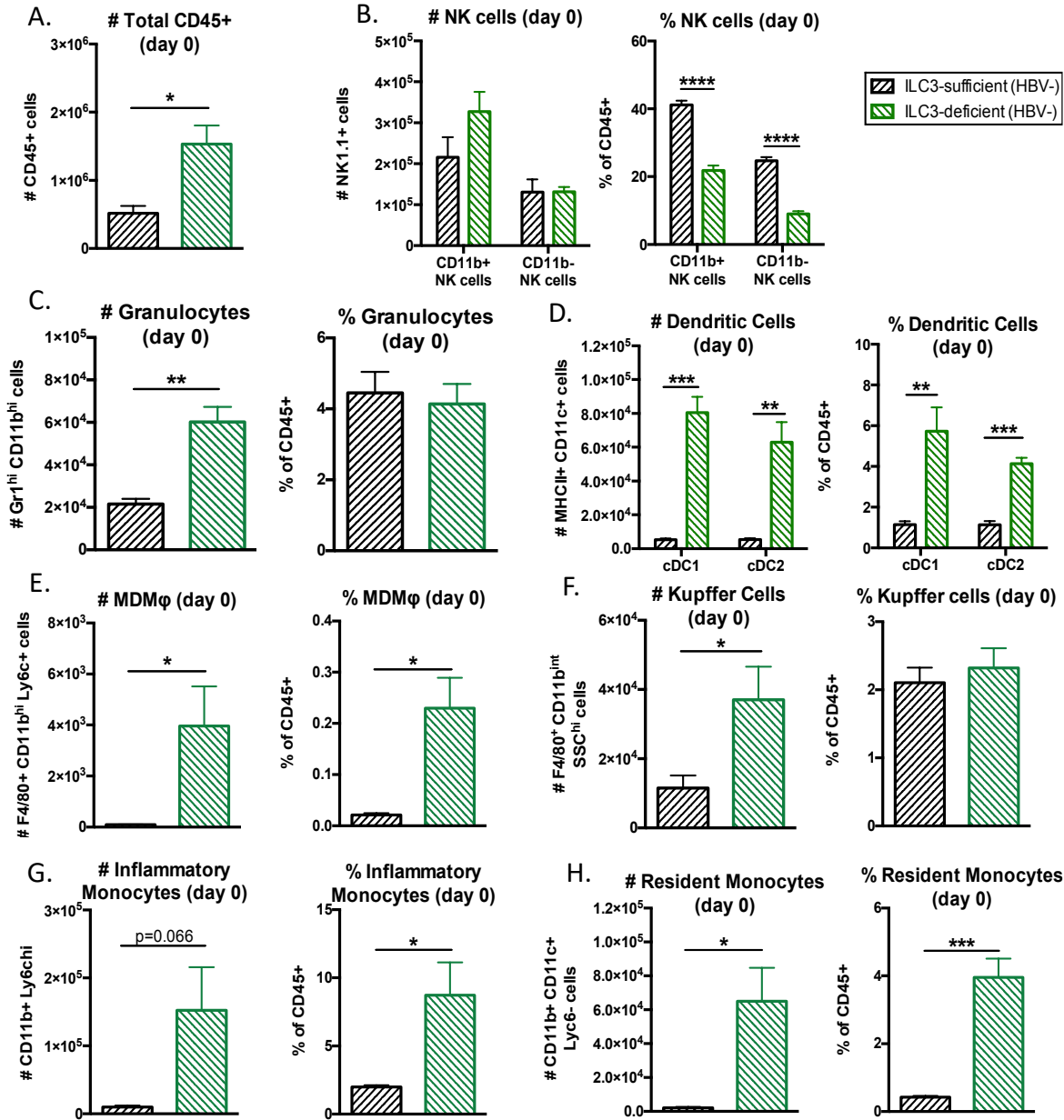
Figure 3.11. ILC3-deficieny causes changes in hepatic innate immune populations at baseline prior to adoptive transfer. Hepatic leukocyte fractions were enriched from adult (>8 wks) HBVtg*Rag1-/-* (ILC3-sufficient) and *Rorc*(γt)GFP/GFPHBVtg*Rag1-/-* (ILC3-deficient) animals eight days after adoptive transfer with HBV-naïve splenocytes. Flow cytometry was used to identify and quantitate numbers and percentages of myeloid cell populations as follows: (**A**) CD45+ (Live CD45+), (**B**) NK cells (Live CD45+ NK1.1+ CD11b+/-), (**C**) granulocytes (Live Gr1+ CD11b+), dendritic cells (DCs; Live CD11c+ MHCII+), further subdivided in to classical dendritic cell subsets 1 (cDC1; CD11b-) and 2 (cDC2;

117

CD11b+), (**D**) monocytes (Live CD11b+ NK1.1- MHCII$_{lo/-}$ SSC$_{lo}$), and (**E**) monocyte derived macrophages (MDMφ; Live F4/80+ CD11b$_{hi}$ Ly6c$_{+/hi}$ MHCII$_{hi/+}$ or MHCII$_{+/lo}$). (**F**) Kupffer cells (Live F4/80+ CD11b$_{int}$ SSC$_{hi}$ Ly6c-), (**G**) inflammatory monocytes (Live CD11b$_{hi}$ Ly6c$_{hi}$ CD11c- NK1.1- MHCII$_{lo/-}$ SSC$_{lo}$), (**H**) resident monocytes (Live CD45+ CD11b+ Ly6c$_{lo/-}$ CD11c+ NK1.1- MHCII$_{lo/-}$ SSC$_{lo}$). Data were analyzed using FlowJo™ Software; statistics determined by unpaired two-tailed t-test with GraphPad Prism Software; * p<0.05, ** p<0.01, *** p<0.001; n=4 per group.

Using qPCR and flow cytometry of hepatic leukocyte-enriched cell preparations, I assessed the expression of molecules we previously identified to play a role in effective anti-HBV immunity and those with known roles in supporting priming of adaptive immune cells. I did not observe any changes in the expression level of *Cxcl13*, a chemokine that is critical for recruitment of CXCR5+ Tfh and B cells, which we have shown to have increased levels in adult animals that control HBV relative to young animals, and for which we have some evidence of regulation by commensal gut microbes (**Fig 3.12 A**; (*14*) and unpublished). We did observe markedly increased expression of *Ox40l*, which, as described in Chapter 1, also plays an essential role in the activation of CD4+ T cells, including Tfh, and in control of viral antigens [**Fig. 3.12 A**; (*15*)]. I did not detect any differences in MHCII (*I-A$_{k/b}$*) or the co-stimulatory molecule *Cd86* by mRNA transcript levels (**Fig. 3.12 A**). However, when analyzed by flow cytometry, I did observe an increase in the median fluorescence intensity (MFI) of MHCII on total MHCII+ myeloid cells, as well as specifically on dendritic cells, and to a lesser degree on Kupffer cells, with a trend towards decreased MHCII expression on monocyte-derived macrophages (**Fig. 3.12 B**). These data suggest that MHCII expression is partially regulated post-transcriptionally in this context. Consistent with the qPCR data, I also observed an increased total number of OX40L+ innate immune cells; however, there was no increase in the MFI of OX40L on any antigen-presenting myeloid cells, indicating increased accumulation of OX40L+ cells without an increase in the expression level of OX40L within individual cells (**Fig. 3.12 C**).
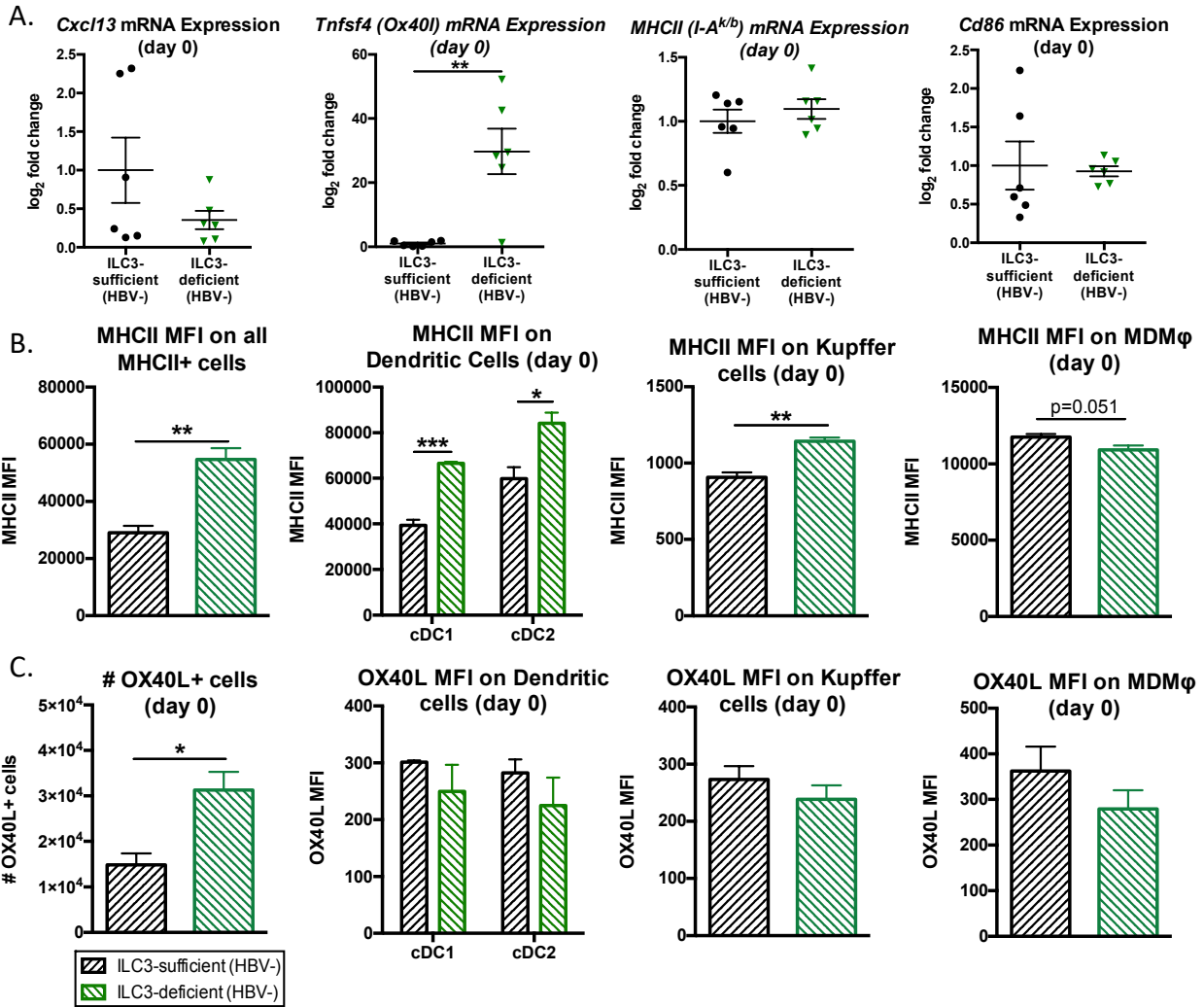
Figure 3.12. ILC3-deficieny causes increased expression of antigen presentation and co-stimulatory molecules. Hepatic leukocyte fractions were enriched from adult (>8 wks) *Rag1-/-* (ILC3-sufficient HBV-) and *Rorc*(γt)GFP/GFP*Rag1-/-* (ILC3-deficient HBV-) animals without the HBV transgene, at baseline (no B, T, or NK T cells present). (**A**) Fold-change expression of *Cxcl13*, *Tnfsf4* (Ox40l), *I-Ak/b* (MHCII), and *Cd86* relative to *Gapdh* was measured in RNA extracted from hepatic leukocyte-enriched cell preparations. (**B**) MHCII protein expression level was measured by flow cytometry and reported as median fluorescence intensity on total MHCII+ cells (Live CD45+ MHCII+), dendritic cells (Live CD11c+ MHCII+ and CD11b- cDC1 or CD11b+ cDC2), Kupffer cells (Live F4/80+ CD11bint SSChi Ly6c-), and monocyte-derived macrophages (MDMφ; Live F4/80+ CD11bhi Ly6c+/hi MHCIIhi/+ or MHCII+/lo). (**C**) The number and percentage of OX40L+ innate immune cells was measured along with the MFI of OX40L on dendritic cells, Kupffer cells, and MDMφ. Data were analyzed using FlowJoTM Software; statistics determined by unpaired two-tailed t-test with GraphPad Prism Software; * p<0.05, ** p<0.01, *** p<0.001; n=7 per group.

Taken together, there was an increased number and relative frequency of phagocytic and antigen-presenting cells, as well as an increase in the expression of antigen presentation and co-stimulatory molecules, suggesting that there may be underlying innate immune stimulation in ILC3-deficient mice. Thus, it is possible that these changes could increase the priming potential and inflammatory milieu within the liver such that the hepatic environment of ILC3-deficient mice favors rapid immune cell activation upon adoptive transfer of splenocytes into HBV transgenic animals, regardless of the ability of ILC3-deficient mice to sustain that response in a way that directs successful HBV immunity.

In light of the observation of increased OX40L expression at baseline in ILC3-deficient mice, we wondered whether an OX40L/OX40 interaction was contributing to the robust expansion of CD4+ T cells in ILC3-deficient mice, and also wondered what portion of this CD4+ T cell skewing might be due to non-HBV antigens. In order to address this question we performed an adoptive transfer experiment comparing early immune responses in the following four groups of mice: (i) HBVtg*Rag1-/-* mice transferred with WT splenocytes [ILC3-sufficient HBV+ (WT)], (ii) *Rorc*(γt)GFP/GFPHBVtg*Rag1-/-* mice transferred with WT splenocytes [ILC3-deficient HBV+ (WT)], (iii) *Rorc*(γt)GFP/GFPHBVtg*Rag1-/-* mice transferred with *Ox40-/-* splenocytes [ILC3-deficient HBV+ (*OX40-/-*)], and (iv) *Rorc*(γt)GFP/GFP*Rag1-/-* mice without the HBV transgene, transferred with WT splenocytes [ILC3-deficient HBV- (WT)]. I assessed the frequency of major hepatic and splenic immune populations eight days after adoptive transfer of each group and compared the results of each group to the ILC3-deficient HBV+ (WT) mice to determine the role of OX40 and the HBV transgene in the phenotype of ILC3-deficient mice. In this experiment, I observed no differences in the total number of CD45+ cells in either the spleen or liver of any group; however, there was a trend towards fewer cells in the HBV- group in the

liver only (**Fig. 3.13 A**). I detected no significant differences in the total number of T cells, but there was a reduction in the percentage of T cells in the liver of ILC3-deficient mice compared to ILC3-sufficient mice that was not affected by the loss of OX40 or absence of the HBV transgene, indicating the total reduction of T cells in ILC3-deficient mice is OX40-independent and HBV-independent (**Fig. 3.13 B-C**). When examining hepatic B cell populations I observed that ILC3-deficiency led to increased accumulation of CD19+ B cells that was HBV-dependent in the liver, but not in the spleen, as ILC3-deficient HBV– mice had a reduced number of B cells relative to ILC3-deficient HBV+ mice in the liver but not in the spleen (**Fig 3.13 D-E**).
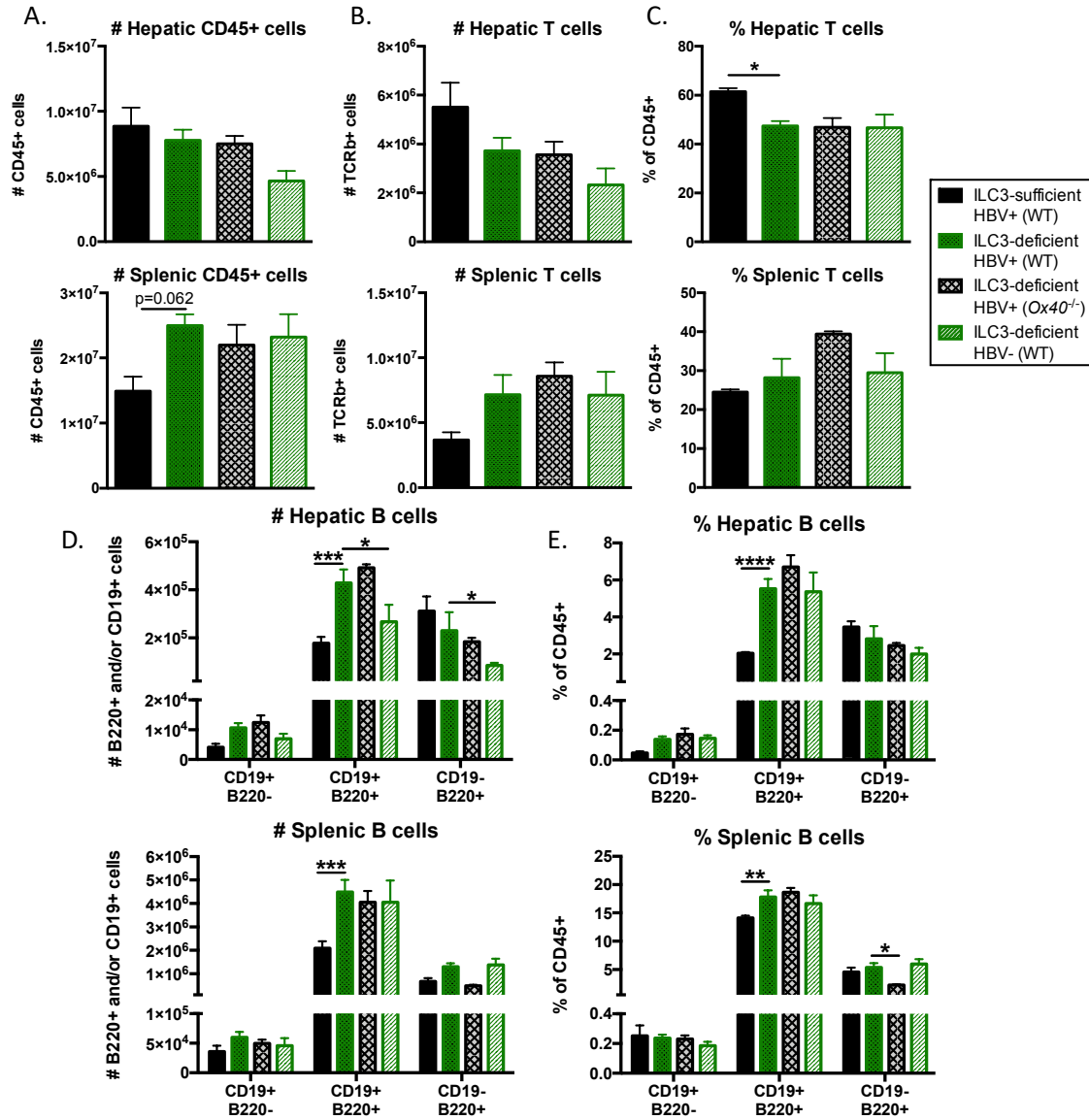
Figure 3.13. ILC3-deficieny leads to OX40-independent and HBV-independent reduction in hepatic T cell accumulation and HBV-dependent B cell expansion in the liver. Hepatic leukocyte fractions were enriched from adult (>8 wks) HBVtg*Rag1-/-* mice transferred with WT splenocytes [ILC3-sufficient HBV+ (WT)], *Rorc*(γt)GFP/GFPHBVtg*Rag1-/-* mice transferred with WT splenocytes [ILC3-deficient HBV+ (WT)], *Rorc*(γt)GFP/GFPHBVtg*Rag1-/-* mice transferred with *Ox40-/-* splenocytes [ILC3-deficient HBV+ (*OX40-/-*)], and *Rorc*(γt)GFP/GFP*Rag1-/-* mice without the HBV transgene transferred with WT splenocytes [ILC3-deficient HBV- (WT)] on day eight post-adoptive transfer with HBV-naïve WT splenocytes. (**A**) The number of hepatic (top) and splenic (bottom) CD45+ cells was measured by flow cytometry, as well as the number and percentage of hepatic (top) and splenic (bottom) (**B-C**) T cells (CD45+ TCRβ+) and (**D-E**) B cells (CD45+ CD19+ and/or B220+). Data were analyzed using FlowJoTM Software; statistics determined by ANOVA with Dunnett's multiple comparison test comparing each group to ILC3-deficient HBV+ (WT) control group (green) with GraphPad Prism Software; * p<0.05, ** p<0.01, *** p<0.001, **** p<0.0001; n≥4 per group.

As expected, ILC3-deficiency led to increased accumulation of CD4+ T cells with a reduction in the number and percentage of CD8+ T cells relative to ILC3-sufficient mice in both the liver and spleen (**Fig. 3.14 A-D**). Interestingly, I noted that either the transfer of *Ox40-/-* splenocytes or the absence of the HBV transgene was able to reverse the increase in the number of CD4+ T cells in ILC3-deficient mice compared to ILC3-sufficient mice (**Fig. 3.14 A**). In the spleen, there was also an increase in the number of CD4+ T cells in ILC3-deficient mice with a trend towards a reduction of CD4+ T cells when the ILC3-deficient mice received *Ox40-/-* splenocytes, though the absence of the HBV transgene did not affect the number of CD4+ T cells in the spleen (**Fig. 3.14 C**). I observed a similar but reciprocal pattern for CD8+ T cells, such that ILC3 deficiency normally reduces CD8+ T cell numbers in the liver after adoptive transfer with WT splenocytes, but with the transfer of *Ox40-/-* splenocytes, the number of CD8+ T cells increased back to similar levels seen in ILC3-sufficient mice (**Fig. 3.14 A, C**). With regard to the percentages of CD4+ versus CD8+ T cells, it was clear that the accumulation of CD4+ T cells that occurs in ILC3-deficient mice in both the liver and the spleen was dependent on an OX40/OX40L interaction (**Fig. 3.14 B, D**). Although I determined that the presence of the HBV transgene may be important in the magnitude of total T cell accumulation in the liver, the skewing towards CD4+ T cells in ILC3-deficient mice occurred independently of the presence or absence of the HBV transgene, supporting the notion that there was a degree of CD4+ T cell expansion that occurs that is HBV non-specific. Together these data indicate that total CD4+ T cell accumulation in the liver is OX40-dependent and HBV-dependent, but that skewing towards a greater percentage of CD4+ T cells over CD8+ T cells still occurs in the absence of HBV. Therefore, we conclude that ILC3s in the liver function in part to restrict OX40L expression by myeloid cells, and in turn, limit CD4+ T cell expansion as a whole, specifically to non-HBV

antigens. However, based on the decreased number of CD4+ T cells in the liver of HBV– ILC3-deficient mice relative to HBV+ mice, HBV drives additional CD4+ T cell accumulation in the liver even in the absence of ILC3s. My ELISpot data and day 29 experiments, however, suggest that the HBV-driven CD4+ T cells in these animals are still impaired in their ability to generate productive and sustained IFNγ and Tfh cell responses.
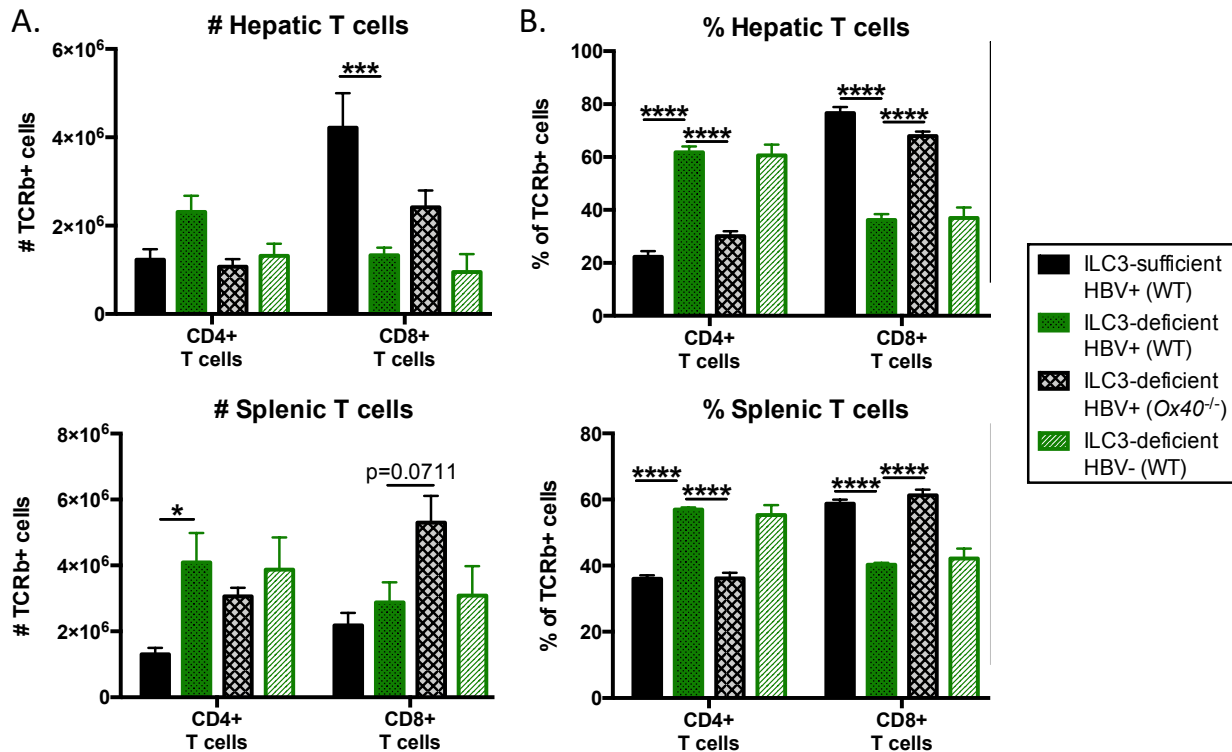
Figure 3.14. ILC3-deficieny leads to OX40-dependent and HBV-independent skewing of T cells towards CD4+ instead of CD8+ T cells in the liver and spleen. Hepatic leukocyte fractions were enriched from adult (>8 wks) HBVtg*Rag1*-/- mice transferred with WT splenocytes [ILC3-sufficient HBV+ (WT)], *Rorc*(γt)GFP/GFPHBVtg*Rag1*-/- mice transferred with WT splenocytes [ILC3-deficient HBV+ (WT)], *Rorc*(γt)GFP/GFPHBVtg*Rag1*-/- mice transferred with *Ox40*-/- splenocytes [ILC3-deficient HBV+ (*OX40*-/-)], and *Rorc*(γt)GFP/GFP*Rag1*-/- mice without the HBV transgene transferred with WT splenocytes [ILC3-deficient HBV- (WT)] on day eight post-adoptive transfer with HBV-naïve WT splenocytes. (**A, C**) The number and (**B, D**) percentage of hepatic (**A-B**) and splenic (**C-D**) CD4+ and CD8+ CD45+ TCRβ+ T cells was measured by flow cytometry. Data were analyzed using FlowJoTM Software; statistics determined by ANOVA with Dunnett's multiple comparison test comparing each group to ILC3-deficient HBV+ (WT) control group (green) with GraphPad Prism Software; * $p<0.05$, ** $p<0.01$, *** $p<0.001$, **** $p<0.0001$; n≥4 per group.

We performed tissue staining and imaging with anti-CD8α and anti-CD4 to visualize the impact that *Ox40-/-* donor splenocytes or the absence of the HBV transgene had on differences in CD4+ and CD8+ T cell localization in ILC3-deficient mice during this early immune period. We noted that similar to the ILC3-deficient mice that received WT splenocytes (**Fig. 3.4 D-F**), ILC3-deficient mice that received *Ox40-/-* splenocytes also had profound periportal inflammation; however, there was a much greater representation of CD8+ T cells compared to CD4+ T cells in these animals, both within immune cell clusters, as well as distributed throughout the liver parenchyma (**Fig. 3.15 A-B**). These data highlight a role for OX40/OX40L in supporting CD4+ T cell accumulation in the liver, but clearly show that this interaction in not critical for the formation of periportal immune cell clusters in ILC3-deficient mice. In the absence of the HBV transgene, we saw that ILC3-deficient *Rag1-/-* mice that received adoptive transfer of WT splenocytes still generate a surprising amount of periportal, and to a lesser degree, intra-parenchymal, inflammation and immune cluster formation, albeit less dramatic than seen in ILC3-deficient HBV+ animals (**Fig. 3.15 C-D**). Similar to the HBV+ ILC3-deficient mice, we still observed a skewing towards greater CD4+ T cell accumulation in the HBV– ILC3-deficient mice than what we detected for ILC3-sufficient (**Fig. 3.4 A-C)** or ILC3-deficient mice that received *Ox40-/-* splenocytes (**Fig. 3.15 A-B**). These data indicate that the absence of ILC3s drives hepatic immune cell clustering – that is mostly restricted to periportal tissue regions – after adoptive transfer, independently of an OX40/OX40L interaction and independently of HBV antigen expression in the liver. These data suggest that the loss of ILC3s alone is sufficient to trigger T cell aggregation in the liver; however, the mechanisms that drive this lymphocyte clustering are still unclear. We will continue to characterize these differences quantitatively using our Ilastik analysis pipeline.
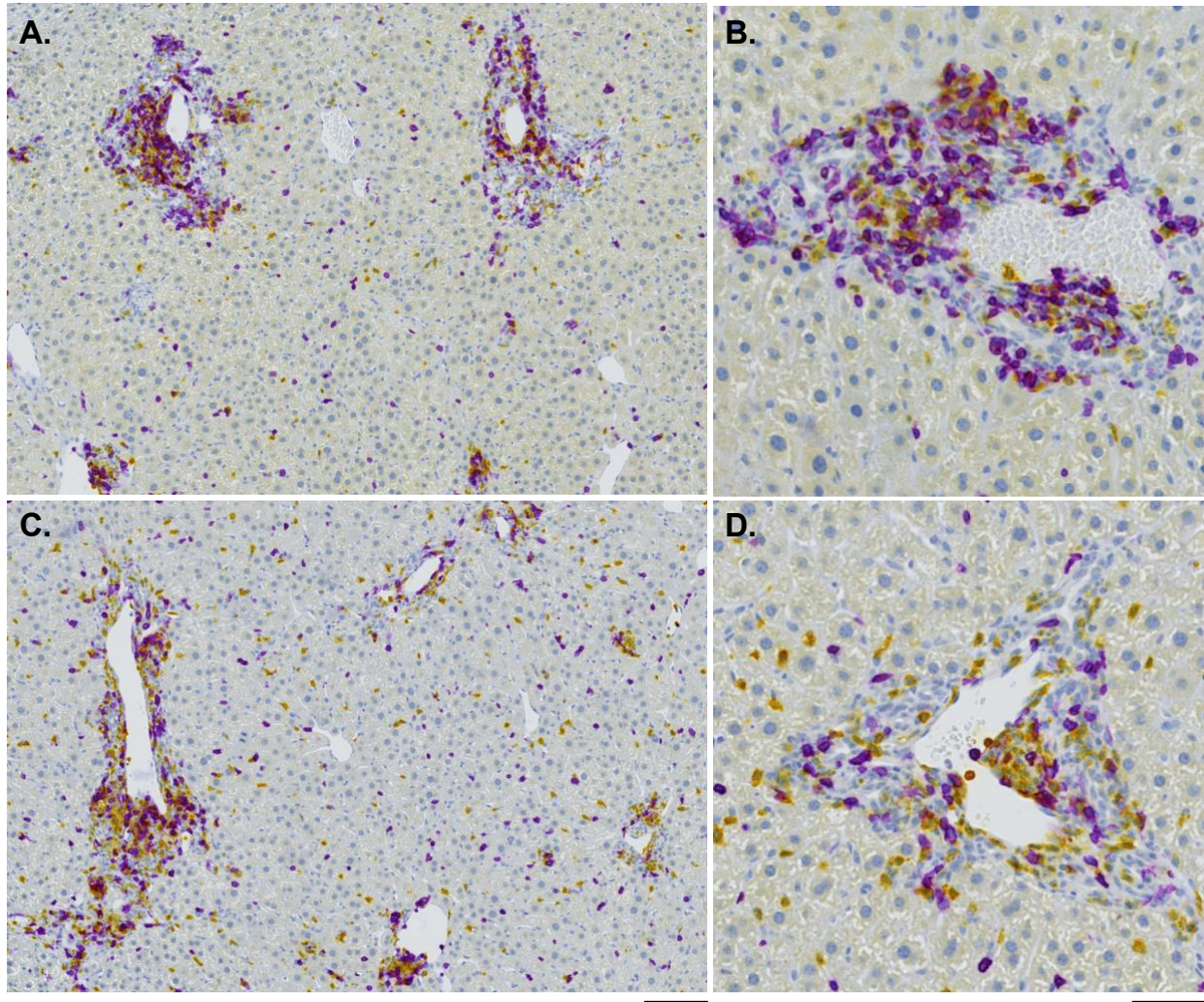
Figure 3.15. Hepatic CD4+ and CD8+ cellular organization in ILC3-deficient mice is partially OX40- and HBV-dependent. Liver tissue was isolated from *Rorc*(γt)GFP/GFPHBVtg*Rag1-/-* ILC3-deficient mice that received *Ox40-/-* splenocytes and (**A-B**) *Rorc*(γt)GFP/GFP*Rag1-/-* ILC3-deficient mice that do not express the HBV transgene (**C-D**) eight days post-adoptive transfer and drop-fixed in formalin for 24 hours, followed by ethanol dehydration and embedding into paraffin wax blocks. FFPE tissue blocks were sectioned at 4 μm and stained with anti-CD4 (yellow), anti-CD8a (purple) using the Ventana Discovery Ultra platform. Stained sections were imaged at 20X resolution with the Zeiss Axioscanner Z1. Scale bars for (**A, C**) represent 100 μm, scale bars for (**B, D**) represent 50 μm.

The data from these day "0" and *Ox40-/-* donor transfer experiments suggest that ILC3-deficiency leads to increased basal accumulation of myeloid antigen-presenting cells ready to prime and activate adaptive immune cells, in particular CD4+ T cells, in an OX40-dependent manner. The early expansion and accumulation of CD4+ T cells occurs independent of HBV antigens and suggests additional sources of T cell priming, potentially via bystander activation of

previous antigen-experienced cells (*80*), or potentially against new microbial antigens not present – or previously anatomically contained – in the wild-type donor mice. Indeed, it has been reported that anti-Thy1 antibody-mediated depletion of ILCs can lead to a loss of containment of bacteria within the gut, and the presence of bacteria and bacterial products can be detected in the liver as a result (*81*). If this were also occurring in our ILC3-deficient recipient mice, these bacteria and their products could provide a source of antigen for CD4+ T cell activation against non-HBV antigens in our model. This may especially be the case if there were opportunistic microbes capable of colonizing ILC3-deficient mice due to a loss of gut immune regulation that would not be present in wild-type mice, from which the donor splenocytes are sourced and thus, did not become tolerized against.

We attempted to address the issue of disrupted microbial colonization by treating ILC3-deficient and ILC3-sufficient HBV+ and HBV- animals with broad spectrum oral antibiotics in the drinking water from gestation through adulthood and monitoring their hepatic inflammation and immune cell localization. I hypothesized that if I could minimize the reported dysbiosis of RORγt-deficient mice that led to CD4+ T cell accumulation through oral antibiotic treatment, as others showed reversed this phenotype, then I might be able to limit one variable that may confound our understanding of the mechanisms of impaired HBV immunity in these ILC3-deficient mice (*35*). I was surprised to find that ILC3-deficient mice continued to have evidence of increased hepatic inflammation, even after weeks of antibiotic administration. ILC3-deficient mice had an increase in the total number of CD45+ immune cells in the liver on day eight post-adoptive transfer, including increases in T cells, B cells, and myeloid cells (**Fig. 3.16 A**). I also found that CD4+ skewing was not affected by antibiotic treatment, as ILC3-deficient mice had a similar increase in CD4+ T cells as was seen in untreated ILC3-deficient mice; however, there

was not a significant block in CD8+ T cell accumulation as was normally seen in the absence of ILC3s (**Fig. 3.16 B** and **Fig. 3.3**). There were also similar changes in the innate immune compartment including a decrease in CD11b+ NK cells and an increase in DCs and inflammatory monocytes, along with an increase in MHCII expression on some myeloid cell populations, as was seen in ILC3-deficient mice that did not receive antibiotics (**Fig 3.16 C-G**).
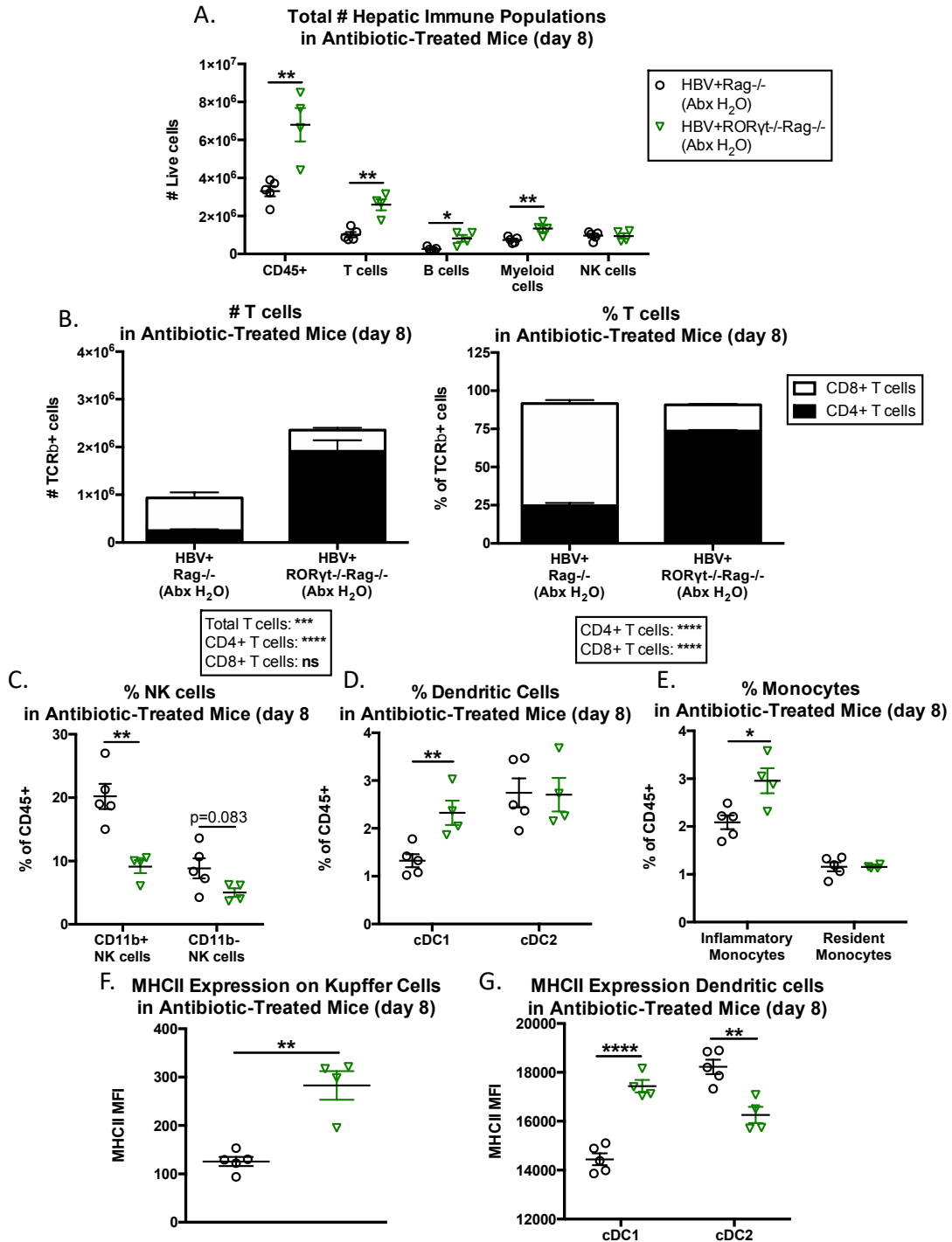
Figure 3.16. Antibiotic treatment of ILC3-deficient mice does not mitigate hepatic immune cell inflammation caused by ILC3-deficiency. Hepatic leukocyte fractions were enriched from adult (>8 wks) HBVtg*Rag1*-/- mice (ILC3-sufficient) or *Rorc*(γt)GFP/GFPHBVtg*Rag1*-/- (ILC3-deficient) mice that were treated with antibiotics in their drinking water [vancomycin (1 g/L), ampicillin (0.5 g/L), neomycin sulfate (1 g/L), and metronidazole (0.5 g/L)] starting during gestation, on day eight post-adoptive transfer with HBV-naïve WT splenocytes. (**A**) The number of hepatic CD45+ cells was measured by flow cytometry, as well as the number and percentage of (**B**) CD4+ and CD8+ T cells (CD45+ TCRβ+ CD4+/-

CD8+/-) and (**C**) NK cells (CD45+ TCRβ- NK1.1+), (**D**) dendritic cells (CD45+ TCRβ+ CD19- CD11c+ MHCII+), and monocytes (CD45+ TCRβ- CD19- CD11b+ NK1.1-). Expression of MHCII was measured as median fluorescence intensity on Kupffer cells (CD45+ TCRβ- CD19- F4/80+ CD11b+ Ly6c- SSChi), Data were analyzed using FlowJo™ Software; statistics determined by unpaired t-test with GraphPad Prism Software; * $p<0.05$, ** $p<0.01$, *** $p<0.001$, **** $p<0.0001$; n≥4 per group.

When looking histologically at tissue from antibiotic-treated ILC3-sufficient and ILC3-deficient animals, we also saw that antibiotic administration did not ameliorate the profound portal inflammation observed in ILC3-deficient animals. In fact, we could see evidence of portal inflammation in both ILC3-sufficient and ILC3-deficient *Rag1*-/- animals that lack the HBV transgene at day 0, without adoptive transfer, though this inflammation was also greatly enhanced in the ILC3-deficient animals (**Fig. 3.17 A-B**). This differs from what we observed in HBV– *Rag1*-/- animals eight days after adoptive transfer, which have very minimal inflammation (data not shown). This suggests that antibiotic treatment itself has led to an increased amount of basal inflammation in both ILC3-sufficient and likely, ILC3-deficient animals. By day 8, we observed that the ILC3-sufficient mice that received antibiotics look similar to non-antibiotic-treated mice, with evidence of modest periportal and intraparenchymal inflammation (**Fig. 3.16 C**). The ILC3-deficient mice that grew up on antibiotic water showed the characteristic dramatic periportal inflammation that is observed in animals without antibiotic treatment. These data suggest that the inflammation that occurs in the absence of ILC3s may not be solely driven by microbiota influences. An important caveat to this interpretation, however, is that I did not assess the microbial burden of these animals – although I have collected the tissue to do so and will follow up on these data to determine how antibiotic treatment may have broadly affected the microbial communities. Indeed, the inflammation present in the ILC3-sufficient *Rag1*-/- mice suggest that perhaps there may be a source of innate immune stimulation present, possibly from an altered, rather than depleted, gut microbial community. Researchers have shown that while antibiotic treatment does initially deplete a large portion of gut bacteria, overtime the community

is repopulated with a shifted composition and that long-term treatment can affect gut barrier

integrity (*82*). Thus, understanding the complex interaction between ILC3s, gut microbiota, and

the effects that antibiotic treatment has on both requires a deeper investigation of the

composition of microbial communities and gut health, beyond the scope of this current project.
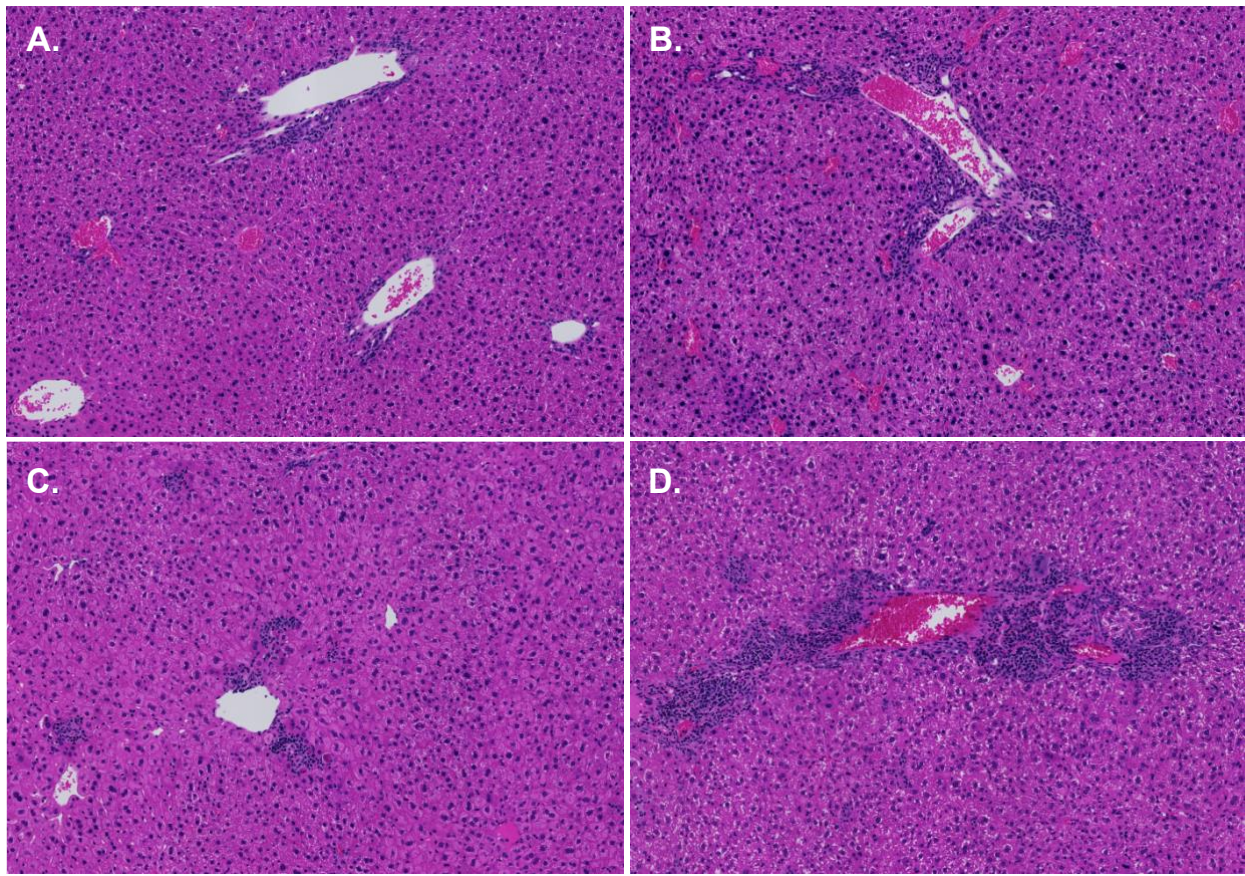
Figure 3.17. Antibiotic treatment of ILC3-sufficient and ILC3-deficient mice alters basal inflammation but does not affect inflammation post immune reconstitution. Liver tissue was isolated from antibiotic-treated *Rag1*-/- ILC3-sufficient (**A**) or *Rorc*(γt)GFP/GFP*Rag1*-/- ILC3-deficient mice (**B**) at baseline (no adoptive transfer) or from adoptively transferred HBVtg*Rag1*-/- ILC3-sufficient (**C**) or *Rorc*(γt)GFP/GFPHBVtg*Rag1*-/- (**D**) mice eight days post transfer and drop-fixed in formalin for 24 hours, followed by ethanol dehydration and embedding into paraffin wax blocks. FFPE tissue blocks were sectioned at 4 μm and stained with hematoxylin (purple/blue) and eosin (pink) using the Ventana Discovery Ultra platform. Stained sections were imaged at 20X resolution with the Zeiss Axioscanner Z1. Scale bars represent 100 μm.

Discussion

We uncovered a major role for ILC3s in supporting productive HBV immunity, as the loss of RORγt+ ILC3 led to impaired HBsAg clearance and seroconversion. Despite a severely impaired anti-HBV immune response, we found that ILC3-deficient mice were not impaired in their ability to drive total immune cell recruitment and inflammation within the liver; however, the immune populations that were recruited in the absence of ILC3s were drastically different compared to ILC3-sufficient mice. The loss of ILC3s led to increased portal inflammation and the formation of large immune cell aggregates, particularly around portal tracts within the liver. These clusters varied both in their immune cell composition, as well as their spatial and organizational aspects, which we are currently in the process of quantitatively assessing through the use of our Ilastik imaging analysis pipeline. We further identified a profound skewing of the T cell compartment towards CD4+ T lymphocytes in the absence of ILC3s, compared to the normally dominant CD8+ T cell accumulation found in mice that do have ILC3s. Although there were many CD4+ T cells present, these cells were unable to support productive anti-HBV immunity. Despite robust early differentiation and production of cytokines by CD4+ T cells in ILC3-deficient mice, evaluation of these cells at later time points revealed this was not a durable response. In particular, ILC3-deficient mice had a reduced frequency of Tfh cells one month after the immune response was initiated. Numerous studies have identified Tfh cells as a critical population for effective HBV immunity, and thus, it is likely that a defect in this subset, both in quantity as well as positional localization, may contribute to the inability of ILC3-deficient mice to control HBV. Furthermore, there was a notable defect in the magnitude of the IFNγ response to the most dominant MHCII-restricted epitope by CD4+ T cells in ILC3-deficient mice. Additionally, there was a reduced frequency of total CD44+ CD62L+ central memory CD4+ T

cells in the absence of ILC3s. Taken together, these data suggest that ILC3s play an important role in supporting the sustained response of HBV-specific CD4+ T cells.

We did not reveal any obvious differences within antigen-presenting cells at early time points that might explain defects in initial priming of CD4+ T cells. We did, however, notice substantial differences in the localization of T cells within the liver. Thus, it is possible that the positional location of T cells relative to antigen-presenting cells, potentially including ILC3s themselves, and the cytokine milieu within that microenvironment, may contribute to sustaining a productive immune response, which becomes disrupted when ILC3s are lost.

Now that we have one HBV tetramer in the lab (MHCII-HBs126), and another three in production at the NIH tetramer core facility, we plan to follow up on the hypotheses raised throughout this chapter by measuring the frequency and function of HBV-specific T cells. Specifically, we will determine whether ILC3-deficient mice have a decreased number of antigen-specific CD4+ T cells, as was suggested by ELISpot data. We will also assess the antigen specificity of Tfh cells at early and late time points to understand whether the initial burst of Tfh, and accompanied B cell responses, are HBV-specific. We will measure antigen-specific CD8+ T cell responses as well, to determine whether the reduction in total hepatic CD8+ T cells also includes a reduced frequency of HBV-specific cells. Finally, we will measure cytokine production, particularly IFNγ, to determine if there are any functional defects in either CD4+ or CD8+ antigen-specific T cells in addition to possible quantitative differences.

Another important focus of our future experiments will include sorting and reconstituting ILC3s before adoptive transfer, to clarify the effects of ILC3s on HBV immunity that may be developmentally related compared to more direct effects. We have worked on developing the

best approach to these "rescue" experiments in recent years; however, we ran into several technical obstacles that we have just recently been able to overcome. The largest setback on these experiments was the dim nature of the *Rorc*(γt)GFP/+ reporter mouse strain we had been using to identify and sort ILC3s, which was not sufficiently bright for this purpose. Now that we have acquired a new strain of RORγt-GFP reporter mice that have 5-10 copies of RORγt-GFP compared to the single copy in the original mouse strain, RORγt+ ILC3s are substantially easier to identify by fluorescence. This improvement now allows us to avoid staining the cells for other immune markers and minimizes their manipulation, both of which we previously found to negatively impact their survival post-sorting. With these improvements in mind, we plan to sort both hepatic and splenic ILC3s, the latter of which are more abundant and easier to obtain, and add them back to both ILC3-deficient mice, and young mice that we know to have fewer ILC3s relative to adult mice. The completion of these experiments will solidify our earlier findings and determine whether targeting of ILC3s in young mice represents a potential therapeutic avenue that could lead to improved HBV immune outcomes.

Chapter 4. Acute depletion of ILC3s alters hepatic immunity and delays HBV antigen clearance

Introduction

To validate our data identifying a role for ILC3s in generating a defective HBV immune response, we explored alternative models of ILC3 loss in a system that did not develop in the absence of ILC3s, which may have led to other disruptions in immunity outside of the liver environment. Because ILC3s share many of their lineage-defining markers with other T cell and ILC subsets, it is challenging to specifically deplete ILC3s without disrupting these other populations. One of the most common methods for studying ILC3 loss has been the use of anti-Thy1 (also known as anti-CD90) depleting antibodies within a *Rag*-/- host, which lack Thy1+ T cells. Although highly effective at depleting ILC3s, this treatment also depletes ILC1 and ILC2, as well as Thy1+ NK cells. Thus, interpreting data from these experiments must be done cautiously. In our case, we aimed to compare the results from *Rorc*(γt)GFP/GFP mice with anti-Thy1 ILC-depleted mice to identify similarities between both models that would allow us to identify effects due to the specific loss of ILC3.

Results

For this model of acute ILC3 depletion, we followed one of two treatment regimens. For the first group, we administered 200 μg anti-Thy1.2 antibody to each adult (> 6 weeks) mouse every three days starting four days before adoptive transfer with Thy1.1+ donor splenocytes and continuing until day five post-transfer; mice were sacrificed on day eight. By using Thy1.1+ donor splenocytes we are able to continue to deplete Thy1.2+ recipient ILCs throughout the

duration of the experiment without depleting the donor T cells. For the second group, we administered the same dose of anti-Thy1.2 antibody every three days, starting when the mice were three weeks old (day -21), and continuing until day 21 post-adoptive transfer; mice were sacrificed on day 22. The first treatment schedule and experimental design was to address the question of how immediate ILC3-depletion affects early immune priming events during HBV immunity. The second set of experiments was designed to determine whether acute ILC3 depletion affected the lasting immune response initiated in the absence of ILCs. We also chose to start anti-Thy1.2 depletion for the second group earlier, at the time of weaning, to understand how ILC3 depletion during the most significant window of microbial colonization and maturation of the immune priming environment within the liver, might also influence HBV immune outcomes. It is important to remember that while the day 8 experiments focus solely on the effects of immediate ILC loss, phenotypes observed in the day 22 experiments could be due to direct loss of ILCs, as well as indirect effects due to either altered microbial colonization or changes in hepatic APCs due to a loss of signals from ILC3s in the liver.

I first evaluated the effect of acute ILC3 loss on the serological profile of treated and control animals. Similar to *Rorc*(γt)-/- mice, acute ILC depletion led to increased inflammation in the majority of the treated animals at both day 7 and day 14 post-transfer, although these differences did not reach significance (**Fig. 4.1 A**). Notably, I observed delayed antigen clearance in anti-Thy1.2-treated animals relative to controls (**Fig. 4.1 B**). These data are similar to those observed in *Rorc*(γt)-/- mice and strongly suggest a role for ILC3s in restricting early hepatic inflammation and supporting HBV antigen clearance.
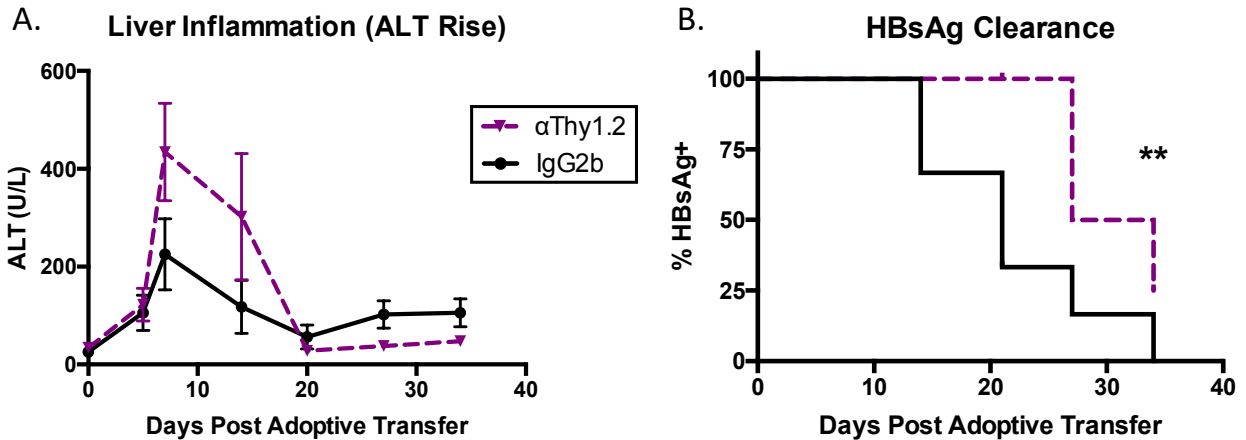
Figure 4.1. Anti-Thy1.2-mediated ILC depletion results in delayed HBV antigen clearance. Adult (>6wks) HBVtg*Rag1*-/- animals were treated with anti-Thy1.2 depleting antibodies (αThy1.2) every three days starting at 3 wks of age (day -21) or at day -4, and adoptively transferred with HBV-naïve Thy1.1 splenocytes on day 0. (**A**) Liver disease was monitored by plasma alanine aminotransferase (ALT). (**B**) Clearance of circulating HBsAg was monitored over time by qualitative ELISA. Statistics determined by a log-rank (Mantel-Cox) Chi square survival test or unpaired two-tailed t-test with GraphPad Prism Software; ** p<0.01, n≥9 per group, pooled from three independent experiments.

I examined the hepatic immune cell composition of anti-Thy1.2-treated and control mice by flow cytometry, initially focusing on T and B cells. There were no differences in the number of total hepatic CD45+ immune cells or the percentages of T cells and B cells at the early day 8 time point (**Fig. 4.2 A-C top**). This differs from the *Rorc*(γt)-/- mice that showed similar numbers of CD45+ T cells at day 8 but had a greater percentage of B cells and reduced percentage of T cells. However, by day 22 I observed that there was an increased number of total CD45+ cells, although the percentages of T and B cells remained constant (**Fig. 4.2 A-C bottom**). This was similar to *Rorc*(γt)-/- mice that also had increased numbers of CD45+ cells in the liver at day 29.
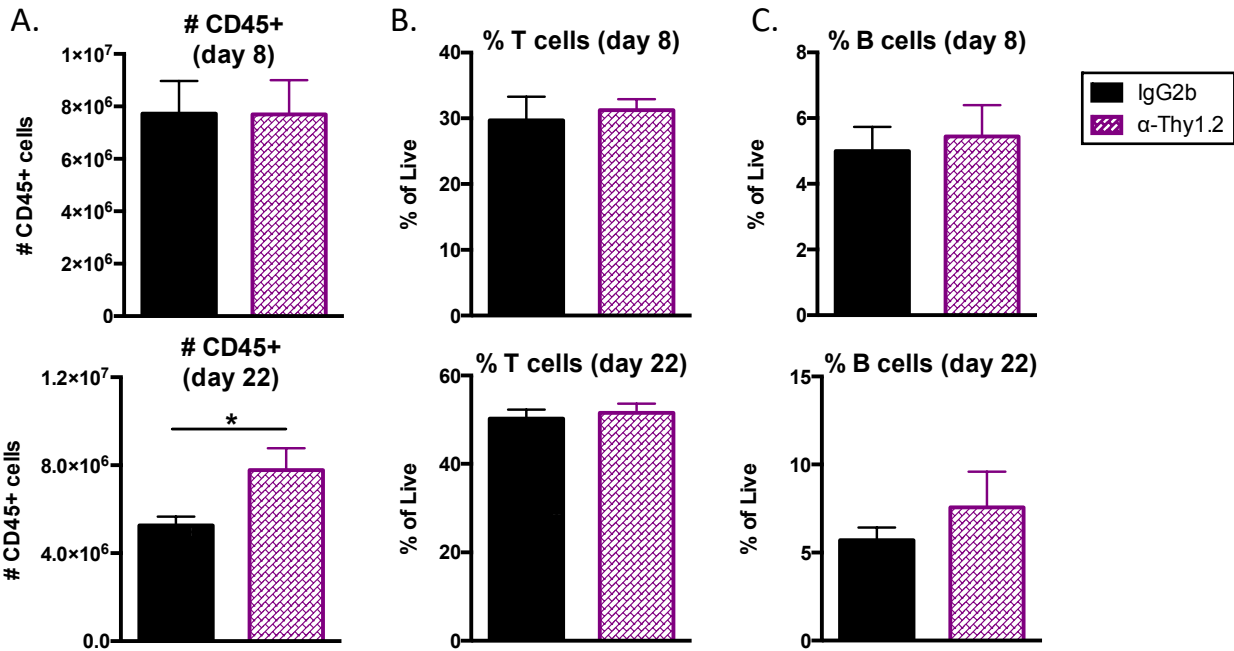
Figure 4.2. Anti-Thy1.2-mediated ILC depletion leads to increased hepatic immune cell infiltration. Adult (>6wks) HBVtg*Rag1*-/- animals were treated with anti-Thy1.2 depleting antibodies (αThy1.2) or IgG2b control antibody every three days starting at 3 wks of age (day -21) and continuing until sacrifice (day 22 group) or were treated every three days starting at day -4 and continuing until sacrifice (day 8 group) with adoptive transfer of HBV naïve Thy1.1 splenocytes on day 0. Flow cytometry was performed and the number of (**A**) CD45+ immune cells and percentages of (**B**) T cells (CD45+ TCRβ+ NK1.1-CD19-) and (**C**) B cells (CD45+ TCRβ- CD19+) were measured on day 8 (top) and day 22 (bottom) post-transfer. Data were analyzed using FlowJo™ Software; statistics determined by unpaired two-tailed t-test with GraphPad Prism Software; * $p<0.05$, n=5 per group.

I did not find a difference in CD4+ or CD8+ T cell skewing during early inflammation; however, there was a significant reduction in the percentage of CD44+ CD62L+ central memory CD4+ T cells in Thy1.2-depleted mice (**Fig. 4.3 A, C**). There was also an increased number of central memory CD8+ T cells in these animals, though the percentage of naïve versus central memory versus effector CD8+ cells was not different (**Fig. 4.3 E**). Interestingly, by day 22, I noted a much greater number of CD4+ T cells in ILC-depleted animals, while the total number of CD8+ T cells remained the same (**Fig. 4.3 B**). The increase in CD4+ T cells was mostly due to a large increase in the number of effector CD4+ T cells with a small increase in the number of CD4+ T_CM cells; however, the fraction of T_CM of total CD4+ T cells was decreased in ILC-

depleted animals (**Fig. 4.3 D**). These data are consistent with the increase observed in CD4+ T$_{Eff}$ cells seen in *Rorc*(γt)$_{-/-}$ mice at day 8 and day 29, as well as the defect in CD4+ T$_{CM}$ cells that was observed at a later time point. Together, these data suggest that a loss of ILC3s results in impaired durability of memory CD4+ T cell responses relative to the total CD4+ T cell response. There were no differences in the number of total CD8+ T cells nor in their differentiation into central memory versus effector cells in anti-Thy1.2-treated and control mice (**Fig. 4.3 F**).
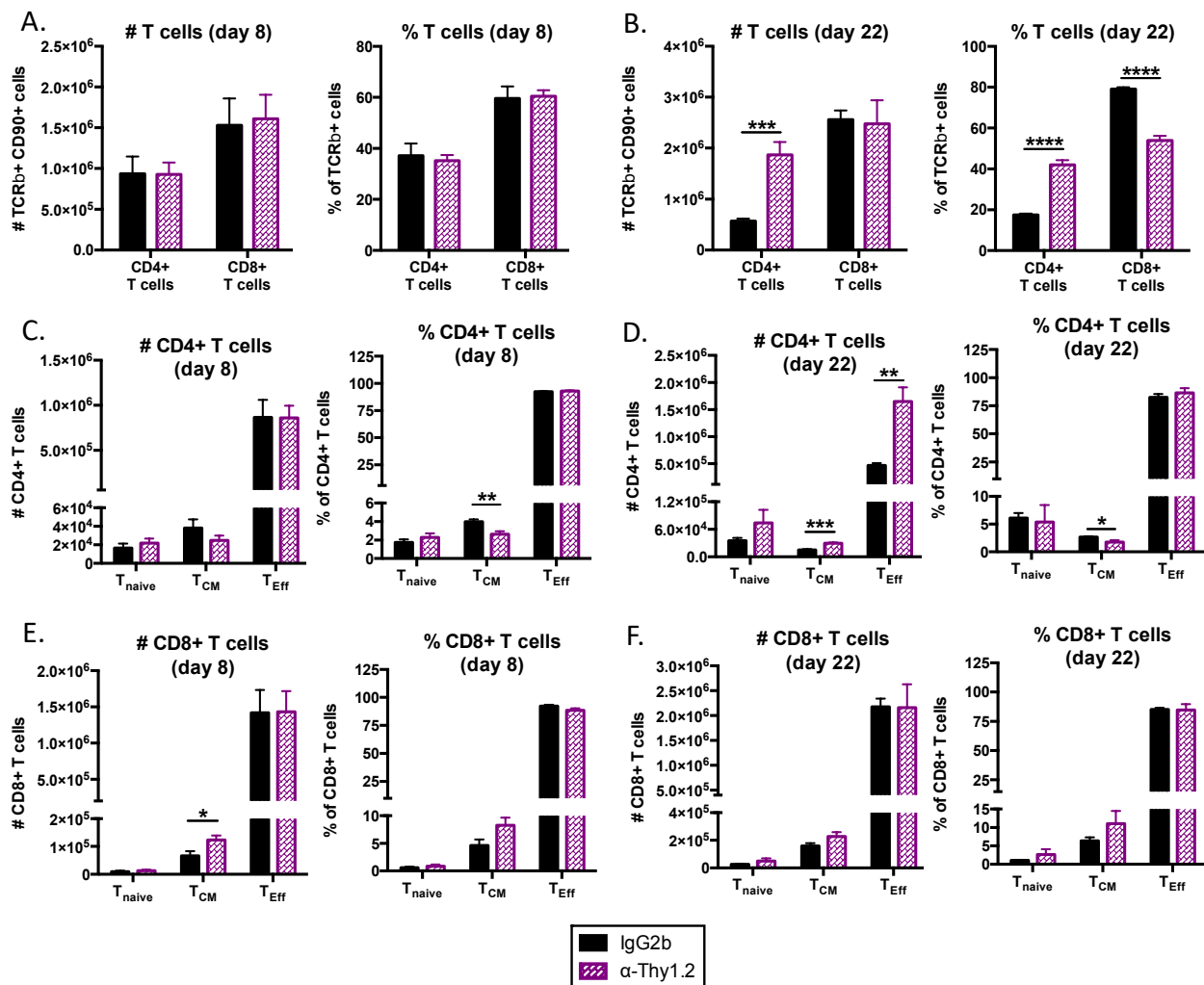
Figure 4.3. Anti-Thy1.2-mediated ILC depletion leads to increased CD4+ T cell accumulation in the liver. Adult (>6wks) HBVtg*Rag1*$_{-/-}$ animals were treated with anti-Thy1.2 depleting antibodies (αThy1.2) or IgG2b isotype-matched control antibody every three days starting at 3 wks of age (day -21) and continuing until sacrifice (day 22 group) or were treated every three days starting at day -4 and continuing

until sacrifice (day 8 group) with adoptive transfer of HBV naïve Thy1.1 splenocytes on day 0. Flow cytometry was performed and the number (left) and percentages (right) of CD4+ T cells (CD45+ TCRβ+ NK1.1- CD19- CD4+ CD8-) and CD8+ T cells (CD45+ TCRβ+ NK1.1- CD19- CD4- CD8+) were measured on day 8 (**A**) and day 22 (**B**). The number and percentage of CD44- CD62L+ T$_{naive}$, CD44+ CD62L+ T$_{CM}$, and CD44+ CD62L- T$_{Eff}$ CD4+ T cells was determined on day 8 (**C**) and day 22 (**D**). The number and percentage of CD44- CD62L+ T$_{naive}$, CD44+ CD62L+ T$_{CM}$, and CD44+ CD62L- T$_{Eff}$ CD8+ T cells was determined on day 8 (**E**) and day 22 (**F**). Data were analyzed using FlowJo™ Software; statistics were determined by the unpaired two-tailed t-test with GraphPad Prism Software; * $p<0.05$, n=5 per group.

We performed chromogen-based IHC staining of liver tissue from control and Thy1.2-depleted animals with anti-RORγ (purple), anti-CD8α (teal), and anti-CD4 (yellow) to visualize the distribution of CD4+ and CD8+ T cells relative to ILC3s. We first looked at the early day 8 time point. Control animal liver sections looked as expected, with many small- and medium-sized T cell clusters spread throughout the liver parenchyma and associated with portal tracts (**Fig. 4.4 A-C**). Interestingly, despite seeing no differences in the numbers or percentages of T cells in anti-Thy1.2-treated mice at this time point by flow cytometry, we did detect marked differences in the distribution of these cells compared to control mice (**Fig. 4.4 D-F**). Notably, there were large portal tract-associated immune infiltrates that were highly reminiscent of the portal-associated inflammation seen in *Rorc*(γt)-/- mice (**Fig. 4.4 D-F** and **Fig. 3.4-3.5**). These differences will be further quantitated using ilastik imaging analysis. These data strongly implicate ILC3s in regulating immune cell localization within the liver such that when the cells are absent the majority of inflammation is restricted to periportal and vascular areas of the liver and the cellularity and size of portal-associated immune clusters is much greater. Importantly, the animals in this group were not affected by potential indirect effects of microbial colonization, as ILCs were depleted only four days before adoptive transfer, when these animals were fully matured and beyond the window of commensal colonization immediately following weaning.
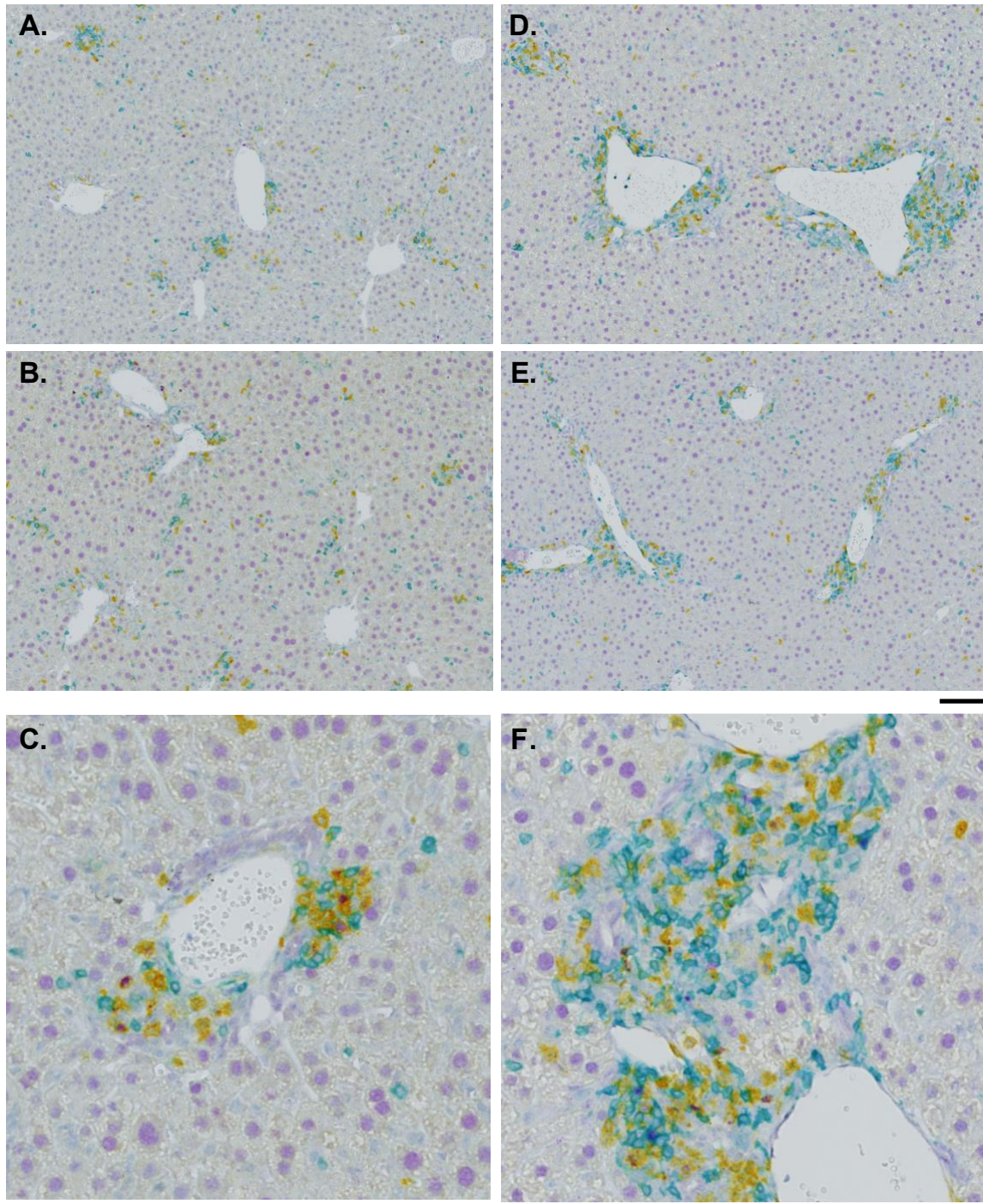
Figure 4.4. Anti-Thy1.2-mediated ILC depletion leads to enhanced portal tract-associated inflammation during acute HBV immunity. Liver tissue was isolated from adult IgG2b isotype-matched control (**A-C**) or anti-Thy1.2 (**D-F**) antibody treated HBVtg*Rag1*-/- mice 8 days post- adoptive transfer with Thy1.1 HBV-naïve splenocytes and drop-fixed in formalin for 24 hours, followed by ethanol dehydration and embedding into paraffin wax blocks. FFPE tissue blocks were sectioned at 4 μm and stained with anti-RORγ (purple), anti-CD8 (teal), and anti-CD4 (yellow) using the Ventana Discovery Ultra platform. Stained sections were imaged at 20X resolution with the Zeiss Axioscanner Z1. Scale bars represent 100 μm for **(A-B, D-E**), and 50 μm for (**C, F**).

A couple of weeks later, we could still see similar patterns of disrupted immune cell localization in the absence of ILCs. We observed isotype-matched control Ig-treated animals had mostly resolved their hepatic inflammation by day 22, with few immune cell clusters left that were mostly portal-associated and predominantly comprised of CD11b+ cells rather than the T cell-rich clusters seen at day 8 (**Fig. 4.5 A-C**). The anti-Thy1.2 ILC-depleted mice on the other hand, had a significant number of large immune cell clusters, including many more T cells compared to the control animals (**Fig. 4.5 D-F)**. These clusters were again mostly associated with portal tracts; however, intraparenchymal clusters could also be found. Of note, ILC3s could be seen associated with the immune cell clusters in both the isotype-matched control Ig- and anti-Thy1.2-treated groups, but there seemed to be many more ILC3s, as well as RORγ+ CD4+ Th17 and RORγ+ Tc17, in the anti-Thy1.2-depleted groups (**Fig 4.5 C, F**). Data discussed in more detail below show that the hepatic ILC3s detected on day 22 are mostly donor derived (Thy1.1+). We also noticed that although ILC3s were often found to be cluster-associated at day 8 as well, we could observe many clusters that did not have a visible ILC3 present. However, by day 22, nearly every cluster in both the control and anti-Thy1.2-treated mice had one or more ILC3(s) present in the cluster, and these ILC3s were often in direct contact with CD4+ T cells and perhaps even more so, CD8+ T cells. While these data are currently being analyzed in a quantitative manner with the approach outlined in Chapter 2, it is an exciting observation that suggests ILC3s may be associated with the sustained maintenance or longevity of hepatic immune cell clusters. This also warrants revisiting tissue staining of later time points in adult and young animals to determine whether there might be a possible defect in ILC3 cluster association in young animals.
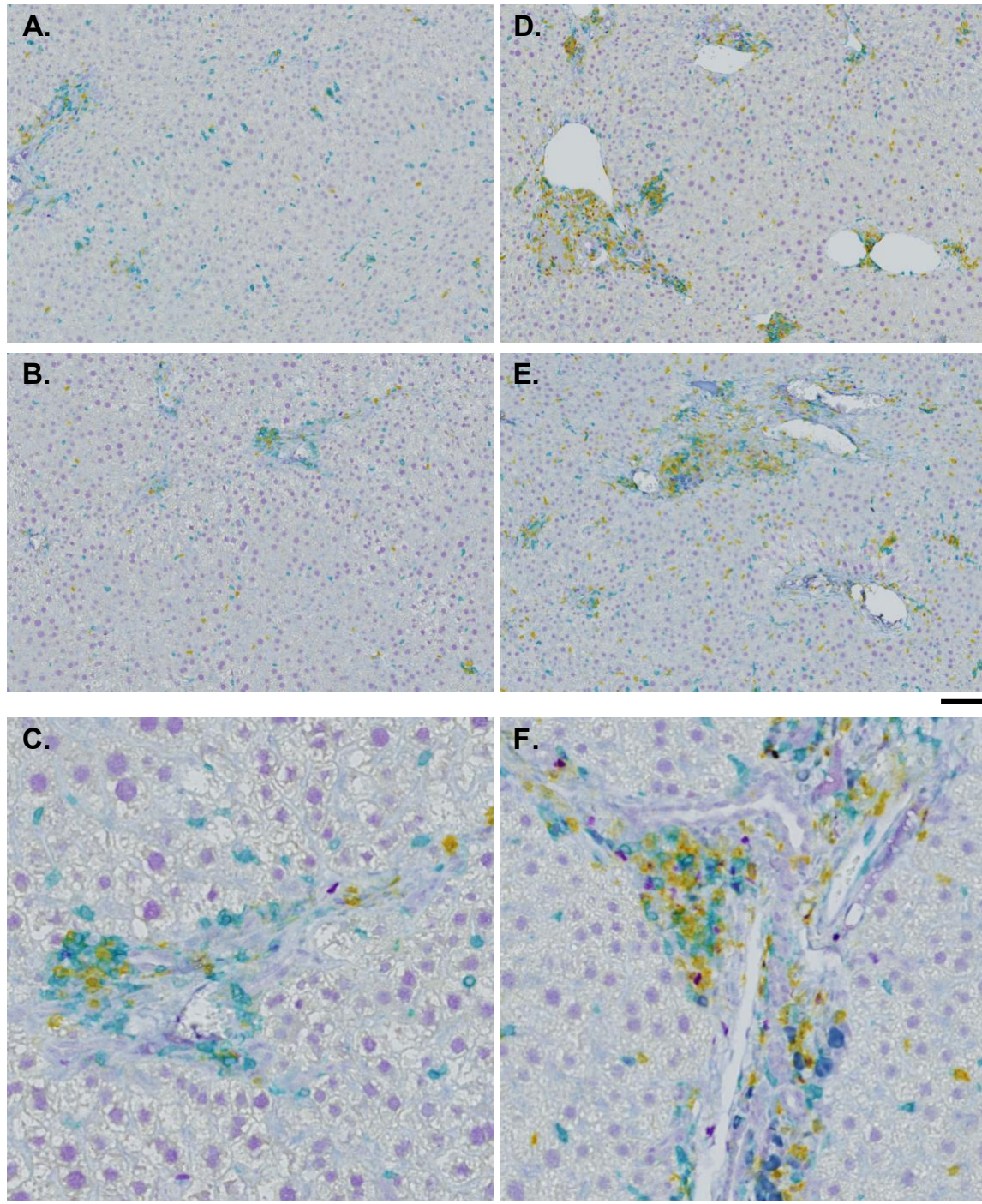
Figure 4.5. Anti-Thy1.2-mediated ILC depletion leads to enhanced portal tract-associated inflammation during sustained HBV immunity. Liver tissue was isolated from adult IgG2b isotype-matched control (**A-C**) or anti-Thy1.2 (**D-F**) antibody treated HBVtg*Rag1*-/- mice 22 days post- adoptive transfer with Thy1.1 HBV-naïve splenocytes and drop-fixed in formalin for 24 hours, followed by ethanol dehydration and embedding into paraffin wax blocks. FFPE tissue blocks were sectioned at 4 μm and stained with anti-RORγ (purple), anti-CD8 (teal), and anti-CD4 (yellow) using the Ventana Discovery Ultra platform. Stained sections were imaged at 20X resolution with the Zeiss Axioscanner Z1. Scale bars represent 100 μm for (**A-B, D-E**), and 50 μm for (**C, F**).

I assessed the production of the crucial cytokine IFNγ by T and NK cell populations in the Thy1.2-depleted mice. I found an overall increase in the number of IFNγ+ cells at both day 8 and day 22 after ILC-depletion (**Fig 4.6 A-B**). This increase in IFNγ+ cells was mostly due to an increased number of T cells at both time points, but there was also an increased number of IFNγ+ NK1.1+ T cells (**Fig. 4.6 C-D**). On the other hand, there was a decreased number of IFNγ+ NK cells at day eight in anti-Thy1.2-treated mice, which is likely explained in part by Thy1.2-mediated depletion of a subset of Thy1.2+ NK cells (**Fig. 4.6 C-D**).
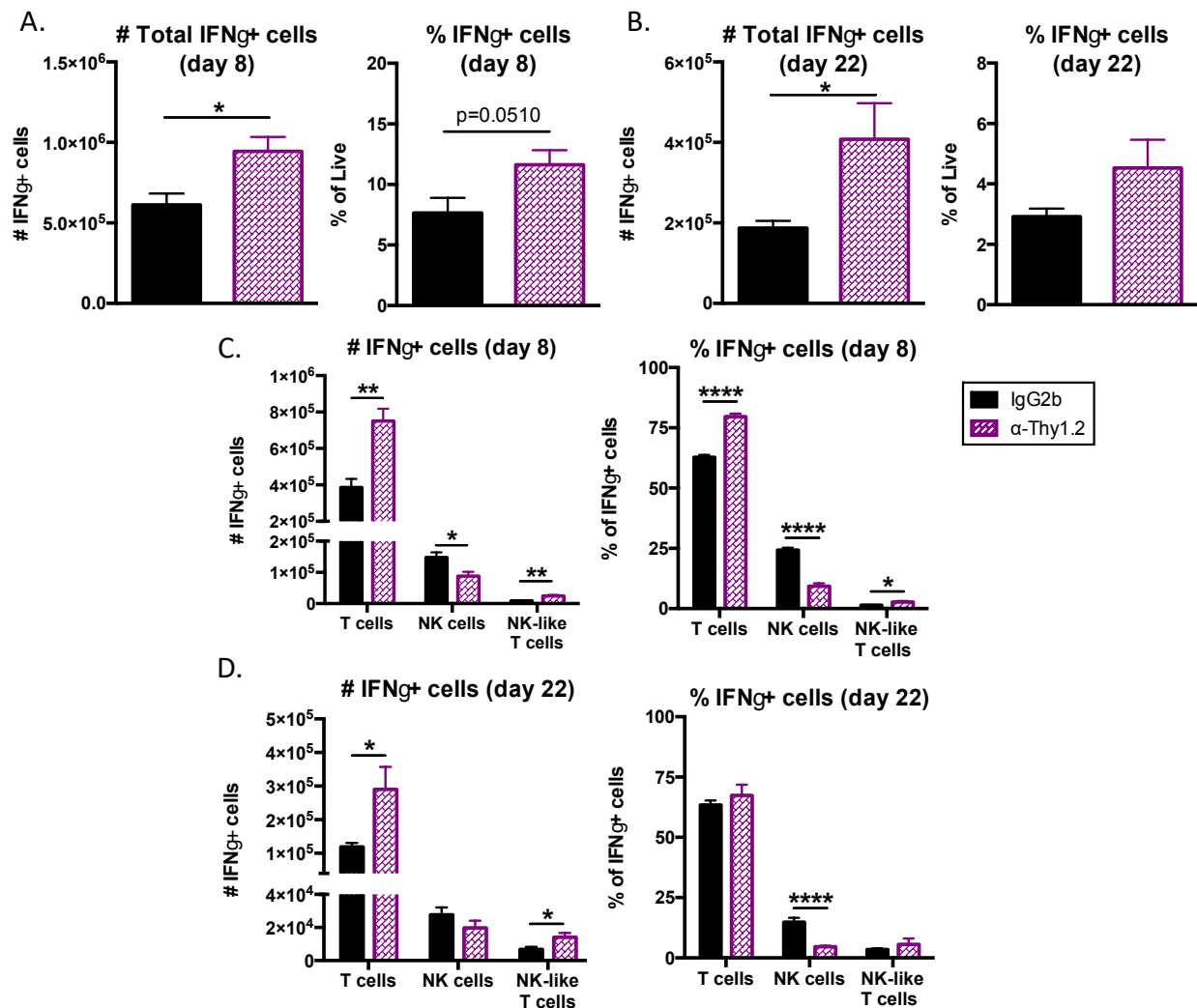
Figure 4.6. Anti-Thy1.2-mediated ILC depletion leads to increased IFNγ production by T cells and NK-like T cells. Adult (>6wks) HBVtg*Rag1*-/- animals were treated with anti-Thy1.2 depleting antibodies (αThy1.2) or IgG2b isotype-matched control antibody every three days starting at 3 wks of age (day -21) and continuing until sacrifice (day 22 group) or were treated every three days starting at day -4 and continuing until sacrifice (day 8 group) with adoptive transfer of HBV naïve WT splenocytes on day 0. Flow cytometry was performed and the number and percentage of CD45+ IFNγ+ cells was determined on day 8 (**A, C**) and day 22 (**B, D**) post-adoptive transfer. (**B-C**) The number and percentage of IFNγ+ T cells (CD45+ TCRβ+ NK1.1-), NK cells (CD45+ TCRβ- NK1.1+), and NK-like T cells (CD45+ TCRβ+ NK1.1+) was determined. Data were analyzed using FlowJo™ Software; statistics determined by unpaired two-tailed t-test with GraphPad Prism Software; * p<0.05, ** p<0.01, *** p<0.001, **** p<0.0001; n=5 per group.

When specifically evaluating the CD4+ T cells I observed that there was an increased number of IFNγ+ CD4+ T cells at both day 8 and day 22 in Thy1.2-depleted animals (**Fig. 4.7 A, D**). This increased number was accompanied by an increased percentage of IFNγ+ CD4+ T cells relative to total CD4+ T cells at day 8 in anti-Thy1.2-treated mice; however, by day 22 a similar percentage of CD4+ T cells were making IFNγ (**Fig. 4.7 A, D**). I also measured a similar increase in the number of IFNγ+ CD4+ T cells at day 8 in *Rorc*(γt)-/- mice (**Fig. 3.6 D**), though the percentage of IFNγ+ cells were similar at this time point. These data suggest that ILC3 do indeed play a role in suppressing the accumulation of total IFNγ-producing CD4+ T cells in the liver, particularly during early inflammation. I also noted that IFNγ production was increased within both T_CM_ and T_Eff_ at day 8 of anti-Thy1.2-treated mice, while only an increase in IFNγ+ T_Eff_ was observed at day 22 (**Fig. 4.7 C, F**). Similar to *Rorc*(γt)-/- mice, we observed that PD-1 expression on IFNγ+ CD4+ T cells was high at day 8, but similar between treatment groups, and came down substantially by day 22, with a trend towards decreased PD-1+ IFNγ+ CD4+ T cells in anti-Thy1.2-treated animals, as was seen in total CD4+ T cells of *Rorc*(γt)-/- mice (**Fig. 3.6 C and Fig. 4.7 B, E**).
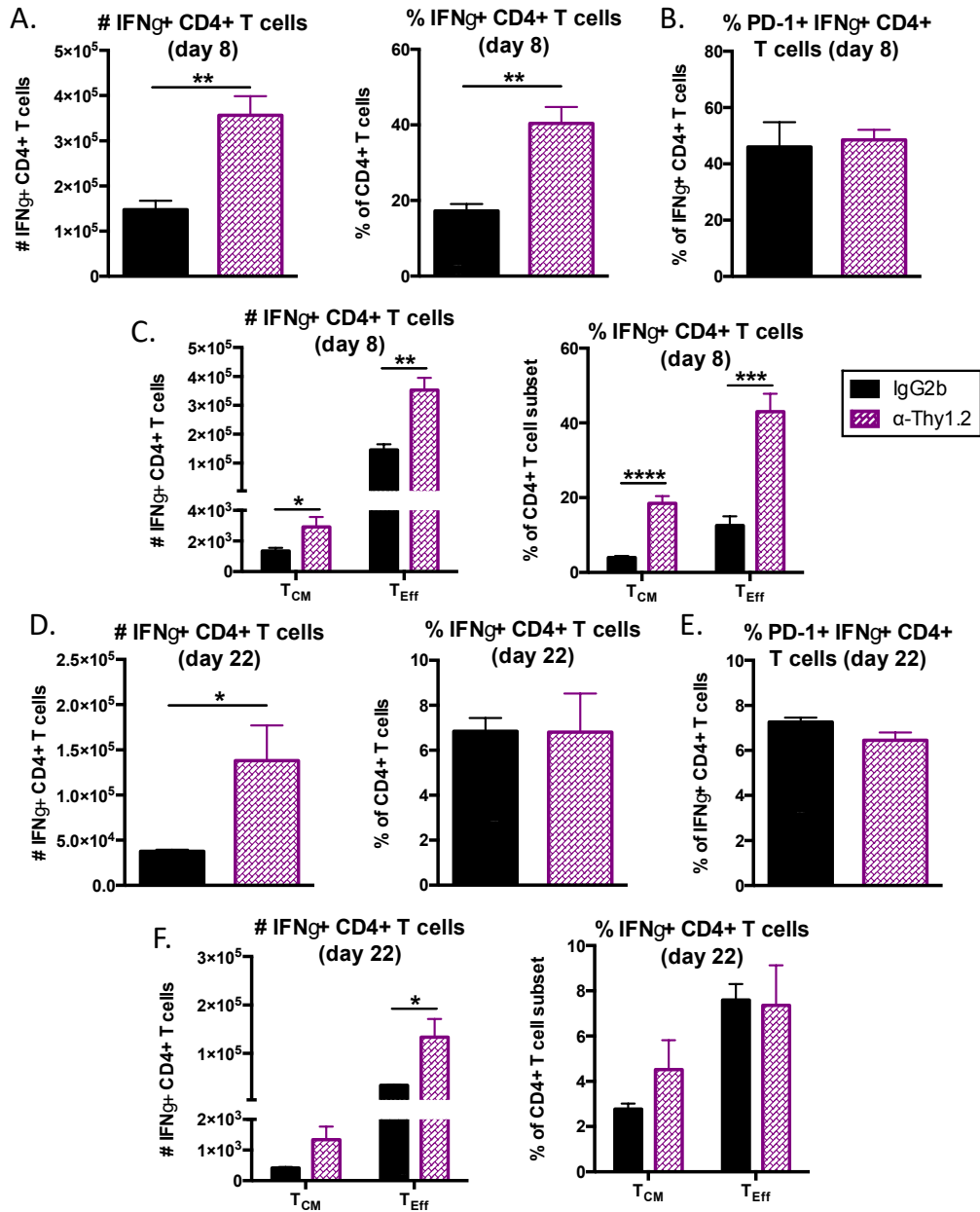
Figure 4.7. Anti-Thy1.2-mediated ILC depletion leads to increased IFNγ production by CD4+ T cells. Adult (>6wks) HBVtg*Rag1*-/- animals were treated with anti-Thy1.2-depleting antibodies (αThy1.2) or IgG2b isotype-matched control antibody every three days starting at 3 wks of age (day -21) and continuing until sacrifice (day 22 group) or were treated every three days starting at day -4 and continuing until sacrifice (day 8 group) with adoptive transfer of HBV naïve WT splenocytes on day 0. Flow cytometry was performed and the number and percentage of CD45+ TCRβ+ CD4+ IFNγ+ cells was determined on day 8 (**A**) and day 22 (**D**) post-adoptive transfer. The number of PD-1+ IFNγ+ CD4+ T cells as a percentage of total IFNγ+ CD4+ cells was determined on day 8 (**B**) and day 22 (**E**). The number and percentage of CD44+ CD62L+ central memory (T$_{CM}$) and CD44+ CD62L- effector/effector memory (T$_{Eff}$) subsets of IFNγ+ CD4+ T cells was determined on day 8 (**C**) and day 22 (**F**). Data were analyzed using FlowJo™ Software; statistics determined by unpaired two-tailed t-test with GraphPad Prism Software; * $p<0.05$, ** $p<0.01$, *** $p<0.001$, **** $p<0.0001$; n=5 per group.

There were no major differences in IFNγ+ CD8+ T cells, although there was a trend towards increased numbers and percentages at both day 8 and day 22 in ILC-depleted animals (**Fig. 4.8 A, D**). PD-1 expression on IFNγ+ CD8+ T cells was also similar between treatment groups at both time points (**Fig. 4.8 B, E**). There was an increased frequency of IFNγ+ TCM and TEff at day 8 in anti-Thy1.2-treated mice; however, there were not any significant differences by day 22, though a trend towards increased IFNγ+ CD8+ TEff cells was noted (**Fig. 4.8 C, F**). These data were somewhat different from what we observed in the *Rorc*(γt)-/- mice, which showed a decreased number of IFNγ+ CD8+ T cells. These data suggest that the inconsistencies between the two models of ILC3-depletion could be accounted for by indirect effects of ILC3 loss from birth in the knock-out mice. Alternatively, the depletion of ILC1, ILC2, and some NK cells in the anti-Thy1.2 depletion experiments may permit IFNγ production by CD8+ T cells that would otherwise be diminished in the absence of ILC3s alone. As we are ultimately interested in understanding how ILC3 loss relates to young mice that have reduced ILC3 numbers and altered functional profiles, we plan to use tetramer staining in young and adult mice compared to the ILC3-deficient mice to help clarify these observations and identify the most important critical differences that are relevant to age-dependent HBV immunity.
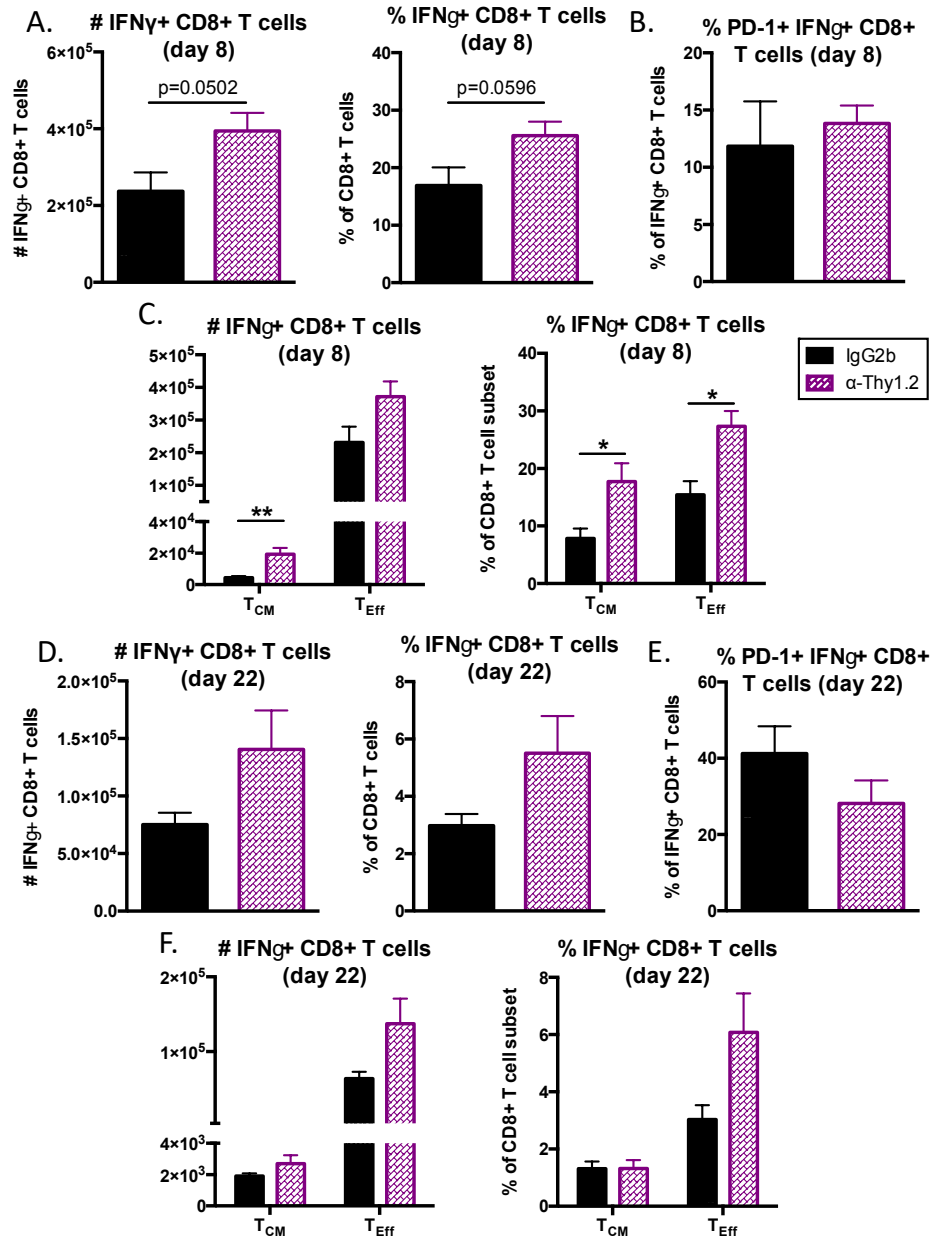
Figure 4.8. Anti-Thy1.2-mediated ILC depletion does not affect IFNγ production by CD8+ T cells.
Adult (>6wks) HBVtg*Rag1-/-* animals were treated with anti-Thy1.2 depleting antibodies (αThy1.2) or
IgG2b isotype-matched control antibody every three days starting at 3 wks of age (day -21) and
continuing until sacrifice (day 22 group) or were treated every three days starting at day -4 and continuing
until sacrifice (day 8 group) with adoptive transfer of HBV naïve WT splenocytes on day 0. Flow
cytometry was performed and the number and percentage of CD45+ TCRβ+ CD8+ IFNγ+ cells was
determined on day 8 (**A**) and day 22 (**D**) post-adoptive transfer. The number of PD-1+ IFNγ+ CD8+ T
cells as a percentage of total IFNγ+ CD8+ cells was determined on day 8 (**B**) and day 22 (**E**). The number
and percentage of CD44+ CD62L+ central memory (Tcm) and CD44+ CD62L- effector/effector memory
(Teff) subsets of IFNγ+ CD8+ T cells was determined on day 8 (**C**) and day 22 (**F**). Data were analyzed
using FlowJoᴛᴍ Software; statistics determined by unpaired two-tailed t-test with GraphPad Prism
Software; * p<0.05, ** p<0.01; n=5 per group.

I used IFNγ ELISpot assays to further assess the magnitude and specificity of the hepatic

IFNγ response in control and anti-Thy1.2-treated animals. Similar to *Rorc*(γt)-/- mice, I

determined that anti-Thy1.2 depleted animals also had a much higher baseline IFNγ response on

day 8 and day 22 (**Fig. 4.9 A, C**). This increase in the baseline IFNγ response can either indicate

increased HBV non-specific IFNγ production, or alternatively could represent IFNγ production

by cells recently activated *in vivo* that are unable to be further stimulated to produce excess IFNγ.

When examining the IFNγ response to individual HBV-derived peptides, I observed that control

animals mounted an antigen-specific response to three of the four dominant epitopes (contained

within peptides, 32, 81, 190/88, and 92) at day 8 and all four dominant epitopes at day 22 (**Fig.

4.9 B, D**). Conversely, cells from ILC-depleted animals showed robust IFNγ production in

general but, relative to their high baseline, HBV-specific peptides did not induce a response of at

least two-fold above baseline for any HBV peptide on day 8 (**Fig. 4.9 B**). By day 22 I detected a

response to peptide 81 (MHCII-restricted) by cells from ILC-depleted animals, though the

magnitude relative to baseline was reduced compared to control mice (**Fig. 4.9 D**). Interestingly,

in *Rorc*(γt)-/- mice the early antigen-specific response was similarly blunted relative to baseline,

but there seemed to be a specific defect in peptide 81 responses that could not be overcome with

time, while MHCI-restricted epitopes within peptide 92 and 190/88 induced a measurable IFNγ

response. It's possible that the repopulation of depleted ILC populations from donor splenocytes

(discussed below in more detail) may contribute to the differences observed at later time points;

however, it would be informative to assess antigen-specific responses at a later time point when

baseline IFNγ is likely to have further decreased. In addition, tetramer data paired with IFNγ

staining will be most informative and will be completed upon receipt of the newly designed

tetramers for peptides 32, 81, 190/88, and 92 discussed in Chapter 1 and 3. Taken together,

however, these data suggest that there is a defect in antigen-specific T cell responses in the absence of ILC3s.
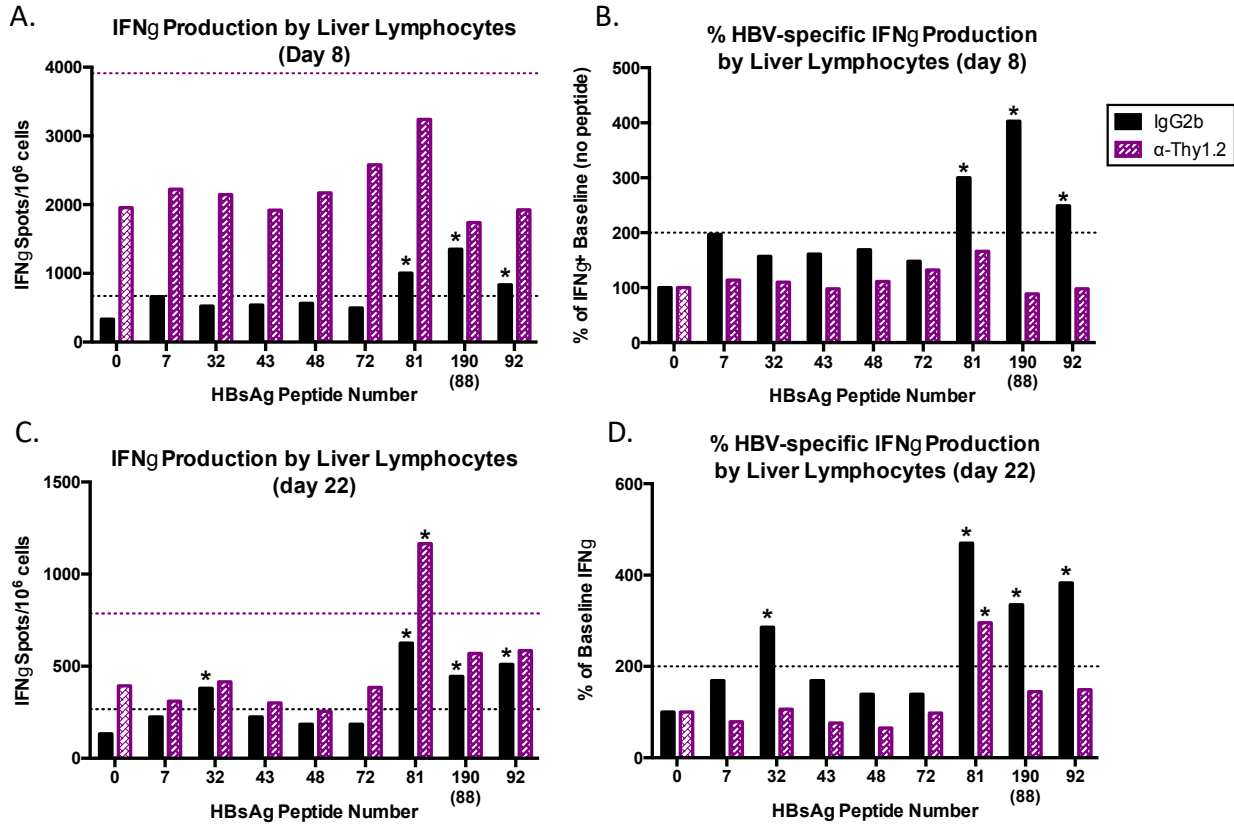
Figure 4.9. Anti-Thy1.2-mediated ILC depletion leads to increased baseline IFNγ production with blunted antigen-specific IFNγ T cell responses. Hepatic leukocyte fractions were enriched adult (>6wks) HBVtg*Rag1-/-* animals were treated with anti-Thy1.2-depleting antibodies (αThy1.2) or IgG2b isotype-matched control antibody every three days starting at 3 wks of age (day -21) and continuing until sacrifice (day 22 group, **C-D**) or were treated every three days starting at day -4 and continuing until sacrifice (day 8, **A-B**) with adoptive transfer of HBV naïve WT splenocytes on day 0. 10_5 liver leukocytes were mixed in a 1:1 ratio with splenocytes from *Rag1-/-* mice as a source of APCs and stimulated overnight at 37°C together with individual peptides derived from the HBV envelope protein (HBsAg peptides) in ELISpot plates pre-coated with anti-IFNγ antibodies. "0" peptide denotes no peptide added. Antigen-specific IFNγ production was measured and displayed as both the total number of IFNγ spots (**A, C**) and as a percentage of baseline (no peptide) IFNγ production (**B, D**). ELISpot plates were counted and analyzed with a CTL Immunospot plate reader and software. The threshold defining a positive response, marked with a *, is ≥2× the baseline (dashed line). N=pooled from ≥3 mice per group.

I did not find any major differences in the hepatic myeloid populations of anti-Thy1.2-depleted animals relative to control mice at day 8 and, thus, it is possible that at least some of the differences observed in *Rorc*(γt)-/- mice may have been from indirect effects of ILC3 loss.

I carefully assessed the ILC and NK cell populations in control and ILC-depleted mice to understand how anti-Thy1.2 depletion affects ILC numbers and the dynamics of ILC repopulation. First, when evaluating the NK cells, I observed a sustained loss of both mature (CD49b+ or CD11b+) and immature (CD49b- or CD11b-) NK cells in anti-Thy1.2-depleted mice (**Fig. 4.10 A-D**). I was also able to assess the numbers and relative frequency of Thy1.1+ donor NK cells versus Thy1.2+ recipient NK cells versus Thy1- NK cells, the latter of which could be from either donor or recipient origin. As expected, on day 8 we detected the population of Thy1.2+ recipient NK cells were nearly completely depleted in the anti-Thy1.2-treated animals (**Fig. 4.10 E**). There was an accompanied increase in the number of Thy1.1+ donor splenocyte-derived NK cells in the treated mice at the same time, possibly as a result of filling the NK cell niche in the liver, which is normally an abundant cell type in this tissue. The number of Thy1- NK cells was not changed by anti-Thy1.2 treatment; however, due to the loss of Thy1.2+ NK cells we observed the percentage of the hepatic NK cell compartment that is comprised of Thy1- NK cells increased from approximately 45 percent in control mice to 75 percent in anti-Thy1.2-treated mice. At day 22, we observed that the Thy1- subset of NK cells dominated the liver, and that there were no longer any differences in the number of Thy1.2+ NK cells, suggesting this population was either semi-resistant to sustained depletion, or instead readily repopulates (**Fig. 4.10 F**). These data indicate that Thy1.2 depletion does deplete some NK cells, particularly ones with an immature phenotype, and that adoptive transfer of Thy1.1+ cells cannot completely rescue this loss; however, the presence of a large Thy1- population of

NK cells makes these cells more resilient to Thy1.2 depletion compared to other ILCs. We also know from experiments in the *Rorc*(γt)-/- mice that NK cell numbers were decreased in the absence of RORγt+ cells alone, suggesting that in addition to direct loss of Thy1.2+ NK cells, it is also possible that the loss of ILC3s, and perhaps ILC1 or ILC2, may contribute to an environment that is less supportive of NK cell accumulation in the liver to the levels that occurs when all other ILC populations are present.
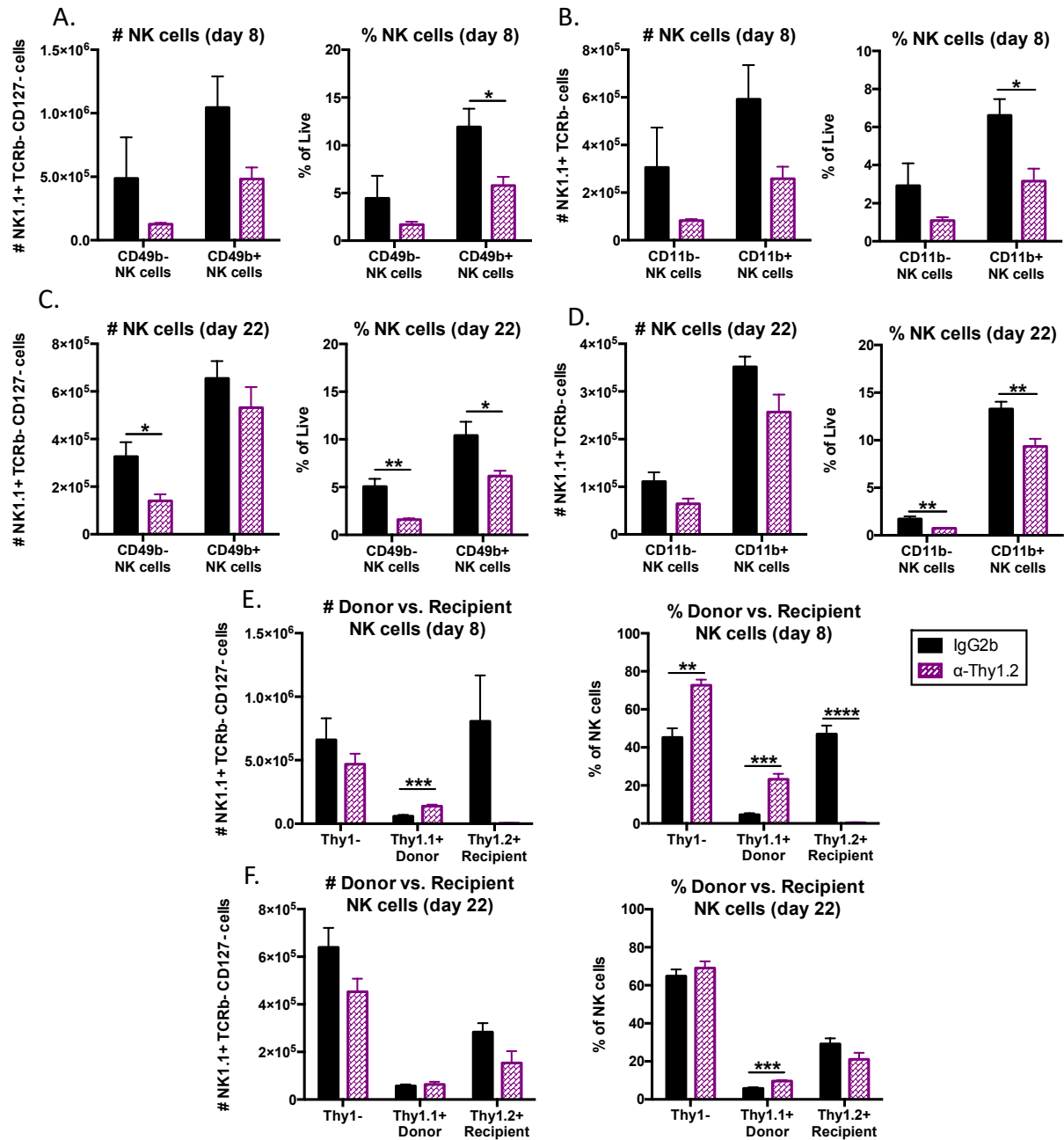
Figure 4.10. Anti-Thy1.2-mediated ILC depletion targets a portion of mature and immature NK cells. Adult (>6wks) HBVtg*Rag1*-/- animals were treated with anti-Thy1.2-depleting antibodies (αThy1.2) or IgG2b isotype-matched control antibody every three days starting at 3 wks of age (day -21) and continuing until sacrifice (day 22 group) or were treated every three days starting at day -4 and continuing until sacrifice (day 8 group) with adoptive transfer of HBV naïve WT splenocytes on day 0. Flow cytometry was performed and the number and percentage of (**A, C**) CD49b+ and CD49b- and (**B, D**) CD11b+ and CD11b- CD45+ TCRβ- NK1.1+ cells was determined on day 8 (**A-B**) and day 22 (**C-D**) post-adoptive transfer. The number and percentage of Thy1.1+ donor, Thy1.2+ recipient, and Thy1- NK cells was determined on day 8 (**E**) and day 22 (**F**) post-adoptive transfer. Data were analyzed using FlowJo™ Software; statistics determined by unpaired two-tailed t-test with GraphPad Prism Software; * p<0.05, ** p<0.01, *** p<0.001, **** p<0.0001; n=5 per group.

I also assessed the numbers and frequencies of hepatic ILC1, ILC2, and ILC3. As expected, there was a decrease in the numbers and percentages of ILC2 and ILC3 at day 8 in anti-Thy1.2-treated mice compared to isotype-matched control Ig-treated mice, with a similar trend towards decreased ILC1 as well, although not significant (**Fig. 4.11 A**). I also saw a similar sustained reduction of ILC1 and ILC2 at day 22 post-adoptive transfer (**Fig. 4.11 B**). Interestingly, however, ILC3 numbers had fully rebounded by day 22 in anti-Thy1.2-treated mice relative to control animals (**Fig 4.11 B**). These data suggested that either the Thy1.2 treatment was losing efficacy against ILC3 over time, or instead that donor Thy1.1+ cells may be compensating for the loss of host Thy1.2+ ILC3.
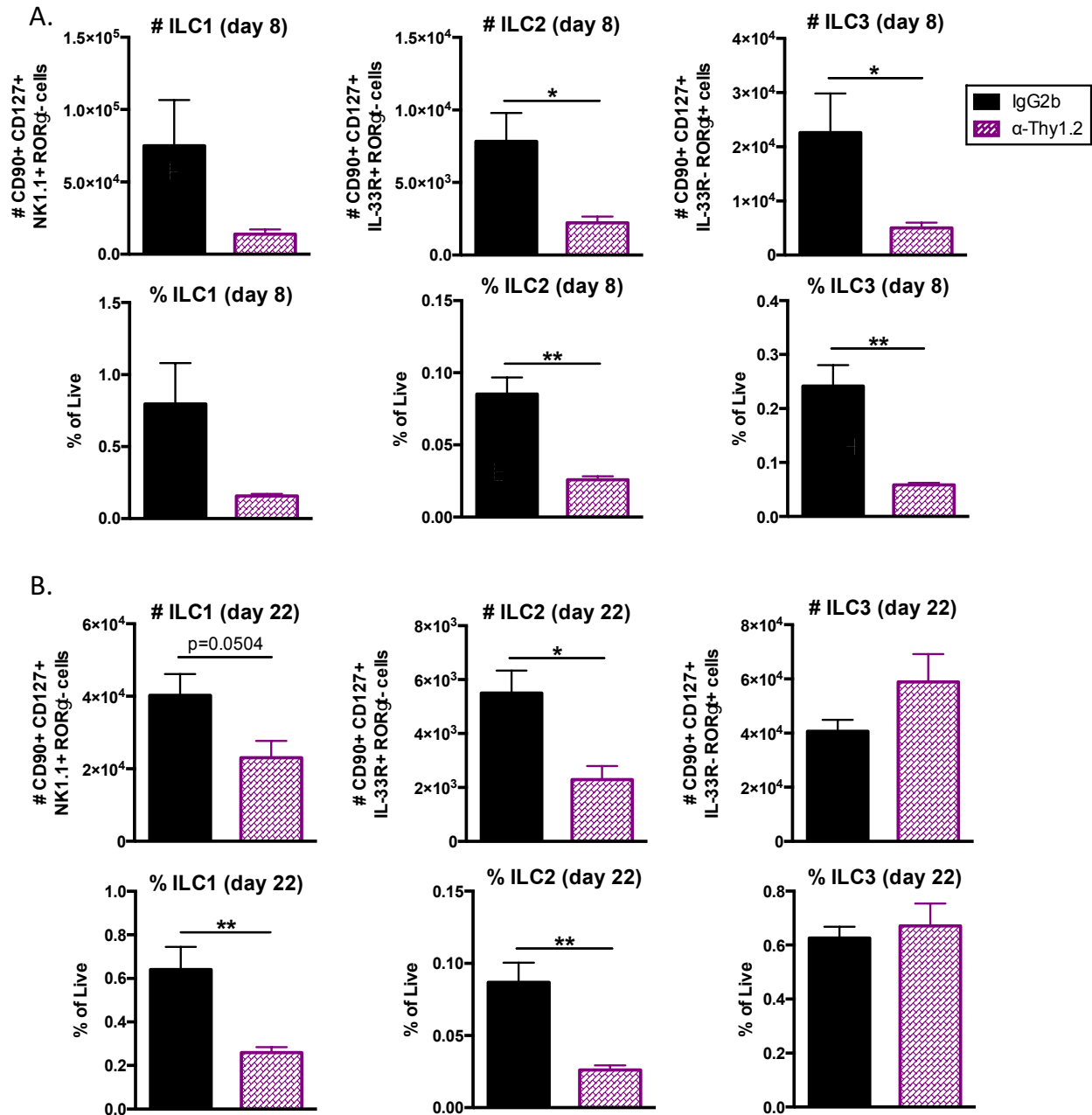
Figure 4.11. Anti-Thy1.2-mediated ILC depletion efficiently reduces but does not eliminate ILCs in the liver after adoptive transfer of Thy1.1 splenocytes. Adult (>6wks) HBVtg*Rag1-/-* animals were treated with anti-Thy1.2-depleting antibodies (αThy1.2) or IgG2b isotype matched control antibody every three days starting at 3 wks of age (day -21) and continuing until sacrifice (day 22 group) or were treated every three days starting at day -4 and continuing until sacrifice (day 8 group) with adoptive transfer of HBV naïve WT splenocytes on day 0. Flow cytometry was performed and the number and percentage of ILC1 (CD45+ TCRβ- Thy1+ CD127+ IL-33R- RORγt- NK1.1+), ILC2 (CD45+ TCRβ- Thy1+ CD127+ IL-33R+ RORγt-), and ILC3 (CD45+ TCRβ- Thy1+ CD127+ IL-33R- RORγt+), was determined on day 8 (**A**) and day 22 (**B**) post-adoptive transfer. Data were analyzed using FlowJoᴛᴍ Software; statistics determined by unpaired two-tailed t-test with GraphPad Prism Software; * p<0.05, ** p<0.01; n=5 per group.

Upon evaluating Thy1.1 and Thy1.2 expression within ILC subsets I was able to better understand the origin of ILC1, ILC2, and ILC3 after adoptive transfer in the control and Thy1.2-depleted mice. In control mice I observed that at the early time point, roughly one third of each ILC subset was donor-derived (Thy1.1+) while roughly two thirds were host-derived (Thy1.2+) (**Fig. 4.12 A**). This has important implications for interpreting imaging data that visualizes hepatic ILC3 localization, as one of every three ILC3s we find in our stained tissue sections may be from donor adult splenocytes rather than the from the host. I could see; however, that the anti-Thy1.2 depletion of ILCs is highly effective initially, particularly for ILC1 and ILC3, while there seems to be a small but present population of Thy1.2+ recipient ILC2 (**Fig. 4.12 A**). We can conclude from this data that Thy1.2-mediated depletion of ILC does not immediately result in a compensatory increase in the number Thy1.1+ ILCs for any subset, suggesting that there is not an early drive to fill this empty niche beyond what normally occurs after adoptive transfer. By day 22, I noted that the number of Thy1.2+ ILC1 and ILC2 starts to rebound significantly, similar to Thy1.2+ NK cells, while Thy1.2+ ILC3 remain depleted (**Fig. 4.12 B**). ILC3 are the highest expressing Thy1+ cell in the liver and, thus, may contribute to their increased susceptibility to anti-Thy1.2 treatment compared to the other subsets. Interestingly, although the absence of Thy1.2+ ILC1 and ILC2 still did not drive a compensatory influx of donor Thy1.1+ ILC, the opposite was true for ILC3. Indeed, the anti-Thy1.2-treated animals had an increased number of Thy1.1+ ILC3 such that the total number of Thy1.1+ and Thy1.2+ ILC3 was equivalent, if not possibly increased, compared to IgG2b control-treated animals. These data suggest that an absence of ILC3s in the liver results in active recruitment of ILC3s back into this tissue and implies that ILC3 may play an important role in liver biology and homeostasis. It remains to be seen whether this repopulation represent *in situ* expansion of a "founder"

population of ILC3s early or immediately after adoptive transfer, or instead if there is a continual

re-seeding of this population from either ILC precursors or now circulating mature splenic ILC3.
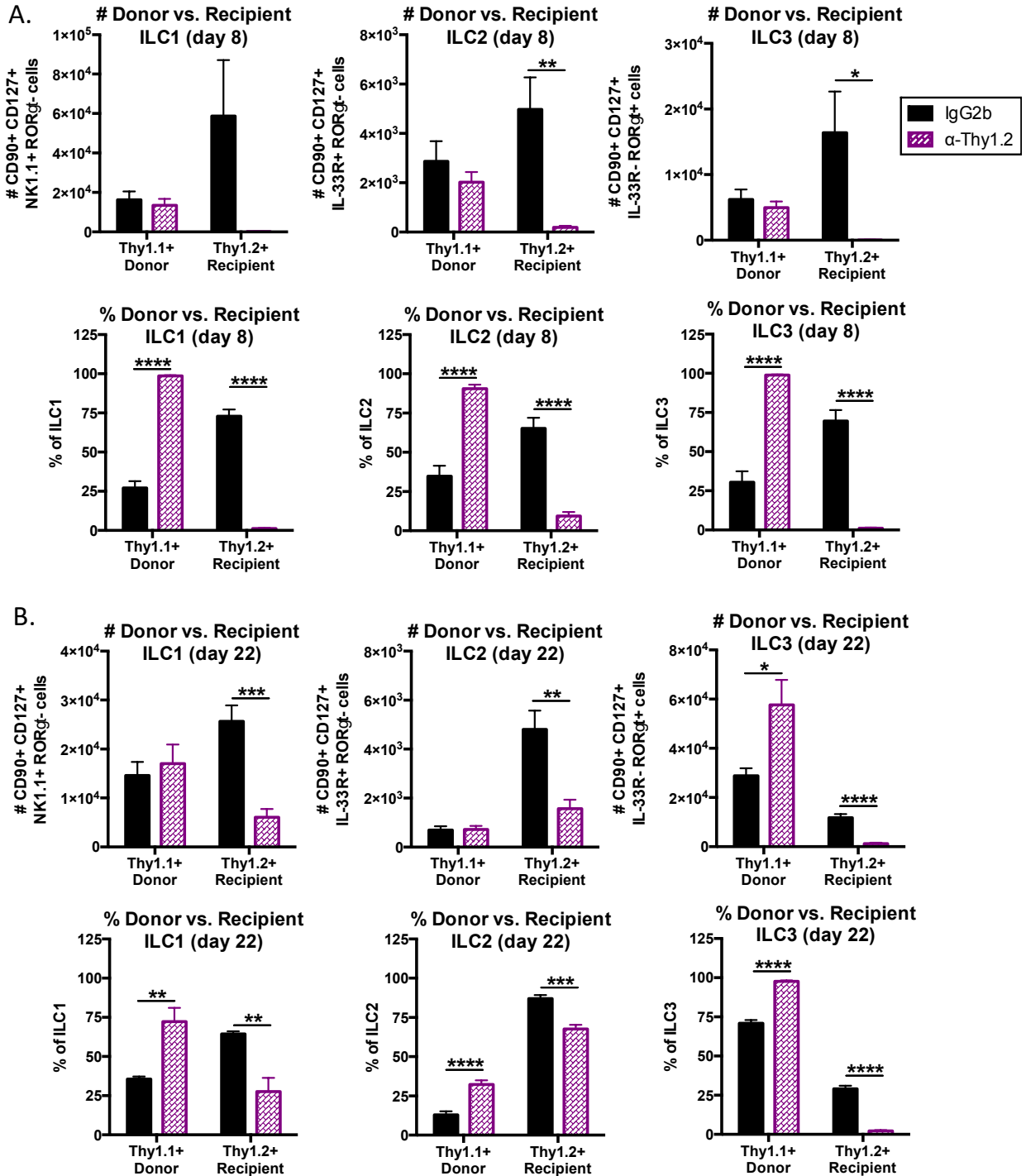
Figure 4.12. Anti-Thy1.2-mediated ILC depletion drives repopulation of donor-derived ILC3s in the liver. Adult (>6wks) HBVtg*Rag1-/-* animals were treated with anti-Thy1.2-depleting antibodies (αThy1.2) or IgG2b control antibody every three days starting at 3 wks of age (day -21) and continuing until sacrifice (day 22 group) or were treated every three days starting at day -4 and continuing until sacrifice (day 8 group) with adoptive transfer of HBV naïve WT splenocytes on day 0. Flow cytometry was performed and the number and percentage of Thy1.1+ donor and Thy1.2 recipient ILC1 (CD45+ TCRβ- Thy1+ CD127+ IL-33R- RORγt- NK1.1+), ILC2 (CD45+ TCRβ- Thy1+ CD127+ IL-33R+ RORγt-), and ILC3 (CD45+ TCRβ- Thy1+ CD127+ IL-33R- RORγt+), was determined on day 8 (**A**) and day 22 (**B**) post-adoptive transfer. Data were analyzed using FlowJo™ Software; statistics determined by unpaired two-tailed t-test with GraphPad Prism Software; * p<0.05, ** p<0.01, *** p<0.001, **** p<0.0001; n=5 per group.

I took a closer look at phenotypic markers of ILC3s to better understand differences between splenic- and hepatic-derived ILC3s. I observed that both Thy1.1+ donor and Thy1.2+ recipient ILC3s were dominated by NKp46- ILC3s, but that anti-Thy1.2-depleted mice had a slight increase in the percentage of Thy1.1+ NKp46+ ILC3s, suggesting that this population was either more enriched in donor spleens compared to liver, or instead that it had a greater capacity to home to the liver relative to the Thy1.1+ NKp46- ILC3s (**Fig. 4.13 A, C**). When examining MHCII expression on ILC3s I noted that although few Thy1.2+ ILC3s could be found in the liver of anti-Thy1.2-treated mice, the ones that were present expressed much higher levels of MHCII compared to control Ig-treated Thy1.2+ ILC3s, as well as Thy1.1+ ILC3s in anti-Thy1.2-treated and control mice, particularly at day 22 (**Fig. 4.13 B, D**). This suggests that the hepatic environment in which tissue-resident ILC3s – or possibly, circulating but host-derived ILC3s – repopulate favors an MHCII+ ILC3 phenotype. This did not appear to be the case for the Thy1.2+ ILC3s in control mice, which indicates that something about the loss of ILC3s within the liver facilitates this differentiation program, possibly related to the cytokine milieu, or instead a feature of all newly differentiated ILC3s in the liver that is normally masked by a population of fully mature hepatic ILC3 in the control mice that have since down regulated MHCII. Donor Thy1.1+ ILC3s from the spleen tended to have more MHCII expression compared to Thy1.2+

ILC3s. These data are consistent with the observation that splenic ILC3s can express high levels of MHCII (*37, 38*).
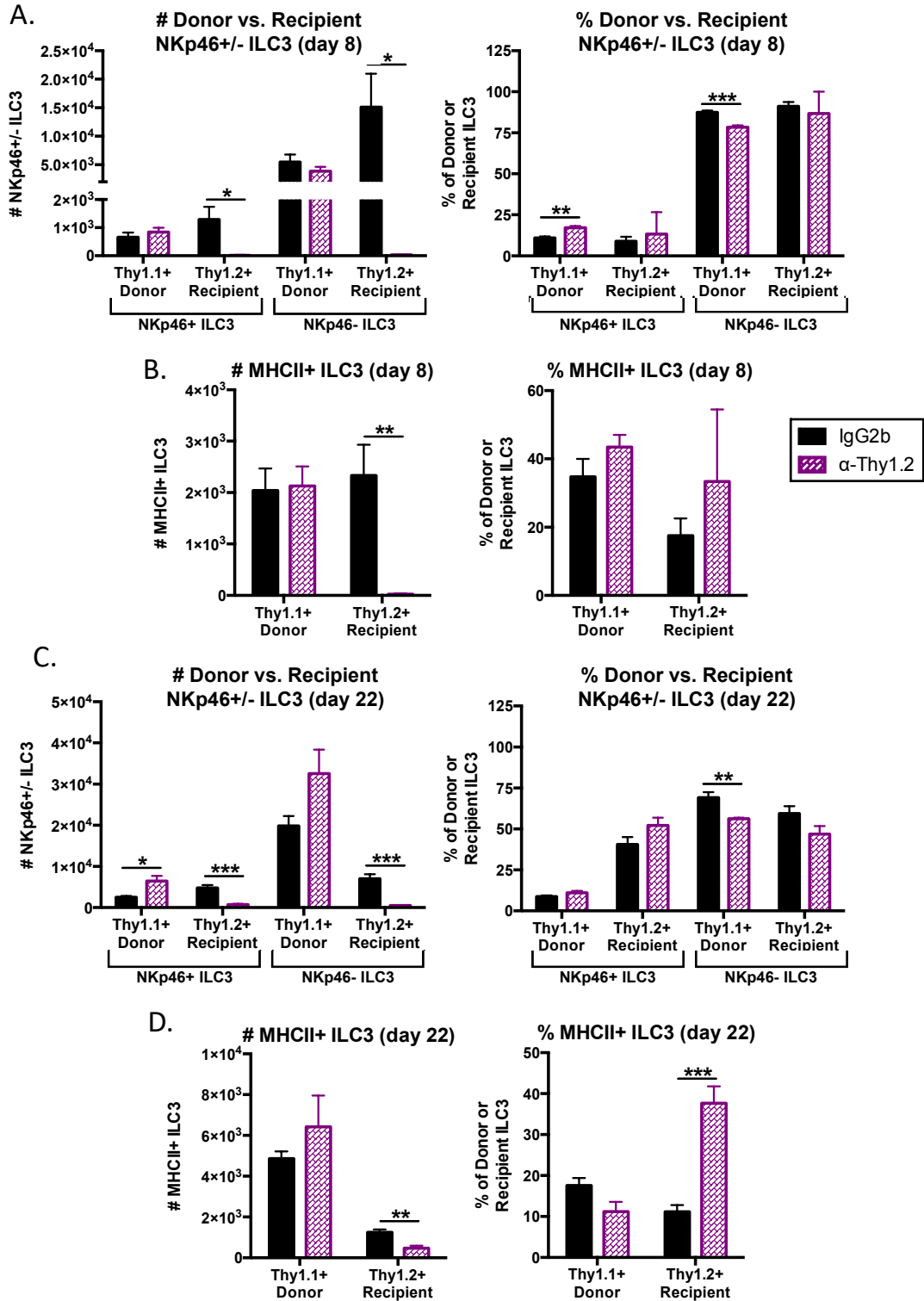
Figure 4.13. Anti-Thy1.2-mediated ILC depletion alters the phenotype of repopulated ILC3 in the liver. Adult (>6wks) HBVtg*Rag1*-/- animals were treated with anti-Thy1.2-depleting antibodies (αThy1.2) or IgG2b control antibody every three days starting at 3 wks of age (day -21) and continuing until sacrifice (day 22 group) or were treated every three days starting at day -4 and continuing until sacrifice (day 8 group) with adoptive transfer of HBV naïve WT splenocytes on day 0. Flow cytometry was performed and the number and percentage of (**A, C**) NKp46+ and NKp46- and (**B, D**) MHCII+ Thy1.1+ donor and Thy1.2+ recipient ILC3 (CD45+ TCRβ- Thy1+ CD127+ IL-33R- RORγt+), was determined on day 8 (**A-B**) and day 22 (**C-D**) post-adoptive transfer. Data were analyzed using FlowJoᴛᴍ Software; statistics determined by unpaired two-tailed t-test with GraphPad Prism Software; * p<0.05, ** p<0.01, *** p<0.001; n=5 per group.

We performed additional tissue staining with anti-RORγ (purple), anti-CD11b (teal), and anti-CD3e (yellow), first looking at tissue from animals on day eight post-splenic reconstitution. As expected, the control adult livers showed patterns of small- and medium-sized clusters spread throughout the liver parenchyma and around portal tracts (**Fig. 4.14 A-C**). The CD11b+ cells that can been seen lining the liver sinusoids, almost certainly liver resident Kupffer cells, form networks of clusters that reach out into the tissue, sometimes forming bridges between other clusters anchored by CD11b+ cells. Within these clusters, purple RORγ+ ILC3 and RORγ+ CD3+ T cells can be seen with other CD3+ T cells. The anti-Thy1.2-depleted mice had distinct periportal inflammation with very large clusters of CD11b+ cells mixed with together with CD3+ and RORγ+ cells, similar to clustering observed in *Rorc*(γt)-/- mice (**Fig 4.14 D-F**). Although CD11b+ cells can still be seen lining the sinusoids, the cluster-associated CD11b+ cells form tighter packed clusters with edges that define more distinct cluster borders relative to control mice. These data clearly show a role for ILC3-mediated immune cell localization in the liver, as both genetic depletion, as well as acute antibody-mediated depletion, led to profound reorganization of immune cells, particularly the CD11b+ cells that form the basis of the immune cell clusters. We are excited to characterize these differences in a quantitative way with the Ilastik imaging analysis approach we have developed.
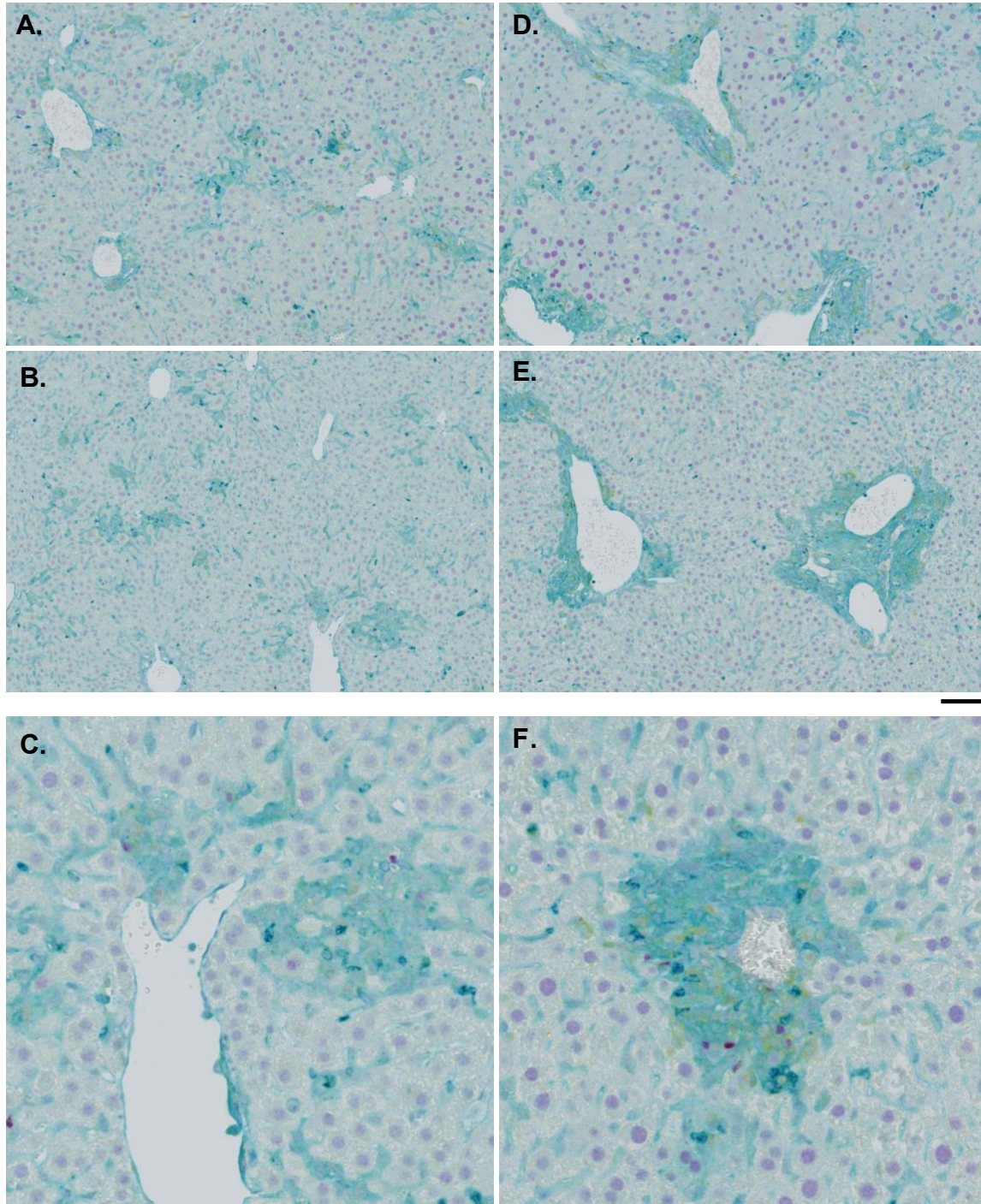
Figure 4.14. Anti-Thy1.2-mediated ILC depletion alters myeloid cell clustering around portal tracts and throughout the liver parenchyma during acute HBV immunity. Liver tissue was isolated from adult IgG2b isotype-matched control (**A-C**) or anti-Thy1.2 (**D-F**) antibody-treated HBVtg*Rag1*-/- mice 8 days post- adoptive transfer with Thy1.1 HBV-naïve splenocytes and drop-fixed in formalin for 24 hours, followed by ethanol dehydration and embedding into paraffin wax blocks. FFPE tissue blocks were sectioned at 4 μm and stained with anti-RORγ (purple), anti-CD11b (teal), and anti-CD3e (yellow) using the Ventana Discovery Ultra platform. Stained sections were imaged at 20X resolution with the Zeiss Axioscanner Z1. Scale bars represent 100 μm for (**A-B, D-E**), and 50 μm for (**C, F**).

On day 22 post-transfer we noted some evidence of residual inflammation in control mice, particularly around portal tract areas, though some small parenchymal clusters were also present (**Fig 4.15 A-C**). Anti-Thy1.2-treated mice again showed enhanced periportal inflammation with more defined cluster edges, similar to the day 8 animals (**Fig. 4.15 D-F**). Consistent with the flow cytometry data that suggested there may be more RORγt+ ILC3 in anti-Thy1.2-treated mice (**Fig 4.11 B**), we saw a high number of RORγ+ ILC3 and RORγ+ CD3+ T cells associated with a majority of the large periportal clusters. These data indicate that despite repopulation of the liver with splenic ILC3s by this time point, the initial loss of hepatic ILC3s by Thy1.2 depletion is sufficient to induce lasting changes in hepatic immune cell organization.
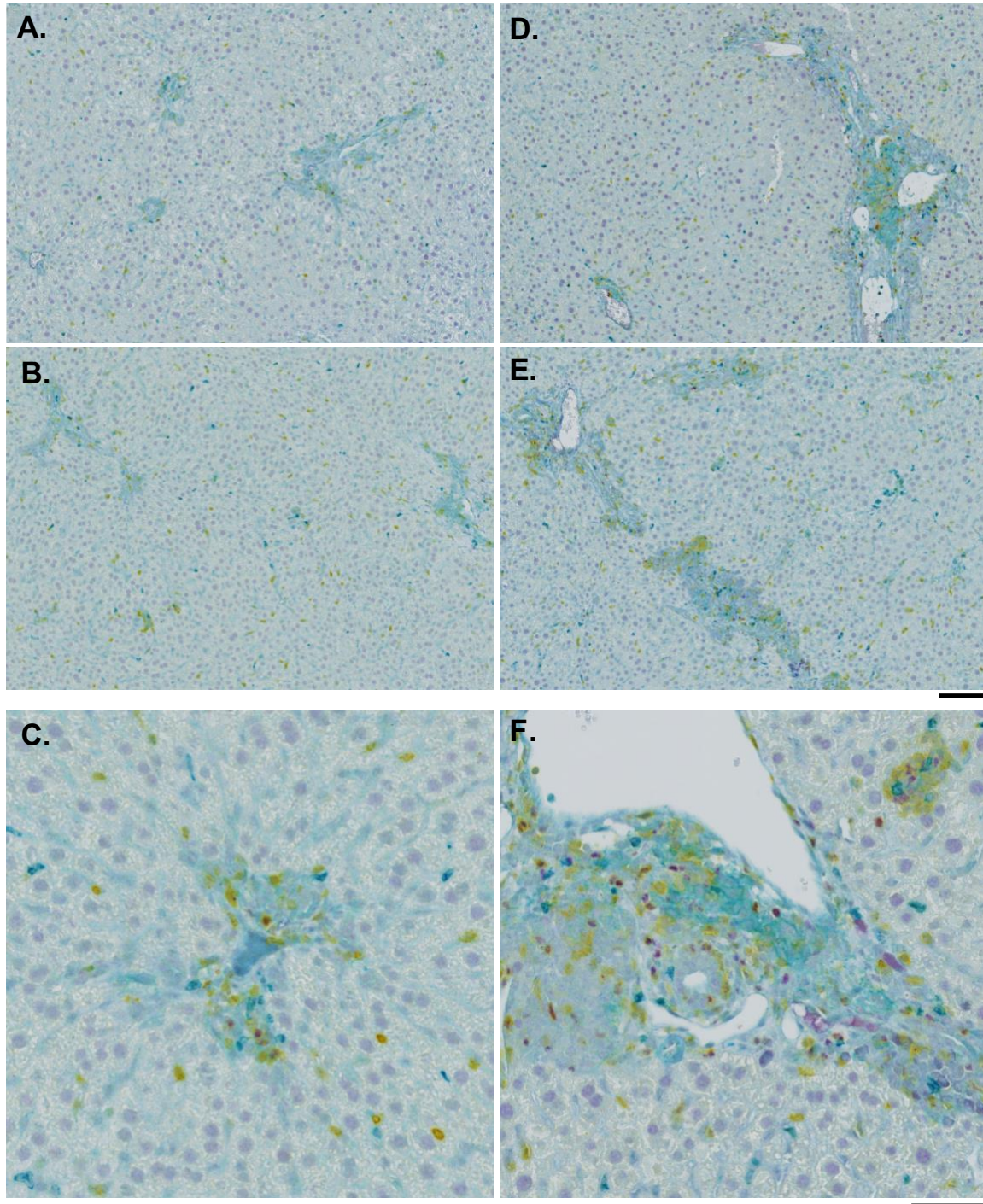
Figure 4.15. Anti-Thy1.2-mediated ILC depletion alters sustained myeloid cell clustering around portal tracts during HBV immunity. Liver tissue was isolated from adult IgG2b isotype-matched control (**A-C**) or anti-Thy1.2 (**D-F**) antibody-treated HBVtg*Rag1*-/- mice 22 days post- adoptive transfer with Thy1.1 HBV-naïve splenocytes and drop-fixed in formalin for 24 hours, followed by ethanol dehydration and embedding into paraffin wax blocks. FFPE tissue blocks were sectioned at 4 μm and stained with anti-RORγ (purple), anti-CD11b (teal), and anti-CD3e (yellow) using the Ventana Discovery Ultra platform. Stained sections were imaged at 20X resolution with the Zeiss Axioscanner Z1. Scale bars represent 100 μm for (**A-B, D-E**), and 50 μm for (**C, F**).

Finally, we also looked at staining of anti-RORγ (purple), anti-CD45R/B220, and anti-CD3 on day 22 post-adoptive transfer, to assess the influx of B cells into the liver (**Fig. 4.16**). The control Ig-treated mouse livers showed a number of B220+ cells within the tissue that could mostly be found associated with immune cell clusters including T cells, ILC3s, and a number of unidentified cells that presumably are partially made up of CD11b+ cells (**Fig. 4.16 A-B**). The anti-Thy1.2-depleted mice also had a number of B cells associated with immune cell clusters; however, there were notably several instances of large B cell-rich clusters that formed, highly reminiscent of that seen in *Rorc*(γt)-/- animals at this same time point (**Fig. 4.16 C-D** and **Fig. 3.10 G-H**). These data suggest that loss of ILC3s does lead to a large influx of B cells; however, the functional role of these B cells, particularly related to HBV immunity, remains unclear.
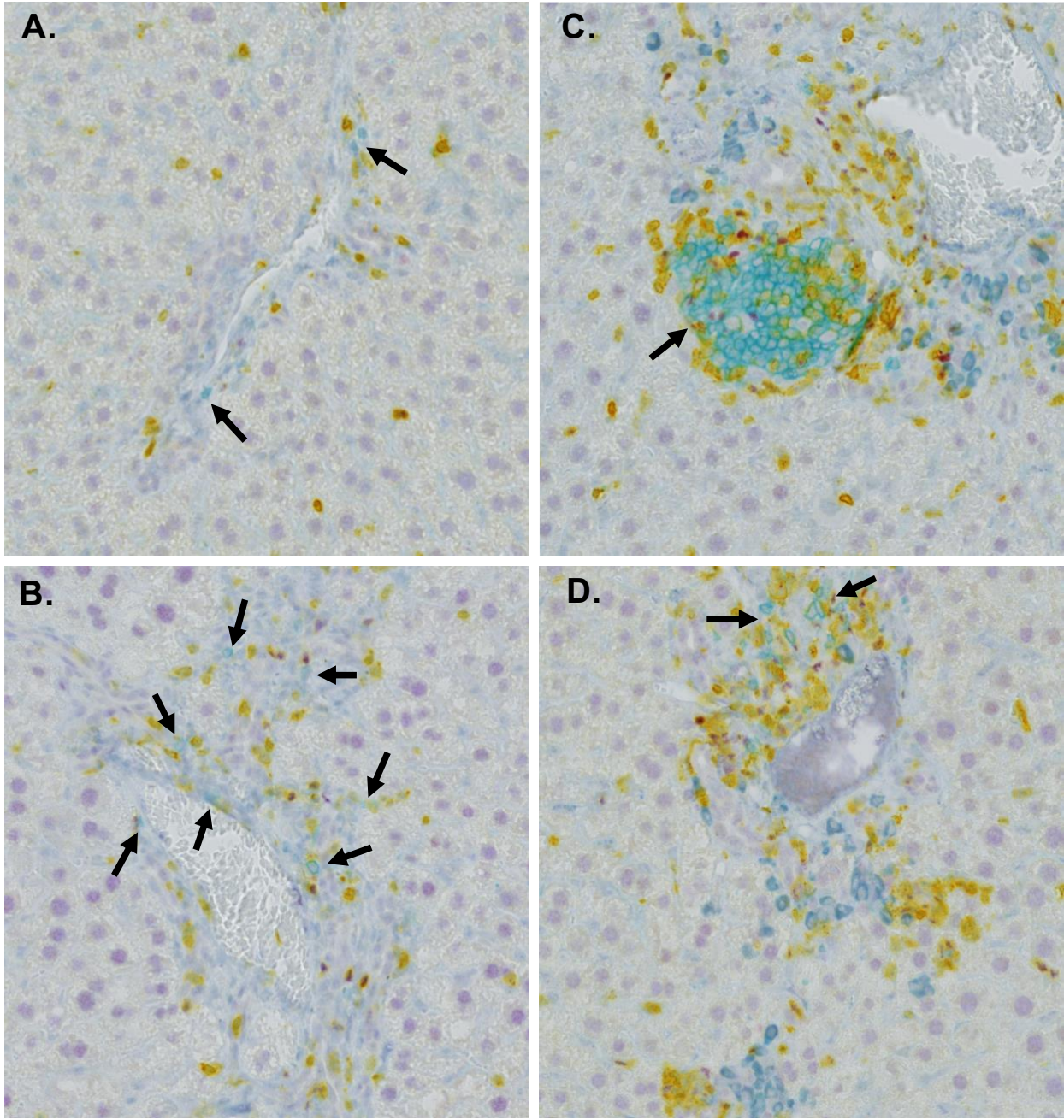
Figure 4.16. Anti-Thy1.2-mediated ILC depletion causes B cell cluster during HBV immunity. Liver tissue was isolated from adult IgG2b isotype-matched control (**A-B**) or anti-Thy1.2 (**C-D**) antibody-treated HBVtg*Rag1*-/- mice 8 days post- adoptive transfer with Thy1.1 HBV-naïve splenocytes and drop-fixed in formalin for 24 hours, followed by ethanol dehydration and embedding into paraffin wax blocks. FFPE tissue blocks were sectioned at 4 μm and stained with anti-RORγ (purple), anti-B220 (teal), and anti-CD3e (yellow) using the Ventana Discovery Ultra platform. Stained sections were imaged at 20X resolution with the Zeiss Axioscanner Z1. Arrows point to B220+ B cells alone or in clusters with other B cells Scale bars represent 50 μm.

Discussion

The experiments and data presented in this chapter helped us to identify important similarities between genetically deficient *Rorc*(γt)-/- mice and acutely ILC3-deficient mice to better understand how the loss of ILC3s contributes to impaired HBV immunity. Although these two models are not without caveats, the concordance between datasets solidifies the observations and conclusions gained from each model separately.

Specifically, we have uncovered a role for ILC3s in affecting the hepatic localization and organization of CD11b+, CD4+, CD8+, and B220+ immune cells. We observed that the loss of ILC3s resulted in extreme periportal inflammation and the generation of large immune clusters with defined edges, which isolate these clusters from the rest of the liver parenchyma. This was in contrast to animals that are sufficient for ILC3s, which demonstrated more moderate immune cell clustering that was both periportal and intraparenchymal. Furthermore, the structures present in ILC3-sufficient mice did not have defined borders, and instead had CD11b+ cells that stretched throughout the parenchyma, in some instances forming loose connections between multiple immune cell clusters. The effects of this immune cell reorganization in the absence of ILC3s is unclear; however, we do know that animals that exhibit these patterns either fail to clear antigens or have delayed antigen clearance, suggesting that they are not efficient sites of HBV-specific immune priming.

We also uncovered a deficit in antigen-specific T cell responses in the absence of ILC3s. Genetically deficient *Rorc*(γt)-/- mice have a clear and sustained defect in response to the most dominant CD4+ HBV epitope identified in this system, peptide 81. Although the magnitude of the response to this peptide was reduced in the acutely depleted anti-Thy1.2-treated mice, we

also observed a decreased response to other HBV dominant epitopes, including MHCI- and MHCII-restricted epitopes. Again, these data highlight that ILC3s play a supportive role in the generation and sustained activities of HBV-specific T cells, with a particular defect in CD4+ T cell responses.

Another consistent difference present in both models was the increased infiltration of total CD4+ T cells with an effector-like phenotype. This influx was particularly dramatic during early time points in the *Rorc*(γt)-/- mice and partially subsided by one-month post-transfer. Anti-Thy1.2-depleted mice, on the other hand, did not have a major CD4+ T cell influx present until later time points, which occurred only in the animals that received a longer Thy1.2-depletion regimen starting at the time of weaning. These data suggest that additional indirect mechanisms of ILC3 loss may contribute to this CD4+ T cell influx, particularly changes in gut microbial communities and/or effects of ILC3 loss on other hepatic innate immune cells capable of activating and recruiting CD4+ T cells.

Despite this CD4+ T cell influx, and substantial IFNγ production by this subset, we know that these cells are less effective at targeting HBV antigens, as demonstrated in the ELISpot assays described above. Furthermore, we also found a defect in support of central memory CD4+ T cells, suggesting that an inability to maintain a population of memory CD4+ T cells may contribute to their inability to control HBV. In order to address this question directly, we will use HBV-specific MHCII tetramers to identify antigen-specific T cells and evaluate markers of T cell memory and function, particularly the expression of the long-lived memory marker CD127 and production of IFNγ by cytokine capture assays.

Another interesting phenotype we would like to follow up on, is the observation of decreased Tfh in *Rorc*(γt)-/- mice that only appeared at later time points. As highlighted throughout this thesis, Tfh play an essential role in HBV immunity, and thus, it is reasonable to predict that a defect in a sustained Tfh response would contribute to impaired HBV immunity in these mice. Unfortunately, I was not able to assess Tfh cells in the anti-Thy1.2 depletion experiments discussed in this chapter. Therefore, this is also an area we plan to revisit to determine if acute ILC3 depletion, even with the infiltration of splenic ILC3s, may also lead to impaired Tfh responses. However, we do know that although antigen clearance was delayed in anti-Thy1.2-depleted mice, it was not blocked as was the case of *Rorc*(γt)-/- mice. Thus, it is possible that Tfh cell responses may not be as impaired in anti-Thy1.2-depleted animals because the influx of splenic ILC3s may help support a delayed, but sufficient, Tfh response that can contribute to HBsAg clearance in these animals at a later time.

Finally, we also plan to further investigate the ability of transferred ILC3s to support improved HBV immunity in the context of ILC3-deficient hosts. We hope to distinguish between the role of adoptively transferred ILC3s in supporting delayed but apparent HBsAg clearance in anti-Thy1.2-depleted mice versus the transfer of splenocytes which lack ILC3s (from donor *Rorc*(γt)-/- mice), which we would hypothesize may prevent the eventual antigen clearance that happened in anti-Thy1.2-depleted mice due to an inability to repopulate hepatic ILC3s.

Chapter 5: Identifying critical functional activities of ILC3s during anti-HBV immunity

Introduction

After identifying a role for ILC3s in supporting HBV-specific T cell responses, immune cell distribution within the liver, and HBV antigen clearance we investigated the functional mediators of ILC3s with a logical experimental approach to identify how ILC3s function to regulate HBV immunity in the liver. As reviewed in earlier chapters, ILC3s have multifaceted roles in regulating immunity that can be generally categorized into three primary effector functions: (1) regulating lymphoid organization, (2) production of cytokines that regulate inflammation and immune priming, and (3) antigen presentation.

The first role of ILC3s in regulating lymphoid organization is most well attributed to a fetal subset of ILC3s, LTi cells, which are critical for lymphoid organogenesis of peripheral lymph nodes and Peyer's patches, but not the spleen. A similar population of cells persists into adulthood, known as LTi-like cells, and has also been shown to be essential for the development of cryptopatches and maturation of isolated lymphoid follicles in the gut, which have features similar to other lymphoid tissues (*24*). These cells can also mediate lymphoid organization within tertiary lymphoid structures, as well as facilitate the recovery of splenic architecture after viral infection and disruption of splenic T and B cell zones (*25*). LTi and LTi-like cells represent a subset of NKp46- ILC3s and are defined in mice by their expression of CD4 and CCR6, the latter of which has been shown to play a role in LTi-like cell recruitment and trafficking in response to the CCR6 ligand, CCL20. LTi and LTi-like cells also express lymphotoxin α (LTα) and LTβ, which together form the trimer LT$\alpha_1\beta_2$, along with LIGHT, a closely related TNF family member that, like lymphotoxin, also binds and stimulates LTβR on hematopoietic cells

and on non-hematopoietic stromal lymphoid "organizer" cells. LTi and LTi-like cells express other TNF family members including RANKL (TNFSF11), which has also been shown to contribute to lymphoid organization. Several studies have pointed to a role for IL-17, which is a major cytokine produced by LTi and LTi-like cells and NKp46- ILC3, in mediating and supporting lymphoid organization, such as in the case of bronchus-associated lymphoid tissue (*44-46*). Although IL-17 specifically from LTi and LTi-like or NKp46- ILC3s does not appear to be the essential source required for lymphoid organization, it is likely that IL-17 secretion by LTi-like cells together with expression of other molecules discussed above contributes in part to lymphoid organization.

The second major functional role of ILC3s is mediated through their secretion of cytokines, in particular IL-17, IL-22, and GM-CSF. IL-17 secretion is known to drive tissue inflammation, including the recruitment of neutrophils, as well as to promote activation of antigen-presenting cells to facilitate immune priming. One study illustrated a role for IL-17F secretion from ILC3s in the recruitment and activation of hepatic CD8+ CTLs, including their production of IFNγ and expression of CD107, a marker of degranulation (*83*). Other effects of IL-17 include controlling fungal and bacterial infections (*47, 48*). IL-17 and IL-22 are both known to regulate secretion of anti-microbial peptides that help regulate microbial colonization (*54, 55, 58*). IL-22 further supports barrier integrity and wound healing through direct actions on epithelial and stromal cells (*57, 60, 61*). IL-22 production by ILC3s plays a critical role in regulating immunity to various bacterial pathogens (*56, 62*). GM-CSF production by ILC3s also contributes to the recruitment and activation of myeloid cells and the priming and maintenance of T cells (*49, 50*).

Finally, ILC3s have also recently been identified as an important antigen-presenting cell that, depending on context, can either promote CD4+ T cell priming and activation, or alternatively, result in cell death. The ability of ILC3s to present antigen is dependent on their expression of MHCII along with associated co-stimulatory molecules. The population of ILC3s that reside in the spleen have been described as having efficient priming capacity, similar to that of DCs under certain *in vitro* conditions, due in part to their high level of MHCII expression and co-expression of CD74, CD86, and OX40L (*37, 38*). In the small intestine, however, a lower level of MHCII expression on ILC3s and a reduced frequency of co-stimulatory molecules results in a diminished capacity to prime CD4+ T cells and, in fact, seems to play a critical role in triggering cell death of commensal microbe-specific T cells to prevent inappropriate gut inflammation (*35, 37, 69*).

We investigated the contributions of ILC3-derived cytokines and their expression of molecules known to regulate lymphoid organization by specifically blocking a number of the molecules, or their receptors, described above. After observing that there was a greatly enriched mRNA transcript signal of CCR6 in adult mice that control HBV compared to young mice that develop "chronic infection" (**Fig. 1.17**), we crossed *Ccr6-/-* mice with our HBVtg*Rag1-/-* mice to investigate whether CCR6 is required for effective HBV control. We investigated the role of lymphotoxins and LIGHT in HBV immune outcomes and in the organization of immune cells within liver tissue by performing a series of experiments using *Tnfsf14-/-* (LIGHT-/-) mice, as well as a blockade of lymphotoxins with a LTβR-Ig fusion protein, the receptor for LIGHT and LTα$_1$β$_2$ (*84*). We chose not to study lymphotoxin-deficient mice, as they have profound immunological defects due to the essential role of this molecule in the formation of all lymphoid tissues. Finally, we performed antibody-mediated cytokine blockade experiments using the

antagonistic antibodies against IL-17RA (the receptor for IL-17A and IL-17F), IL-17F, IL-22, and GM-CSF to address the role of each cytokine in HBV immunity.

Results

5.1 – The role of CCR6 in HBV immunity

I assessed anti-HBV immunity in ILC3-sufficient HBVtg*Rag1*-/-*Ccr6*-/- compared to HBVtg*Rag1*-/- and ILC3-deficient HBVtg*Rag1*-/-*Rorc*(γt)GFP/GFP mice. These *Ccr6*-/- mice lack expression of CCR6 on resident innate immune cells but were reconstituted with wild-type CCR6-replete splenocytes after adoptive transfer. Compared to HBVtg*Rag1*-/- mice, *Ccr6*-/- mice had similar levels of plasma ALT, which were both reduced relative to ILC3-deficient mice (**Fig. 5.1 A**). I also found no difference in the clearance of HBsAg by *Ccr6*-/- mice as compared to HBVtg*Rag1*-/- controls, though as previously seen, ILC3-deficient animals failed to clear HBsAg (**Fig. 5.1 B**). When I measured HBV antigen-specific IFNγ production by *Ccr6*-/- mice at a late time point, I found these mice were able to mount a response to three different pools of HBsAg peptides: pool 4, 6, and 7, which contain peptides 48, 82, and 88/190 and 92/207, respectively (**Fig. 5.1 C**). Control animals also responded to three peptide pools: pool 3, 6, and 7. Peptide pool 3 contains peptide 32, another sub-dominant epitope described in more detail in Chapter 1 (also referred to as HBs126). These data suggested that CCR6 deficiency does not impair IFNγ responses or HBsAg clearance and indicated that CCR6 was likely not a major contributor to the phenotype observed in ILC3-deficient animals. Importantly, although CCR6 expression is found within LTi/LTi-like cells, the lack of CCR6 dependency does not rule out a potential role for this subset of ILC3s independent of CCR6-mediated trafficking, as the loss of CCR6 does not affect the number of these ILC3s.
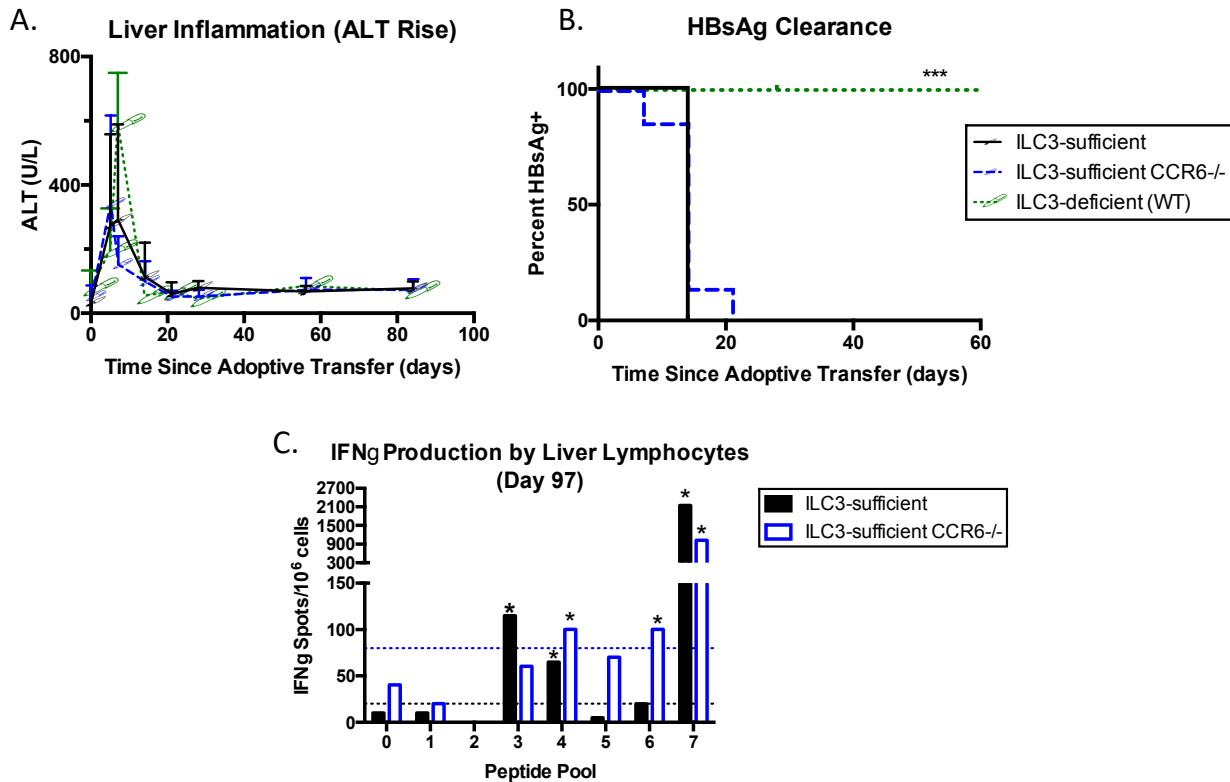
Figure 5.1. CCR6 deficiency does not impair HBV immunity. Adult (>8 wks) HBVtg*Rag1*-/- animals (ILC3-sufficient), HBVtg*Rag1*-/-*Ccr6*-/- (ILC3-sufficient CCR6-/-), and *Rorc*(γt)GFP/GFPHBVtg*Rag1*-/- (ILC3-deficient) animals were adoptively transferred with HBV-naïve WT splenocytes. (**A**) Liver disease was monitored by plasma alanine aminotransferase (ALT). (**B**) Clearance of circulating HBsAg was monitored over time by qualitative ELISA. (**C**) Hepatic leukocyte-enriched cell preparations were isolated from animals on day 97 post adoptive transfer. 10_5 liver leukocytes were mixed in a 1:1 ratio with splenocytes from *Rag1*-/- mice as a source of APCs and stimulated overnight at 37°C together with pools of 12-14 fifteen-mer peptides spanning the entire length of the HBV envelope protein in ELISpot plates pre-coated with anti-IFNγ antibodies. "0" peptide pool denotes no peptide added. Antigen-specific IFNγ production was measured and displayed as the total number of IFNγ spots per 10_6 cells. ELISpot plates were counted and analyzed with a CTL Immunospot plate reader and software. The threshold defining a positive response, marked with a *, is ≥2× the baseline (dashed line). Statistics for (**B**) determined by a log-rank (Mantel-Cox) Chi square survival test with GraphPad Prism Software; *** p<0.001, n≥7 per group for (**A-B**), n=pooled from 7 mice per group for (**C**).

5.2 – The role of LIGHT in HBV immunity

I investigated the effect of LIGHT-deficiency [*Tnfsf14*-/- (*85*)] on HBV disease outcome when absent on the recipient innate immune compartment in HBVtg*Rag1*-/-*Tnfsf14*-/- mice. I

observed a marked increase in early inflammation and hepatitis, as measured by plasma ALT, in LIGHT-deficient animals relative to controls (**Fig. 5.2 A**). The absence of LIGHT on recipient immune cells did not impair HBV antigen clearance compared to controls, as 6 out of 7 animals in the *Tnfsf14*-/- group had cleared antigen by day 14, with the same number of mice clearing HBsAg in the control group by day 21 (**Fig. 5.2 B**). I found evidence of enhanced HBV immunity in LIGHT-deficient mice, as 5 of 7 animals had made detectable anti-HBs antibodies by day 36 post-transfer, compared to only 1 control animal (**Fig. 5.2 C**). In our system, we usually begin to detect anti-HBs antibodies as early as one-month post-transfer, but it can often take up to two or three months for the majority of the animals to generate a detectable response. The early antibody response in LIGHT-deficient animals highlights a potential role for this molecule on innate immune cells in suppressing B cell secretion of antibodies. I found additional evidence suggesting LIGHT on innate immune cells normally restricts effective HBV immunity, as LIGHT-deficient animals had a highly robust IFNγ response to HBV peptide stimulation, beyond what was seen in control mice (**Fig. 5.2 D**). Taken together these experiments indicate that LIGHT expression within an innate immune population present in *Rag1*-/- recipient mice can restrict both T and B cell responses towards HBV antigens. Although LIGHT does interact with the lymphotoxin receptor, LTβR, it has another receptor – HVEM (herpesvirus entry mediator/TNFSF14R) – which is known to exert negative regulatory effects on lymphocytes in certain contexts (*86-88*). Thus, further dissection of this system is required to understand how LIGHT mediates its anti-HBV immune suppressive effects and which receptor(s) contribute to these effects.
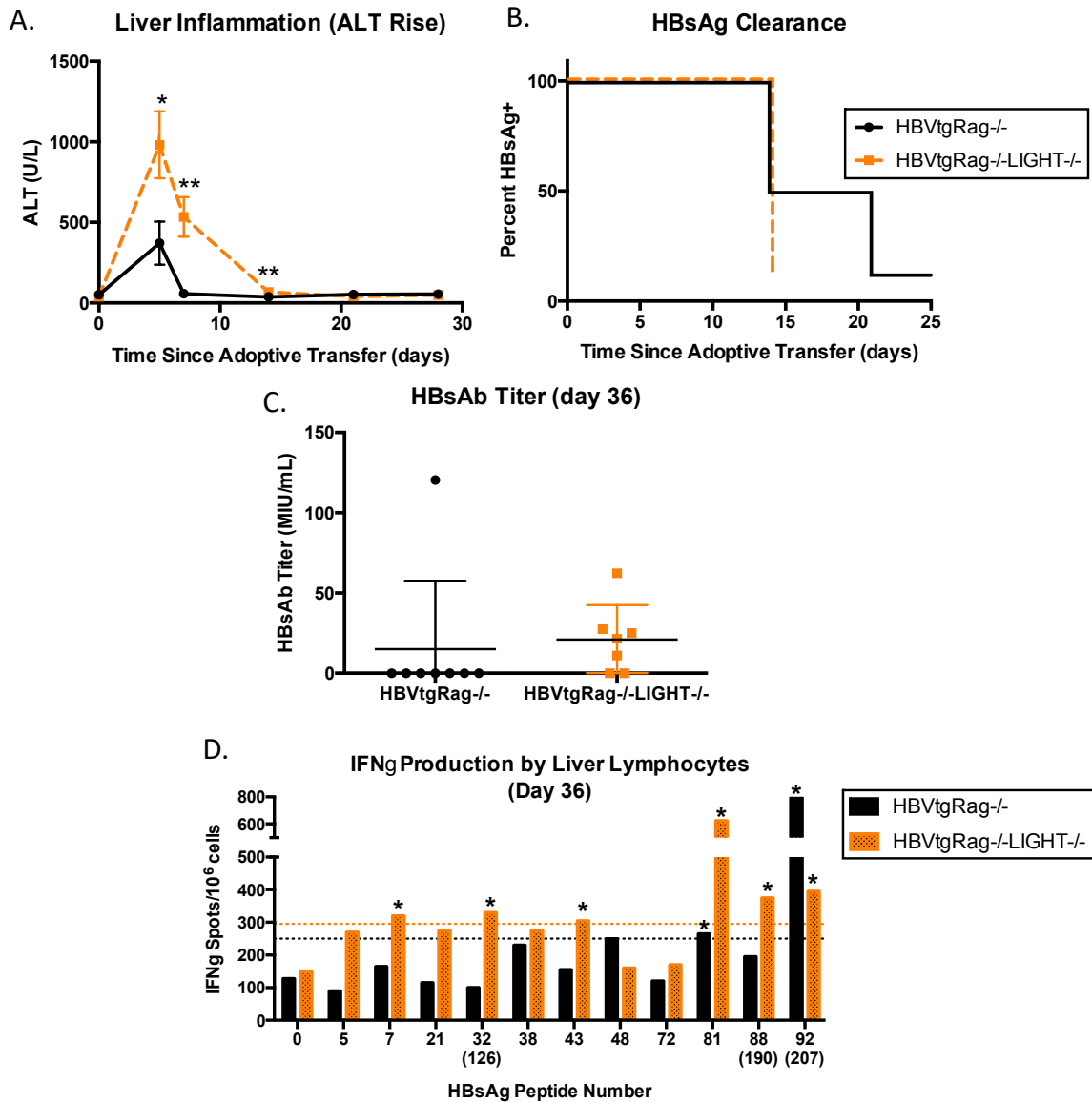
Figure 5.2. LIGHT deficiency in host animals leads to enhanced HBV immunity. Adult (>8 wks) HBVtg*Rag1-/-* and HBVtg*Rag1-/-Tnfsf14-/-* (LIGHT-/-) mice were adoptively transferred with HBV-naïve WT splenocytes. (**A**) Liver disease was monitored by plasma alanine aminotransferase (ALT). (**B**) Clearance of circulating HBsAg and (**C**) production of anti-HBs antibodies were monitored over time by qualitative and quantitative ELISAs, respectively. (**D**) Hepatic leukocyte-enriched cell preparations were isolated from animals on day 97 post adoptive transfer. 10_5 liver leukocytes were mixed in a 1:1 ratio with splenocytes from *Rag1-/-* mice as a source of APCs and stimulated overnight at 37°C together with individual peptides spanning the entire length of the HBV envelope protein in ELISpot plates pre-coated with anti-IFNγ antibodies. "0" peptide pool denotes no peptide added. Antigen-specific IFNγ production was measured and displayed as the total number of IFNγ spots per 10_6 cells. ELISpot plates were counted and analyzed with a CTL Immunospot plate reader and software. The threshold defining a positive response, marked with a *, is ≥2× the baseline (dashed line). Statistics for determined by a unpaired two-tailed t-ted or log-rank (Mantel-Cox) Chi square survival test with GraphPad Prism Software; * p<0.05, ** p<0.01, n≥7 per group for (**A-B**), n=pooled from 7 mice per group for (**C**).

5.3 – The role of LTβR in HBV immunity and lymphoid organization

We took another approach to explore the possible effects of lymphotoxins, LIGHT, and the receptor LTβR on HBV-mediated immunity by treating adult HBVtg*Rag1*-/- mice with a LTβR-Ig fusion protein (hereafter referred to as LTβR-Fc) that binds and sequesters LTβR ligands – LTα₁β₂ and LIGHT – such that it prevents their signaling through endogenous LTβR and HVEM receptors (*89*). We initiated a collaboration with Dr. Carl Ware to receive and test this reagent in our model. We were particularly interested in using this reagent to determine whether blockade of this pathway might have effects on lymphoid organization. In contrast to *Tnfsf14*-/- mice, animals treated with LTβR-Fc had greatly diminished hepatitis as measured by plasma ALT (**Fig. 5.3 A**). There was some evidence of delayed HBsAg clearance in LTβR-Fc-treated animals as only 2 of 7 mice had cleared antigen by day 14 compared to 6 of 7 control mice; however, these groups were not statistically different (**Fig. 5.3 B**). We have yet to follow these mice for longer-term experiments, since it is known that mice eventually develop antibodies against the fusion protein, which contains the mouse LTβR fused to a human IgG1 Fc; even so, it will be interesting to understand if this early blockade may have lasting effects on antigen clearance.

Despite seeing evidence of reduced hepatitis in LTβR-Fc-treated mice, there was evidence of increased portal-associated inflammation in these same mice (**Fig. 5.4 C-E**). It is worth noting, however, that this response was only seen in some of the LTβR-Fc-treated mice, particularly the ones that did have a substantial ALT rise. However, when comparing two mice that had identical ALT rises, we observed that the LTβR-Fc-treated mouse had more dramatic portal inflammation compared to the control mouse, particularly with an influx of CD4+ T cells

(**Fig. 5.4 C-D**). It will be important to also look at tissue staining patterns of CD11b+ myeloid cells – crucial participants in the formation hepatic immune clusters that– to determine whether LTβR-Fc blocking treatments also influence the distribution and organization of these cells.

I assessed HBV-specific immunity in these animals by performing an IFNγ ELISpot assay and found that, similar to ILC3-deficient animals, there was increased baseline IFNγ production in LTβR-Fc-treated mice with a restricted HBV-specific response (**Fig. 5.3 F**). Distinct from the ILC3-deficient mice, LTβR-Fc-treated animals were able to mount a robust response to peptide 81, suggesting that the consistently impaired response to peptide 81 in ILC3-deficient mice is likely a result of LTβR-independent mechanisms.

Finally, I assessed the abundance of CD4+ and CD8+ T cells in the livers of treated and control mice by flow cytometry. There was a trend towards a greater number of total T cells, caused mainly by a statistically significant increase in the number of hepatic CD4+ T cells, in the LTβR-Fc-treated mice (**Fig. 5.4 G**). This translated into an increased percentage of CD4+ T cells in LTβR-Fc-treated mice relative to control mice, although CD8+ T cells were still the dominant type of T cell recovered at this time point, which is different than what we observed in ILC3-deficient mice that are dominated by CD4+ T cells at day 8 (**Fig. 5.4 H**).
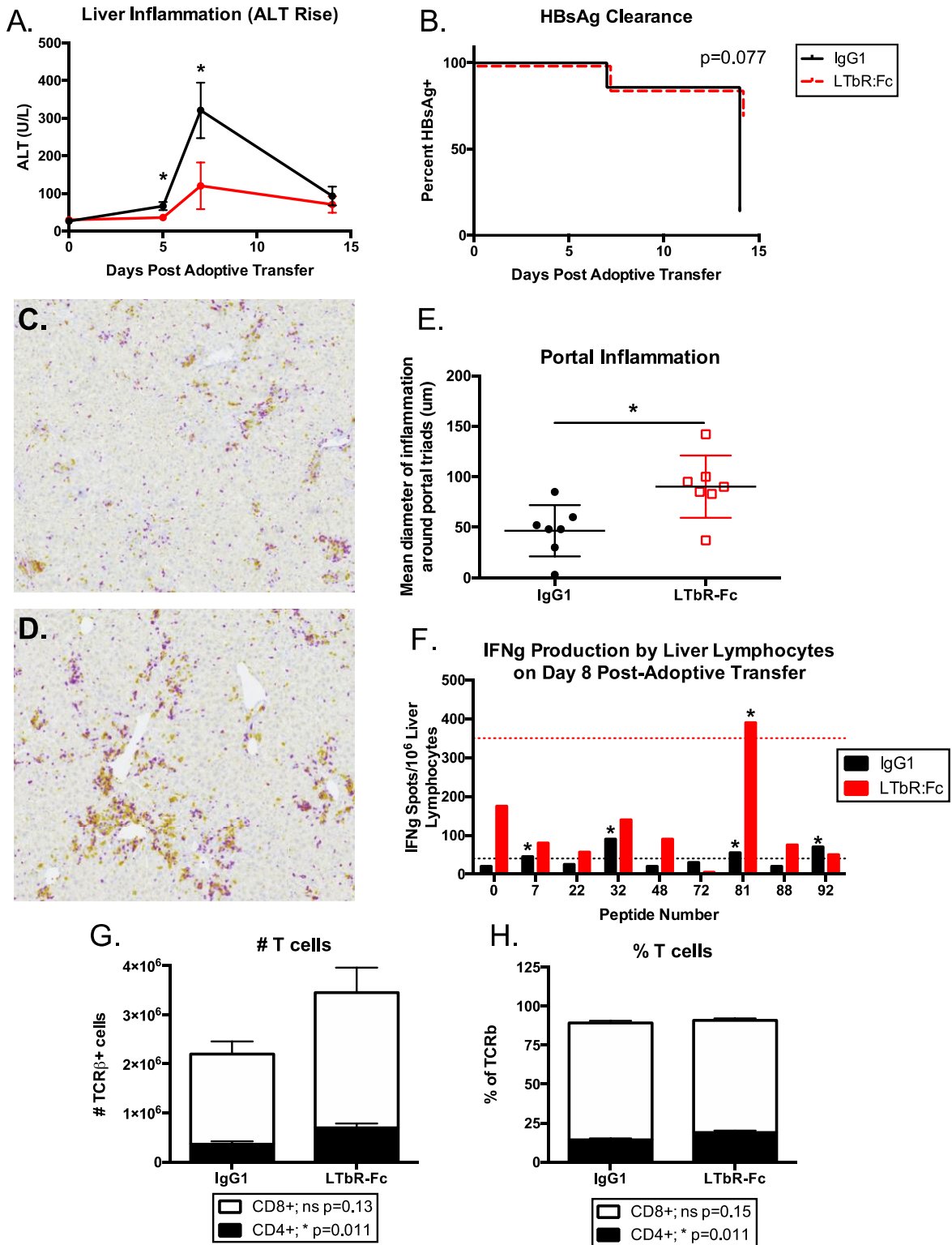
Figure 5.3. LTβR blockade alters HBV immunity and immune cell distribution in the liver. Adult (>8 wks) HBVtg*Rag1*-/- mice were treated with anti-LTβR- adoptively transferred with HBV-naïve WT

splenocytes. (**A**) Liver disease was monitored by plasma alanine aminotransferase (ALT). (**B**) Clearance of circulating HBsAg was monitored over time by qualitative ELISAs. (**C**) Control and (**D**) LTbR-Fc-treated liver sections from day 8 post-transfer were stained with anti-CD8 (purple) and anti-CD4 (yellow) using the Ventana Discovery Ultra platform. Stained sections were imaged at 20X resolution with the Zeiss Axioscanner Z1. (**E**) The mean diameter of portal associated inflammation was quantitated by a pathologist blinded to sample identity. (**F**) Hepatic leukocyte-enriched cell preparations were isolated from animals on day 8 post adoptive transfer. 10_5 liver leukocytes were mixed in a 1:1 ratio with splenocytes from *Rag1-/-* mice as a source of APCs and stimulated overnight at 37°C together with individual peptides from the HBV envelope protein in ELISpot plates pre-coated with anti-IFNγ antibodies. "0" peptide pool denotes no peptide added. Antigen-specific IFNγ production was measured and displayed as the total number of IFNγ spots per 10_6 cells. ELISpot plates were counted and analyzed with a CTL Immunospot plate reader and software. The threshold defining a positive response, marked with a *, is ≥2× the baseline (dashed line). Flow cytometry was performed and the number (**G**) and percentage (**H**) of CD4+ T cells (CD45+ TCRβ+ NK1.1- CD4+ CD8-) and CD8+ T cells was (CD45+ TCRβ+ NK1.1- CD4- CD8+) were determined. Statistics for determined by an unpaired two-tailed t-ted or log-rank (Mantel-Cox) Chi square survival test with GraphPad Prism Software; * p<0.05, n≥7 per group for (**A-E, G-F**), n=pooled from 7 mice per group for (**F**).

When taken together, these data suggest that a portion of the phenotype observed in ILC3-deficient mice may be due to a loss of lymphotoxin and/or LIGHT signaling, particularly related to immune cell distribution within the liver, and possibly a small contribution towards CD4+ T cell skewing. It remains to be seen whether LTβR-Fc treatment has a major effect on HBsAg clearance or HBs antibody seroconversion. The lack of hepatocyte necrosis and ALT release despite evidence of increased portal inflammation is intriguing; it is possible that these cells are less inflammatory in their production of cytokines and granules that have the potential to kill "infected" hepatocytes. Furthermore, the distinct difference in the antigen-specific response to peptide 81 suggests that there may be an antigen presentation defect in ILC3-deficient mice that is not recapitulated by LTβR-Fc treatment. It will be of great interest to further interrogate these antigen-specific T cell responses both at later time points and with the use of tetramers, to better understand the phenotype of these cells.

5.4 – The role of IL-17 in HBV immunity

I investigated the role of IL-17 by treating mice with antibodies targeting IL17RA – the receptor for both IL-17A and IL-17F – and IL-17F provided by a collaborator, Dr. Stephen Nishimura. At the time of these experiments I did not determine the effect of IL-17A-specfic blockade; however, I inferred that differences between IL-17R-blocked and IL-17F-blocked animals were likely due to IL-17A-mediated effects. When evaluating early liver inflammation measured by plasma ALT, I did not find any effect of IL-17 blockade compared to control animals (**Fig. 5.4**).

Liver Inflammation (ALT Rise)
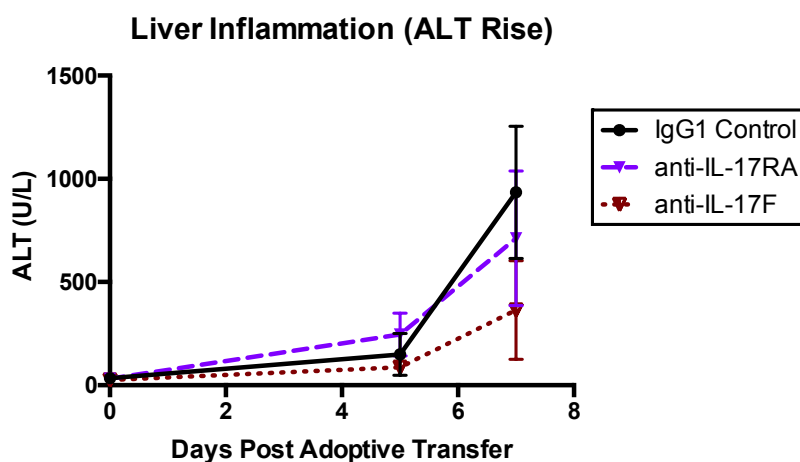
Figure 5.4. IL-17 blockade does not affect early liver inflammation during HBV immunity. Adult (>8 wks) HBVtg*Rag1-/-* animals were treated with anti-IL-17R blocking (dashed purple line), anti-IL-17F blocking (red dotted line), or IgG1 control (solid black line) antibodies every two days starting at day -1, and adoptively transferred with HBV-naïve WT splenocytes on day 0. Liver disease was monitored by plasma alanine aminotransferase (ALT). Statistics determined by one-way ANOVA with Dunnett's multiple comparison test with GraphPad Prism Software; n=5 per group.

I performed flow cytometry to assess immune cell infiltration of the liver and found a trend towards reduced total CD45+ lymphocytes (p=0.11) and T cells (p=0.22) in anti-IL-17F-treated animals, though this was not statistically different (**Fig. 5.5 A-B**). The anti-IL-17RA-treated mice were identical to control animals, suggesting that if the trend towards decreased T

cells were true in anti-IL-17F-treated mice, that IL-17A may have opposing roles. I did not

observe any differences in CD4+ versus CD8+ T cell accumulation in the liver by either

treatment (**Fig. 5.5 C**).
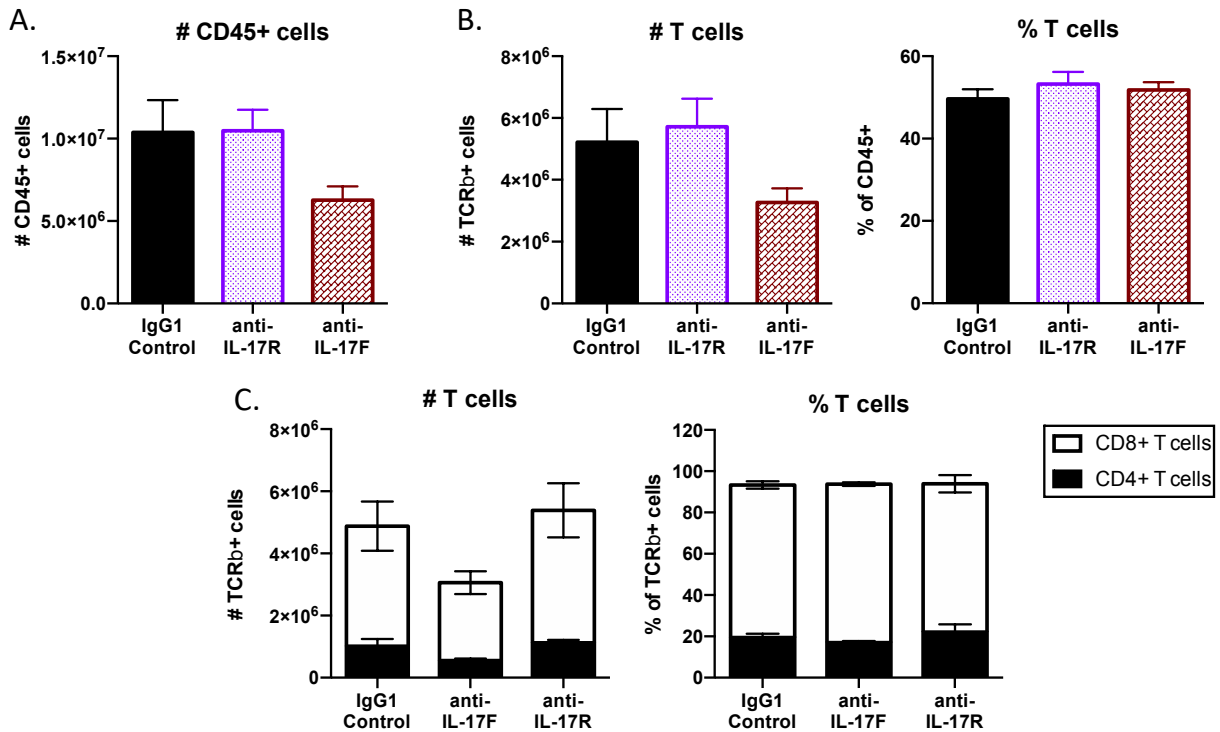
Figure 5.5. IL-17 blockade does not affect T cell accumulation in the liver during HBV immunity.
Adult (>8 wks) HBVtg*Rag1*-/- animals were treated with anti-IL-17R (purple), anti-IL-17F (red), or IgG1
control (black) antibodies every two days starting at day -1, and adoptively transferred with HBV-naïve
WT splenocytes on day 0. Leukocyte-enriched cell preparations were isolated on day 8 post-transfer and
flow cytometry was performed to measure the number of (**A**) total CD45+ cells and the number and
percentage of (**B**) total T cells (CD45+ TCRβ+ NK1.1-) and (**C**) CD4+ T cells (CD45+ TCRβ+ NK1.1-
CD4+ CD8-) and CD8+ T cells (CD45+ TCRβ+ NK1.1- CD4- CD8+). Data were analyzed using
FlowJoᴛᴍ Software; statistics determined by unpaired two-tailed t-test with GraphPad Prism Software;
n=5 per group.

When taking a closer look at CD4+ T cell differentiation I detected no differences in the

number or percentage of naïve, central memory, or effector/effector memory cells as defined by

CD44 and CD62L expression (**Fig. 5.6 A**). There was a trend towards a reduction in the number

of CD44+ CD62L- CD8+ Tᴇff cells after anti-IL-17F treatment (p=0.054), which was not present

in anti-IL-17RA-treated mice (**Fig. 5.6 B**). I found no differences in the number or percentages

of CXCR5+ PD-1+ T follicular helper cells after IL-17 blockade at this early time point (**Fig. 5.6**

C-D). It remains to be seen whether IL-17 blockade may contribute any of the longer-term

effects we saw as a result of ILC3 depletion.
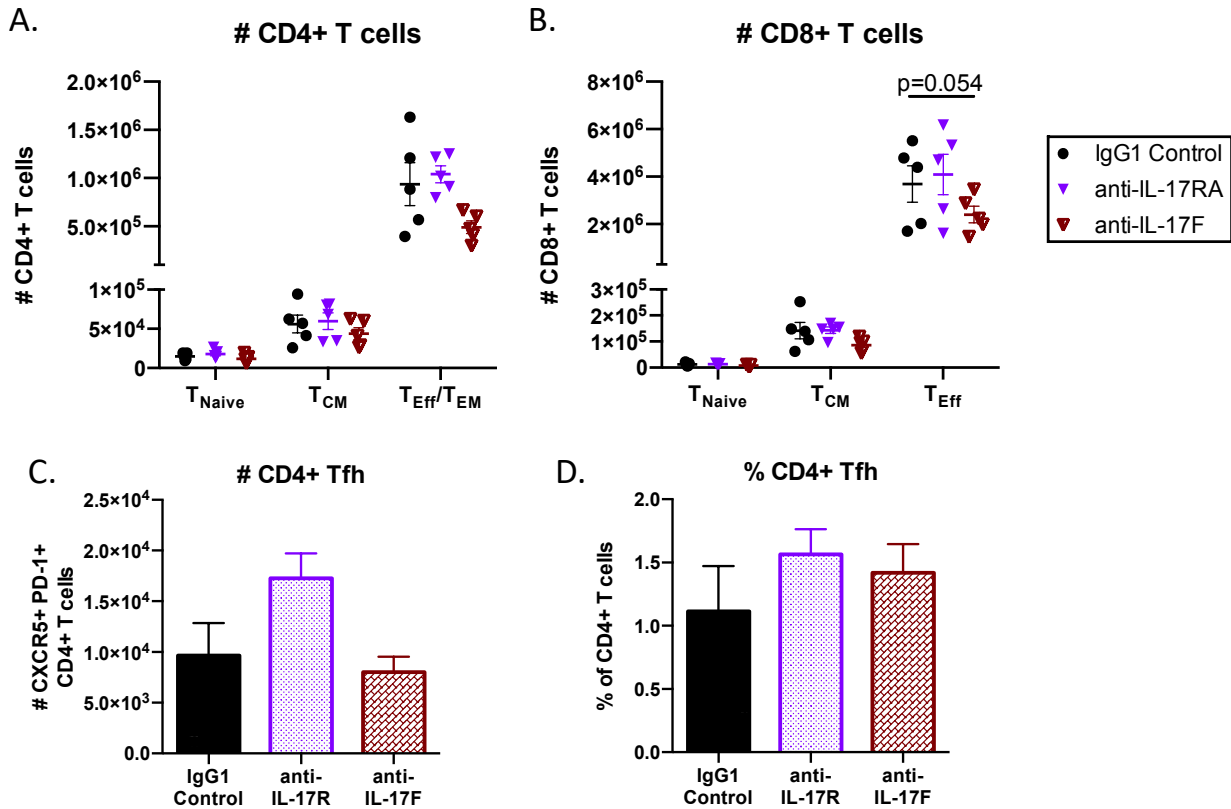
Figure 5.6. IL-17 blockade does not affect T cell differentiation in the liver during HBV immunity.
Adult (>8 wks) HBVtg*Rag1*-/- animals were treated with anti-IL-17R (purple), anti-IL-17F (red), or IgG1
control (black) antibodies every two days starting at day -1, and adoptively transferred with HBV-naïve
WT splenocytes on day 0. Leukocyte-enriched cell preparations were isolated on day 8 post-transfer and
flow cytometry was performed to measure the number of CD44- CD62L T_{naive}, CD44+ CD62L+ T_{CM}, and
CD44+ CD62L- T_{Eff}/T_{EM} (**A**) CD4+ T cells and (**B**) CD8+ T cells, as well as the number (**C**) and
percentage (**D**) of CXCR5+ PD-1+ CD4+ T follicular helper (Tfh) cells relative to total CD4+ T cells.
Data were analyzed using FlowJo™ Software; statistics determined by unpaired two-tailed t-test with
GraphPad Prism Software; n=5 per group.

Finally, I assessed antigen-specific IFNγ T cell responses by ELISpot assay. In this

experiment control animals had a very high baseline IFNγ response and did not mount an

antigen-specific response to any of the individual peptides (**Fig 5.7**). Relative to the controls, anti-IL-17RA-treated mice had the lowest baseline IFNγ response followed by anti-IL-17F treatment. Blockade of IL-17RA clearly did not impair HBV-specific IFNγ production, as these animals had a clear response to five peptides including each of the four major dominant epitopes (32, 81, 88, and 92). Mice treated with anti-IL-17F showed detectable antigen-specific IFNγ production in response to peptide 81, with a near response to peptide 92. These data suggest that IL-17A and IL-17F likely do not contribute a great deal to the generation of antigen-specific T cell responses. An important caveat to these experiments, however, is the fact that antibody-mediated blockade may only partially block IL-17 signaling when compared to studies that use genetically deficient IL-17 or IL-17R mice. Indeed, I found no differences in the expression of a number of genes shown to be regulated downstream of IL-17R signaling including GM-CSF (*Csf2*) lipocalin 2 (*Lcn2*), C/EBPd (*Cebpd*), and IκB-ζ (*Nfkbiz*) (*90*) in anti-IL-17F- and anti-IL-17RA-treated animals, suggesting that a more robust system may be required to efficiently block IL-17 signaling in the liver.

IFNg Production by Liver Lymphocytes
(Day 8)
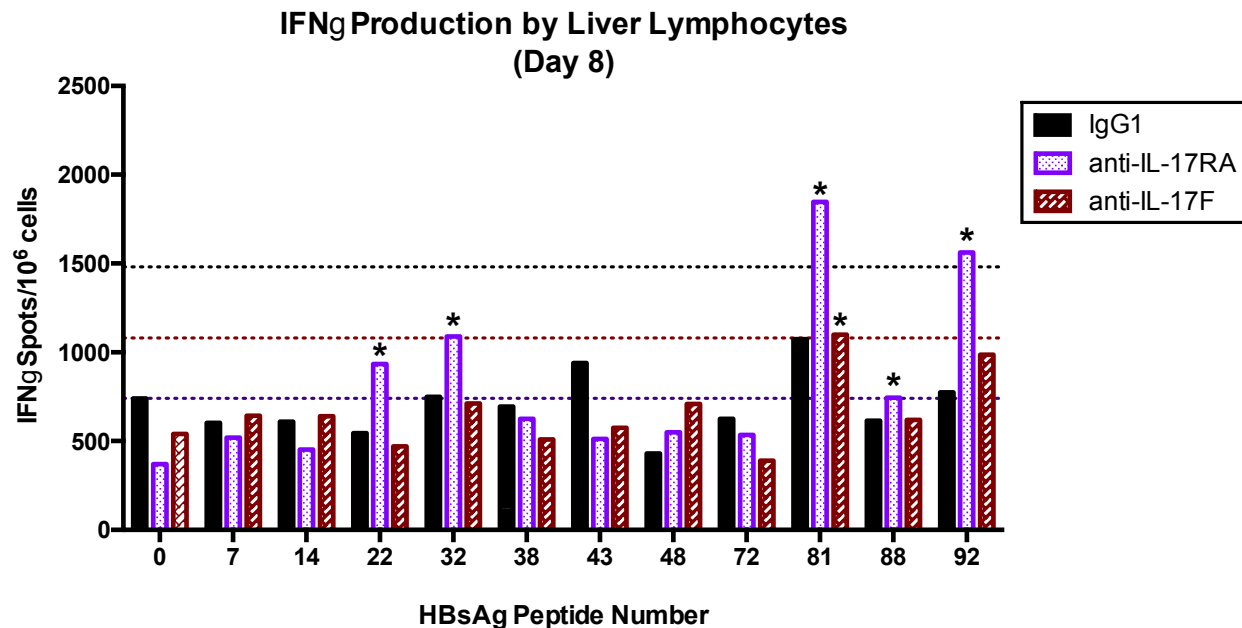
Figure 5.7. IL-17F blockade supports early antigen-specific IFNγ responses during HBV immunity.
Adult (>8 wks) HBVtg*Rag1-/-* animals were treated with anti-IL-17R (purple), anti-IL-17F (red), or IgG1
control (black) antibodies every two days starting at day -1, and adoptively transferred with HBV-naïve
WT splenocytes on day 0. Hepatic leukocyte-enriched cell preparations were isolated from animals on
day 8 post adoptive transfer. 10_5 liver leukocytes were mixed in a 1:1 ratio with splenocytes from *Rag1-/-*
mice as a source of APCs and stimulated overnight at 37°C together with individual peptides derived
from the HBV envelope protein (HBsAg peptides) in ELISpot plates pre-coated with anti-IFNγ
antibodies. "0" peptide denotes no peptide added. Antigen-specific IFNγ production was measured and
displayed as the total number of IFNγ spots per 10_6 cells. ELISpot plates were counted and analyzed with
a CTL Immunospot plate reader and software. The threshold defining a positive response, marked with a
*, is ≥2× the baseline (dashed line). N=pooled from =5 mice per group.

5.5 – The role of IL-22 in HBV immunity

We also investigated the role of another major ILC3-derived cytokine, IL-22. I first

approached this question by using antibody-mediated blockade of IL-22; however, due to cost

and efficacy of this approach we have also acquired so-called "Catch-22" mice from Dr. Richard

Locksley's laboratory, which have tdTomato knocked in to the endogenous *Il22* locus such that

heterozygotes are IL-22 reporter mice and homozygotes are IL-22 knockouts (*91*). My initial

experiments with anti-IL-22 blockade showed no effects on early hepatitis (**Fig. 5.8**). This

cytokine has previously been shown to play a role in liver inflammation, both pro- and anti-

inflammatory depending on the context, and so I am interested to understand whether this

observation may be due to partial IL-22 blockade or, alternatively, whether the window in which

I tested was too early to identify these effects, both of which will be easiest to evaluate in the

Catch22 knock-out mice (*61, 63*).
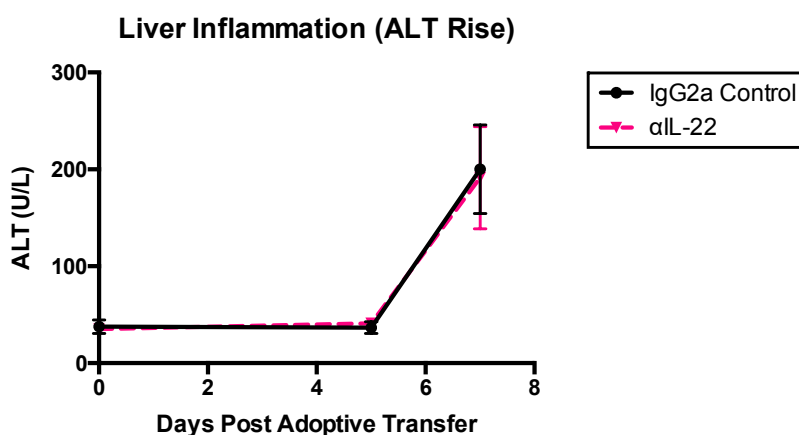
Figure 5.8. IL-22 blockade does not affect early liver inflammation during HBV immunity. Adult (>8 wks) HBVtg*Rag1*-/- animals were treated with anti-IL-22 blocking (pink dashed line) or IgG2a control antibodies every two days starting at day -1, and adoptively transferred with HBV-naïve WT splenocytes on day 0. Liver disease was monitored by plasma alanine aminotransferase (ALT). Statistics determined by one-way ANOVA with Dunnett's multiple comparison test with GraphPad Prism Software; n=7 per group.

I assessed the accumulation of total immune cells, T cells, and B cells in the livers of

anti-IL-22 and control IgG2a-treated mice by flow cytometry. I found no differences in the

number of CD45+ cells in the liver, nor in the number or relative percentage of T cells and B

cells after IL-22 blockade compared to controls (**Fig. 5.9**).
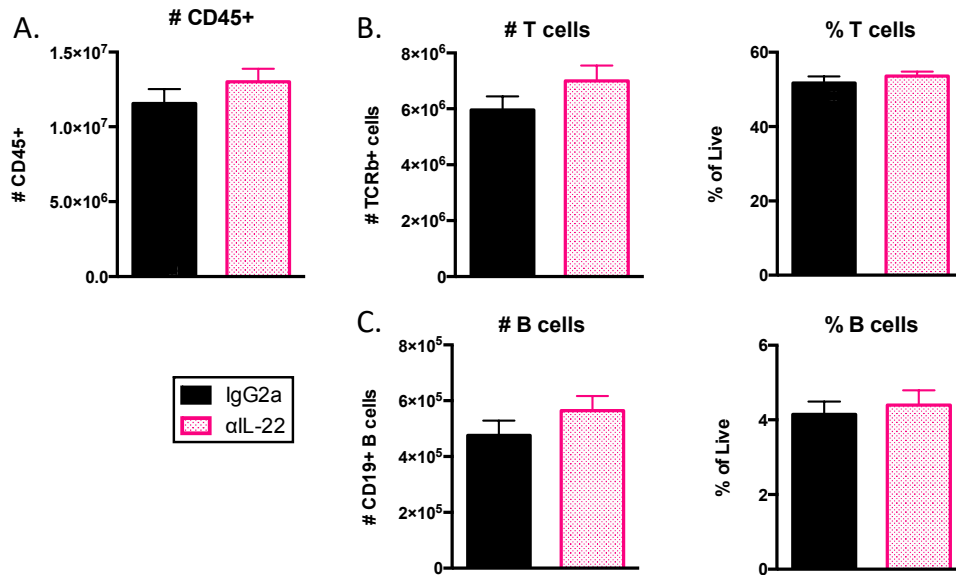
Figure 5.9. IL-22 blockade does not affect T or B cell accumulation in the liver during early HBV immunity. Adult (>8 wks) HBVtg*Rag1*-/- animals were treated with anti-IL-22 (pink) or IgG2a control (black) antibodies every two days starting at day -1, and adoptively transferred with HBV-naïve WT splenocytes on day 0. Leukocyte-enriched cell preparations were isolated on day 8 post-transfer and flow cytometry was performed to measure the number of (**A**) total CD45+ cells and the number and percentage of (**B**) T cells (CD45+ TCRβ+ NK1.1-) and (**C**) B cells (CD45+ TCRβ- NK1.1- CD19+). Data were analyzed using FlowJo™ Software; statistics determined by unpaired two-tailed t-test with GraphPad Prism Software; n=7 per group.

When looking at the composition of TCRβ+ cells, I found no differences in the number or relative percentages of CD4+ and CD8+ T cells in anti-IL-22-treated mice (**Fig. 5.10 A**). Furthermore, the differentiation of central memory and effector/effector memory cells within the population of CD4+ and CD8+ T cells was also unchanged by IL-22 blockade, with control and blocked mice demonstrating a strong skewing towards T$_{Eff}$ cells, as typically seen in the liver of adult mice (**Fig. 5.10 B-C**).
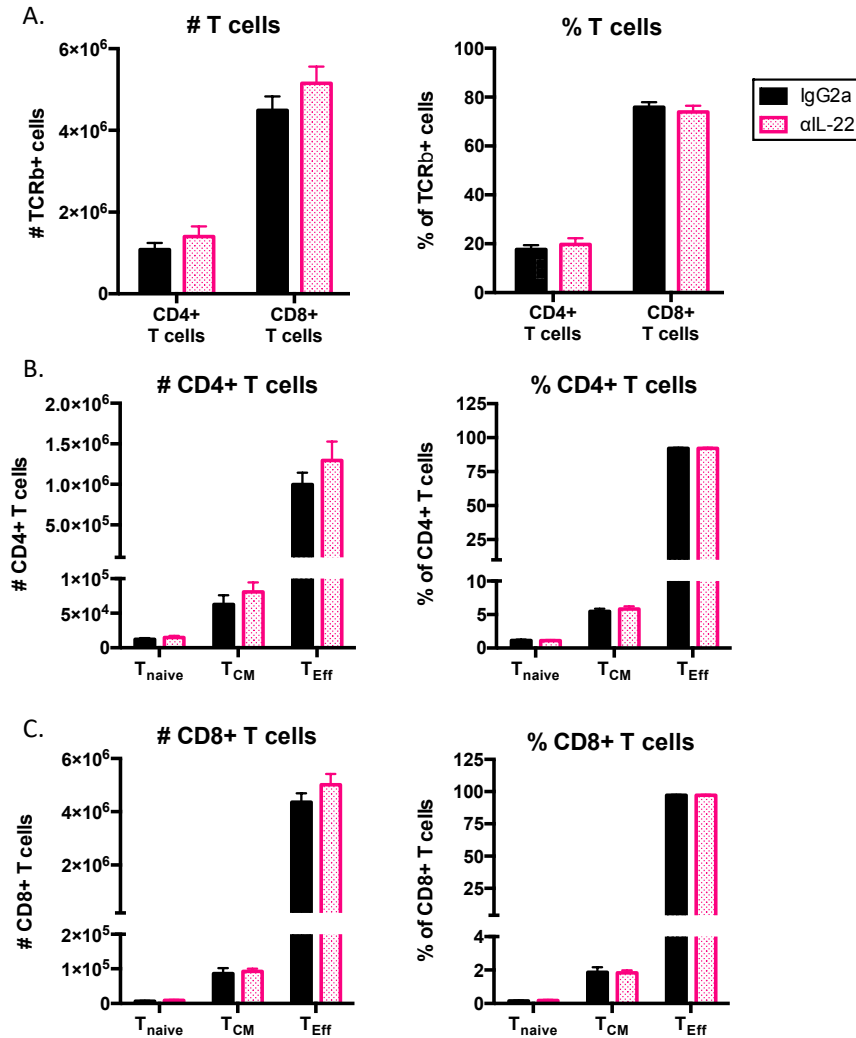
Figure 5.10. IL-22 blockade does not affect T cell differentiation in the liver during early HBV immunity. Adult (>8 wks) HBVtg*Rag1*-/- animals were treated with anti-IL-22 (pink) or IgG2a control (black) antibodies every two days starting at day -1, and adoptively transferred with HBV-naïve WT splenocytes on day 0. Leukocyte-enriched cell preparations were isolated on day 8 post-transfer and flow cytometry was performed to measure the number and percentage of (**A**) CD4+ and CD8+ T cells and CD44- CD62L T$_{naive}$, CD44+ CD62L+ T$_{CM}$, and CD44+ CD62L- T$_{Eff}$/T$_{EM}$ CD4+ (**B**) and CD8+ (**C**) T cells. Data were analyzed using FlowJo™ Software; statistics determined by unpaired two-tailed t-test with GraphPad Prism Software; n=7 per group.

I also assessed the effect of IL-22 blockade on the differentiation of Tfh cells, CXCR5+ CD8+ T cells, RORγt+ Th17 and Tc17, as well as the expression of PD-1 and OX40 on both CD4+ and CD8+ T cells and found no differences in any of these populations as a result of anti-IL-22 treatment compared to controls (**Fig. 5.11**). There was a small but insignificant trend

towards an increase in the number and percentage of Tfh cells in IL-22-blocked mice that

warrants follow up in IL-22 knockout mice, as this was also a feature observed in ILC3-deficient

mice at this early time point (**Fig. 5.11 A**).
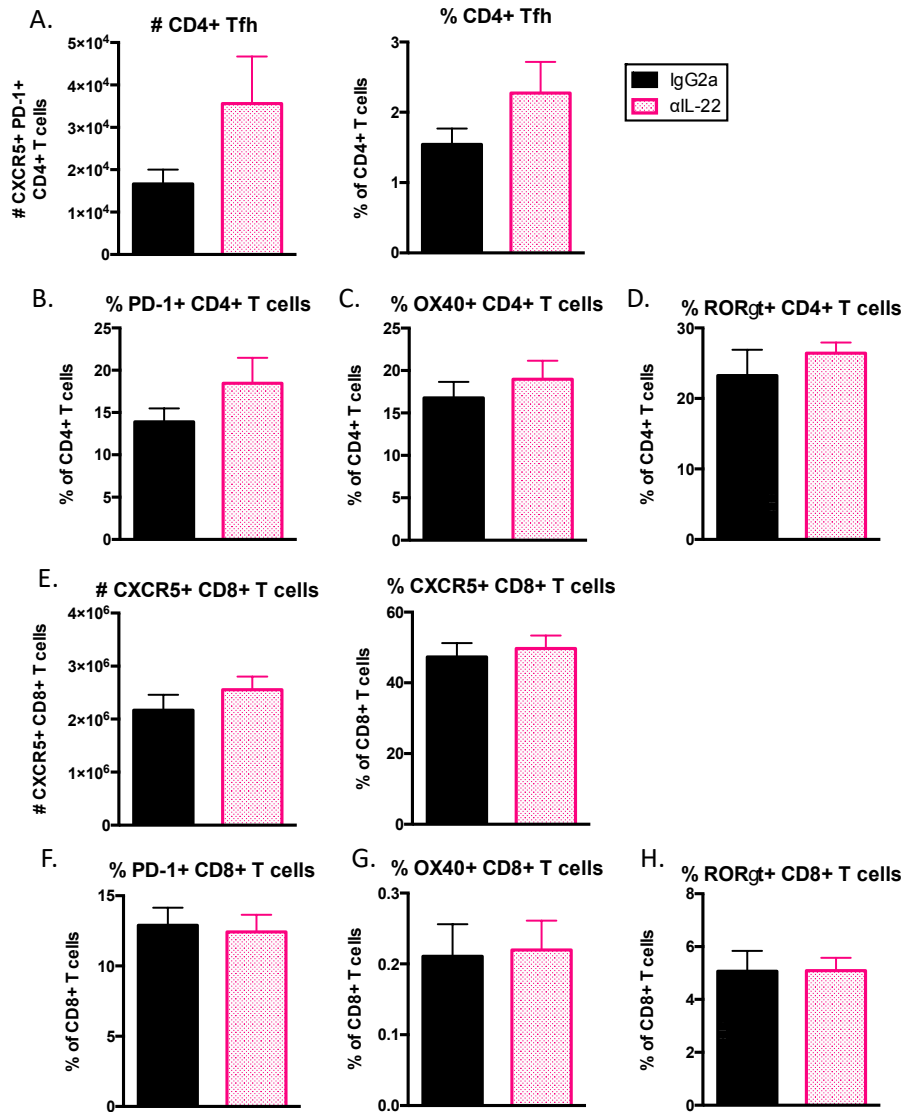
Figure 5.11. IL-22 blockade does not affect Tfh cell accumulation or surface marker expression of CD4+ and CD8+ T cells in the liver during early HBV immunity. Adult (>8 wks) HBVtg*Rag1-/-* animals were treated with anti-IL-22 (pink) or IgG2a control (black) antibodies every two days starting at day -1, and adoptively transferred with HBV-naïve WT splenocytes on day 0. Leukocyte-enriched cell preparations were isolated on day 8 post-transfer and flow cytometry was performed to measure the number and percentage of (**A**) CXCR5+ PD-1+ CD4+ Tfh, the percentage of (**B**) PD-1+, (**C**) OX40+, and (**D**) RORγ+ CD4+ T cells, as well as the number and percentage of (**E**) CXCR5+ CD8+ T cells, and the

percentage of (**F**) PD-1+, (**G**) OX40+, and (**H**) RORγ+ CD8+ T cells. Data were analyzed using FlowJoᴛᴍ Software; statistics determined by unpaired two-tailed t-test with GraphPad Prism Software; n=7 per group.

When examining the effect of IL-22 on various IFNγ producing populations I also found no differences between anti-IL-22-treated mice and controls. IL-22 blockade did not increase or decrease the number of IFNγ+ CD4+ or CD8+ T cells, nor did it affect the expression of PD-1 or OX40 on IFNγ+ T cells or the percentages of IFNγ+ Tfh and CXCR5+ T cells (**Fig. 5.12**).
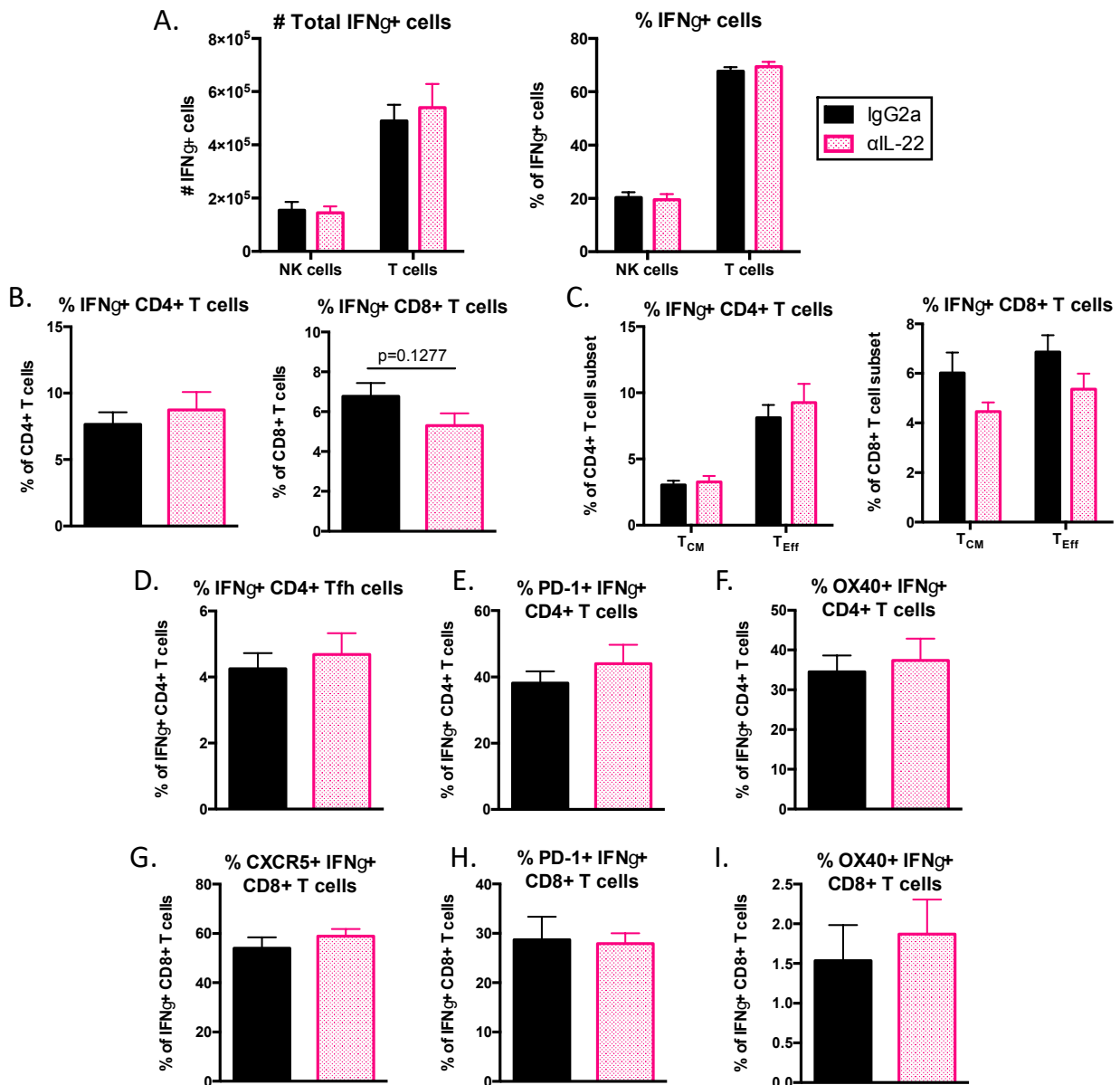
Figure 5.12. IL-22 blockade does not affect IFNγ production by T cells in the liver during early HBV immunity. Adult (>8 wks) HBVtg*Rag1-/-* animals were treated with anti-IL-22 (pink) or IgG2a control (black) antibodies every two days starting at day -1, and adoptively transferred with HBV-naïve WT splenocytes on day 0. Leukocyte-enriched cell preparations were isolated on day 8 post-transfer and flow cytometry was performed to measure the number and percentage of (**A**) total IFNγ+ NK cells (CD45+ TCRβ- NK1.1+) and T cells (CD45+ TCRβ+ NK1.1-), as well as the percentage of (**B**) IFNγ+ CD4+ and CD8 + T cells, (**C**) IFNγ+ CD44+ CD62L+ T_{CM} and IFNγ+ CD44+ CD62L- T_{Eff} CD4+ and CD8+ T cells, (**D**) CXCR5+ PD-1+ IFNγ+ CD4+ T cells, (**E**) PD-1+ IFNγ+ CD4+ T cells, (**F**) OX40+ IFNγ+ CD4+ T cells, (**G**) CXCR5+ IFNγ+ CD8+ T cells, (**H**) PD-1+ IFNγ+ CD8+ T cells, and (**I**) OX40+ IFNγ+ CD8+ T cells. Data were analyzed using FlowJo_{TM} Software; statistics determined by unpaired two-tailed t-test with GraphPad Prism Software; n=7 per group.

I measured antigen-specific T cell responses by IFNγ ELISpot assay and found that IL-22-blocked mice had no defect in early HBV-specific T cell priming. Mice that received anti-IL-22 treatment responded to each of the four dominant epitopes, including a response to peptide 32, which was not seen in control animals (**Fig. 5.13**). Notably, I also detected an increased magnitude of the response to peptide 81 in these animals, inconsistent with the phenotype of ILC3-deficient mice. I did not find substantial differences in the baseline IFNγ response between treatment groups, which is consistent with the flow cytometry data that did not find an overall difference in the number of IFNγ+ cells in the liver at this early time point in treated mice compared to control mice. It remains to be seen whether these early responses are sufficiently durable to result in antigen clearance and antibody production in the absence of IL-22 signaling, which we will address in the Catch22 knockout mice.

IFNg Production by Liver Lymphocytes (Day 8)
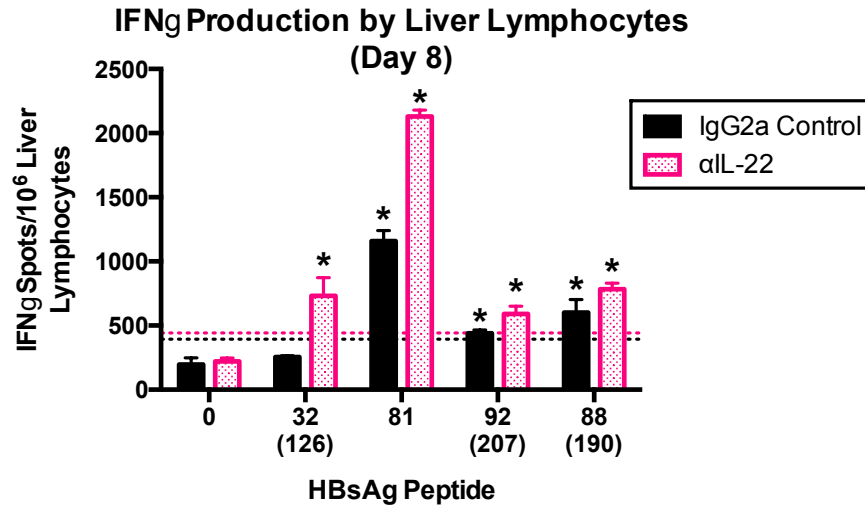
Figure 5.13. IL-22 blockade supports enhanced early antigen-specific IFNγ responses during HBV immunity. Adult (>8 wks) HBVtg*Rag1-/-* animals were treated with anti-IL-22 (pink) or IgG2a control (black) antibodies every two days starting at day -1, and adoptively transferred with HBV-naïve WT splenocytes on day 0. Hepatic leukocyte-enriched cell preparations were isolated from animals on day 8 post adoptive transfer. 10_5 liver leukocytes were mixed in a 1:1 ratio with splenocytes from *Rag1-/-* mice as a source of APCs and stimulated overnight at 37°C together with individual peptides derived from the HBV envelope protein (HBsAg peptides) in ELISpot plates pre-coated with anti-IFNγ antibodies. "0" peptide denotes no peptide added. Antigen-specific IFNγ production was measured and displayed as the total number of IFNγ spots per 10_6 cells. ELISpot plates were counted and analyzed with a CTL Immunospot plate reader and software. The threshold defining a positive response, marked with a *, is ≥2× the baseline (dashed line). N=pooled from =5 mice per group.

I also measured the number and frequency of the major hepatic myeloid populations in control and anti-IL-22-treated mice. I found no differences in the abundance of Kupffer cells, monocyte-derived macrophages, granulocytes, dendritic cells, or inflammatory or resident monocytes (**Fig. 5.14 A-E**). Furthermore, I also found no difference in the expression of MHCII or the costimulatory molecule OX40L on these myeloid populations (**Fig. 5.14 F-G**). These data suggest that IL-22 does not play a major role in regulating myeloid populations at this time point.
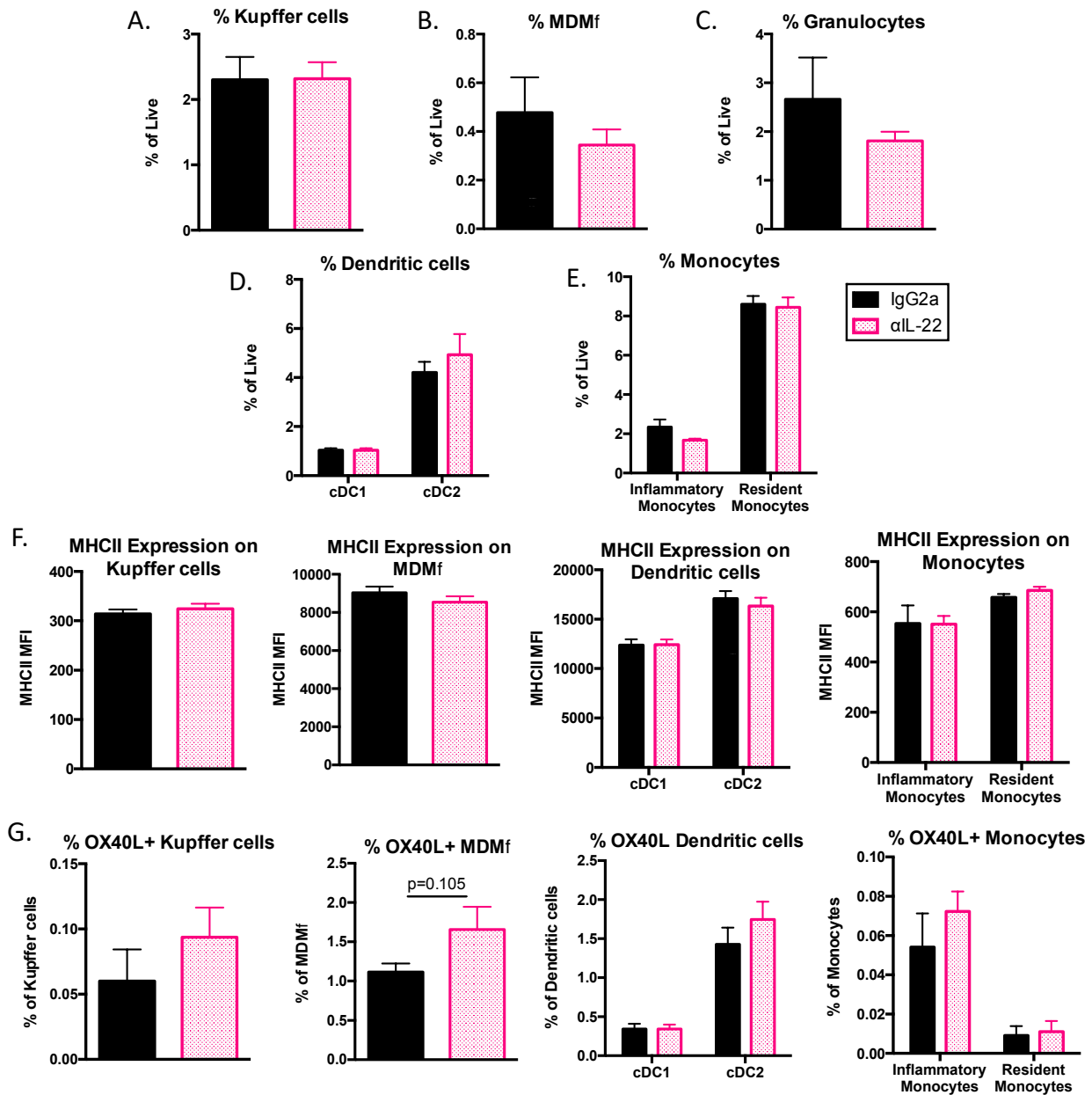
Figure 5.14. IL-22 blockade does not affect myeloid populations the liver during early HBV immunity. Adult (>8 wks) HBVtg*Rag1*-/- animals were treated with anti-IL-22 (pink) or IgG2a control (black) antibodies every two days starting at day -1, and adoptively transferred with HBV-naïve WT splenocytes on day 0. Leukocyte-enriched cell preparations were isolated on day 8 post-transfer and flow cytometry was performed to measure the percentage of (**A**) Kupffer cells (CD45+ F4/80+ CD11b$_{int}$ SSC$_{hi}$ Ly6c-), (**B**) monocyte-derived macrophages (MDMϕ; CD45+ F4/80+ CD11b$_{hi}$ Ly6c+), (**C**) granulocytes (CD45+ Gr1$_{hi}$ CD11b$_{hi}$), (**D**) dendritic cells (DCs; Live CD11c+ MHCII+), further subdivided into classical dendritic cell subsets 1 (cDC1; CD11b-) and 2 (cDC2; CD11b+), and (**E**) monocytes subdivided into inflammatory monocytes (CD45+ CD11b$_{hi}$ Ly6c$_{hi}$ CD11c- NK1.1- MHCII$_{lo/-}$ SSC$_{lo}$) and resident monocytes (CD45+ CD11b+ Ly6c$_{lo/-}$ CD11c+ NK1.1- MHCII$_{lo/-}$ SSC$_{lo}$). (**F**) The median fluorescence intensity of MHCII on Kupffer cells, MDMϕ, DCs, and monocytes. (**G**) The percentage of OX40L+ Kupffer cells, MDMϕ, DCs, and monocytes relative to the total number of each myeloid cell subset. Data

were analyzed using FlowJo™ Software; statistics determined by unpaired two-tailed t-test with GraphPad Prism Software; n=7 per group.

Finally, I determined if IL-22 blockade had any effect on the composition of ILC and NK cell populations in the liver. Similar to the other results, I found no differences in the number or percentages of NK cells, ILC1, ILC2, or ILC3 (**Fig. 5.15 A-E**). I also found no change in the percentage of ILC3s that were NKp46+, CD4+, MHCII+, or Ki67+ on day 8 (**Fig. 5.15 F-I**).
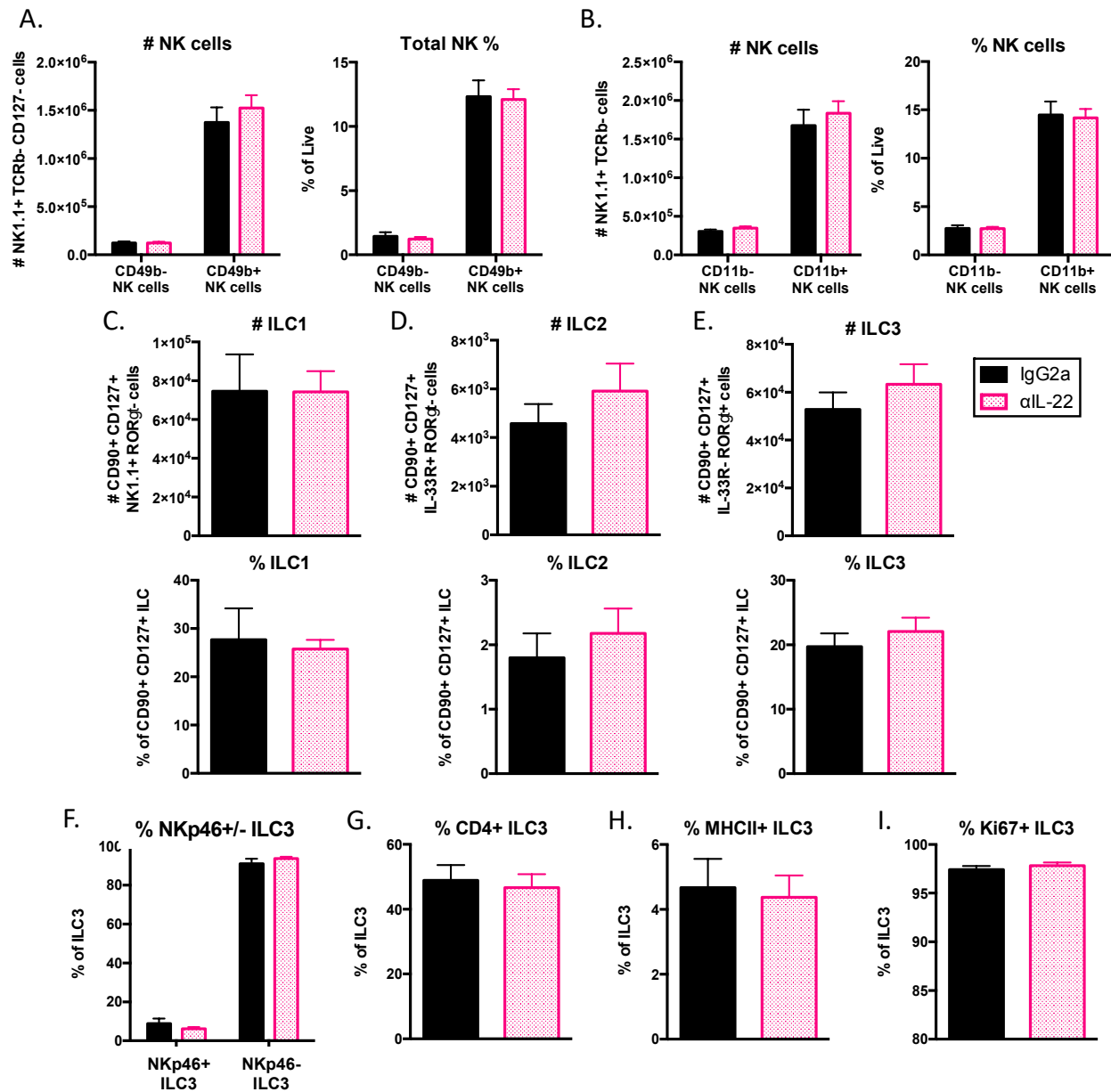
Figure 5.15. IL-22 blockade does not affect NK cell or ILC populations in the liver during early HBV immunity. Adult (>8 wks) HBVtg*Rag1*-/- animals were treated with anti-IL-22 (pink) or IgG2a control (black) antibodies every two days starting at day -1, and adoptively transferred with HBV-naïve WT splenocytes on day 0. Leukocyte-enriched cell preparations were isolated on day 8 post-transfer and flow cytometry was performed to measure the number and percentage of (**A**) CD49b+ mature and CD49b- immature NK cells (CD45+ TCRβ- NK1.1+), (**B**) CD11b+ mature and CD11b- immature NK cells (CD45+ TCRβ- NK1.1+), (**C**) ILC1 (CD45+ TCRβ- CD90+ CD127+ NK1.1+ RORγt-), (**D**) ILC2 (CD45+ TCRβ- CD90+ CD127+ RORγt- IL-33R+), and (**E**) ILC3 (CD45+ TCRβ- CD90+ CD127+ RORγt+ IL-33R-). The percentage of (**F**) NKp46+ and NKp46-ILC3, (**G**) CD4+ ILC3, (**H**) MHCII+ ILC3, and (**I**) Ki67+ ILC3 were also measured. Data were analyzed using FlowJo™ Software; statistics determined by unpaired two-tailed t-test with GraphPad Prism Software; n=7 per group.

When taken together, blockade of IL-22 signaling had minimal effects on hepatic immunity at this early time point, eight days post-adoptive transfer. Much of the reported literature that describes a role for ILC3s in regulating immunity to microbes points towards IL-22 as a major mediator of this process. Thus, we are still very interested to understand whether complete ablation of IL-22 secretion and signaling by genetic depletion of the *Il22* locus has any effects on HBV immunity that may have been muted by incomplete blockade via antibody treatment. Furthermore, we know that expression of the IL-22 receptor is restricted to non-hematopoietic cells, and thus, any effects of IL-22 blockade on immune cells are due to indirect mechanisms, and perhaps may be temporally delayed relative to a cytokine that can directly act on hematopoietic cells, warranting investigation of hepatic immunity at later time points.

5.6 – The role of GM-CSF in HBV immunity

The last functional mediator of ILC3s that I investigated was GM-CSF. I treated adult HBVtg*Rag1*-/- mice with anti-GM-CSF-blocking antibodies every other day starting one day before adoptive transfer. Animals were sacrificed on day eight post-transfer and the numbers and phenotypes of lymphocytes and myeloid cells were assessed. I measured hepatic inflammation at

day five and seven post-transfer and found no major differences in hepatitis, though there was a

trend towards lower ALT values in anti-GM-CSF-treated animals (**Fig. 5.16**).

Liver Inflammation (ALT Rise)
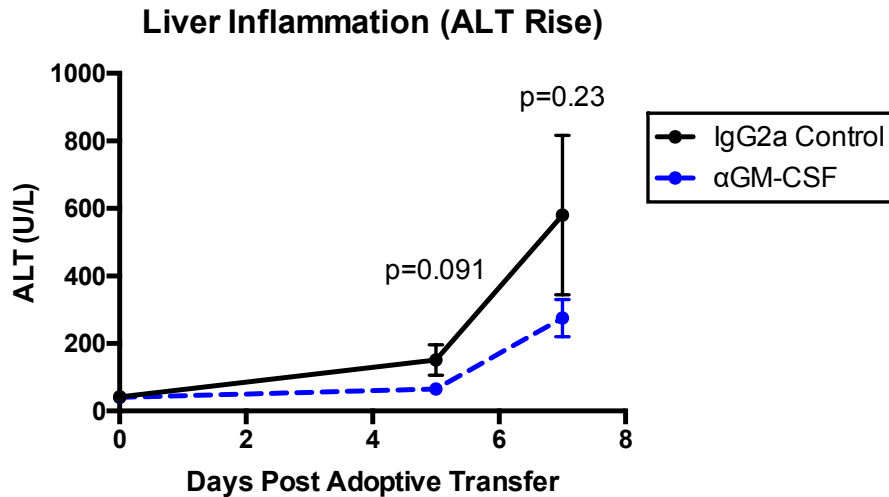
Figure 5.16. GM-CSF blockade may reduce early liver inflammation during HBV immunity. Adult (>8 wks) HBVtg*Rag1*-/- animals were treated with anti-GM-CSF-blocking (blue dashed line) or IgG2a control antibodies every two days starting at day -1, and adoptively transferred with HBV-naïve WT splenocytes on day 0. Liver disease was monitored by plasma alanine aminotransferase (ALT). Statistics determined by one-way ANOVA with Dunnett's multiple comparison test with GraphPad Prism Software; n=7 per group.

We measured the number of total CD45+ immune cells, T cells, γδ T cells and B cells in

the liver at day eight. Again, there were no significant differences between treated and control

animals, although there was a trend towards a decreased frequency of hepatic T cells in anti-GM-

CSF-treated mice (**Fig. 5.17**).
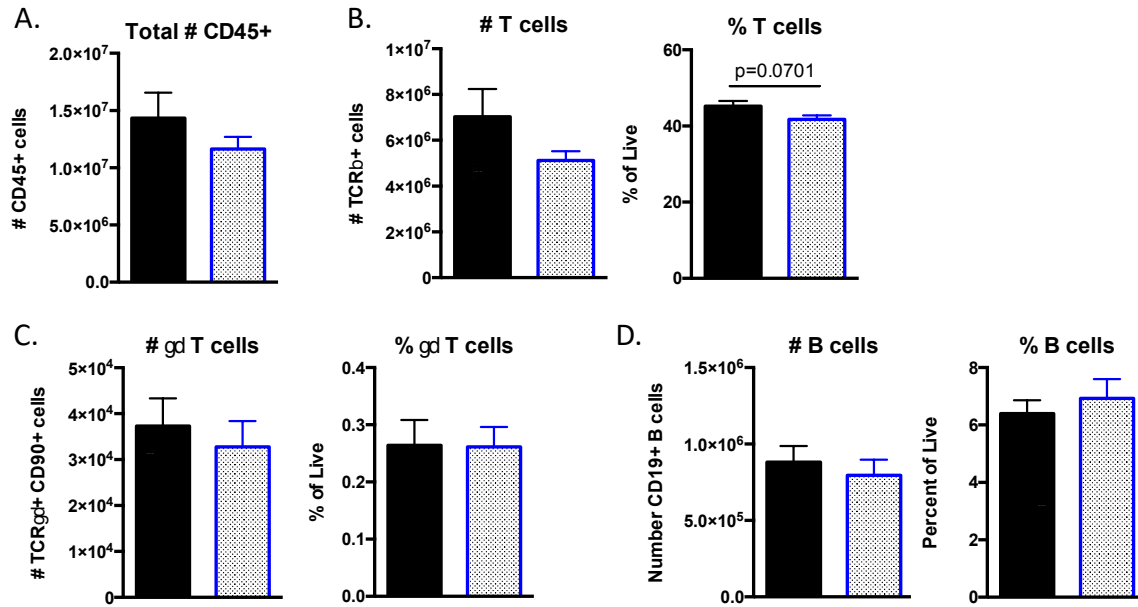
Figure 5.17. GM-CSF blockade does not dramatically affect T or B cell accumulation in the liver during early HBV immunity. Adult (>8 wks) HBVtg*Rag1*-/- animals were treated with anti-GM-CSF (blue) or IgG2a control (black) antibodies every two days starting at day -1, and adoptively transferred with HBV-naïve WT splenocytes on day 0. Leukocyte-enriched cell preparations were isolated on day 8 post-transfer and flow cytometry was performed to measure the number of (**A**) total CD45+ cells and the number and percentage of (**B**) T cells (CD45+ TCRβ+ NK1.1-), (**C**) γδ T cells (CD45+ TCRβ- TCRγδ+ CD90+) and (**D**) B cells (CD45+ TCRβ- NK1.1- CD19+). Data were analyzed using FlowJo™ Software; statistics determined by unpaired two-tailed t-test with GraphPad Prism Software; n=7 per group.

Within the T cell compartment, I found equivalent numbers of CD4+ T cells between GM-CSF-blocked and control animals that comprised 25-30 percent of total T cells (**Fig. 5.18 A**). There was a trend towards a reduced number and frequency of CD8+ T cells, but this did not reach significance. Hepatic central memory and effector T cell differentiation of CD4+ T cells was not affected by GM-CSF blockade (**Fig. 5.18 B**). There was, however, a lower percentage of CD8+ T$_{Eff}$ cells with an increase in the percentage of naïve CD8+ T cells in anti-GM-CSF-treated animals (**Fig. 5.18 C**).

196
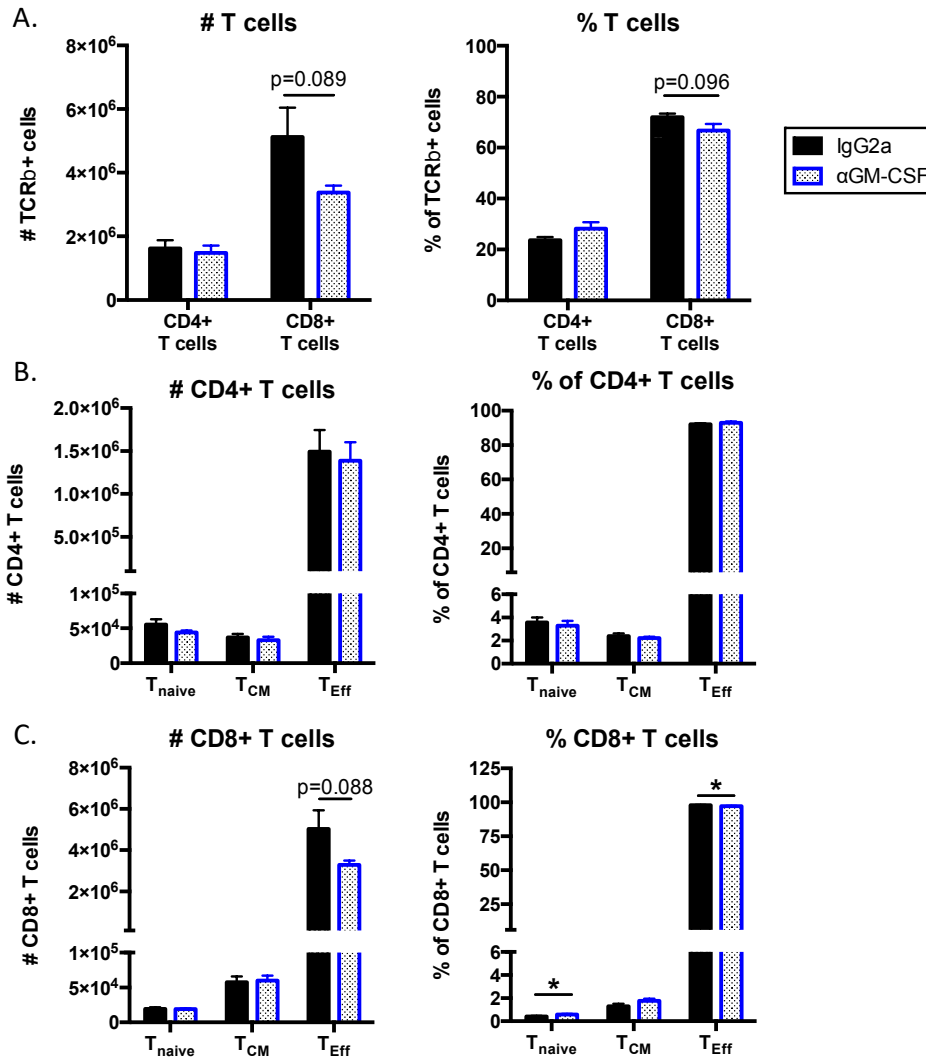
Figure 5.18. GM-CSF blockade CD8+ T$_{Eff}$ cell accumulation in the liver during early HBV immunity. Adult (>8 wks) HBVtg*Rag1*$_{-/-}$ animals were treated with anti-GM-CSF (blue) or IgG2a control (black) antibodies every two days starting at day -1, and adoptively transferred with HBV-naïve WT splenocytes on day 0. Leukocyte-enriched cell preparations were isolated on day 8 post-transfer and flow cytometry was performed to measure the number and percentage of (**A**) CD4+ and CD8+ T cells and CD44- CD62L T$_{naive}$, CD44+ CD62L+ T$_{CM}$, and CD44+ CD62L- T$_{Eff}$/T$_{EM}$ CD4+ (**B**) and CD8+ (**C**) T cells. Data were analyzed using FlowJo™ Software; statistics determined by unpaired two-tailed t-test with GraphPad Prism Software; n=7 per group.

GM-CSF blockade had no effect on the differentiation of Tfh cells or the percentage of

PD-1+ and OX40+ CD4+ T cells (**Fig. 5.19 A-C**). There was a trend towards a decreased

frequency of CD4+ RORγt+ Th17 cells and a statistically significant decrease in CD8+ RORγt+

Tc17 cells in anti-GM-CSF-treated mice, suggesting that GM-CSF normally supports the

differentiation of RORγt+ cells (**Fig 5.19 D, H**). There was no difference in the percentage of

CXCR5+ CD8+ T cells, or in the small population of OX40+ CD8+ T cells as a result of anti-

GM-CSF treatment (**Fig 5.19 E, G**). GM-CSF blockade caused an increased frequency of total

PD-1+ CD8+ T cells (**Fig. 5.19 F**). Together these data implicate GM-CSF in supporting CD8+

T cell responses and RORγt+ differentiation of T cells during early HBV immunity.
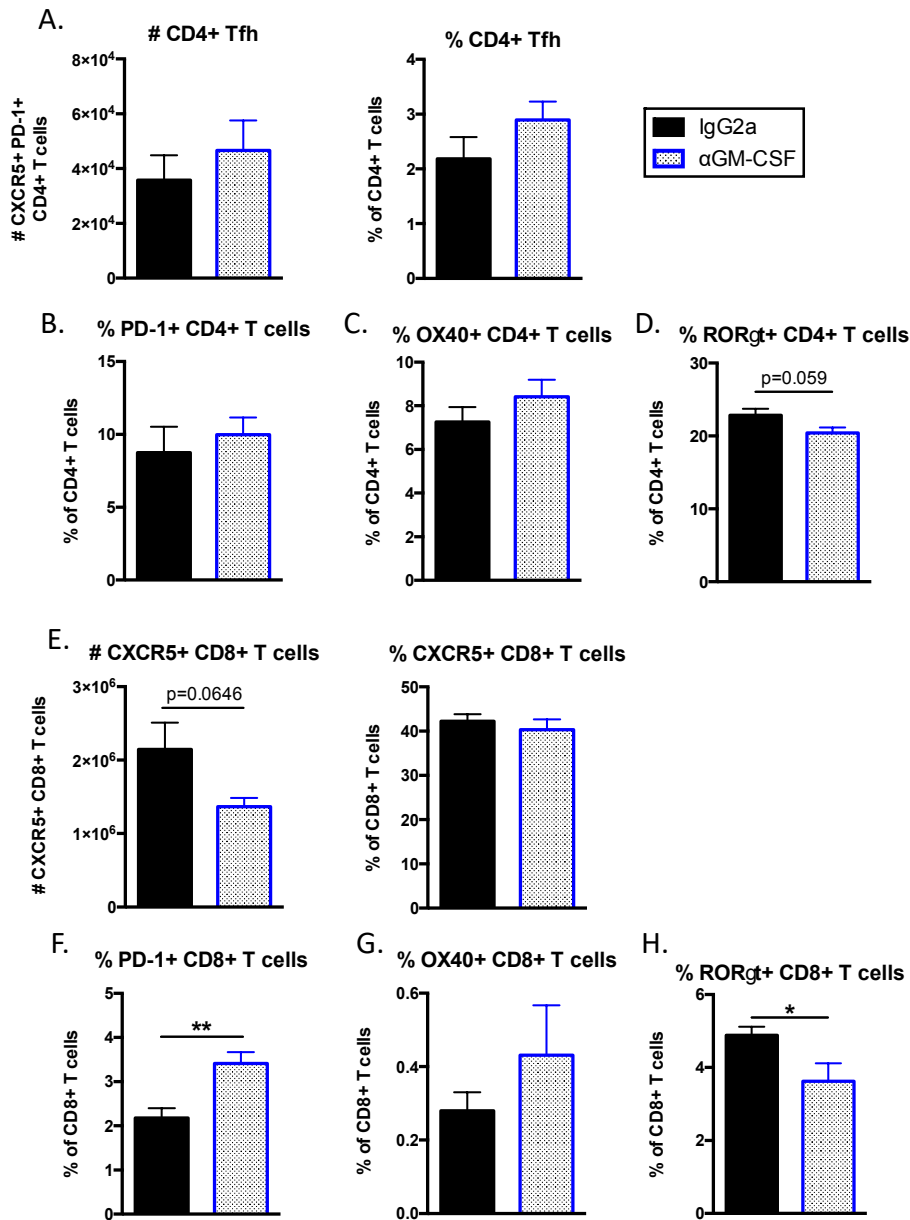
Figure 5.19. GM-CSF blockade does not affect Tfh cell accumulation, but does impair differentiation of RORγ+ CD4+ and CD8+ T cells in the liver during early HBV immunity. Adult (>8 wks) HBVtg*Rag1-/-* animals were treated with anti-GM-CSF (blue) or IgG2a control (black) antibodies every two days starting at day -1, and adoptively transferred with HBV-naïve WT splenocytes on day 0. Leukocyte-enriched cell preparations were isolated on day 8 post-transfer and flow cytometry was performed to measure the number and percentage of (**A**) CXCR5+ PD-1+ CD4+ Tfh, the percentage of (**B**) PD-1+, (**C**) OX40+, and (**D**) RORγ+ CD4+ T cells, as well as the number and percentage of (**E**) CXCR5+ CD8+ T cells, and the percentage of (**F**) PD-1+, (**G**) OX40+, and (**H**) RORγ+ CD8+ T cells**.** Data were analyzed using FlowJoᴛᴍ Software; statistics determined by unpaired two-tailed t-test with GraphPad Prism Software; n=7 per group.

Some of the most notable effects of anti-GM-CSF blockade could be seen within IFNγ-producing cells. Blockade of GM-CSF led to decreased production of IFNγ from T cell sources with an increase in the relative contribution of IFNγ-producing NK cells (**Fig. 5.20 A**). There were no differences in the number of CD4+ IFNγ+ T cells nor in the frequencies of IFNγ+ CD4+ central memory or effector T cells (**Fig. 5.20 B-C**). Anti-GM-CSF treatment did lead to a greater percentage of IFNγ-producing Tfh relative to other IFNγ+ CD4+ T cells, as well as a substantial increase in the percentage of OX40+ IFNγ+ CD4+ T cells, with no differences in PD-1 expression on IFNγ+ CD4+ T cells (**Fig. 5.20 D-F**). These data suggest that GM-CSF normally plays a role in suppressing IFNγ production by Tfh cells and limits OX40 expression within IFNγ+ CD4+ T cells, which could be a result of decreased OX40/OX40L interactions during immune priming in the presence of GM-CSF. GM-CSF blockade also led to a significant reduction in the number of IFNγ-producing CD8+ T cells, which was mostly due to a loss of IFNγ+ Tᴇff cells (**Fig. 5.20 G-H**). Anti-GM-CSF-treated mice had increased expression of PD-1 in IFNγ+ CD8+ T cells relative to control animals, which may contribute to the decreased amount of IFNγ+ CD8+ T cells, as PD-1 is known to restrict effector CD8+ T cells even during acute phase immune responses (**Fig. 5.20 K**).
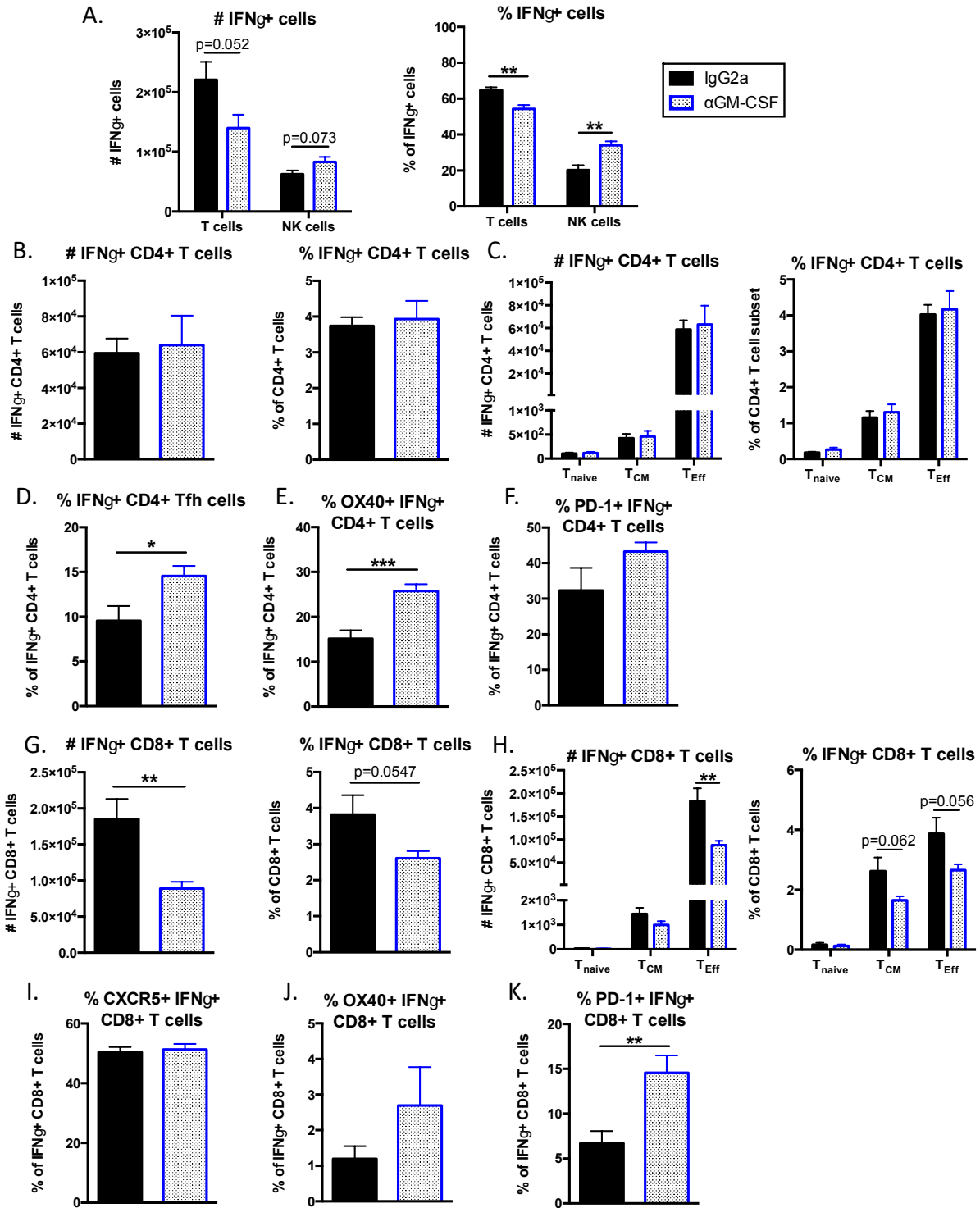
Figure 5.20. GM-CSF blockade impairs IFNγ production by CD8+ T cells in the liver during early HBV immunity. Adult (>8 wks) HBVtg*Rag1-/-* animals were treated with anti-GM-CSF (blue) or IgG2a control (black) antibodies every two days starting at day -1, and adoptively transferred with HBV-naïve WT splenocytes on day 0. Leukocyte-enriched cell preparations were isolated on day 8 post-transfer and

flow cytometry was performed to measure the number and percentage of (**A**) total IFNγ+ NK cells (CD45+ TCRβ- NK1.1+) and T cells (CD45+ TCRβ+ NK1.1-), (**B**) IFNγ+ CD4+ T cells, (**C**) IFNγ+ CD44+ CD62L+ T$_{CM}$ and IFNγ+ CD44+ CD62L- T$_{Eff}$ CD4+ T cells, as well as the percentage of (**D**) CXCR5+ PD-1+ Tfh, (**E**) PD-1+, and (**F**) OX40+ cells as a percentage of total IFNγ+ CD4+ T cells. (**G**) IFNγ+ CD4+ T cells, (**H**) IFNγ+ CD44+ CD62L+ T$_{CM}$ and IFNγ+ CD44+ CD62L- T$_{Eff}$ CD4+ T cells, as well as the percentage of (**I**) CXCR5+, (**J**) PD-1+, and (**K**) OX40+ IFNγ+ cells as a percentage of total IFNγ+ CD4+ T cells. Data were analyzed using FlowJo™ Software; statistics determined by unpaired two-tailed t-test with GraphPad Prism Software; n=7 per group.

I evaluated antigen-specific CD4+ T cell responses to the MHCII-restricted HBV surface antigen-derived epitope, HBs126, using tetramer staining. There was a trend towards an increased number of total HBs126+ CD4+ T cells as well as HBs126+ CD4+ effector T cells in GM-CSF-blocked mice, but those differences were not present in HBs126+ central memory cells (**Fig. 5.21 A-D**). Consistent with these data, there was a decreased percentage of CD127+ HBs126+ cells, which is a marker of long-lived cells, in anti-GM-CSF-treated animals compared to controls (**Fig. 5.21 E**). Furthermore, HBs126+ CD4+ T cells in GM-CSF-blocked mice had an increased expression of PD-1 and Ki67 (**Fig. 5.21 F-G**). Collectively, these data suggest that GM-CSF plays a role in promoting differentiation of long-lived antigen-specific cells and that in the absence of GM-CSF antigen-specific CD4+ T cells exhibit a phenotype associated with highly activated effector cells with increased proliferative capacity.
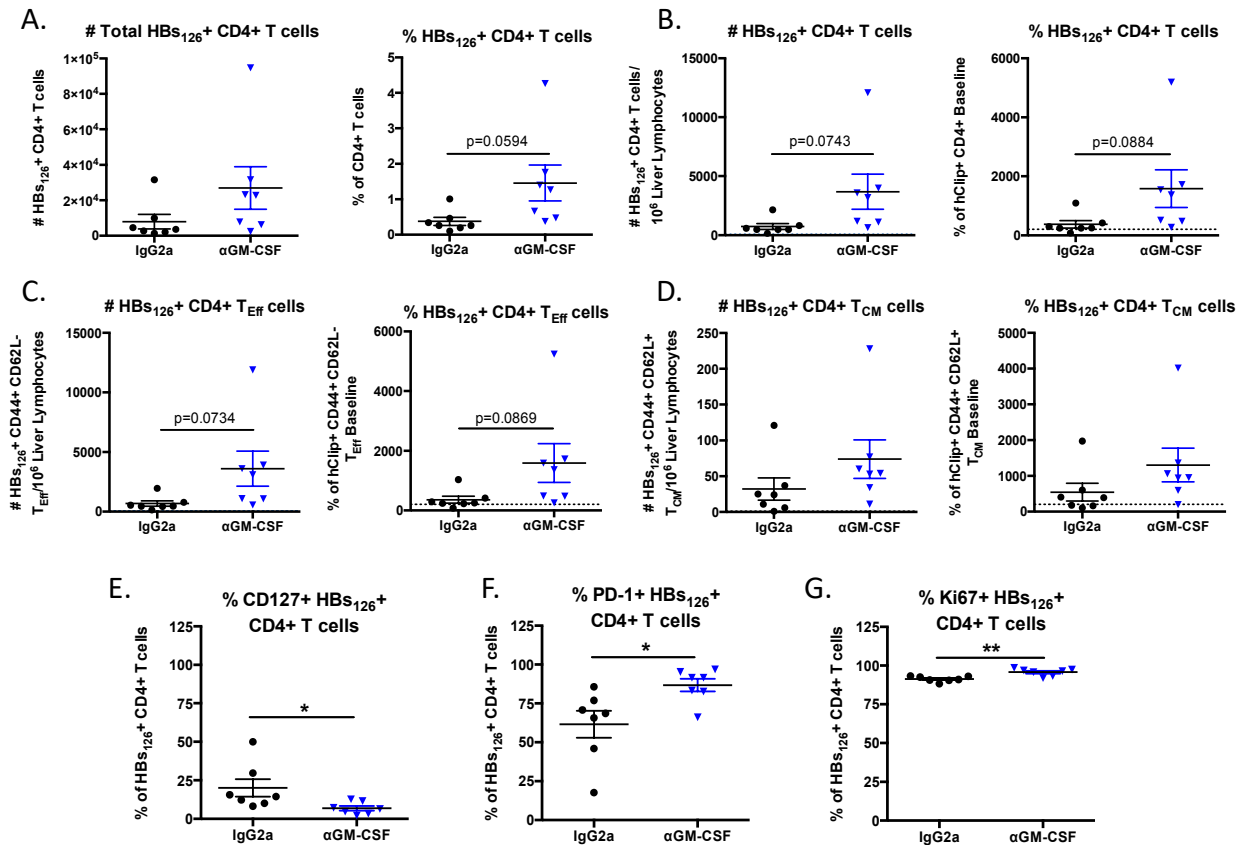
Figure 5.21. GM-CSF blockade may lead to increased HBs$_{126}$ antigen-specific T cells with an altered phenotype in the liver during early HBV immunity. Adult (>8 wks) HBVtg*Rag1*$_{-/-}$ animals were treated with anti-GM-CSF (blue) or IgG2a control (black) antibodies every two days starting at day -1, and adoptively transferred with HBV-naïve WT splenocytes on day 0. Hepatic leukocyte fractions were enriched from animals eight days after adoptive transfer and stained with I-A(b)-HBs$_{126}$ (RGLYFPAGGSSSG) tetramer, followed by antibody staining for additional surface proteins. (**A**) Total HBs$_{126}$+ CD4+ T cells were measured and reported as numbers and percentage of total CD4+ T cells. (**B**) HBs$_{126}$+ CD4+ T cells per million liver lymphocytes and the percentage relative to an irrelevant peptide (I-A(b)-human CLIP, PVSKMRMATPLLMQA) baseline frequency was determined. A true antigen-specific population is defined as two-fold higher than baseline and is marked by a dotted line. Numbers per million hepatic lymphocytes and percentages above I-A(b)-hCLIP baseline of (**C**) CD44+ CD62L-T$_{Eff}$ and (**D**) CD44+ CD62L+ T$_{CM}$ were measured. Frequencies of CD127+ (**D**), PD-1+ (**E**), and Ki67+ (**F**) HBs$_{126}$+ CD4+ T cells were measured. Data were analyzed using FlowJo™ Software; statistics determined by unpaired two-tailed t-test with GraphPad Prism Software; * $p<0.05$; n=7 per group.

When looking at multiple HBV antigens by IFNγ ELISpot assay I observed that both control and anti-GM-CSF-treated animals mount a robust response to each of the four dominant HBV epitopes (**Fig. 5.22**). Thus, although GM-CSF blockade seemed to affect total IFNγ production by CD8+ T cells and led to an increased frequency of one antigen-specific CD4+ T

202

cell population, the absence of GM-CSF did not impair the ability of hepatic T cells to mount a diverse antigen-specific anti-HBV immune response. These data suggest that GM-CSF normally plays a role in supporting CD8+ T cells and their production of IFNγ and perhaps also contributes towards establishing long-lived antigen-specific CD4+ T cells, although the early T cell response was quite strong even in the absence of GM-CSF. It will be of particular interest to understand whether the phenotypic differences observed within antigen-specific CD4+ T cells and IFNγ+ CD8+ T cells have any lasting effects on the long-term response to HBV, including HBsAg clearance and HBs antibody seroconversion, in experiments now underway.
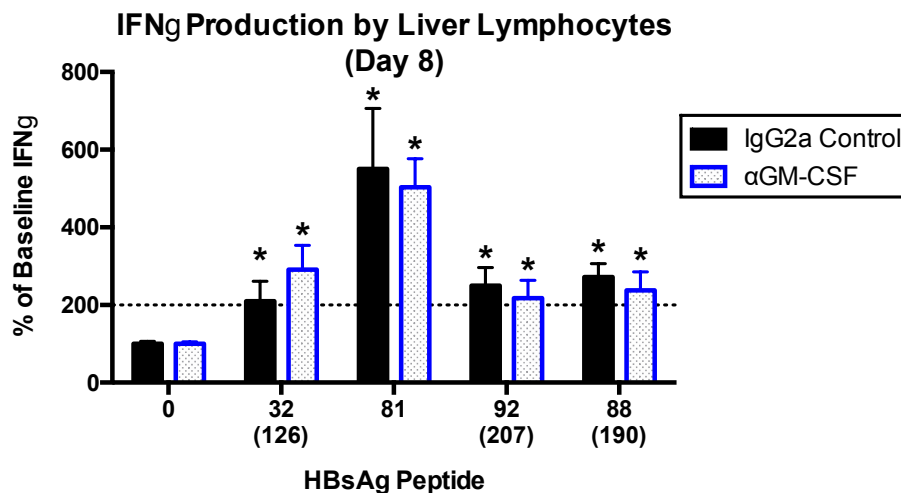
Figure 5.22. GM-CSF blockade does not affect total early antigen-specific IFNγ responses during HBV immunity. Adult (>8 wks) HBVtg*Rag1*-/- animals were treated with anti-GM-CSF (blue) or IgG2a control (black) antibodies every two days starting at day -1, and adoptively transferred with HBV-naïve WT splenocytes on day 0. Hepatic leukocyte-enriched cell preparations were isolated from animals on day 8 post adoptive transfer. 10^5 liver leukocytes were mixed in a 1:1 ratio with splenocytes from *Rag1*-/- mice as a source of APCs and stimulated overnight at 37°C together with individual peptides derived from the HBV envelope protein (HBsAg peptides) in ELISpot plates pre-coated with anti-IFNγ antibodies. "0" peptide denotes no peptide added. Antigen-specific IFNγ production was measured and displayed as the total number of IFNγ spots per 10^6 cells. ELISpot plates were counted and analyzed with a CTL Immunospot plate reader and software. The threshold defining a positive response, marked with a *, is ≥2× the baseline (dashed line); n=5 mice per group.

I also assessed the composition of the hepatic myeloid compartment at this early time point. There were no differences in the percentages of Kupffer cells, granulocytes, cDC1, or

monocytes, but there was an increase in the percentage of monocyte-derived macrophages and a trend towards increased cDC2 in anti-GM-CSF-treated mice suggesting GM-CSF production normally restricts the expansion of these two populations (**Fig. 5.23 A-E**). I also observed increased expression of MHCII on Kupffer cells and monocyte-derived macrophages in GM-CSF-treated mice, with no differences in MHCII expression on DCs or monocytes (**Fig. 5.23 F**). Anti-GM-CSF treatment led to increased OX40L expression on a number of myeloid cells, including monocyte-derived macrophages, cDC2, and inflammatory monocytes (**Fig. 5.23 G**). These data support the observation of increased OX40+ IFNγ+ T cells that have the ability to interact with and become stimulated by OX40L+ APCs.
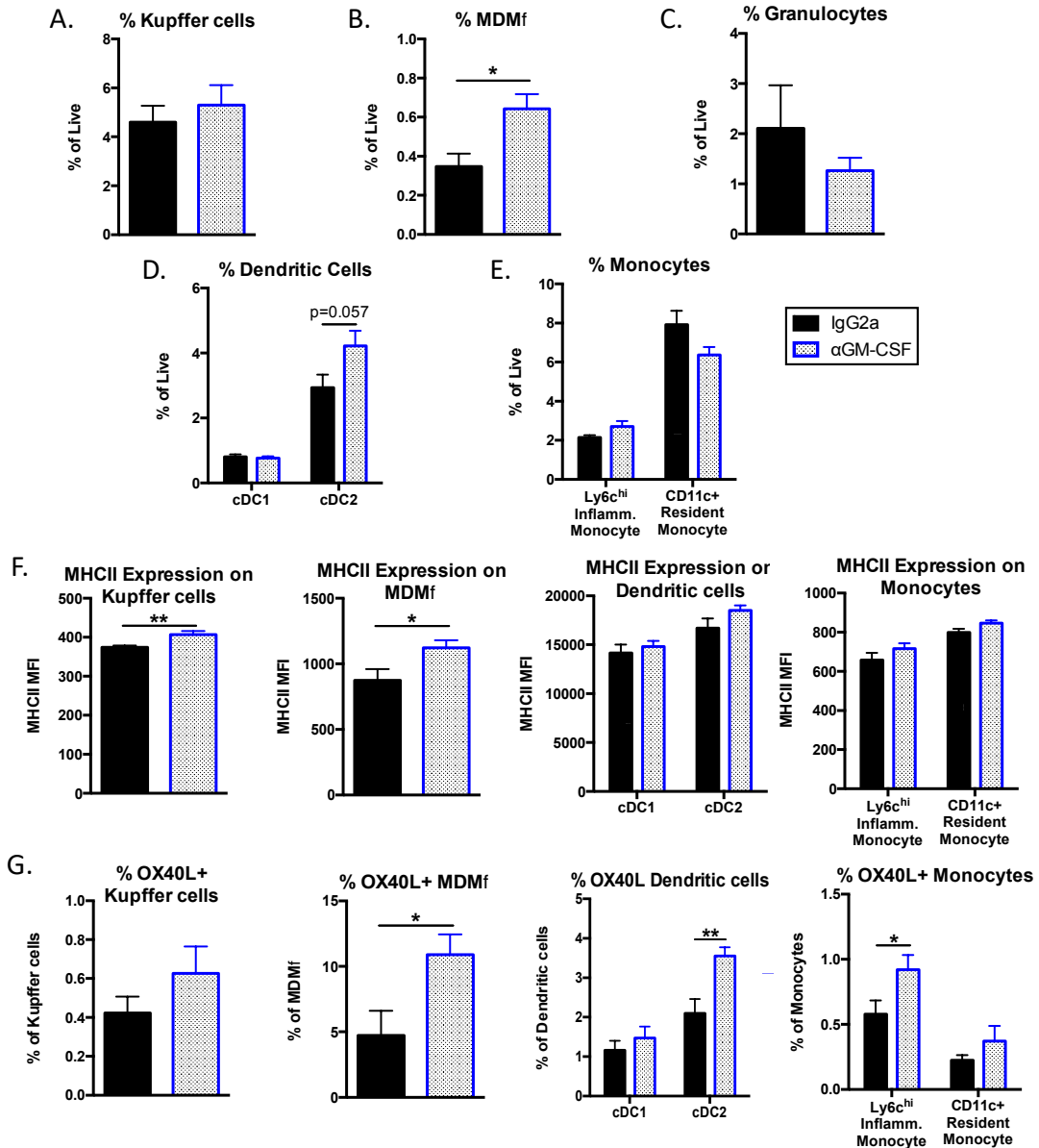
Figure 5.23. GM-CSF blockade leads to increased monocyte-derived macrophages and increased MHCII and OX40L on select myeloid populations in the liver during early HBV immunity. Adult (>8 wks) HBVtg$Rag1_{-/-}$ animals were treated with anti-GM-CSF (blue) or IgG2a control (black) antibodies every two days starting at day -1, and adoptively transferred with HBV-naïve WT splenocytes on day 0. Leukocyte-enriched cell preparations were isolated on day 8 post-transfer and flow cytometry was performed to measure the percentage of (**A**) Kupffer cells (CD45+ F4/80+ CD11b$_{int}$ side-scatter (SSC)$_{hi}$ Ly6c-), (**B**) monocyte-derived macrophages (MDMφ; CD45+ F4/80+ CD11b$_{hi}$ Ly6c+), (**C**) granulocytes (CD45+ Gr1$_{hi}$ CD11b$_{hi}$), (**D**) dendritic cells (DCs; Live CD11c+ MHCII+), further subdivided into classical dendritic cell subsets 1 (cDC1; CD11b-) and 2 (cDC2; CD11b+), and (**E**) monocytes subdivided into inflammatory monocytes (CD45+ CD11b$_{hi}$ Ly6c$_{hi}$ CD11c- NK1.1- MHCII$_{lo/-}$ SSC$_{lo}$) and resident monocytes (CD45+ CD11b+ Ly6c$_{lo/-}$ CD11c+ NK1.1- MHCII$_{lo/-}$ SSC$_{lo}$). (**F**) The median fluorescence intensity of MHCII on Kupffer cells, MDMφ, DCs, and monocytes. (**G**) The percentage of OX40L+ Kupffer cells, MDMφ, DCs, and monocytes relative to the total number of each myeloid cell subset. Data were analyzed using FlowJo™ Software; statistics determined by unpaired two-tailed t-test with GraphPad Prism Software; n=7 per group.

Lastly, I assessed the effect of GM-CSF blockade on the hepatic NK cell and ILC compartment. Mice that received anti-GM-CSF antibody treatment exhibited a decrease in the abundance of hepatic immature NK cells, as marked by a lack of CD49b or CD11b expression (**Fig. 5.24 A-B**). Blockade of GM-CSF, however, had no effect on the number or percentage of hepatic ILC1, ILC2, or ILC3 (**Fig. 5.24 C-E**). There were also no differences in the frequency of NKp46+ versus NKp46- ILC3, nor in the percentage of CD4+, MHCII+, or Ki67+ ILC3s (**Fig. 5.24 F-H**). These data suggest that GM-CSF acts down stream of most ILC subsets and does not positively or negatively regulate expansion of these cells in the liver.
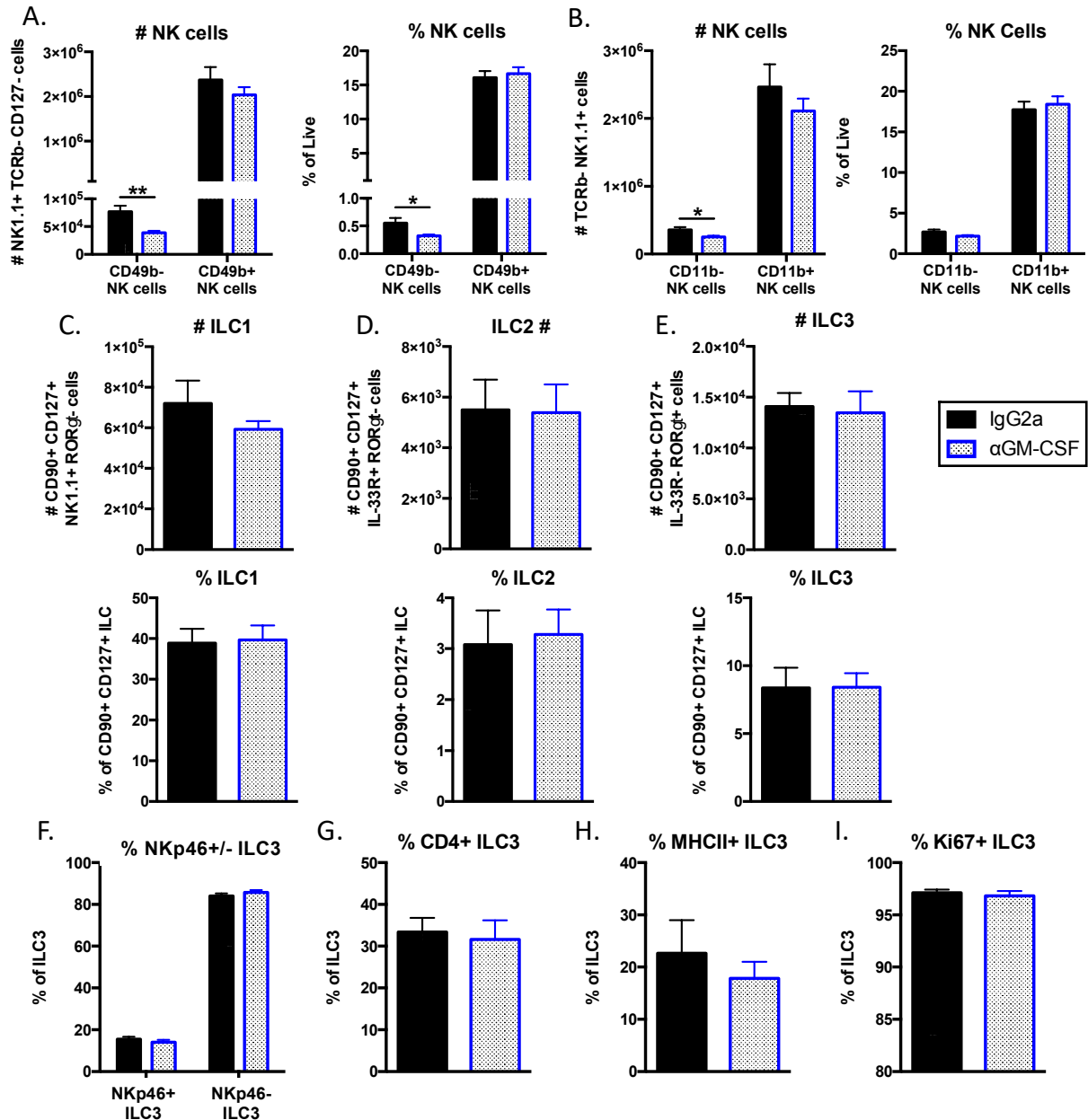
Figure 5.24. GM-CSF blockade impairs accumulation of immature NK cells, but not other ILC populations in the liver during early HBV immunity. Adult (>8 wks) HBVtg*Rag1-/-* animals were treated with anti-GM-CSF (blue) or IgG2a control (black) antibodies every two days starting at day -1, and adoptively transferred with HBV-naïve WT splenocytes on day 0. Leukocyte-enriched cell preparations were isolated on day 8 post-transfer and flow cytometry was performed to measure the number and percentage of (**A**) CD49b+ mature and CD49b- immature NK cells (CD45+ TCRβ- NK1.1+), (**B**) CD11b+ mature and CD11b- immature NK cells (CD45+ TCRβ- NK1.1+), (**C**) ILC1 (CD45+ TCRβ- CD90+ CD127+ NK1.1+ RORγt-), (**D**) ILC2 (CD45+ TCRβ- CD90+ CD127+ RORγt- IL-33R+), and (**E**) ILC3 (CD45+ TCRβ- CD90+ CD127+ RORγt+ IL-33R-). The percentage of (**F**) NKp46+ and NKp46- ILC3, (**G**) CD4+ ILC3, (**H**) MHCII+ ILC3, and (**I**) Ki67+ ILC3 were also measured. Data were analyzed using FlowJo™ Software; statistics determined by unpaired two-tailed t-test with GraphPad Prism Software; n=7 per group.

Discussion

The experiments discussed in this chapter began to elucidate the mechanisms of ILC3 functions that, when disrupted, contribute to an impaired HBV immune response. We learned from *Ccr6*-/-HBVtg*Rag1*-/- mice that the loss of CCR6 expression did not impair HBV immunity. Animals that lacked CCR6 within the recipient innate immune environment were able to efficiently clear HBsAg and mount robust HBV-specific IFNγ T cell responses. Although CCR6 expression is restricted to LTi and LTi-like ILC3s, it remains to be determined whether this population of ILC3s may still contribute to effective HBV immunity in a manner that is not dependent on the actions of CCR6 signaling as *Ccr6*-/- mice do not lack LTi and LTi-like cells, but rather lack the expression of this chemokine receptor within these cells.

We found that the deletion of LIGHT from innate immune cells in recipient HBVtg mice led to improved HBV immune outcomes. *Tnfsf14*-/- mice experienced an early increase in hepatic inflammation followed by rapid clearance of HBsAg and anti-HBs seroconversion compared to LIGHT-sufficient control animals. Furthermore, the T cell response that was primed in the absence of LIGHT was robust and diverse. These data indicate that the loss of LIGHT expression by ILC3s when these cells are depleted either in *Rorc*(γt)-/- mice or by anti-Thy1.2 antibody depletion, is not a driver of the ineffective immune response generated in the absence of ILC3s. The finding that LIGHT deficiency leads to improved HBV immunity, however, highlights an important pathway that regulates effective HBV immune responses and underscores the need to better understand which of the LIGHT receptors may be mediating its suppressive functions.

We further tested the role of the LIGHT/lymphotoxin pathway by targeting the commonly shared receptor of these ligands – LTβR. We used a LTβR-Fc fusion protein that binds and sequesters both LIGHT and LT, such that the ligands cannot bind endogenous LTβR

present on a variety of immune cells. These experiments showed that blockade of LTβR

signaling led to decreased hepatitis and a possible delay in HBsAg clearance. Disruption of this

signaling pathway resulted in altered immune cell localization in the liver, such that there was

increased periportal inflammation reminiscent of our observations in ILC3-deficient mice.

Furthermore, there was a slight, but significant, skewing towards increased CD4+ T cells after

LTβR blockade, also in line with increased CD4+ T cell accumulation in ILC3-deficient mice.

Finally, we observed an increased basal IFNγ response with an impaired HBV-specific T cell

response, although notably these mice were not impaired in their response to the MHCII-

restricted epitope within peptide 81 that is impaired in ILC3-deficient mice. These data support

the hypothesis that diminished LTβR signaling in ILC3-deficient mice may contribute to

impaired HBV-specific T cell responses, accumulation of CD4+ T cells, disrupted immune cell

organization within the liver, and possibly, impaired HBsAg clearance. LTβR signaling is likely

not essential, however, for the early HBV-specific immune response to peptide 81. Future

experiments in these LTβR-Fc treated animals will focus on determining whether or not HBsAg

clearance is truly impaired, and additionally whether there is a defect in anti-HBs

seroconversion. Furthermore, we would also like to evaluate the number and function of HBV-

specific T cells using tetramer staining, with a particular focus on identifying phenotypes of

antigen-specific T cells at later time points, where the defect is most prominent in ILC3-deficient

mice. Considering the large body of evidence showing a role for LTβR signaling in regulating

lymphoid organization, we are most interested in characterizing the quantitative and qualitative

differences in hepatic immune cell distribution in control versus LTβR-Fc treated mice through

the Ilastik analysis pipeline discussed in Chapter 2.

We used cytokine blocking experiments to determine if the most common ILC3-derived cytokines might play a role in HBV immunity. Our initial experiments, focused on blockade of IL-17, showed that the loss of IL-17RA or IL-17F signaling did not cause any obvious defects in HBV disease or immune responses at an early, day 8, time point. There was some suggestion that IL-17F blockade may have had different effects on immunity as compared to a blockade of IL-17RA, the latter of which prevents IL-17A- and IL-17F-mediated signaling. This observation is consistent with other published reports in the liver that showed while IL-17F played an important role in recruitment and activation of CD8+ CTLs in a model of viral infection, IL-17A did not – it antagonized the effects of IL-17F (83). This study made use of genetically deficient IL-17F and IL-17A mice instead of antibody blockade. Thus, it is possible that our antibody-based approach was not sufficient to completely block the effects of IL-17 signaling and therefore future studies are needed before ruling out a role for either IL-17A or IL-17F in mediating the protective effects of ILC3s during HBV immunity. Furthermore, some studies have shown partially redundant roles between IL-17 and other ILC3-derived cytokines including IL-22 and GM-CSF; thus, combinatorial treatments that block two or three of these cytokines at the same time may reveal additional unappreciated phenotypes that more closely mimic ILC3 depletion.

We examined the effects of IL-22 blockade on HBV immunity and, similar to IL-17, found no major defects in the early immune response. Reports in the literature point towards IL-22 in mediating the resolution of inflammation and hepatitis, and as a result we were surprised to find no differences in hepatitis in anti-IL-22-treated animals. One possible explanation for this finding is that IL-22 may play a more important role during the resolution of the HBV immune response. Alternatively, like the IL-17 antibody blockade, it is possible that the antibody treatment against IL-22 did not completely block IL-22 signaling. For these reasons, we have

already begun to cross IL-22-deficient "Catch22" mice to our HBVtg mice in order to study the long-term effects of IL-22 loss on HBV immune responses. We are particularly interested in understanding the role that IL-22 plays in supporting disease resolution, HBsAg clearance, and anti-HBs seroconversion.

Finally, we used antibody-mediated blockade of GM-CSF to determine if this ILC3-derived cytokine may also contribute towards an effective HBV immune response. The results from these experiments suggested that GM-CSF is most important in supporting CD8+ T cell responses. Mice that received anti-GM-CSF treatments tended to have fewer CD8+ effector T cells, including a reduced number of IFNγ+ CD8+ T cells and more PD-1 expression on these cells. Thus, the loss of GM-CSF production by ILC3s in ILC3-deficient mice, may contribute to the impaired CD8+ T cell responses we observed in these mice. Similar to the ILC3-deficient mice, we also found that GM-CSF blockade led to increased OX40L expression within myeloid cells and a concomitant increase in the expansion of OX40+ IFNγ+ T cells. These data suggest that in addition to a possible increase in OX40L driven by a disruption in microbial communities of ILC3-deficient mice, that a reduction of GM-CSF in those animals may also have facilitated increased OX40L expression and expansion of OX40+ T cells. Finally, although we did find a robust early HBV-specific IFNγ response by ELISpot assay, and an equivalent, if not enhanced, HBs$_{126}$+ CD4+ T cell response determined by tetramer staining, a decreased expression of CD127 within the antigen-specific CD4+ T cells suggested that there may be an impairment in the generation of long-lived memory cells. Thus, our future experiments using anti-GM-CSF blockade will focus on characterizing HBV-specific T cells at late time points, as well as monitoring HBsAg clearance and anti-HBs seroconversion to determine if a loss of GM-CSF also impairs a durable antigen-specific response, similar to that seen in ILC3-deficient mice.

Chapter 6: Working Model

The data discussed in this thesis have provided further insights into age-dependent mechanisms of HBV immunity, including revealing a role for hepatic ILC3s in shaping an effective HBV immune response. As mice age from pre-weaning to early adulthood (8-12 weeks-old), the population of ILC3s increases in the liver, similar to these cells in other tissues – most notably the small and large intestine. This time period coincides with a period of substantial gut microbial colonization by commensal organisms. Signals from these microbiota have been shown to contribute to the age-dependent increase of intestinal ILC3s. We hypothesize that this same mechanism also contributes to the increase of hepatic ILC3s because most of the blood in the liver comes through the portal vein, which flows directly from the small intestine and provides a rich source of antigens and pathogen-associated molecular patterns (PAMPs). Experiments comparing the number and phenotype of ILC3s within the livers of young and adult gnotobiotic mice to those of conventional specific pathogen-free (SPF) mice will validate this hypothesis. Nevertheless, due to this high influx of foreign-derived substrates, the immune system within the liver must carefully balance tolerogenic immune responses necessary to prevent pathogenic inflammation – especially during the early microbial colonization period – with the need to protect the liver from hepatotropic pathogens such as HBV. In early life, these hepatic immune responses are more tolerogenic; while, later in life, the liver acquires the ability to mount a protective immune response.

We have begun to identify the molecular and cellular mechanisms that underpin this transition. Early studies in our laboratory identified myeloid cell maturation, including increased expression of antigen presentation and co-stimulatory molecules on these cells, as a critical part

of this process. We went on to show that increased expression of OX40L by various hepatic antigen presenting cells (APCs), as well as a population of CD11b- CD11c- NK1.1- cells in *Rag1*-/- mice we now presume to include ILC3s, is another critical step in this process (*15*). Increased OX40L in adult animals supports enhanced differentiation of Tfh cells and increased production of IL-21 by these cells. Blockade of the OX40/OX40L interaction in adult mice led to impaired HBV antigen clearance and seroconversion, similar to the phenotype of young mice.

We further characterized a defect in CD4+ T cell responses in young mice that revealed impaired early T effector and Tfh cell differentiation along with impaired generation of antigen-specific cells. These T cell defects developed in young mice despite the fact that the T cells themselves originated from an adult animal, highlighting the importance of the immune priming environment in dictating immunity.

In adult animals, the response to HBV antigens results in the aggregation of innate and adaptive immune cells within the liver into distinct clusters of cells, which are localized both around periportal regions and throughout the liver parenchyma. HBV-specific T cells are first detected in the liver – as early as three days post "infection" – and only later, 12 days post-"infection," can these HBV-specific T cells be found within the hepatic draining lymph nodes and the spleen (*14*). These data suggest that the initial immune response to HBV is primed in the liver, not the secondary lymphoid tissues, highlighting the potential role for these clusters in serving as a site of coordinated immune priming. These clusters largely resolve as HBV antigens are cleared from circulation in adult mice, with the exception of few remaining aggregates, which likely serve as a hub for continued activation of long-lived HBV-specific T and B cells that are required to maintain suppression of viral gene expression and detectable secretion of

HBsAg subviral particles. Young mice are impaired in their ability to form these hepatic immune cell aggregates and in their priming of T and B cell responses.

We found that ILC3s associate with these immune cell clusters in both adult and young mice, particularly at later time points, suggesting these cells may support the formation and/or maintenance of these structures. We also found that the organization of immune cell distribution was dramatically disrupted in the absence of ILC3s. Clustering was not prevented when ILC3s were lost, but rather the clusters that did form were more associated with periportal regions of tissue and formed more isolated structures as compared to the clusters that formed in the presence of ILC3s. Evidence from studies in ILC3-deficient mice that did not express the HBV transgene showed that a large portion of the periportal inflammation that occurs in these mice was not dependent on HBV antigens. Thus, this inflammation was likely in part directed at microbial-derived substrates, which may have caused additional bystander activation of non-HBV-specific T cells, particularly CD4+ T cells that were found in great abundance in ILC3-deficient mice. ILC3s are important sources of both lymphotoxins and the related protein, LIGHT, which signal through the receptor LTβR and have known roles in coordinating the organization of lymphoid structures. We found that a blockade of LTβR signaling in adult mice partially recapitulated the phenotype of ILC3 loss, particularly the disruption of immune cell organization and enhanced periportal inflammation. Thus, we hypothesize that the expression of LTα/β and/or LIGHT on hepatic ILC3s contributes to their ability to regulate immune organization and effective immune priming.

Despite the influx of many CD4+ helper T cells, a loss of ILC3s led to impaired antigen-specific CD4+ T cell responses, especially against the most dominant MHCII-restricted HBsAg epitope, indicating that the quality of the CD4+ T cell response was impaired in the absence of

ILC3s. We also found evidence of decreased memory CD4+ T cell populations at later time points in ILC3-deficient mice, suggesting the long-term survival of antigen-specific cells is impaired when ILC3s are lost. Given the known role of MHCII+ ILC3s in supporting CD4+ T cell priming and continued activation beyond the priming window, we hypothesize that impaired antigen presentation by ILC3s either when they are lost, or due to altered expression of MHCII and co-stimulatory molecules including OX40L and CD30L in young mice – both which have been reported by many groups to increase with age on ILC3s – contributes to impaired HBV-specific CD4+ T cell responses. We can validate these hypotheses by testing the ability of hepatic ILC3s from adult versus young mice to effectively prime and/or promote the survival of antigen-specific T cells by sorting and *ex vivo* culturing of ILC3s and tetramer positive CD4+ T cells in the presence of their cognate antigen. Targeted blockade of OX40L and/or CD30L in these assays will pinpoint the role of each or both of these molecules in the abilities of adult and young hepatic ILC3s to support CD4+ T cell responses.

Furthermore, we also found that ILC3 deficiency resulted in a delayed, but significant, defect in the Tfh cell response that correlated with an inability of mice to seroconvert and produce anti-HBs antibodies. Altogether, these immune defects contributed to the impaired ability of ILC3-deficient mice to clear circulating HBsAg. Therefore, hepatic ILC3s play a critical role in supporting the priming, and perhaps even more so, the sustained activation of a pool of effective HBV-specific CD4+ T cells.

In addition, ILC3-deficient mice were impaired in their ability to generate a sufficient CD8+ T cell response, with a dramatic decrease in the number of total hepatic CD8+ T cells. This decrease in CD8+ T cells was not just in numbers, but also in the functional capacity of these cells to produce IFNγ. CD8+ CTLs are known to play an absolutely essential role in the

control of HBV, and thus a reduction in IFNγ-producing CD8+ T cells during early HBV immunity of ILC3-deficient mice likely contributes to their impaired ability to clear HBV antigens. We also identified increased expression of PD-1 on the IFNγ+ CD8+ T cells present in ILC3-deficient mice, indicating these cells may be functionally impaired, as has been reported in studies of acute LCMV infection (75). We found decreased expression of CXCR3 in hepatic CD8+ T cells of ILC3-deficient mice, suggesting that chemokine-mediated recruitment and/or retention of CD8+ T cells in the liver may contribute to the defect in this population.

ILC3s are known to secrete GM-CSF and the actions of this cytokine have important effects on other immune cells. We found that blockade of GM-CSF with antibody treatments led to decreased accumulation of hepatic CD8+ T cells, decreased IFNγ production by these cells, and increased surface expression of PD-1. Thus, we hypothesize that the decrease in GM-CSF in the absence of ILC3s may in part explain impaired CD8+ effector T cell responses. Furthermore, we also found evidence of decreased CD127 expression on antigen-specific CD4+ T cells, suggesting a potential impairment in the generation of long-lived memory cells in the absence of GM-CSF. Thus, we also hypothesize that GM-CSF from ILC3s may contribute to supporting memory T cell generation, which will be further validated by evaluating the pool of antigen-specific memory T cells at a later time point. A longer-term GM-CSF blocking experiment will also reveal whether GM-CSF secretion plays an essential role in supporting an effective immune response that leads to HBsAg clearance and seroconversion.

In sum, we propose a model by which a decrease in the number of ILC3s in young mice that express antigen presentation molecules including MHCII and OX40L results in impaired priming and differentiation of long-lived HBV-specific CD4+ T cells, including Tfh cells. Furthermore, the decreased abundance of LTα/β- and/or LIGHT-expressing ILC3s in young

mice causes impaired immune cell organization resulting in fewer intraparenchymal clusters with decreased cellular diversity. In addition, a defect in early GM-CSF secretion by ILC3s in young mice may contribute to impaired effector CD8+ T cell responses and reduced IFNγ production. Together, these defects result in impaired HBV antigen clearance and seroconversion in young mice that may be overcome in adult mice in part through a more abundant and functionally mature population of hepatic ILC3s.

Chapter 7 – Materials and Methods

Mice and experimental system

All mice were bred and housed in specific pathogen–free housing under an IRB approved protocol (IACUC AN170936) and in accordance with the guidelines of the Laboratory Animal Resource Center of the University of California, San Francisco. WT C57BL/6 mice were purchased from Jackson Laboratory and subsequently bred at UCSF. HBVEnv*Rag1*-/- and HBVRpl*Rag1*-/- mice were previously described (*29*). Briefly, HBVEnv*Rag1*-/- mice were generated using HBV-Env$^+$ mice [lineage 107-5D; gift from F. Chisari, Scripps Research Institute (*6*)] backcrossed to *Rag1*-/- C57BL/6 mice for 15 generations. HBVEnv*Rag1*-/- mice contain the entire envelope (subtype ayw) protein-coding region under the constitutive transcriptional control of the mouse albumin promoter. HBVRpl*Rag1*-/- mice were generated using HBV replication mice [lineage 1.3.46; gift from F. Chisari (*1*)] crossed to *Rag1*-/- C57BL/6 mice for 15 generations. HBVRpl*Rag1*-/- mice contain a terminally redundant HBV DNA construct and produce infectious virus in their hepatocytes and in the proximal convoluted tubules of their kidneys. Young (3 to 3.5 weeks old, before weaning) or adult (>8 weeks old) HBVtg*Rag1*-/- mice were given 0.8-1.0 10$_8$ syngeneic splenocytes pooled from adult (>8 weeks old) WT or mutant mouse strains in 0.5 ml of phosphate-buffered saline via tail vein injection. Mice were followed for plasma ALT using an ALT-L3K kit (Sekisui Diagnostics) on a Cobas Mira Plus analyzer (Roche Diagnostics). *Rorc*(γt)GFP/GFP knockout and *Rorc*(γt)GFP/+ reporter mice (B6.129P2(Cg)-Rorc<tm2Litt>/J; JAX stock #007572) were obtained from Jackson Laboratories (*23*). *Ox40*-/- mice were generated at UCSF (*92*), but provided to us by M. Croft (La Jolla Institute for Allergy and Immunology). *Ccr6*-/- mice (B6.129P2-ccr6<tm1Dgen>/J) were a gift from S. Nishimura, UCSF, which were originally obtained from Jackson Laboratory (JAX stock

#005793). LIGHT-/- (*Tnfsf14*-/-) mice were generated by the UC San Diego Health Sciences transgenic mouse core facility and provided as a gift by M. Kronenberg (La Jolla Institute for Allergy and Immunology) (*93*).

HBV protein assays

Plasma was collected and assayed for the presence of HBsAg by using the ETI-MAK-2 Plus ELISA kit (DiaSorin). HBsAg results are reported as positive or negative, determined by parameters programmed by DiaSorin in an ELx800 plate reader (BioTek). Total HBsAb was quantified by using the ETI-AB-AUK PLUS ELISA kit and ABAU standard set (DiaSorin). Plasma from transferred HBVRpl*Rag1*-/- mice was assayed for the presence of total HBcAb using the ETI-AB-COREK PLUS ELISA kit (DiaSorin).

Cell preparations

Hepatic leukocytes were isolated from the liver after perfusion and digestion. Mice were perfused via the inferior vena cava for 6 minutes using 30 mL of digestion media [HBSS with collagenase type IV (92.53 units/mL; Worthington Biochemical Corporation), and DNase I (0.02 mg/ml; Roche Diagnostics)] per mouse. Livers were chopped and further digested with liberase and DNase I (Roche Diagnostics) [1 Wünsch Units (WU) and 0.8 mg, respectively, in 10 ml of HBSS] for 30 min at 37°C in an orbital shaker. Livers were forced through a 70-mm filter, and debris was removed by centrifugation (30g for 3 min). Supernatants were collected and centrifuged for 10 min at 650g. Cells were resuspended in RPMI 1640 with 5% FBS and were underlayed with a 40%:60% Percoll® gradient (GE Healthcare). Leukocytes were isolated from the Percoll® interface and washed with RPMI 1640 containing 5% FBS or flow cytometry

staining buffer (PBS with 0.5% BSA and 2 mM EDTA). Total live cells isolated from each sample were counted on a Luna-FL™ dual fluorescence cell counter (Logos Biosystems) using acridine orange/propidium iodide (Logos Biosystems) according to manufacturer instructions.

Antibodies and Flow Cytometry

Hepatic leukocytes were prepared as above. Cells were stained according to standard protocols in staining buffer (PBS with 0.5% BSA and 2 mM EDTA) with combinations of anti-mouse antibodies listed below.

Mouse specific antibodies purchased from BD Biosciences™ included: CD11b-PerCP/Cyanine(Cy)5.5 (clone M1/70); CD19-APC/Cy7 (clone 1D3); CD4-APC/Cy7 (clone GK1.5); CD8-Pacific Blue (clone 53-6.7), -Pacific Orange (clone 5H10); CD43-Alexa Fluor (AF)700 (clone S7); CD86-PE (clone GL1); CXCR5/CD185-biotin (clone 2G8) followed by streptavidin-FITC, streptavidin-QDot605, or streptavidin-APC detection; Fas/CD95-PE/Cy7 (clone Jo2); IgG2b (clone R12-3); IgG3 (clone R40-82); Ly6c-AF700 (clone AL-21); Ly6g-PerCP/Cy5.5 (clone 1A8); TCRβ-Pacific Blue (H57-597).

Mouse-specific antibodies purchased from Invitrogen™ (formerly eBioscience™) included: CD11c-APC (clone N418); CD19-AF700 (clone ebio1D3); CD4-FITC (GK1.5); CD44-eFluor450 (clone IM7); F4/80-PE/Cy7 (clone BM8); ICOS-PE (clone 7E.17G9) MHCII (I-A/I-E)-eFluor450 (clone M5/114.15.2); NK1.1-PE/Cy7 (clone PK136); OX40-APC (clone OX86); OX40L-PE (clone RM134L); RORγt-PE (clone B2D), -APC (clone B2D); TCRγδ-PE/Cy7 (clone GL3).

Mouse-specific antibodies purchased from BioLegend® included: B220/CD45R-Brilliant Violet (BV)650 (clone RA3-6B2), -BV711 (clone RA3-6B2), -APC/Cy7 (clone RA3-6B2);

CD11c-APC (N418); CD117/cKit-BV605 (clone 2B8); CD127/IL-7Rα-PE/Cy7 (clone A7R34),
-BV421 (clone A7R34), -APC (clone A7R34); CD138-PerCP/Cy5.5 (clone 281-2); CD19-PE
(clone 6D5), -PerCP/Cy5.5 (clone ID3), -BV570 (clone 6D5); CD3-PE-Cy7 (clone 17A2); CD4-
BV605 (clone RM4-5), -BV650 (clone RM4-5), -AF700 (clone RM4-5); CD44-APC/Fire 750
(clone IM7); CD45-PerCP/Cy5.5 (clone 30-F11), -AF700 (clone 30-F11), -APC/Fire 750 (clone
30-F11); CD49b-PE (clone DX5), -PE/Cy7 (clone DX5), -APC/Cy7 (clone DX5); CD62L-
PE/Cy7 (clone MEL-14), -BV605 (clone MEL-14); CD69-PE (clone H1.2F3), -PE/Cy7 (clone
H1.2F3); CD8-BV570 (clone 53-6.7); CD80-PE (clone 16-10A1); CD90.1/Thy1.1-BV605 (clone
OX-7), -AF700 (clone OX-7); CD90.2/Thy1.2-BV570 (clone 30/H12), -BV605 (clone 30/H12);
CXCR3/CD183-FITC (clone CXCR3-173); CXCR4/CD184-BV605 (clone L276F12);
CXCR5/CD185-BV605 (clone L138D7); F4/80-PE/Cy7 (clone BM8); GL7-FITC (clone GL7);
GM-CSF-PE (clone MP1-2259); Gr1-BV650 (clone RB6-8C5), -APC/Cy7 (clone RB6-8C5);
IgD-APC (clone 11-26c.2a); IgM-PE/Cy7 (clone RMM-1); IL-22-PE (clone Poly5164); Ki67-
BV421 (clone 16A8); KLRG1-PE (clone 2F1/KLRG1); MHCII (I-A/I-E)-BV711 (clone
M5/114.15.2); NK1.1-FITC (clone PK136), -PerCP/Cy5.5 (clone PK136), -BV510 (clone
PK136), -BV605 (clone PK136), -BV650 (clone PK136), APC/Fire 750 (clone PK136); NKp46-
PerCP/Cy5.5 (clone 29A1.4); PD-1/CD279-FITC (clone 29F.1A12), -BV711 (clone 29F.1A12);
Tbet-PE (clone 4B10); TCRβ-PerCP/Cy5.5 (clone H57-597), -BV421 (clone H57-597), -BV650
(clone H57-597), -BV711 (clone H57-597), -APC/Fire 750 (clone H57-597).

The mouse specific anti-IL-33R/ST2-biotin (clone DJ8) antibody was purchased from
MD Bioscienes and secondary detection of the biotinylated antibody was performed with
streptavidin-FITC or streptavidin-APC. The mouse specific anti-IgG1-FITC antibody (clone
SB77e) was purchased from SouthernBiotech.

In most experiments, before surface antibody staining, cells were stained with Zombie Aqua or NIR Fixable Viability Dye Kits for live cell discrimination (BioLegend®). In all experiments, Fc receptors were blocked with anti-mouse CD16/CD32 antibodies from BD BiosciencesTM before surface and intracellular staining.

Cytokine secretion assays were used according to instruction to detect mouse-specific IFNγ and IL-17a (Miltenyi Biotech). Briefly, 10_6 cells were incubated with a "catch" antibody that attached to the cell surface for 5 minutes at 4°C. Next cells are incubated in RPMI 1640 media with 1% mouse serum for 45 minutes at 37°C with gentle shaking (125 rpm) to allow for secretion of the cytokine and sequestration at the cell surface by the "catch" antibody. Afterwards, cells are processed and stained for any additional cell surface antibodies along with a mouse-specific IFNγ or IL-17a secondary detection antibody, which is either directly conjugated to PE or APC, or conjugated to biotin (for IL-17a) and followed by a streptavidin-PE-based detection step.

Intracellular antibody staining for cytokines IL-22 and GM-CSF was performed by resuspending 10_6 cells in RPMI with 10% FBS in the presence of 1 μg/mL Brefeldin A and incubated for 4 hours at 37°C and 5% CO_2. After staining cells with surface antibodies, cells were fixed and permeabilized using the eBioscienceTM FoxP3/Transcription Factor Staining Buffer set according to manufacturer instructions. Cells were stained with intracellular anti-GM-CSF or anti-IL-22 along with anti-RORγt overnight in permeabilization buffer. Cells were washed twice the following morning with permeabilization/wash buffer and finally washed and resuspended in staining buffer (PBS with 0.5% BSA and 2 mM EDTA) before running on the flow cytometer. Cells that were stained for intracellular/nuclear Tbet or RORγt without cytokines

were treated the same as described above with the exception of the 4-hour incubation with Brefeldin A.

Following staining and washing back into staining buffer, cells were analyzed using an LSR II flow cytometer (BD Biosciences) or sorted on an Aria III (BD Biosciences) with FACSDivaTM software (BD Biosciences). Data were analyzed using FlowJo® Software (TreeStar). Absolute numbers of cells were calculated using by comparing the number of live cells determined immediately after cell isolation, and prior to cell staining, using Luna FL cell counter-based cell counts to the number of live, single cell events, as determined by standard forward scatter (FSC)-height (H) by FSC-area (A) single cell discrimination and negative staining with Zombie Fixable Viability dye kits (BioLegend®). The ratio of total live cells from Luna counts to the number of live single cell events was then multiplied by the number of events for each individual cell population identified. Percentages of each cell population are reported as a percentage of the population described on the y-axis of each graph, usually total live cells, CD45+ cells, or in some cases T cells or other specified sub-populations.

Enzyme-Linked ImmunoSpot (ELISpot)

IFNγ ELISpot assays (BD Biosciences) were performed on unstimulated liver leukocytes. Liver cells were prepared as described above. Equivalent numbers of hepatic leukocytes and splenocytes from *Rag1-/-* mice, as a source of optimal antigen presentation, were plated in ELISpot membrane plates pre-coated with immobilized anti-mouse IFNγ capture antibodies. Cells were incubated overnight at 37°C at 5% CO_2 in the presence of HBV-derived peptides. Peptide pool ELISpot assays were performed using fifteen-mer peptides that were generated across the whole envelope protein with 11 overlapping amino acids between peptides (Sigma-

Aldrich); 12 to 14 sequential peptides were combined in seven pools. Subsequent assays were performed with individual peptides identified to represent the dominant and subdominant epitopes and varying in length from 8-15 amino acids. Cells were incubated with peptides at a final concentration of 5 mg/ml for each peptide in RPMI 1640 media with 10% FBS. ELISpot assays were performed and developed following the manufacturer's instructions (BD Biosciences). Developed and dried plates were analyzed and individual IFNγ spots counted using an ImmunoSpot® plate reader and software (Cellular Technology Limited).

OX40L blocking antibody and OX40 agonist

For specified experiments, HBVEnv*Rag1*-/- adult mice received intraperitoneal (i.p.) injection of 100 μg of OX40L blocking antibody (RM134L, BioXCell) or control immunoglobulin G (IgG) (purified rat IgG2b isotype control, UCSF Monoclonal Antibody Core Facility) on days 0, 2, 4, and 6 after adoptive transfer of adult WT splenocytes. Similarly, 3-week-old HBVEnv*Rag1*-/- mice received i.p. injection of 150 μg of OX40 agonist antibody (OX86, BioXCell) or with control IgG (purified rat IgG1 isotype control, UCSF Monoclonal Antibody Core Facility) on days 0, 3, and 5 after adoptive transfer of adult WT splenocytes. For experiments treating mice confirmed to have the serological profile of CHB (adoptively transferred at 3 weeks of age; no early ALT rise, HBsAg$^+$, and HBsAb$^-$ and allowed to rest for 3 months), mice received an intraperitoneal injection of 150 μg of OX40 agonist antibody or with control IgG either on days 84, 87, 89 and 168, 171, 173, 175 after adoptive transfer of adult WT splenocytes or three times per week for eight treatments starting on day ≥84 after adoptive transfer of adult WT splenocytes.

Anti-Thy1.2-mediated ILC depletion

For experiments using anti-Thy1.2-mediated depletion of ILCs and some NK cells, one of two treatment regimens were followed. For day 8 experiments, mice received 200 μg of anti-Thy1.2 blocking antibody (30H12, BioXCell) or isotype control rat IgG2b antibody (LTF-2, BioXCell) via i.p. injection. Animals were treated every 3 days starting 4 days before adoptive transfer and continuing through day 5 post-adoptive transfer. For day 22 experiments, mice received the same quantity of anti-Thy1.2 or control antibodies via i.p. injection. Animals were treated every 3 days starting at 3-weeks old, 21 days before adoptive transfer, and continuing through day 21 post-adoptive transfer, such that animals were adoptively transferred at 6 weeks of age and sacrificed at 9 weeks of age.

Blockade of LTβR signaling

For experiments blocking signaling via LTβR signaling, a murine LTβR-human immunoglobulin Fc receptor fusion protein (LTβR-Fc) was used, provided by Dr. Carl Ware [Sanford Burnham Prebys Medical Discovery Institute, (*89*)]. This LTβR-Fc protein with mouse specificity functions by binding to lymphotoxin α/β and LIGHT and preventing their binding and signaling to endogenous LTβR. Mice were treated with 100 μg of LTβR-Fc (mLTβR:huFc-IgG1) or human IgG1 isotype control antibodies (BE0297, BioXCell) via i.p. injection. Mice were treated every three days beginning four days before adoptive transfer and continuing through either day 5, for experiments ended at day 8, or through day 11, for experiments ended at day 14.

Anti-IL-17RA/-IL-17F cytokine blockade

For experiments blocking IL-17 signaling, animals were treated with IL-17 blocking antibodies gifted by S. Nishimura. Mice were treated with 500 μg of anti-IL-17RA (M751, Amgen), anti-IL-17F (M850VL, Amgen), or mouse IgG1 isotype control antibodies (MOPC-21, BioXCell) via i.p. injection. Mice were treated every two days starting one day before adoptive transfer and continuing through day 7 post-transfer. Animals were sacrificed 8 days post-adoptive transfer.

Anti-IL-22 cytokine blockade

For experiments targeting IL-22 signaling, animals were treated with 150 μg of either anti-IL-22 blocking antibodies (IL22JOP, eBioscience/Invitrogen) or rat IgG2a isotype control antibodies (2A3, BioXCell) via i.p. injection. Mice were treated every two days starting one day before adoptive transfer and continuing through day 5 post-transfer. Animals were sacrificed 8 days post-adoptive transfer.

Anti-GM-CSF cytokine blockade

For experiments targeting GM-CSF signaling, animals were treated with 300 μg of either anti-GM-CSF blocking antibodies (MP1-22E9, BioXCell) or rat IgG2a isotype control antibodies (2A3, BioXCell) via i.p. injection. Mice were treated every two days starting one day before adoptive transfer and continuing through day 5 post-transfer. Animals were sacrificed 8 days post-adoptive transfer.

Antibiotic administration

Broad spectrum antibiotics were dissolved in the drinking water of HBVtg*Rag1*-/- or

HBVtg*Rag1*-/-*Rorc*(γt)GFP/GFP mice starting during gestation and through adulthood and the

completion of the specified experiments. Specifically, Vancomycin (1 g/L), Ampicillin (0.5 g/L),

Neomycin Sulfate (1 g/L), and Metronidazole (0.5 g/L) antibiotics were used to target most

Gram-positive, Gram-negative, and anaerobic species. Antibiotic drinking water was changed

three times per week. Animal weight was monitored to ensure sufficient hydration.

Liver hematoxylin and eosin histology

For OX40/OX40L related experiments, liver tissue was fixed in 4% paraformaldehyde

(PFA) or 10% formalin and embedded in paraffin blocks. Five-micrometer slices were cut. PFA-

and formalin-fixed tissues were stained with hematoxylin and eosin (H&E) according to standard

protocols by the Gladstone Histology and Light Microscopy Core and scored by a pathologist

who was blinded to sample identity.

For subsequent experiments, liver tissue was fixed in 10% formalin for 2 hours at 4°C

followed by 22 hours at room temperature (2 + 22 method). Samples washed three times for 5

minutes at room temperature in PBS to remove the fixative, followed by dehydration in a graded

ethanol series from 30 percent to 50 percent to 70 percent ethanol, for one hour at each step at

room temperature. Samples were stored in 70 percent ethanol at room temperature for up to two

weeks before embedding in paraffin blocks at the UCSF Biorepository and Tissue Biomarker

Technology Core (BTBTC). Two or three 4 μm serial sections per sample were cut and stained

with H&E according to standard protocols by the BTBTC. Images were scanned using an

automated Zeiss Axioscanner Z1 whole-slide scanning system at 20X resolution. Where specified, images were scored by a pathologist who was blinded to sample identity.

HBsAg protein detection and scoring by immunohistochemistry

Liver tissue was collected 1, 8, or 24 weeks after adoptive transfer of HBVRpl*Rag1*-/- mice with either WT or *Ox40*-/- splenocytes and fixed in 10% formalin for 24 hours. Fixed liver tissue was subsequently processed and embedded in paraffin following standard protocols. Paraffin blocks were sectioned at 5 mm, and immunohistochemistry for HBV surface antigen was performed on these formalin-fixed paraffin-embedded (FFPE) tissues. Briefly, molecular localization studies were conducted using a Ventana Discovery XT autostainer (Ventana Medical Systems, Roche Group). FFPE tissues were sectioned at 5 mm, barcoded, and then placed in the autostainer for paraffin extraction and rehydration. A rabbit polyclonal antibody (Bio-Rad) was found to be specific for HBV surface antigen and was used at a final con- centration of 1.3 mg/ml. Antigen retrieval (CC1 mild; Ventana Medical Systems), primary antibody dilution, incubation temperature and duration, detection technique, and 3,3′-diaminobenzidine (DAB) chromogen (ChromoMap DAB Kit, Ventana Medical Systems) were optimized on sections of HBV-infected positive control liver (Newcomer Supply) and included evaluation of isotype-matched irrelevant antibody controls, as well as known negative liver tissue. Slides were counterstained (hematoxylin, Ventana Medical Systems) and cover-slipped (Micromount, Leica Biosystems). HBsAg expression was scored qualitatively by an unbiased pathologist using the following criteria: 0, no staining; 1, multifocal granular or diffuse staining in hepatocytes involving <25% of section; 2, granular or diffuse staining around centrilobular hepatocytes with no staining in portal regions; 3, diffuse positivity of hepatocytes restricted to the centrilobular

region; granular cytoplasmic positivity in the remaining hepatocytes; 4, diffuse positivity of hepatocytes restricted to the centrilobular and mid zonal regions; granular cytoplasmic positivity in the remaining hepatocytes; and 5, diffuse positivity of all hepatocytes.

Chromogenic immunohistochemistry (IHC) tissue staining and imaging

Samples were fixed and embedded in paraffin blocks according to the 2 + 22 method described above. Paraffin block embedding, tissue sectioning, staining, and imaging was completed at the UCSF BTBTC with guidance and scientific input from Jillian Jespersen and Dr. Jody Baron. Two to three 4 μm serial sections were cut and mounted on the same slide for each sample. Tissue sections were stained according to optimized protocols developed in collaboration between Jillian Jespersen and Jennifer Bolen; which were programmed into the automated slide staining Ventana Discovery Ultra platform. The following antibodies were used: rabbit anti-mouse/human CD3 (SP7, Abcam), rabbit anti-mouse CD4 (EPR19514, Abcam), rat anti-mouse CD8α (4SM15, eBioscience/Invitrogen), rabbit anti-mouse CD11b (Rb Poly, Novus Biosciences), rat anti-mouse/human CD45R/B220 (RA3-6B2, eBioscience/Invitrogen), and rabbit anti-mouse RORγ (EPR20006, Abcam). These antibodies were combined into the following duplex and triplex stains: (i) CD8α-purple, CD4-yellow, protocol #2154; (ii) RORγ-purple, CD8α-teal, CD4-yellow, protocol #3908, (iii) RORγ-purple, CD11b-teal, CD3-yellow, protocol #3911; (iv) RORγ-purple, CD45R/B220-teal, CD3-yellow, protocol #3904, (v) CD45R/B220-purple, CD11b-teal, CD3-yellow, protocol #3902. Sections were dried and coverslipped followed by imaging at 20X resolution on the Zeiss Axioscanner Z1. Native, uncompressed CZI imaging files were used as a starting point for subsequent image analysis.

Ilastik imaging analysis

Image analysis was completed in collaboration between Jillian Jespersen and Austin Edwards, a bioinformatician in the UCSF Biological Imaging Development Center (BIDC). CZI images were converting to the Big Tiff file format using Zen software (Zeiss), and then to HDF5 format using the Ilastik plug-in for FIJI (*94-96*).

We trained two Random Forest classifiers in the 1.3.3 version of Ilastik (*97*). The training set was 58 2000x2000-pixel images taken across 4 tissue samples from the RORγ/CD8α/CD4 triplex stain. One classifier is a binary classifier used to predict nuclei pixels and stroma pixels in an RGB image. The nuclei pixels were segmented into objects using hysteresis thresholding (Gaussian smoothing σ = 1.0, core threshold = 0.55, final threshold = 0.65). The second classifier was trained to classify these objects into one of 6 cell types: CD4, CD8, Th17, ILC3, Tc17 and other. The output of this classifier provided the predicted label and the coordinates of the center of these objects.

Austin built a GUI to take these coordinates and labels as input, visualize and filter them based on user-provided parameters. The GUI also allows users to create custom ROIs on the raw image to filter out tissue and staining artefacts. Using the GUI, Austin filtered the output of each sample prediction to include only immune cells (i.e. removed "other"-type cells) and remove tissue artefacts.

We used the scikit-learn (*98*) Python implementation of Density-Based Spatial Clustering of Applications with Noise (DBSCAN) (*99*) to cluster the filtered immune cell objects. All parameters used were default, except for the eps parameter, which is "the maximum distance between two samples for one to be considered as in the neighborhood of the other," which we specified as 100 pixels.

Vessel segmentation is done by training a third classifier in Ilastik to predict lumen, blood and stroma pixels. Lumen and blood pixels are grouped together to create a new vessel class. We then use these vessel objects to calculate distance metrics between immune cell clusters and the vessels.

RNA extraction and quantitative real-time PCR

RNA isolated from hepatic leukocyte-enriched cell preparations was prepared using a RNeasy micro kit (Qiagen) with vortex and QIAshredder (Qiagen) disruption. RNA isolated from liver tissue was prepared using a RNeasy mini kit (Qiagen) using bead beat lysing (MP Biomedicals) and QIAshredder (Qiagen) disruption. cDNA was generated on 0.25 to 1.00 μg of RNA using an iScript cDNA synthesis kit (Bio-Rad). Real-time PCR was performed on 2.5 μl of cDNA product using iTaq Universal SYBR Green Supermix with ROX (Bio-Rad) and the following mouse gene primers: *Gapdh*, 5′-GGAGCGAGACCCCACTAACA-3′ (forward) and 5′-ACATACTCAGCACCGGCCTC-3′ (reverse); *Il21*, 5′-TCATCATTGACCTCGTGGCCC-3′ (forward) and 5′-ATCGTACTTCTCCACTTGCAATCC-3′ (reverse); and *Ox40l*, 5′-TCTGTGCTTCATCTATGTCTGC-3′ (forward) and 5′-CATCCTCACATCTGGTAACTGC-3′ (reverse). Real-time PCR was performed on the 7300 Real-Time PCR System (Applied Biosystems) for OX40/OX40L experiments. For subsequent experiments, qPCR was performed on the Quant Studio 6 PCR System (Applied Biosystems). Data is presented as log2 fold change (2-ΔCt) expression relative to *Gapdh* or log2 fold change expression relative to *Gapdh* normalized to a control group (2-$\Delta\Delta$Ct), as specified.

Patient samples and OX40L RNA expression

Twenty-four infants (6 to 12 weeks of age) were liver-biopsied to rule out biliary atresia at the UCSF Medical Center. Six of these patients were found to have biliary atresia, 6 had neonatal non-viral hepatitis, 10 were found to have a nonspecific liver disease diagnosis, including cholestasis and ductopenia, and 2 had an unknown diagnosis. Nine adult liver samples were obtained from donor livers before transplantation. RNA from FFPE tissue was extracted using the RNeasy FFPE kit (Qiagen) following the manufacturer's instructions. Isolated RNA (150 ng) was reverse-transcribed using the QuantiFast Probe assay (Qiagen) and amplified using specific probes and primers to human *GAPDH* and *OX40L* or using by the prime PCR probe assay (Bio-Rad) for *CD14, CD68*, and *GAPDH*.

PBMC were obtained from eight patients with confirmed AHB infection at the time of active hepatitis and confirmed subsequent viral clearance and HBsAb seroconversion, eight patients with con- firmed CHB infection exhibiting a flare of disease (ALT rise), as well as six patients with confirmed CHB with inactive disease (normal ALT), and six healthy individuals. Cells were stained according to standard protocols with combinations of the following antihuman antibodies: TCRαβ-PE-Cy7 (BioLegend; clone, IP26), CD4-BV785 (BioLegend; clone, OKT4), OX40-PE [BioLegend; clone, Ber-ACT35 (ACT35)], ICOS–PerCP–eFluor 710 (eBioscience; clone, ISA-3), CXCR5-APCs (BD Biosciences; clone, RF8B2), CD8-BV570 (BioLegend; clone, RPA-T8), CD56-BV605 (BioLegend; clone, HCD56), CD16-AF700 (BioLegend; clone, 3G8), and CD19-BV650 (BioLegend; clone, HIB19).

Acutely infected HBV patients had confirmed elevated viral loads ($6.3 \times 10^6 \pm 5.1 \times 10^6$ IU/ml), elevated ALT (146 to 2996 U/liter), HBsAg$^+$ and IgM core antibody–positive, and a clinical history of exposure. CHB patients exhibiting a flare in disease had confirmed elevated

viral loads ($1.4 \times 10_7 \pm 5.1 \times 10_6$ IU/ml), elevated ALT (133 to 1307 U/liter), HBsAg$^+$, and known history of chronic infection. Chronic inactive HBV patients not on antiviral therapy had confirmed low ALT (16 to 32 U/liter) and confirmed viral loads (2453 ± 1262 IU/ml). Uninfected controls had confirmed low ALT (16 to 32 U/liter) and were HBsAg$^-$.

Gene expression by microarray

RNA was isolated using QIAGEN RNeasy micro kits, as described above, and 1 μg of RNA was submitted to the UCSF Functional Genomics core for microarray analysis. Total RNA quality was assessed using a Pico Chip on an Agilent 2100 Bioanalyzer (Agilent Technologies, Palo Alto, CA). RNA was amplified and labeled with Cy3-CTP using the Agilent low RNA input fluorescent linear amplification kits following the manufacturers protocol (Agilent). Labeled cRNA was assessed using the Nandrop ND-100 (Nanodrop Technologies, Inc., Wilmington DE), and equal amounts of Cy3 labeled target were hybridized to Agilent whole mouse genome 4x44K Ink-jet arrays (Agilent). Hybridizations were performed for 14 hrs, according to the manufacturers protocol (Agilent). Arrays were scanned using the Agilent microarray scanner (Agilent) and raw signal intensities were extracted with Feature Extraction v10.1 software.

This dataset was normalized using the quantile normalization method that is proposed by Bolstad et al. (*100*). No background subtraction was performed, and the median feature pixel intensity was used as the raw signal before normalization.

A one-way ANOVA linear model was fit to the comparison to estimate the mean M values and calculated moderated t-statistic, B statistic, false discovery rate and p-value for each gene for the comparison of interest. Adjusted p-values were produced by the method proposed by Holm

(*101*). All procedures were carried out using functions in the R package limma in Bioconductor (*102, 103*).

The heat map presented was generated by Andrew Schroeder, using the *aveA* values, which represent the average log$_2$ based intensity of the same probe across all arrays – a proxy for gene expression level – on selected genes relevant to ILC3 and/or HBV biology.

HBV transcript measurement by Northern blot

RNA was extracted from flash-frozen liver pieces collected 1, 8, or 24 weeks after adoptive transfer of HBVRpl*Rag1*-/- recipient mice with either WT or *Ox40*-/- splenocytes using a modified TRIzol extraction (*38*). Briefly, 1 ml of TRIzol (Life Technologies) was added to 25 mg of tissue and homogenized at 6000 rpm for 30 s using the MagNA Lyser instrument (Roche). RNA was extracted into the aqueous phase with the addition of 0.2 ml of chloroform (Sigma-Aldrich) and precipitated in 0.5 ml of isopropanol (Sigma-Aldrich). The pellet was washed with 1 ml of 75% ethanol and resuspended in RNase-free water. Ten-microliter RNA samples were separated by denaturizing 1.2% agarose gel electrophoresis with reagents from the NorthernMax Kit (ThermoFisher) and transferred to a Nytron membrane using the TurboBlotter apparatus (Sigma-Aldrich). A DIG-labeled (−) strand HBV RNA probe was transcribed from Sca I– linearized pGEM3Z- HBV plasmid with the DIG Northern Starter Kit (Sigma-Aldrich) according to the manufacturer's instructions. Hybridization at 68°C, washes, and detection with CDP-Star were carried out according to the DIG Wash and Block buffer set instructions (Sigma-Aldrich), and images were acquired with the Azure c300 system (Azure Biosystems). HBV envelope transcript abundance was quantitated using FIJI (*94-96*) software analysis of HBV

envelope large (2.4 kb) and middle/small (2.1 kb) RNA transcript band intensities detected on the Northern blots and normalized to detected 18S RNA band intensities for each sample.

Statistical analysis

Statistics were performed using Prism (Graph Pad Software). Statistical significance was determined by two-tailed unpaired Student's t test (when two groups were compared), two-tailed paired Student's t test (for longitudinal analyses of the same mice), one-way ANOVA with Dunnett's correction for multiple comparisons to a control group (when one parameter was compared between more than two groups and a defined control group), or one-way ANOVA with Tukey's multiple-comparison test (when one parameter was compared for more than two biological groups, and all groups were compared to each other), or two-way ANOVA with Dunnett's correction for multiple comparisons to a control group (when multiple parameters were compared between more than two groups and a defined control group), or two-way ANOVA with Tukey's multiple-comparison test (when one parameter was compared for more than two biological groups, and all groups were compared to each other). For significance of HBsAg clearance, in which one of two possible outcomes was compared (clearance=1 versus no clearance=0), log-rank (Mantel-Cox) Chi-square test was used. For ordinal or ranked data (histology scores), the Mann-Whitney rank sum test was used. In all figures with multiple n, data are presented as means ± SEM. $P < 0.05$ was considered significant.

References

1.   F. V. Chisari, Hepatitis B virus transgenic mice: insights into the virus and the disease. *Hepatology* **22**, 1316-1325 (1995).

2.   F. V. Chisari, C. Ferrari, Hepatitis B virus immunopathogenesis. *Annu Rev Immunol* **13**, 29-60 (1995).

3.   W. J. Edmunds, G. F. Medley, D. J. Nokes, A. J. Hall, H. C. Whittle, The influence of age on the development of the hepatitis B carrier state. *Proceedings. Biological sciences* **253**, 197-201 (1993).

4.   C. f. D. C. a. Prevention, Viral hepatitis surveillance — United States, 2017. (2019).

5.   W. H. O. (WHO), Global hepatitis report, 2017. 83 (2017).

6.   F. V. Chisari *et al.*, Expression of hepatitis B virus large envelope polypeptide inhibits hepatitis B surface antigen secretion in transgenic mice. *J Virol* **60**, 880-887 (1986).

7.   L. G. Guidotti, B. Matzke, H. Schaller, F. V. Chisari, High-level hepatitis B virus replication in transgenic mice. *J Virol* **69**, 6158-6169 (1995).

8.   U. S. Gill, N. E. McCarthy, CD4 T cells in hepatitis B virus: "You don't have to be cytotoxic to work here and help". *Journal of Hepatology* **72**, 9-11 (2020).

9.   J. Publicover *et al.*, IL-21 is pivotal in determining age-dependent effectiveness of immune responses in a mouse model of human hepatitis B. *The Journal of clinical investigation* **121**, 1154-1162 (2011).

10.   Y. Li *et al.*, Circulating chemokine (C-X-C Motif) receptor 5(+) CD4(+) T cells benefit hepatitis B e antigen seroconversion through IL-21 in patients with chronic hepatitis B virus infection. *Hepatology* **58**, 1277-1286 (2013).

11. H. C. Yang, J. H. Kao, Persistence of hepatitis B virus covalently closed circular DNA in hepatocytes: molecular mechanisms and clinical significance. *Emerg Microbes Infect* **3**, e64 (2014).

12. I. Dervite, D. Hober, P. Morel, Acute hepatitis B in a patient with antibodies to hepatitis B surface antigen who was receiving rituximab. *N Engl J Med* **344**, 68-69 (2001).

13. T. H. Westhoff *et al.*, Fatal hepatitis B virus reactivation by an escape mutant following rituximab therapy. *Blood* **102**, 1930 (2003).

14. J. Publicover *et al.*, Age-dependent hepatic lymphoid organization directs successful immunity to hepatitis B. *The Journal of clinical investigation* **123**, 3728-3739 (2013).

15. J. Publicover *et al.*, An OX40/OX40L interaction directs successful immunity to hepatitis B virus. *Sci Transl Med* **10**, (2018).

16. H. D. Marshall *et al.*, Differential expression of Ly6C and T-bet distinguish effector and memory Th1 CD4(+) cell properties during viral infection. *Immunity* **35**, 633-646 (2011).

17. A. D. Sette *et al.*, Overcoming T cell tolerance to the hepatitis B virus surface antigen in hepatitis B virus-transgenic mice. *J Immunol* **166**, 1389-1397 (2001).

18. Q. You, L. Cheng, R. M. Kedl, C. Ju, Mechanism of T cell tolerance induction by murine hepatic Kupffer cells. *Hepatology* **48**, 978-990 (2008).

19. P. Knolle *et al.*, Human Kupffer cells secrete IL-10 in response to lipopolysaccharide (LPS) challenge. *J Hepatol* **22**, 226-229 (1995).

20. G. Thomas, R. Tacke, C. C. Hedrick, R. N. Hanna, Nonclassical patrolling monocyte function in the vasculature. *Arterioscler Thromb Vasc Biol* **35**, 1306-1316 (2015).

21.   Y. R. Yu *et al.*, A Protocol for the Comprehensive Flow Cytometric Analysis of Immune Cells in Normal and Inflamed Murine Non-Lymphoid Tissues. *PLoS One* **11**, e0150606 (2016).

22.   C. S. N. Klose *et al.*, Differentiation of type 1 ILCs from a common progenitor to all helper-like innate lymphoid cell lineages. *Cell* **157**, 340-356 (2014).

23.   G. Eberl *et al.*, An essential function for the nuclear receptor RORγt in the generation of fetal lymphoid tissue inducer cells. *Nature Immunology* **5**, 64-73 (2004).

24.   M. Tsuji *et al.*, Requirement for Lymphoid Tissue-Inducer Cells in Isolated Follicle Formation and T Cell-Independent Immunoglobulin A Generation in the Gut. *Immunity* **29**, 261-271 (2008).

25.   E. Scandella *et al.*, Restoration of lymphoid organ integrity through the interaction of lymphoid tissue–inducer cells with stroma of the T cell zone. *Nature Immunology* **9**, 667-675 (2008).

26.   M. Lochner *et al.*, In vivo equilibrium of proinflammatory IL-17+ and regulatory IL-10+ Foxp3+ RORγt+ T cells. *Journal of Experimental Medicine* **205**, 1381-1393 (2008).

27.   M. L. Robinette *et al.*, Transcriptional programs define molecular characteristics of innate lymphoid cell classes and subsets. *Nat Immunol* **16**, 306-317 (2015).

28.   H. Peng *et al.*, Liver-resident NK cells confer adaptive immunity in skin-contact inflammation. *The Journal of clinical investigation* **123**, 1444-1456 (2013).

29.   J. L. Baron *et al.*, Activation of a Nonclassical NKT Cell Subset in a Transgenic Mouse Model of Hepatitis B Virus Infection. *Immunity* **16**, 583-594 (2002).

30.   S. Vilarinho, K. Ogasawara, S. Nishimura, L. L. Lanier, J. L. Baron, Blockade of NKG2D on NKT cells prevents hepatitis and the acute immune response to hepatitis B virus. *Proc Natl Acad Sci U S A* **104**, 18187-18192 (2007).

31.   T. McHedlidze *et al.*, Interleukin-33-Dependent Innate Lymphoid Cells Mediate Hepatic Fibrosis. *Immunity* **39**, 357-371 (2013).

32.   Z. Al Nabhani *et al.*, A Weaning Reaction to Microbiota Is Required for Resistance to Immunopathologies in the Adult. *Immunity* **50**, 1276-1288.e1275 (2019).

33.   F. Melo-Gonzalez, M. R. Hepworth, Functional and phenotypic heterogeneity of group 3 innate lymphoid cells. *Immunology* **150**, 265-275 (2017).

34.   C. L. Franklin, A. C. Ericsson, Microbiota and reproducibility of rodent models. *Lab Anim (NY)* **46**, 114-122 (2017).

35.   M. R. Hepworth *et al.*, Innate lymphoid cells regulate CD4+ T-cell responses to intestinal commensal bacteria. *Nature* **498**, 113-117 (2013).

36.   M.-Y. Kim *et al.*, CD4+CD3− Accessory Cells Costimulate Primed CD4 T Cells through OX40 and CD30 at Sites Where T Cells Collaborate with B Cells. *Immunity* **18**, 643-654 (2003).

37.   F. M. Lehmann *et al.*, Microbiota-induced tissue signals regulate ILC3-mediated antigen presentation. *Nature Communications* **11**, 1794 (2020).

38.   N. von Burg *et al.*, Activated group 3 innate lymphoid cells promote T-cell-mediated immune responses. *Proc Natl Acad Sci U S A* **111**, 12835-12840 (2014).

39.   F. J. Jacobi *et al.*, OX40 stimulation and PD-L1 blockade synergistically augment HBV-specific CD4 T cells in patients with HBeAg-negative infection. *J Hepatol* **70**, 1103-1113 (2019).

40.   A. P. Benechet *et al.*, Dynamics and genomic landscape of CD8(+) T cells undergoing hepatic priming. *Nature* **574**, 200-205 (2019).

41.   A. P. Theiss, D. Chafin, D. R. Bauer, T. M. Grogan, G. S. Baird, Immunohistochemistry of colorectal cancer biomarker phosphorylation requires controlled tissue fixation. *PLoS One* **9**, e113608 (2014).

42.   S. Berg *et al.*, ilastik: interactive machine learning for (bio)image analysis. *Nat Methods* **16**, 1226-1232 (2019).

43.   Z. Sun *et al.*, Requirement for RORgamma in thymocyte survival and lymphoid organ development. *Science* **288**, 2369-2373 (2000).

44.   H. Takatori *et al.*, Lymphoid tissue inducer-like cells are an innate source of IL-17 and IL-22. *J Exp Med* **206**, 35-41 (2009).

45.   J. Rangel-Moreno *et al.*, The development of inducible bronchus-associated lymphoid tissue depends on IL-17. *Nature immunology* **12**, 639-646 (2011).

46.   H. C. Hsu *et al.*, Interleukin 17-producing T helper cells and interleukin 17 orchestrate autoreactive germinal center development in autoimmune BXD2 mice. *Nat Immunol* **9**, 166-175 (2008).

47.   A. Gladiator, N. Wangler, K. Trautwein-Weidner, S. LeibundGut-Landmann, Cutting Edge: IL-17–Secreting Innate Lymphoid Cells Are Essential for Host Defense against Fungal Infection. *The Journal of Immunology* **190**, 521 (2013).

48.   H. Ishigame *et al.*, Differential Roles of Interleukin-17A and -17F in Host Defense against Mucoepithelial Bacterial Infection and Allergic Responses. *Immunity* **30**, 108-119 (2009).

49.   A. Mortha *et al.*, Microbiota-Dependent Crosstalk Between Macrophages and ILC3 Promotes Intestinal Homeostasis. *Science* **343**, 1249288 (2014).

50.   C. Pearson *et al.*, ILC3 GM-CSF production and mobilisation orchestrate acute intestinal inflammation. *Elife* **5**, e10066 (2016).

51.   G. Eberl, D. R. Littman, Thymic Origin of Intestinal αß T Cells Revealed by Fate Mapping of RORγt+ Cells. *Science* **305**, 248 (2004).

52.   C. Vonarbourg *et al.*, Regulated Expression of Nuclear Receptor RORγt Confers Distinct Functional Fates to NK Cell Receptor-Expressing RORγt+ Innate Lymphocytes. *Immunity* **33**, 736-751 (2010).

53.   J. H. Bernink *et al.*, Human type 1 innate lymphoid cells accumulate in inflamed mucosal tissues. *Nature Immunology* **14**, 221-229 (2013).

54.   Y. Zheng *et al.*, Interleukin-22 mediates early host defense against attaching and effacing bacterial pathogens. *Nature Medicine* **14**, 282-289 (2008).

55.   N. Satoh-Takayama *et al.*, Microbial flora drives interleukin 22 production in intestinal NKp46+ cells that provide innate mucosal immune defense. *Immunity* **29**, 958-970 (2008).

56.   G. F. Sonnenberg, L. A. Monticelli, M. M. Elloso, L. A. Fouser, D. Artis, CD4(+) lymphoid tissue-inducer cells promote innate immunity in the gut. *Immunity* **34**, 122-134 (2011).

57.   J. Li, D. S. Shouval, A. L. Doty, S. B. Snapper, S. C. Glover, Increased Mucosal IL-22 Production of an IL-10RA Mutation Patient Following Anakin Treatment Suggests Further Mechanism for Mucosal Healing. *J Clin Immunol* **37**, 104-107 (2017).

58.   K. Wolk *et al.*, IL-22 Increases the Innate Immunity of Tissues. *Immunity* **21**, 241-254 (2004).

59.   Y. Goto *et al.*, Innate lymphoid cells regulate intestinal epithelial cell glycosylation. *Science (New York, N.Y.)* **345**, 1254009-1254009 (2014).

60.   G. Pickert *et al.*, STAT3 links IL-22 signaling in intestinal epithelial cells to mucosal wound healing. *Journal of Experimental Medicine* **206**, 1465-1472 (2009).

61.   X. Kong, D. Feng, S. Mathews, B. Gao, Hepatoprotective and anti-fibrotic functions of interleukin-22: therapeutic potential for the treatment of alcoholic liver disease. *J Gastroenterol Hepatol* **28 Suppl 1**, 56-60 (2013).

62.   M. S. Wilson *et al.*, Redundant and pathogenic roles for IL-22 in mycobacterial, protozoan, and helminth infections. *J Immunol* **184**, 4378-4390 (2010).

63.   Y. Zhang *et al.*, A proinflammatory role for interleukin-22 in the immune response to hepatitis B virus. *Gastroenterology* **141**, 1897-1906 (2011).

64.   J. Zhao *et al.*, Pathological functions of interleukin-22 in chronic liver inflammation and fibrosis with hepatitis B virus infection by promoting T helper 17 cell recruitment. *Hepatology* **59**, 1331-1342 (2014).

65.   T. Verrier *et al.*, Phenotypic and Functional Plasticity of Murine Intestinal NKp46+ Group 3 Innate Lymphoid Cells. *The Journal of Immunology* **196**, 4731 (2016).

66.   Jochem H. Bernink *et al.*, Interleukin-12 and -23 Control Plasticity of CD127+ Group 1 and Group 3 Innate Lymphoid Cells in the Intestinal Lamina Propria. *Immunity* **43**, 146-160 (2015).

67. M. B. M. Teunissen *et al.*, Composition of Innate Lymphoid Cell Subsets in the Human Skin: Enrichment of NCR+ ILC3 in Lesional Skin and Blood of Psoriasis Patients. *Journal of Investigative Dermatology* **134**, 2351-2360 (2014).

68. K. Hoorweg *et al.*, Functional Differences between Human NKp44− and NKp44+ RORC+ Innate Lymphoid Cells. *Frontiers in Immunology* **3**, (2012).

69. M. R. Hepworth *et al.*, Immune tolerance. Group 3 innate lymphoid cells mediate intestinal selection of commensal bacteria-specific CD4+ T cells. *Science (New York, N.Y.)* **348**, 1031-1035 (2015).

70. G. R. Yannam, T. Gutti, L. Y. Poluektova, IL-23 in infections, inflammation, autoimmunity and cancer: possible role in HIV-1 and AIDS. *J Neuroimmune Pharmacol* **7**, 95-112 (2012).

71. J. Qiu *et al.*, The aryl hydrocarbon receptor regulates gut immunity through modulation of innate lymphoid cells. *Immunity* **36**, 92-104 (2012).

72. M. H. Kim, E. J. Taparowsky, C. H. Kim, Retinoic Acid Differentially Regulates the Migration of Innate Lymphoid Cell Subsets to the Gut. *Immunity* **43**, 107-119 (2015).

73. G. Gasteiger, X. Fan, S. Dikiy, S. Y. Lee, A. Y. Rudensky, Tissue residency of innate lymphoid cells in lymphoid and nonlymphoid organs. *Science* **350**, 981-985 (2015).

74. A. I. Lim *et al.*, Systemic Human ILC Precursors Provide a Substrate for Tissue ILC Differentiation. *Cell* **168**, 1086-1100.e1010 (2017).

75. E. Ahn *et al.*, Role of PD-1 during effector CD8 T cell differentiation. *Proceedings of the National Academy of Sciences* **115**, 4749 (2018).

76. J. R. Groom, A. D. Luster, CXCR3 in T cell function. *Exp Cell Res* **317**, 620-631 (2011).

77.   A. R. Burton *et al.*, Circulating and intrahepatic antiviral B cells are defective in hepatitis B. *The Journal of clinical investigation* **128**, 4588-4603 (2018).

78.   L. Salimzadeh *et al.*, PD-1 blockade partially recovers dysfunctional virus-specific B cells in chronic hepatitis B infection. *The Journal of clinical investigation* **128**, 4573-4587 (2018).

79.   K. Kimura *et al.*, Dysregulated balance of retinoid-related orphan receptor gammat-dependent innate lymphoid cells is involved in the pathogenesis of chronic DSS-induced colitis. *Biochem Biophys Res Commun* **427**, 694-700 (2012).

80.   O. Boyman, Bystander activation of CD4+ T cells. *Eur J Immunol* **40**, 936-939 (2010).

81.   G. F. Sonnenberg *et al.*, Innate Lymphoid Cells Promote Anatomical Containment of Lymphoid-Resident Commensal Bacteria. *Science* **336**, 1321 (2012).

82.   Y. Feng *et al.*, Antibiotics induced intestinal tight junction barrier dysfunction is associated with microbiota dysbiosis, activated NLRP3 inflammasome and autophagy. *PloS one* **14**, e0218384-e0218384 (2019).

83.   Z. Jie *et al.*, Intrahepatic innate lymphoid cells secrete IL-17A and IL-17F that are crucial for T cell priming in viral infection. *Journal of immunology (Baltimore, Md. : 1950)* **192**, 3289-3300 (2014).

84.   J. L. Gommerman *et al.*, A role for surface lymphotoxin in experimental autoimmune encephalomyelitis independent of LIGHT. *The Journal of clinical investigation* **112**, 755-767 (2003).

85.   S. Scheu *et al.*, Targeted disruption of LIGHT causes defects in costimulatory T cell activation and reveals cooperation with lymphotoxin beta in mesenteric lymph node genesis. *J Exp Med* **195**, 1613-1624 (2002).

86. D. A. Giles *et al.*, The Tumor Necrosis Factor Superfamily Members TNFSF14 (LIGHT), Lymphotoxin β and Lymphotoxin β Receptor Interact to Regulate Intestinal Inflammation. *Frontiers in Immunology* **9**, (2018).

87. K. Schneider, K. G. Potter, C. F. Ware, Lymphotoxin and LIGHT signaling pathways and target genes. *Immunol Rev* **202**, 49-66 (2004).

88. M. L. del Rio, C. L. Lucas, L. Buhler, G. Rayat, J. I. Rodriguez-Barbosa, HVEM/LIGHT/BTLA/CD160 cosignaling pathways as targets for immune regulation. *J Leukoc Biol* **87**, 223-235 (2010).

89. J. L. Browning *et al.*, Characterization of lymphotoxin-alpha beta complexes on the surface of mouse lymphocytes. *J Immunol* **159**, 3288-3298 (1997).

90. S. L. Hall *et al.*, IL-17A enhances IL-13 activity by enhancing IL-13-induced signal transducer and activator of transcription 6 activation. *J Allergy Clin Immunol* **139**, 462-471.e414 (2017).

91. A. K. Savage, H.-E. Liang, R. M. Locksley, The Development of Steady-State Activation Hubs between Adult LTi ILC3s and Primed Macrophages in Small Intestine. *The Journal of Immunology* **199**, 1912 (2017).

92. S. D. Pippig *et al.*, Robust B cell immunity but impaired T cell proliferation in the absence of CD134 (OX40). *J Immunol* **163**, 6520-6529 (1999).

93. G.-Y. Seo *et al.*, LIGHT-HVEM Signaling in Innate Lymphoid Cell Subsets Protects Against Enteric Bacterial Infection. *Cell Host & Microbe* **24**, 249-260.e244 (2018).

94. J. Schindelin *et al.*, Fiji: an open-source platform for biological-image analysis. *Nature Methods* **9**, 676-682 (2012).

95.   C. A. Schneider, W. S. Rasband, K. W. Eliceiri, NIH Image to ImageJ: 25 years of image analysis. *Nature Methods* **9**, 671-675 (2012).

96.   J. Schindelin, C. T. Rueden, M. C. Hiner, K. W. Eliceiri, The ImageJ ecosystem: An open platform for biomedical image analysis. *Molecular Reproduction and Development* **82**, 518-529 (2015).

97.   C. Sommer, C. Straehle, U. Köthe, F. A. Hamprecht, in *2011 IEEE International Symposium on Biomedical Imaging: From Nano to Macro*. (2011), pp. 230-233.

98.   F. Pedregosa *et al.*, Scikit-learn: Machine Learning in Python. *J. Mach. Learn. Res.* **12**, 2825–2830 (2011).

99.   M. Ester, H.-P. Kriegel, J. Sander, X. Xu, paper presented at the Proceedings of the Second International Conference on Knowledge Discovery and Data Mining, Portland, Oregon, 1996.

100.   B. M. Bolstad, R. A. Irizarry, M. Astrand, T. P. Speed, A comparison of normalization methods for high density oligonucleotide array data based on variance and bias. *Bioinformatics* **19**, 185-193 (2003).

101.   S. Holm, A Simple Sequentially Rejective Multiple Test Procedure. *Scandinavian Journal of Statistics* **6**, 65-70 (1979).

102.   R. C. Gentleman *et al.*, Bioconductor: open software development for computational biology and bioinformatics. *Genome Biol* **5**, R80 (2004).

103.   G. K. Smyth, Linear models and empirical bayes methods for assessing differential expression in microarray experiments. *Stat Appl Genet Mol Biol* **3**, Article3 (2004).

Publishing Agreement

It is the policy of the University to encourage open access and broad distribution of all theses, dissertations, and manuscripts. The Graduate Division will facilitate the distribution of UCSF theses, dissertations, and manuscripts to the UCSF Library for open access and distribution. UCSF will make such theses, dissertations, and manuscripts accessible to the public and will take reasonable steps to preserve these works in perpetuity.

I hereby grant the non-exclusive, perpetual right to The Regents of the University of California to reproduce, publicly display, distribute, preserve, and publish copies of my thesis, dissertation, or manuscript in any form or media, now existing or later derived, including access online for teaching, research, and public service purposes.

_____ Author Signature

6/4/2020
_____
                                    Date